
An Integrative Approach to Dynamic Processes in Reverse Osmosis Desalination

Omomayowa Akele

Thesis submitted to the University of Nottingham for the degree of Doctor of
Philosophy, October 2021

Supervisors:

Prof John King

Dr Matteo Icardi

Dr Veerle Vandeginste

University of Nottingham
School of Mathematical Sciences
Project funded by The Leverhulme Trust

Abstract

The reverse osmosis membrane module is an integral element of a desalination system as it determines the overall performance of the desalination plant. The fraction of clean water that can be recovered via this process is often limited by salt precipitation. It has become apparent that precipitation plays a critical role in the sustainability of reverse osmosis desalination. Hence, the main objective that guides this research is unravelling some of the mysteries associated with precipitation, whilst considering it in the context of the other dynamic processes at work.

Overall, in this thesis we focus on three main topics:

- Calcium carbonate (CaCO_3) precipitation: In Chapter 2 we conduct batch experiments to investigate the effect of SO_4^{2-} on CaCO_3 precipitation. The results from this study informs the model formulation and also provides new insights into the precipitation that occurs in desalination.
- Macroscopic reverse osmosis model: A search of the literature revealed that the fundamental processes in reverse osmosis desalination are often studied in isolation. In this study, the individual mechanisms that are considered to play a critical role in the system behaviour are amalgamated. Our main contribution here is a model framework based on experimental observations and existing literature.
- Nondimensionlisation: We nondimensionalised the governing equations in Chapter 4, allowing us to identify the dimensionless groups which control the solution behaviour. These dimensionless groups served as an important tool for understanding the physics of the various phenomena.
- Analysis: In Chapter 5, we made some physical interpretations of the dimensionless numbers and investigated the influence of different dimensionless groups on four quantities: namely, concentration polarisation, osmotic pressure, recovery and porosity. It was shown that the influence of each dimensionless group changes when we move from a single-solute systems to a multi-component system. The results also provided significant insight on the relative influence of fluid dynamics and solute transport on precipitation and recovery.

Taken collectively, the content of this thesis establishes a framework for analysing and understanding reverse osmosis membrane operations. The study undertaken by the author sheds light on some of the complex interplay between sub-processes

such as precipitation, fluid flow, mass transport which together influence recovery and in turn process sustainability. It also lays the groundwork for future research into the control of precipitation.

Acknowledgements

First and foremost, I would like to thank God, Yahweh, I would not be where I am now without divine intervention. I have been given the gift of creating connection between texts and synthesising information/ideas. There is also a constant yearning for knowledge and a determination to see a problem through to its resolution, no matter how formidable. No other traits could possibly have served me better for working on this project.

I am particularly thankful for my family. The endorsement, support and advice from my parents, Ayodele and Omotayo kept me grounded in the midst of chaos. I'm particularly grateful to my mum for her unfaltering belief in me and for always lending a listening ear, especially when I needed it the most.

My two elder sisters, Sola and Lara never let me lose sight of the things which matter the most. Thanks for always being there for me, guiding me through some of the most important years of my life. Sola's confidence in my capability has been truly encouraging. Lara's ability to relate to my struggles when it seemed nobody else could has helped me overcome adversity in numerous occasions.

I am thankful for Toyon who has also been a voice of encouragement not only for the project but also for my career. He taught me the basis of my profession which has underpinned many of my career achievements.

Matteo Icardi deserves special thanks for steering the direction of this project and assisting in the organisation of this thesis. He saw early on that what I was doing had value. He provided much guidance on physical interpretations of models and also unspoken conventions and practices in Mathematics. His enthusiasm for the project was always encouraging - our conversations always pushed me in the right direction especially when a problem seemed just out of my reach. Our discussions were also useful in discerning many items that needed inclusion in this thesis and produced questions that readers were sure to ask.

I am thankful to John King for highlighting early on the importance of a working document which encouraged me to write often. This has been extremely useful as the thesis you now read is a synthesis of all the working documents I produced over the years. Thanks also go out to Veerle Vandigenste who provided guidance and direction on experimental methods.

I would also like to thank Markus Owen and the Leverhulme Trust for their steadfast belief in the value of this project and their consistent support of it.

Dedication

This thesis is dedicated to my father - he was one of a kind. His exemplary traits and highly principled personality instilled self-discipline and hard work into me at a young age, which has helped me achieve anything I set my mind to. You are my inspiration and will always be in my heart.

Contents

1	Introduction	1
1.1	What is Desalination?	1
1.2	What is Reverse Osmosis Desalination?	2
1.3	Environmental & Technical Issues	3
1.3.1	Energy Requirements	3
1.3.2	Environmental Impacts	4
1.3.3	Mineral Scaling	4
1.4	Research & Limitations	6
1.4.1	Research Approach	6
1.4.2	Inadequacies of Modelling Studies	6
1.4.3	Inadequacies of Experimental Studies	7
1.5	Research Aims & Contributions	8
1.5.1	Experimental Aims	8
1.5.2	Mathematical Aims	9
1.5.3	Specific Contributions	9
1.6	Outline	11
2	Experimental Study	12
2.1	Literature Review	12
2.1.1	CaCO ₃ Precipitation	13
2.1.2	Brief History of CaCO ₃ Investigations	15
2.1.3	Why study CaCO ₃ Precipitation?	16
2.1.4	Previous Research	16
2.1.5	Our Approach	17
2.2	Experimental Procedure	19
2.2.1	Materials and Methods	20
2.2.2	Sample Characterisation	22
2.3	Results	22
2.3.1	General Observations	22
2.3.2	ICP-EOS - Calcium Evolution	24

2.3.3	PXRD - Precipitate Mineralogy	24
2.3.4	SEM & EDX Analysis - Precipitate Morphology	27
2.4	Discussion	27
2.4.1	Influence of Sulphate Anions on CaCO_3 Scale	33
2.4.2	Co-precipitation of NaCl with CaCO_3	35
2.5	Kinetic Model	36
2.5.1	Reaction Network	36
2.5.2	Rate Equations	38
2.5.3	Simulation	42
2.6	Summary	42
3	Model Development	44
3.1	Introductory Remarks	44
3.1.1	Membrane Terms and Definitions	44
3.1.2	Membrane Mode of Operation	47
3.1.3	Membrane Configuration	48
3.2	Literature Review	51
3.2.1	Fluid Dynamics	52
3.2.2	Membrane Transport Theory	53
3.2.3	Design Studies	55
3.2.4	Geometry Studies	56
3.2.5	Precipitation Studies	56
3.2.6	Our Approach	59
3.3	Model Formulation	60
3.3.1	Interactions & Feedbacks	60
3.3.2	Model Geometry	63
3.3.3	Fluid Flow	65
3.3.4	Solute Transport	68
3.4	Model Implementation	72
3.4.1	Numerical Procedure	72
3.5	Summary	74
4	Mathematical Treatment	76
4.1	Stationary States and Stability	76
4.1.1	Linear Stability Analysis	77
4.2	Non-dimensionalisation	82
4.2.1	Fluid Flow	82
4.2.2	Solute Transport	87
4.2.3	Single-precipitation	91
4.2.4	Co-precipitation	93

4.2.5	Characteristic Timescales	94
4.2.6	Summary of Dimensionless Equations	94
4.3	Summary	97
5	Model Assessment	100
5.1	Outline of Model Assessment	100
5.2	Single-precipitation	101
5.2.1	Concentration Polarisation & Osmotic Pressure	103
5.2.2	Recovery	117
5.2.3	Porosity	125
5.3	Co-precipitation	128
5.3.1	Effect of Co-precipitation on Da & Re	132
5.3.2	Effect of Co-precipitation on Ma	132
5.3.3	Effect of Co-precipitation on θ	134
5.3.4	Effect of Co-precipitation on D_A	134
5.3.5	Effect of Co-precipitation on Pe	137
5.3.6	Effect of Co-precipitation on β	137
5.3.7	Effect of Co-precipitation on ϑ_g	141
5.4	Comparison with Literature	141
5.5	Summary	143
6	Summary and Conclusions	147
6.1	Future Work	149
	Bibliography	150

List of Figures

1.1	Layout of a desalination system [88].	2
1.2	Schematic of the separation process through a cross-flow reverse osmosis membrane. The blue circles represent water molecules whilst the grey circles represent salt ions. The permeate contains mostly water molecules and the retentate is mostly made up of salt ions [88].	3
1.3	Energy consumption at different stages of a reverse osmosis desalination plant [6].	4
1.4	White CaCO_3 scale on a spiral wound reverse osmosis membrane module [40].	5
2.1	The various morphologies of CaCO_3 polymorphs. Calcite is seen to have a cubic/rhombohedral shape whereas vaterite and aragonite respectively have a spherical and needle-like shape [26].	14
2.2	Experimental setup.	21
2.3	The colour of the individual solutions serves as an indication for saturation. E1 and E5 turned cloudy when the reaction was initiated - this suggests that these solutions are supersaturated.	23
2.4	The residual concentration of cations (from inductively coupled plasma-optical emission spectrometry (ICP-EOS) analyses) in the samples obtained from experiments E1 and E5. It is worth noting that error bars are not presented because the experiment was only carried out once	24
2.5	The XRD patterns of the precipitates obtained from (a) experiment E1 containing SO_4^{2-} and HCO_3^- anion (b) experiment E5, containing HCO_3^- anion.	25
2.6	SEM and EDX images of the precipitate formed in experiment E1 containing SO_4^{2-} and HCO_3^- anions. In these images, calcite appears as a rhombohedral crystal, vaterite appears as spherical crystals and halite as an elongated crystal.	28

2.7	SEM and EDX images of the precipitate from E1. The green pointers in the SEM images on the left hand side points to the crystal of interest and the right images are the corresponding elemental composition in that location.	29
2.8	SEM and EDX images of the precipitate from E2. The green pointers in the SEM images (c & e) points to the crystal of interest and the right images (d & f) are the corresponding elemental composition in that location.	30
2.9	SEM and EDX images of the precipitate from E5. Calcite appears as cuboid/rhombohedral aggregates while halite appears as an elongated crystal.	31
2.10	Sequential process that led to precipitation in E1, E2 and E5. . .	32
2.11	Sequential processes leading to precipitation in E1.	32
2.12	Fit between model and experimental results for cation concentrations in E1.	41
3.1	Illustration of the polarised layer occurring as a result of concentration polarisation.	47
3.2	Schematic representation of (a) cross-flow mode and (b) dead-end mode.	48
3.3	This illustration depicts an unwound configuration to demonstrate the flow direction in a spiral wound configuration [73].	49
3.4	The assembly and fabrication of spiral wound membrane module [73].	50
3.5	(a) Schematic illustration of the arrangement of the feed channel, spacer, membrane and permeate channel in a spiral wound membrane module (b) Typical industrial unit showing several spiral wound elements in series [124].	50
3.6	Schematic of (a) spiral wound reverse osmosis membrane module and (b) cross section of a feed channel sandwiched by two pieces of membranes.	57
3.7	Schematic illustration of the interactions between flow, solute transport processes and scaling in RO feed channel.	60
3.8	Coupling between processes can be seen in the governing equations describing the system.	62
3.9	Geometry for flow through a membrane channel, three-dimensional.	63
3.10	Rectangular two-dimensional domain with boundary locations. . .	64
3.11	Schematic illustration of the membrane boundary conditions used in the simulation.	65

3.12	Illustration of the fluxes at the membrane.	70
3.13	Computational domain and mesh of the main study.	73
4.1	Time plots for calcium concentration (ϕ_1) in experiment E1.	81
5.1	Effect of $Da\delta_f$ on (a) polarisation and (b) osmotic pressure.	105
5.2	Concentration profile observed at different times when $Da\delta_f = 1.67 \times 10^{-15}$	106
5.3	Effect of Re on (a) polarisation and (b) osmotic pressure.	108
5.4	Effect of Ma^* on (a) polarisation and (b) osmotic pressure.	110
5.5	The effect of θ on (a) polarisation and (b) osmotic pressure.	111
5.6	Concentration profile observed at 60 seconds for different values of D_{AII}^*	112
5.7	The effect of D_{AII}^*/δ_f on (a) polarisation and (b) osmotic pressure.	113
5.8	The effect of Pe on (a) polarisation and (b) osmotic pressure.	115
5.9	The effect of β on (a) polarisation and (b) osmotic pressure.	116
5.10	The effect of $\vartheta_g\delta_f$ on (a) polarisation and (b) osmotic pressure.	118
5.11	Graph of recovery as a percentage against the dimensionless group $Da\delta_f$, which shows how the recovery depends on Darcy's number.	119
5.12	Graph of recovery as a percentage against the dimensionless group Re , which shows how the recovery depends on Reynold's number.	120
5.13	Graph of recovery as a percentage against the dimensionless group Ma^* , which shows how the recovery depends on how quickly precipitation occurs.	121
5.14	Graph of recovery as a percentage against the dimensionless group θ , which shows how the recovery depends on the relation between the osmotic pressure and the channel's pressure.	122
5.15	Graph of recovery as a percentage against the dimensionless group D_{AII}^*/δ_f , which shows how the recovery depends on Damköhler number.	123
5.16	Graph of recovery as a percentage against the dimensionless group Pe , which shows how the recovery depends on Peclet number.	124
5.17	Graph of recovery as a percentage against the dimensionless group $ \beta $, which shows how recovery depends on the ratio between the pressure gradient across the feed channel (i.e $P_{in} - P_{out}$) and the pressure gradient between the feed channel and permeate channel (i.e $P_p - P_{out}$).	124
5.18	Graph of recovery as a percentage against the dimensionless group $\vartheta_g\delta_f$, which shows how the recovery depends on the ratio between the channel's length and width.	125

5.19	Graph of porosity (as a pore fraction of the membrane) against the dimensionless group Ma^* , which shows how the porosity depends on the severity of precipitation.	126
5.20	Increasing these dimensionless groups (Pe, β , Da, Re) results in a minimal decrease in porosity.	127
5.21	Increasing these dimensionless groups ($\vartheta_g \delta_f, D_{AII}^*/\delta_f$) results in a minimal increase in porosity	129
5.22	Graph of porosity (as a pore fraction of the membrane) against the dimensionless group θ , which shows that the ratio between the osmotic pressure and the channel's pressure has no effect on porosity	130
5.23	Comparison between single-precipitation and co-precipitation at different values of $Da\delta_f$	131
5.24	Comparison between single-precipitation and co-precipitation at different values of Re	133
5.25	Comparison between single-precipitation and co-precipitation at different values of Ma	135
5.26	Comparison between single-precipitation and co-precipitation at different values of θ	136
5.27	Comparison between single-precipitation and co-precipitation at different values of D_A	138
5.28	Comparison between single-precipitation and co-precipitation at different values of Pe	139
5.29	Comparison between single-precipitation and co-precipitation at different values of β	140
5.30	Comparison between single-precipitation and co-precipitation at different values of $\vartheta_g \delta_f$	142
5.31	Summary of results obtained from varying the dimensionless groups.	146

List of Tables

2.1	Summary of the initial fluid chemistry.	19
2.2	Mineral identity of the precipitate recovered in each experiment. .	26
2.3	$\text{SO}_4^{2-}:\text{HCO}_3^-$ of the solutions from which precipitate was recovered.	34
4.1	Summary of the chosen scales for the several variables.	95
4.2	Characteristic timescales.	96
4.3	Dimensionless numbers obtained from non-dimensionalisation of Navier–Stokes Equations and Solute Transport Equation.	98
5.1	Range of the dimensional variables from the Navier-Stokes equation and the solute transport equation.	102
5.2	Table showing the range of physically realistic dimensionless group values deduced from Table 5.1 and the range of dimensionless group values used in simulations	103

Chapter 1

Introduction

This chapter provides an introduction to membrane based desalination mainly from a theoretical point of view, in order to lay the proper groundwork for the mathematical and experimental investigation to follow in subsequent chapters. It begins with some basic definitions and principles of desalination, then goes on to introduce the concept of desalination sustainability and its underlying elements. We shed light on some topics specifically related to reverse osmosis such as precipitation and reverse osmosis modelling. We remark on why an integrative study of reverse osmosis processes is important and conclude with a list of contributions that this project makes to the literature.

1.1 What is Desalination?

Desalination - the conversion of saline water to potable water is a widely-applied technology [62]. It plays a vital role in addressing the issue of water scarcity in various parts of the world, such as Saudi Arabia, United Arab Emirates, Australia, United States of America, Spain, Portugal, Greece, China and India [28, 54, 88].

Figure 1.1 shows the key elements in a desalination system. This includes the feed water intake, the pretreatment, the desalination process and the post-treatment [88]. The feed water intake is the structure that extracts seawater or saline ground water (commonly referred to as brackish water) from a water source and transports it to the process system. During pretreatment, suspended solids are removed from the seawater and chemicals are added to control biological growth and prevent mineral scaling. The desalination step is the main process where salt ions are removed from seawater. Following this, chemicals are added to the treated water during post-treatment to prevent

corrosion and ensure compatibility with potable water standards [88].

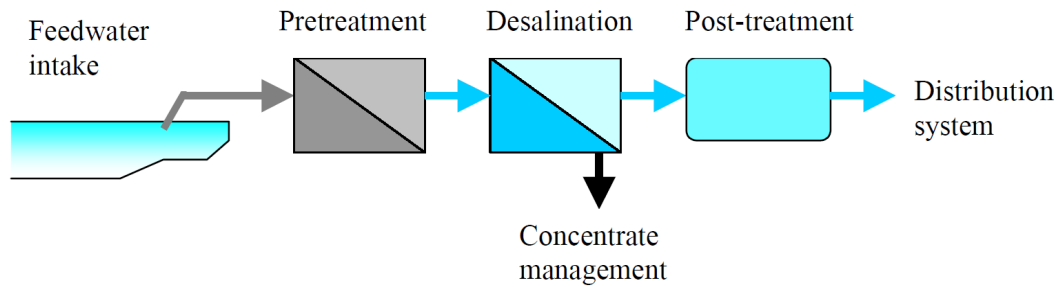


Figure 1.1: Layout of a desalination system [88].

The desalination process, that is, the removal of salt ions from seawater is usually achieved via thermal desalination or membrane-based desalination [6, 28]. The former mimics the natural cycle of evaporation and condensation. The saline water is heated until it is vaporised then the salt-free vapour is condensed and recovered as potable water. The latter employs a reverse osmosis membrane barrier which selectively allows water to pass through [6]. Reverse osmosis (RO) desalination has emerged as the technology of choice for most large-scale industrial plants and is therefore the main focus of this project. We discuss the process in more detail below.

1.2 What is Reverse Osmosis Desalination?

To understand the process of reverse osmosis, it is necessary to first explain the naturally occurring phenomenon known as osmosis. Osmosis is the flow of water/solvent through a semipermeable membrane from a less concentrated solvent to a more concentrated solvent [22]. Some examples of osmosis include: the absorption of water and mineral from soil by the roots of plants and the absorption of water from our blood by kidneys [55]. Osmosis occurs naturally without any external energy so to reverse osmotic flow some pressure must be applied to the more concentrated solution. This prevents salt ions from going through the semipermeable membrane. The pressure required to counter osmosis is known as the osmotic pressure.

In reverse osmosis desalination, a “force” (pressure) greater than the naturally occurring osmotic pressure is applied on the feed side of the reverse osmosis membrane [22]. This creates a pressure gradient across the membrane that retains unwanted salt ions on the feed side and allows water molecules to pass through the membrane. As unwanted salt ions are rejected, the feed solution becomes more concentrated as shown in Figure 1.2. This concentrated solution is called the concentrate (also commonly known as the retentate or brine). The purified

water that passes through the membrane is often referred to as the permeate and is relatively free of the targeted salt ions [22]. The permeate stream exits at nearly atmospheric pressure while the concentrate remains at nearly the feed pressure [22, 51].

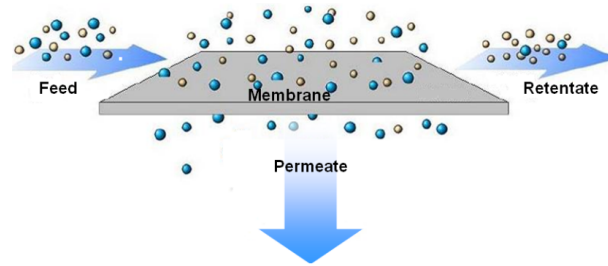


Figure 1.2: Schematic of the separation process through a cross-flow reverse osmosis membrane. The blue circles represent water molecules whilst the grey circles represent salt ions. The permeate contains mostly water molecules and the retentate is mostly made up of salt ions [88].

The energy requirements for reverse osmosis is significantly lower than the energy required for thermal desalination [28]. As a result, reverse osmosis has become the technology of choice for most desalination plants.

1.3 Environmental & Technical Issues

In this section, we briefly review some of the technical and environmental issues associated with reverse osmosis desalination. We focus on the energy requirements, environmental impacts and a phenomenon known as mineral scaling. This phenomenon will later become a central element of this thesis.

1.3.1 Energy Requirements

The energy required to power desalination in reverse osmosis based plants is around 2-4 kWh/m³ [6, 28]. This energy is usually generated by conventional power plants, which rely on burning fossil fuel, thereby emitting significant quantities of greenhouse gases [6].

Figure 1.3 provides an estimate of the proportion of energy consumed at different stages of a RO-based desalination plant. It can be seen that the RO-based process (i.e., membrane process) is the most energy intensive process, accounting for almost 70% of the total energy consumption. Given the rapidly growing demand for potable water and the limited supply of freshwater resources in many parts of the world, suitable modifications in the RO process is necessary in order to reduce the energy consumption and ensure the sustainability of reverse osmosis desalination.

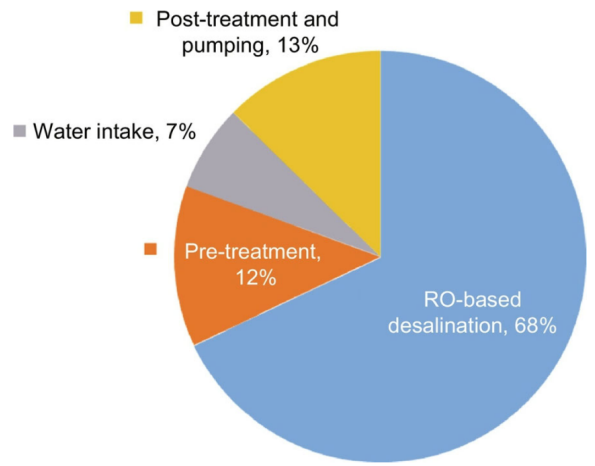


Figure 1.3: Energy consumption at different stages of a reverse osmosis desalination plant [6].

1.3.2 Environmental Impacts

There are major concerns regarding the environmental impact of desalination plants. A well known problem associated with desalination is the discharge of brine (usually about twice the salinity level of the source water) into the sea [127]. Typically, the brine contains chemicals used in pretreatment and membrane cleaning which could pose a risk to organisms in marine environment [6, 28].

To minimize the adverse impact of desalination on the environment, a variety of strategies are being adopted to increase the recovery of water. It is expected that recovering a higher fraction of the feed water will reduce the volume of concentrate that must be disposed of. However, we will see shortly in the next subsection that this is often not the case; water recovery is limited by scaling of sparingly soluble salts.

1.3.3 Mineral Scaling

As we mentioned in the preceding subsection, there is significant interest in increasing the recovery of RO desalination because this decreases the quantity of brine discharge. Other benefits of increased recovery includes: reduced operating cost and reduced environmental impacts [65]. However, a key challenge associated with an increase in water recovery is mineral scaling. Scaling occurs when sparingly soluble salt become concentrated as more unwanted ions are retained on the feed side of the membrane. As a result, cationic and anionic species such as $\text{Ca}^{2+}/\text{Mg}^{2+}$ and $\text{CO}_3^{2-}/\text{SO}_4^{2-}$ begin to exceed their solubility limit, forming salt precipitate such as CaCO_3 . These precipitates deposit on the membrane surface as shown in Figure ??.

Generally, mineral scalants are present near saturation levels in natural water, thus even the extraction of small volumes of water raises their concentration level, increasing the likelihood of precipitation [22, 107]. Therefore recovery is usually limited to 35 - 50% in seawater desalination and 70 - 85% in brackish water desalination [3, 65]. The scalants usually encountered in desalination plants include CaCO_3 , CaSO_4 , BaSO_4 , CaF_2 , SrSO_4 and $\text{Ca}_3(\text{PO}_4)_2$ [22, 65]. Of these, CaCO_3 is the most common so we will restrict attention to this scalant [107].



Figure 1.4: White CaCO_3 scale on a spiral wound reverse osmosis membrane module [40].

Impact of scaling

The mineral scale that forms on the membrane surface has well known detrimental effects on the performance of the membrane [93]. It reduces water permeability by blocking the membrane surface which disrupts the fluid flow. This reduces permeate quantity [40, 48], consequently desalination operators increase feed pressures to force water through the membrane and maintain the desired permeate flows. This in turn increases the operating costs and energy consumption of the membrane system which is the opposite of what is desired [14, 22].

Chemical cleaning is usually employed to restore the membrane after scaling. However with severe scaling, the membrane is left permanently damaged. Antiscalants and scale inhibitors are often employed to tackle scaling, however their effectiveness is limited so scales still often clog RO membranes, reducing the efficiency of the reverse osmosis desalination process.

We see from this that the techniques adopted to control these scalants are usually detrimental to the sustainability of desalination. It would thus seem useful to conduct more research into scaling, antiscalant, scaling inhibitors and scaling

promoters to ensure the sustainability of desalination. In this study, we make some contributions to the subject by conducting investigations into CaCO_3 as it is the most common scalant observed in desalination operations.

1.4 Research & Limitations

As we have alluded to earlier, the reverse osmosis membrane module is an integral element of a membrane based desalination system as it determines the overall performance of the plant. Hence scientific investigations are currently focused on technological advances, that might lead to significant improvement in the design and performance of reverse osmosis modules. In this section, a brief review of the relevant studies concerning reverse osmosis membrane models and CaCO_3 scale is presented. We also shed some light on research limitations and the difficulties encountered when investigating reverse osmosis desalination.

1.4.1 Research Approach

Research on reverse osmosis desalination has been considerably constrained by the compact design of the membrane elements. The membrane channels are incredibly narrow (width $< 1\text{mm}$) with high packing density, that is high specific membrane surface area [22, 59]. This makes it difficult to gather data on local processes occurring inside real membrane modules during operation [58]. Usually researchers only have access to post mortem membrane autopsies or average operating parameters which obviously have limitations [59].

Research on reverse osmosis desalination is usually restricted mostly to idealised models and experiments in simplified geometries which attempt to mimic conditions in reverse osmosis modules. These models and experiments are often targeted at small size test sections which correspond to “local” conditions in a much larger membrane sheet [59]. For example, the fluid dynamics and transport is investigated over a macro length scale, covering a few “unit cells” of the membrane element [59]. It is assumed that the results can be directly translated to the entire membrane module [35].

1.4.2 Inadequacies of Modelling Studies

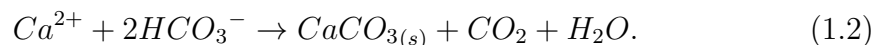
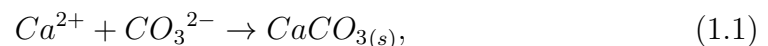
A search of the literature revealed that the models describing fundamental processes in reverse osmosis desalination are normally studied in isolation. These models have the advantage that they are specialised and advanced often focusing on individual features such as geometry, fluid dynamics, mass

transport, polarisation, crystal nucleation/growth and spacer geometry. However, this specialist approach does not fully explain the complex interplay of material flow, transport, and reactions occurring at multiple time scales which characterize most desalination systems. Therefore a need was perceived for a more integrative model, which provides an objective and systematic means of evaluating the effects of coupled dynamic chemical and physical processes occurring in desalination systems. This model is not designed to replace or improve upon industrial scale reverse osmosis models; but to provide qualitative and quantitative information on the relative importance and role of fundamental processes that are normally studied in isolation.

1.4.3 Inadequacies of Experimental Studies

It is probably useful at this point to define precipitation which is one of the key terms used in this thesis. Precipitation - sometimes referred to as reactive crystallization is the formation of a sparingly soluble solid phase from a liquid solution [53, 92]. In this study, the term “precipitate” and “scale” are used interchangeably to refer to the sparingly soluble salt (for instance CaCO_3) that crystallises during desalination. Precipitation is governed by factors such as supersaturation and nucleation, in fact high supersaturation conditions are necessary to initiate precipitation.

As we mentioned earlier in this chapter, calcium carbonate (CaCO_3) precipitate will be the one of the two major focus points of this thesis. Therefore we will briefly describe the calcium carbonate precipitation process and factors that influence it. As the aims of our investigations ties strongly to this process, understanding the factors that influence the calcium carbonate precipitation process is crucial to understanding the overall purpose of the current research



Calcium carbonate precipitation occurs when calcium ion is combined with either carbonate or bicarbonate ions as shown in (1.1) and (1.2) [9, 44]. It has been widely reported that the presence of anions in the feed such as SO_4^{2-} alters the growth, size, composition and morphology of the CaCO_3 that crystallises [33, 123]. This has significant implications on the sustainability of desalination. Understanding the specific role of sulphate (SO_4^{2-}) anion could inform decisions relating to scaling mitigation or inhibition. Surprisingly, there

is minimal research in the literature specifically addressing the effect of this ion on CaCO_3 precipitation in desalination systems. One of the few studies [123] which addressed this investigated the induction times of CaCO_3 in the presence of Mg^{2+} and SO_4^{2-} . However, there was no clear comparison between the CaCO_3 formed in a pure solution and the CaCO_3 formed in the presence of SO_4^{2-} . Hence we are still unable to draw general conclusions on the specific influence of sulphate anions on CaCO_3 precipitation in desalination systems. Most of the other studies conducted have been outside a desalination context [33, 71, 81, 119]. Therefore, these failed to mimic the saturation levels and water chemistry encountered in feed/concentrate streams of desalination systems. In addition, the fluid chemistry often used is vastly different from that observed in reality. For instance investigations made by [33] illustrated the effect of SO_4^{2-} on the mineralogical evolution of CaCO_3 precipitates however it's again difficult to draw general conclusions from their results as their studies excludes NaCl which is the major salt present in desalination processes.

1.5 Research Aims & Contributions

The main objective that guides this research is the sustainability of reverse osmosis desalination. The only way to ensure sustainability is to increase water recovery, prevent or control precipitation and minimize the brine discharged. In this study, we focus on precipitation because it directly controls the fraction of the feed water that can be recovered and the volume of brine discharged.

We adopt both modelling and experimentation in this study to provide a rounded and detailed illustration of the individual processes such as fluid dynamics, mass transport and precipitation. We note at the outset that the models and experiments presented in this thesis are based on idealised desalination systems. The simplicity of an idealised system allows us to easily unravel the complex interactions between material flow, transport, reaction and multiple timescales which characterize most membrane based desalination systems.

1.5.1 Experimental Aims

We already know from preceding sections that understanding the role of SO_4^{2-} anion on calcium carbonate scale (CaCO_3) precipitation has significant implications on the sustainability of desalination. Understanding the kinetics can assist in the development of new effective measures which could alleviate or eliminate scaling. The other potential benefits of research on this subject are [6]:

1. Increased recovery & reduced brine: Recovery of RO based desalination is limited by scaling so alleviating scaling could increase the quantity of potable water produced. This could also reduce the quantity of brine discharged into the ocean which is one of the most cited environmental impacts of desalination [6].
2. Increased membrane durability: Eliminating scaling could reduce the frequency of membrane cleaning and also extend the membrane life [65].
3. Improved process economics: Desalinated water cost could reduce considerably (currently estimated to be 0.5-0.7USD/m³), making the process affordable for developing countries, the same countries in a dire state of water scarcity [6].

One can easily see the benefits of precipitation research. In this study we will conduct experiments which will generate fresh insights on the specific role of SO₄²⁻ ion on calcium carbonate scale (CaCO₃) precipitation. It is hoped that the results would lay the groundwork for future research into the control of scale formation.

1.5.2 Mathematical Aims

As we mentioned in section 1.4.2, many studies have focused on only individual mechanisms considered to play a critical role in the system behaviour. While such an approach is absolutely vital in advancing our scientific understanding of individual processes, there is also a need to take a broader view of integrated system behavior. This is the second focus point of this study. We adopt an integrative mathematical approach whereby the individual mechanisms and time and space dependent processes which are normally studied in isolation are all synthesised. This permits us to:

- evaluate the relative importance of individual sub-processes by considering them in the context of the other dynamic processes at work
- evaluate the interplay between fluid flow, mass transport and precipitation and the resulting effect on recovery.

1.5.3 Specific Contributions

This study makes the following specific contribution to the field of reverse osmosis desalination:

1. A holistic macroscopic model applicable to reverse osmosis desalination

was developed. The model is time dependent, two-dimensional and the governing equations are solved using a Cartesian coordinate. Various phenomenological approaches for describing the temporal evolution of macroscale parameters such as porosity and permeability are also presented. In addition, the complex interplay between fluid dynamics, mass transport and mineral scaling is analysed.

2. The influence of SO_4^{2-} ions on the formation of CaCO_3 scale was analysed experimentally. To achieve this, we carried out multiple batch experiments. The synthetic solutions prepared were representative of the molar ratios and chemistry found in feed streams of desalination plants. Some experiments were conducted without SO_4^{2-} present to understand what happens in pure CaCO_3 precipitation without SO_4^{2-} ions. The rest of the experiments were conducted with SO_4^{2-} ions present to understand its specific role. To the best of our knowledge, this is the first study to distinguish the specific influence of dissolved SO_4^{2-} ions on the CaCO_3 precipitate formed in a desalination context.

The CaCO_3 crystals from the experiments were characterised by different techniques to determine the mineralogy and morphology. The effect of SO_4^{2-} on the CaCO_3 crystal morphology, shape, size and roughness were discussed. The morphology of the mineral phases of the precipitate was imaged using Scanning Electron Microscope (SEM). Semi-qualitative chemical analyses of the precipitate were obtained using Energy Dispersive X-ray (EDX) software and Powder X-ray diffraction (PXRD) was used to identify the mineral phases. These techniques provided a more complete and scientifically defensible interpretation of experimental observations.

3. A kinetic model to simulate the transient rate of mineral scaling was developed. The kinetic model is linked to other sub-processes which introduces non-linearity and additional complexities to the overall model. The model framework presented in this thesis also served as an interpretive tool for unravelling the complex interactions between coupled processes.
4. Nondimensionlisation - In an attempt to identify the dimensionless groups (ratios of dimensional parameters) which control the solution behaviour, nondimensionlisation was performed. This provided an objective and systematic means of interpreting the effects of the coupled dynamic process and the relative influence of each of them.
5. In order to establish the sources of instability in experimental results,

stability analysis of the experimental results was performed. A further qualitative characterisation of the systems properties by means of stability analysis provided a clearer understanding of the process itself.

6. OpenFOAM (an opensource computational fluid dynamics software) was used to discretise and solve the governing equations and calculate the flow variables of all the simulations. The full source code developed for this project was made publicly accessible. This means the source code will be available to download and install on any computer. We believe this will make it easier for interested researchers to build upon or reproduce this research. They will have the freedom to examine the code, learn from it, adapt it and more importantly introduce concepts/features which the research community could benefit from. The ultimate goal of this project is to contribute to the sustainability challenges facing our world and that is what we hope to achieve with sharing this project's source code.

1.6 Outline

This thesis is organized as follows: Chapter 2 is initially devoted to the presentation of the known theory and elementary topics that are specifically related to CaCO_3 precipitation. In the latter part of Chapter 2, we present the experimental results and elaborate on the specific contributions of this study. The beginning of Chapter 3 is devoted to a number of key terms and definitions which are needed to develop, implement and analyse the model. Following this a review of literature is presented. The governing equations are defined and the problem is formulated with a description of the system and the relevant parameters. We also provide some details about the implementation of the mathematical model in OpenFOAM. Chapter 4 begins with the stability analysis of the nonlinear differential equations which describe experimental observations. Comments are provided about how this translates to the physics of the experiments. In the latter part of the chapter, we nondimensionalise the governing equations and present the dimensionless groups which control the solution behaviour. In Chapter 5 we investigate the influence of each dimensionless group on precipitation and recovery. We present results which describe different regimes and different precipitation mechanisms. The final chapter, Chapter 6 consolidates all of our findings. We highlight their implications on desalination and how all of these ties in with our main objective which is the sustainability of desalination.

Chapter 2

Experimental Study

In the previous chapter we established the context of this research. We highlighted that both modelling and experimentation is adopted in this study to provide a rounded and detailed illustration of individual processes. This chapter focuses on a number of the experimental themes. We begin with an overview of the relevant literature whilst drawing attention to the knowledge gap in the field of study. Subsequently we explain the significance and value of our experimental research. We present the results and also document experimental observations and findings. Following this, we derive a set of ordinary differential equations (ODEs) to describe the rate of change of concentration as observed in the experiments. The chapter concludes with a synthesis of findings, highlighting their implications in a desalination context.

2.1 Literature Review

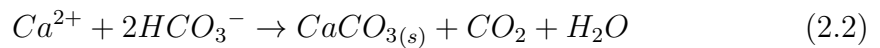
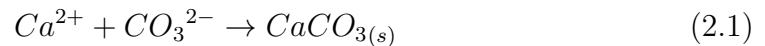
The reader will recall that earlier (when precipitation was introduced in Chapter 1), we noted that the presence of other constituents in the solution may alter the precipitation reaction. In this section, we provide more details on previous investigations on the subject. This is to establish what is already known and provide motivation/justification for the experimental analysis that is described in this chapter.

Thus, we begin our review with a discussion of CaCO_3 precipitation and its polymorph. Then we present a (nearly) chronological historical development of research on the subject, but we make no claim as to completeness of this; the intent is merely to indicate the amount of work that has been done. We follow this with a review of the work by [33, 105, 123] because it contains elements that are important for a basic understanding of the experimental method we will use.

We also provide some remarks specifically associated with the context of their work. Finally, we consider how our research addresses the limitations of these previous studies.

2.1.1 CaCO₃ Precipitation

We have already presented a general background of calcium carbonate precipitation in our earlier discussions in Chapter 1. As noted at that time, calcium carbonate precipitation occurs when calcium ion is combined with either carbonate or bicarbonate ions as shown in (2.1) and (2.2) [9]



We will now provide details of the precipitation characteristics and CaCO₃ polymorphs in order to lay the groundwork for the experimental treatments to follow subsequently.

Precipitation Characteristics

Precipitation is known to generally follow three sequential steps which are: supersaturation, nucleation and crystal growth [65]. Supersaturation conditions are necessary to initiate crystallisation, during which a small nucleus consisting of the salt ions are formed. Upon acquiring stability, the nuclei agglomerate to form salt crystals [70]. This initial nucleation acts as a catalyst, promoting additional scale formation and exponentially increasing the rate of nucleation and precipitation of crystalline scales [40]. Thereafter, subsequent growth occurs due to the adsorption of more ions from the bulk solution [65]. Eventually a scale film is observable on the membrane surface [65]. Nucleation and agglomeration play important roles during precipitation as they can greatly affect the properties of the resulting precipitates [53, 111].

The precipitation reaction is known to occur either by bulk crystallization or surface crystallisation. In the former, the crystals form in the bulk solution and are transported to the membrane surface by convection. In the latter, nucleation and crystal growth occur at the membrane surface [65, 70]. A much debated question is whether the dominant precipitation mechanism in RO membrane operation is bulk or surface crystallisation. Some studies believe that the mineral scaling observed in RO membrane operation is a combination of the two mechanisms whilst others believe surface crystallisation is the dominant

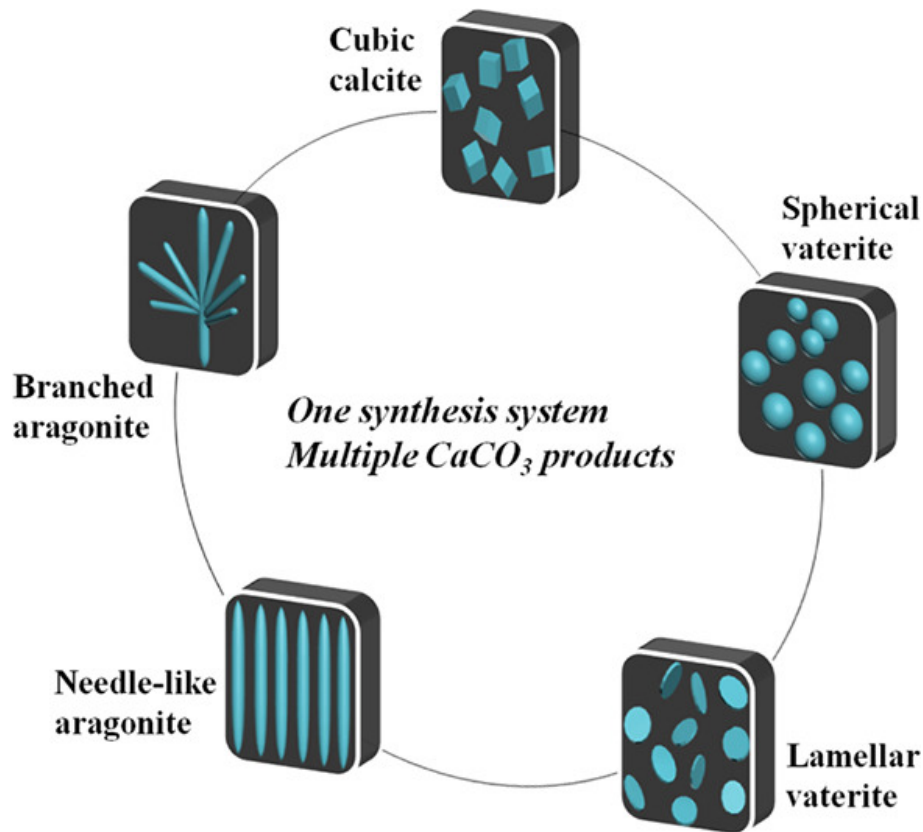


Figure 2.1: The various morphologies of CaCO₃ polymorphs. Calcite is seen to have a cubic/rhombohedral shape whereas vaterite and aragonite respectively have a spherical and needle-like shape [26].

mechanism [5, 70].

CaCO₃ polymorphs

Central to the theme of calcium carbonate precipitation is the concept of polymorphs [78]. Polymorphs are crystalline materials that have the same chemical composition but different molecular arrangements, that is the packing, conformation and orientation of molecules are different [64].

Calcium carbonate is generally classified into three polymorphs: calcite, vaterite and aragonite [33, 95, 97]. Calcite is the most stable polymorph of these three. Calcite crystals can be identified through their cubic shape as shown in Figure 2.1 [97]. Aragonite, a less stable form is mainly found in biosynthetic substances such as shells and corals [97]. Aragonite crystals can be identified by their needle-like shape as shown in Figure 2.1. Vaterite, the least stable polymorph which rarely occurs naturally has a spherical shape as can be seen in Figure ???. We again emphasise that these three polymorphs: vaterite, calcite and aragonite have the same chemical composition (that is they are all CaCO₃) but different molecular arrangements.

2.1.2 Brief History of CaCO₃ Investigations

Although it is beyond the scope of this thesis to provide a thorough review of the historical development of CaCO₃ precipitation, a few observations are in order to provide some context. During the 20th Century, the precipitation of the various types of calcium carbonate polymorphs received increasing attention following the early studies of Credner [21] in the late 19th Century. The work of Johnson, Merwin, and Williamson [49] in the early 20th Century was one of the first detailed investigation into the chemistry of calcium carbonate formation. They found that the factors involved in the precipitation of calcium carbonate, both in nature and artificially, are not direct and simple but, rather, indirect and extremely complex. However, due to inadequate technological facilities, during this early period it was difficult to fully characterise the precipitate. It was not until the mid 20th Century that researchers could employ more robust techniques such as energy dispersive spectroscopy (EDS), X-Ray diffraction (XRD) and Scanning Electron Microscopy (SEM) to fully analyse and characterise the calcium carbonate precipitate. The work of Johnson, Merwin, and Williamson [49] spurred considerable development in the mid 20th Century. From the mid to late 20th Century numerous works began to appear [19, 25, 75, 89, 90, 131, 134] which established that the presence of other constituents in precipitating solution influences the rate and type of calcium carbonate polymorph that crystallises. However, it is important to note that many of the scientific investigations conducted were in a geological context.

Studies conducted in the 21st Century have corroborated the findings from preceding centuries, particularly those relating to the impact of coexisting ions. For example, [61, 136] found that the presence of dissolved organic matter in the precipitating solution inhibits calcite formation whereas [123] and [56] reported that high to moderate concentrations of Mg²⁺, Ni²⁺, Fe³⁺, Zn²⁺, Cu²⁺ promotes the formation of aragonite instead of calcite. It was also revealed by [123] that the presence of Mn²⁺, Cd²⁺, Sr²⁺, Pb²⁺ or Ba²⁺ favours the formation of calcite. In addition, the study by [33] demonstrated that ions such as sulphate inhibit the transformation of calcite.

Although these studies have investigated the role of coexisting ions in calcium carbonate precipitation, much of the focus has been on the interpretation of geologic phenomena. This is because many of these studies have been considered in a geological context. There is minimal research in the literature addressing the effect of foreign ions on CaCO₃ precipitation in desalination systems. Hence, the goal of this chapter is to examine the specific influence of SO₄²⁻ ions on CaCO₃ precipitation in a desalination context.

2.1.3 Why study CaCO₃ Precipitation?

Before launching into a scientific investigation of CaCO₃ precipitation, we need to provide a rationale for doing so. The first point to be aware of is that in the 21st Century, desalination has become extremely crucial for many regions experiencing water scarcity. In Arabian Gulf countries, desalination constitutes more than 90% of the total potable water supply and other countries such as the United States, Spain, China, Australia, and Singapore are increasing their portfolio [6]. However, the water recovery achievable in these desalination systems is often limited by CaCO₃ precipitation. As a result, the quantity of brine discharge increases which in turn increases the operating cost and environmental impacts of desalination [65]. It has become apparent that CaCO₃ precipitation plays a critical role in the sustainability of desalination. In order to provide recommendations on CaCO₃ mitigation or inhibition measures, it is important to understand the mechanisms of the precipitation process and more importantly how different ions influences the CaCO₃ that forms. This is why one of the main goals of this project is to provide the reader with sufficient understanding of how SO₄²⁻ ions directly or indirectly influences the crystallization mechanism of CaCO₃ polymorphs and how this can be translated to desalination systems.

2.1.4 Previous Research

We begin by noting that numerous studies [20, 33, 56, 57, 76, 89, 104, 105, 119, 123] have shown that even at very low concentrations, the presence of sulphate ion could have a tremendous effect on the morphology, mineralogy and composition of the calcium carbonate polymorph that precipitates. The approach we follow in this study is similar to that used in [33, 105, 123]. We will now go on summarising some key elements from their research.

We first observe that authors [33, 105, 123] studied the mechanism of formation of CaCO₃ precipitate by conducting batch experiments and identifying the resulting precipitate using XRD and/or SEM. [105] studied the thermodynamics and kinetics of calcium carbonate and calcium sulfate at varying concentrations of NaCl. They observed that co-precipitation changed the scale morphology of the precipitated crystals. Co-precipitation is generally understood to mean the simultaneous precipitation of more than one mineral salt. At high concentrations, they detected spontaneous precipitation which resulted in instantaneous precipitation of crystals. The study offers more insight into the effect of salinity on co-precipitation.

Waly *et al.* [123] on the other hand investigated the induction time of CaCO₃

precipitation in an effort to quantify the time period preceding the start of CaCO_3 formation. In their study, the residual concentration of the bulk fluid was measured using inductively coupled plasma optical emission spectrometry (ICP-EOS) in order to determine the rate of reaction. They found that the induction time for CaCO_3 precipitation increased when SO_4^{2-} anion was present. However, the authors offer no explanation in regards to the specific role of SO_4^{2-} ions on the CaCO_3 formed. Hence, we are still unable to draw general conclusions on the influence of sulphate anions on CaCO_3 precipitation in desalination systems. Their findings would have been more relevant if there was a comparison between the CaCO_3 formed in a pure solution and the CaCO_3 formed in the presence of SO_4^{2-} .

One of the few studies which have addressed the specific influence of SO_4^{2-} on CaCO_3 precipitation is the work by Fernández-Díaz *et al.* [33]. They studied the nucleation and growth of CaCO_3 from synthetic salt solutions in batch reactors. Their findings indicate that the mineral composition of the precipitates is determined by two factors: the high supersaturation of the solution and the dissolved sulfate content of the solution. The saturation level of the solution controls the phases that form at the initial stages of the crystallization process whereas the sulfate content controls the mineral evolution of the precipitates over time. The results of their investigation also show that the $\text{SO}_4^{2-}:\text{HCO}_3^-$ ratio in the solution affects the morphology of the crystals. For high ratios vaterite is the major constituent phase and for low ratios calcite is the major constituent phase. Although these findings shed new light on the specific role of SO_4^{2-} on CaCO_3 precipitation, the application of these findings to desalination conditions remains obscure as the saturation levels and water chemistry used in their study is vastly different from that observed in desalination plants.

2.1.5 Our Approach

In this project, we will conduct batch experiments to investigate the effect of SO_4^{2-} on CaCO_3 precipitation. Similar to the authors above, we will employ XRD, EDS and SEM to study the mineralogical and chemical composition of the resulting precipitate and ICP-EOS to measure the residual cation concentration of the bulk fluid. The reader should note that we were unable to replicate the experiments or measure the residual anion concentration of the bulk fluid due to equipment constraints. In addition, errors bars are not presented in the quantitative charts because the individual experiments were only carried out once.

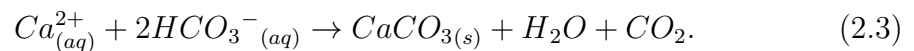
Although our objective is quite similar to those presented above, there are

important differences we should note. First, our prime concern is the interpretation of desalination phenomena and although our study is essentially of a laboratory nature, we hope our findings are applicable to studies concerning the origin of calcium carbonate in industrial scale desalination. For this reason, we will:

1. Prepare synthetic solutions representative of the molar ratios and chemistry found in feed streams of desalination plants.
2. Offer a comparison between the CaCO_3 formed in a pure solution and the CaCO_3 formed in the presence of SO_4^{2-} .
3. Highlight the implications of findings on desalination.

We emphasize that the combination of these was lacking in previous studies.

At this point we now have in place the tools needed to conduct an experimental study so it is now time to begin our investigation. First, we recall that the main reaction to be studied in the experiment is the reaction between calcium cations and bicarbonate ion which is given by



Essentially much of what we will do subsequently in this chapter is analyse how the nature of CaCO_3 scale produced from (2.3) changes when sulphate anions are introduced into the system. We do this by examining the mineralogy, morphology, and composition of the resulting precipitates. The reaction kinetics is monitored by measuring the bulk concentrations of one of the reactant species (Ca^{2+} in this case due to convenience) over the course of the experiment.

The rate of the reaction is then described by

$$\text{rate} = -\frac{d[\text{Ca}^{2+}]}{dt} = -\frac{d[\text{HCO}_3^-]}{dt} = \frac{d[\text{CaCO}_3]}{dt}, \quad (2.4)$$

where [] denotes concentration.

At the time of the study, it was not possible to repeat the experiment for a wide range of concentrations. Therefore detailed characterisation of all the processes occurring during precipitation was limited however we were still able to draw general conclusions on the influence of sulphate anions on CaCO_3 precipitation in desalination systems.

2.2 Experimental Procedure

Batch experiments were conducted with synthetic solutions that were representative of the molar ratios and chemistry encountered in feed/concentrate streams of desalination systems. The solutions prepared were based on concentrate seawater composition for a desalination plant in the Gulf of Oman [123]. Calcium chloride (CaCl_2) was used as the source of Calcium, Ca^{2+} , sodium bicarbonate (NaHCO_3), as the source of bicarbonate HCO_3^- , sodium sulphate (Na_2SO_4), as the source of SO_4^{2-} and sodium chloride (NaCl), was included to mimic the salinity levels found in natural waters. The composition of the salts in each of the experiment is shown in Table 2.1

Table 2.1: Summary of the initial fluid chemistry.

Exp	Solution Composition (mg/L)				Species (mg/L)		
	NaHCO_3	CaCl_2	Na_2SO_4	NaCl	HCO_3^{2-}	SO_4^{2-}	Ca^{2+}
E1	403	2625	8195	78396	293	5540	958
E2	253	2625	8195	79238	183	5540	958
E3	54	2625	8195	89515	39	5540	958
E4	-	2625	8195	89356	-	5540	958
E5	403	2625	0	89356	293	-	958

Table 2.1 summarises the fluid chemistry of the 5 main experiments conducted.

- E1: SO_4^{2-} and HCO_3^- anions were present in the fluid. This is to examine how SO_4^{2-} anions changes the CaCO_3 scale that is formed.
- E2 & E3: SO_4^{2-} and HCO_3^- anions were also present however the concentration of HCO_3^- is lower. This was done to illustrate the effect of a lower HCO_3^- concentration on the rate of reaction.
- E4: HCO_3^- was excluded to examine what happens in a system with only SO_4^{2-} .
- E5: SO_4^{2-} was excluded to understand what happens in a pure CaCO_3 precipitation.

2.2.1 Materials and Methods

The following items were required for the experiments.

Equipment

1. 100 mL volumetric flask
2. 4 magnetic stir plate
3. 4.9mL volumetric pipet
4. 200 μ l volumetric pipet
5. 1 wash bottle
6. 1 PH meter and PH probe
7. 50 centrifuge tubes
8. Filter paper

Reagents

1. NaCl
2. Na₂SO₄
3. CaCl₂
4. NaHCO₃
5. NaOH

Synthetic Solution Preparation

The synthetic solutions used in the experiments were prepared using the following procedure.

1. Firstly, a NaCl and CaCl₂ solution was prepared by dissolving the salts in sequence into 100mL milli-Q water.
2. A NaHCO₃ and Na₂SO₄ solution was prepared by dissolving NaHCO₃ and Na₂SO₄ salts into 100mL milli-Q water.
3. The resulting solutions were shaken manually and poured into reactors.
4. The reactors were placed on a magnetic stirrer plate (see Figure 2.2).
5. A magnetic stirrer bar was inserted to the reactor to mix the solution.



Figure 2.2: Experimental setup.

6. The magnetic stirrer plate was turned on and the temperature was set to 25°C as shown in Figure 2.2.
7. The reaction was initiated by adding the NaHCO_3 and Na_2SO_4 solution into the reactor containing $\text{NaCl} + \text{CaCl}_2$ solution followed by NaOH solution for pH correction (if needed).
8. The reactors were sealed tight to reduce the flow of air and prevent the loss of CO_2 into the air.

Sample collection

Once the reaction was initiated, 100 μL sample was removed from the reactors and the pH of the sample was measured. As the reaction proceeded, 100 μL sample were withdrawn at selected time intervals so the residual concentration of calcium ions (Ca^{2+}) in the bulk fluid could be measured. The collected samples were diluted with HNO_3 . This was done to minimize metal cation precipitation and prevent its adsorption onto the storage tube.

Precipitate collection

At the end of the experiments, the precipitate that adhered to the base of the reactors was recovered by scraping it off the base of the reactor. A centrifuge was used to separate any liquid that was still in contact with the precipitate and accelerate the settling of the precipitate. The centrifuge was allowed to run for 4 minutes and the precipitate recovered was dried in an oven and subsequently characterised.

2.2.2 Sample Characterisation

The solid precipitate recovered from the experiments were characterised by different techniques to determine the mineralogy and morphology. The precipitates were first analysed by powder X-ray diffraction (PXRD) to identify the mineral phases. Then the morphology of the precipitate was imaged using Scanning Electron Microscope (SEM). Semi-qualitative chemical analyses of the precipitate were obtained using Energy Dispersive X-ray (EDX) software. The Ca^{2+} concentration of the samples obtained during the experiment was measured using inductively coupled plasma optical emission spectrometry (ICP-EOS).

2.3 Results

2.3.1 General Observations

There are a few observations we need to make regarding the colour of the solutions at the start of the experiment and over the course of the experiment.

Observations at the start of the experiment

- E1 & E5 - As shown in Figure 2.3, the solutions turned cloudy once the reaction was initiated. This cloudiness implies supersaturation hence the induction period is zero.
- E2, E3 & E4 - There was no change in colour when the reaction was initiated. This indicates that these solutions may either be saturated or unsaturated.

Observations over the course of the experiment

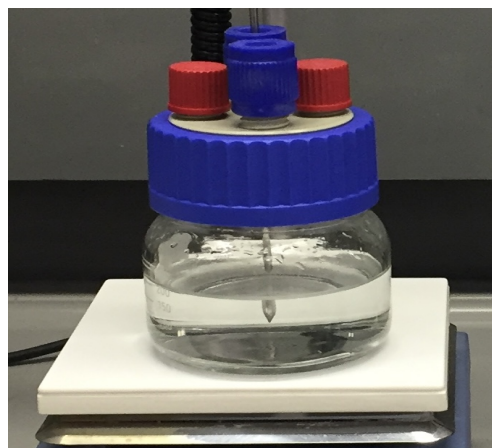
- E1 & E5 - At some point, the cloudy portion of the solution settled to the base of the reactor. Thereafter we observed the adherence of the white precipitate to the bottom of the reactor.
- E2 - We observed the adherence of a white precipitate at the bottom of the reactor after 22hours.
- E3 & E4 - No precipitate was observed over the course of the reaction.

Observations at the end of the experiment

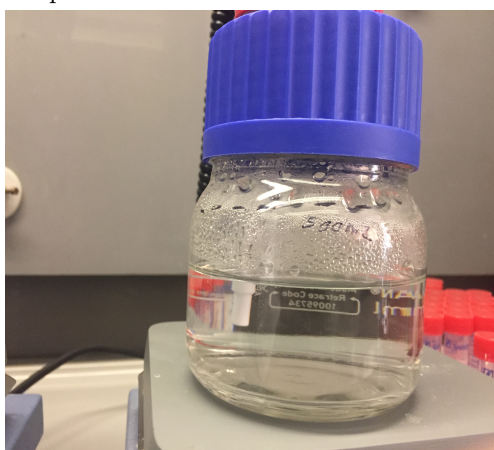
- E1 & E5 - Significant quantity of precipitate recovered.



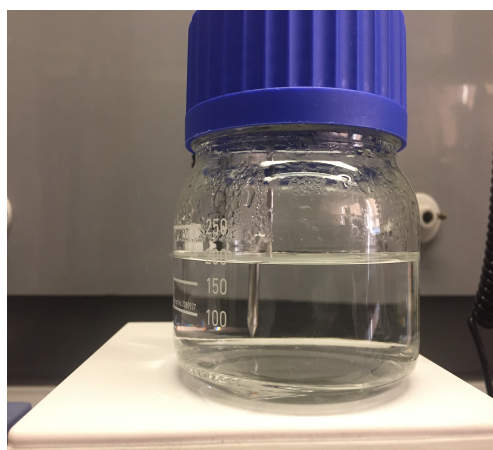
(a) E1: SO_4^{2-} and HCO_3^- anions present. Cloudy solution is observed at the beginning of the experiment, $t = 0$, indicating that the solution is supersaturated.



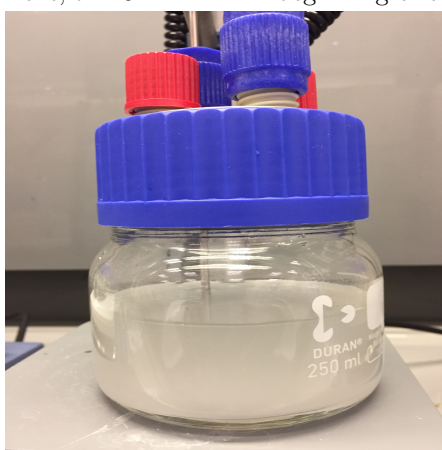
(b) E2: SO_4^{2-} and HCO_3^- anions present. At $t = 0$, Clear and colourless solution is observed at the beginning of the experiment, $t = 0$.



(c) E3: SO_4^{2-} and HCO_3^- anions present. Clear and colourless solution is observed at the beginning of the experiment, $t = 0$.

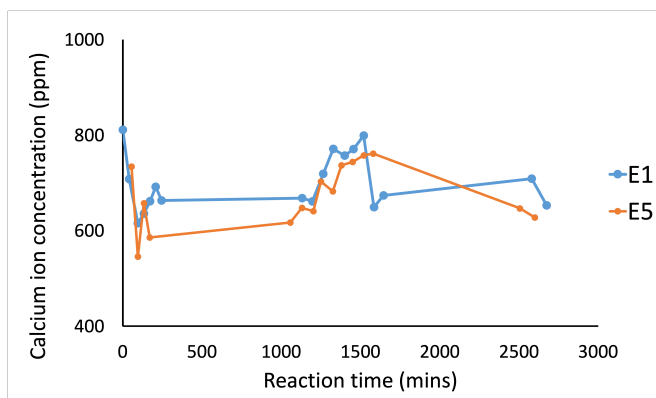


(d) E4: SO_4^{2-} anions present. Clear and colourless solution is observed at the beginning of the experiment, $t = 0$.

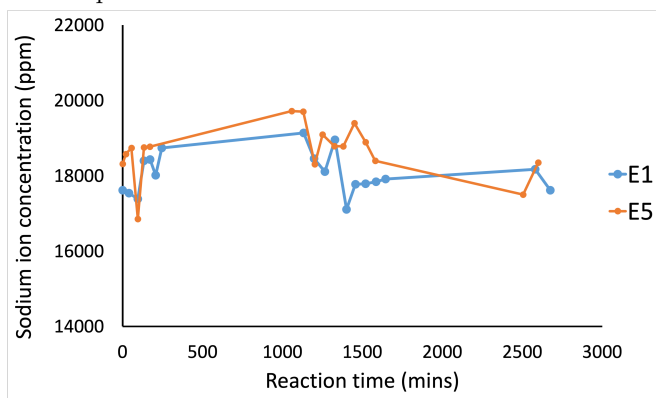


(e) E5 - HCO_3^- anions present. Cloudy solution is observed at the beginning of the experiment, $t = 0$, indicating that the solution is supersaturated.

Figure 2.3: The colour of the individual solutions serves as an indication for saturation. E1 and E5 turned cloudy when the reaction was initiated - this suggests that these solutions are supersaturated.



(a) The residual calcium concentration obtained from experiments E1 and E5.



(b) The residual sodium concentration obtained from experiments E1 and E5.

Figure 2.4: The residual concentration of cations (from inductively coupled plasma-optical emission spectrometry (ICP-EOS) analyses) in the samples obtained from experiments E1 and E5. It is worth noting that error bars are not presented because the experiment was only carried out once

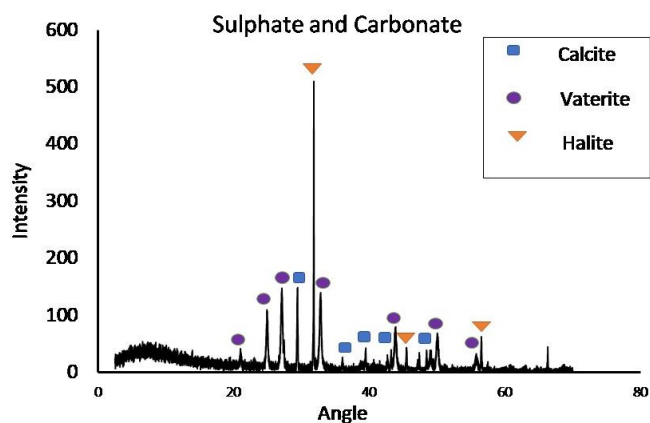
- E2 - Small quantity of precipitate recovered.
- E3 & E5 - No precipitate was recovered.

2.3.2 ICP-EOS - Calcium Evolution

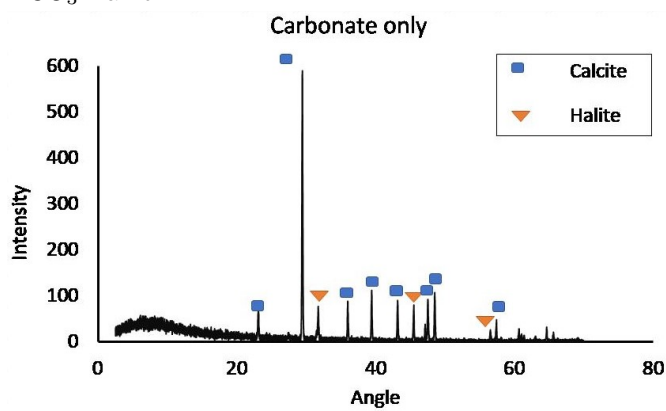
Figure 2.4 shows that the residual concentration of calcium, Ca^{2+} in E1, E2 & E5. It appears that the calcium evolution is characterised by a rapid drop in concentration followed by some variability.

2.3.3 PXRD - Precipitate Mineralogy

The precipitates recovered from E1 & E5 were first analysed using powder X-ray diffraction (PXRD) to identify the mineral phases. Only a small quantity of precipitate was recovered in E2 and it was not enough to characterise the precipitate both by PXRD and SEM. Thus in this case, only SEM was employed



(a) XRD for E1, which contained SO_4^{2-} and HCO_3^- anion



(b) XRD for E5, which contained HCO_3^- anion

Figure 2.5: The XRD patterns of the precipitates obtained from (a) experiment E1 containing SO_4^{2-} and HCO_3^- anion (b) experiment E5, containing HCO_3^- anion.

as it was deemed more important than a PXRD analysis.

Figures 2.5a and 2.5b show the diffraction patterns obtained from experiment E1 and E5. The diffraction patterns were compared to standard powder diffraction files from the PROFEX 3.14.2 database (release 2019) for calcite, halite and vaterite. The PXRD analyses of the precipitates from experiment E1 which contained SO_4^{2-} and HCO_3^- anions show that the constituents of the precipitate are: halite, calcite and vaterite. The PXRD analyses of the precipitates from experiment E5 which contained HCO_3^- anion shows that the constituents of the precipitate are: halite and calcite. It is worth mentioning that halite is the mineral form of sodium chloride (NaCl) while calcite and vaterite are polymorphs of calcium carbonate (CaCO_3).

We assume the peak integrals from the PXRD in Figure 2.5 are proportional to the phase fraction of the minerals present. Therefore, we computed the peak integral of each mineral and divided this by the sum of all the peak integrals. We assume this ratio is a rough estimate of the relative proportion of each of the minerals identified. The mineral fractions computed are shown in Table 2.2. It can be seen that in E1, 67% of the minerals identified is vaterite, 18% is calcite and 15% is halite whereas in E5, 85% of the crystals is calcite and 15% is halite.

Table 2.2: Mineral identity of the precipitate recovered in each experiment.

Exp	SO_4^{2-} (mg/L)	HCO_3^- (mg/L)	Mineral recovered
E1	5540	293	halite (15%) + calcite (18%) + vaterite (67%)
E2	5540	183	¹ halite + calcite
E3	5540	39	-
E4	5540	0	-
E5	0	293	halite (15%) + calcite (85%)

¹Unable to conduct a PXRD analysis on this sample so only SEM and EDX were employed to characterise the sample.

2.3.4 SEM & EDX Analysis - Precipitate Morphology

Experiment E1

Figures 2.6 and 2.7 shows the SEM and EDX images of the precipitate formed from experiment E1. The SEM analyses conducted on this crystals show that the ‘spherical’ shaped crystals are vaterite, the small ‘rhombohedral’ crystals are calcite and the elongated crystal on which calcite and vaterite nucleate is halite (see Figures 2.6a and 2.6b). Elemental mapping shown in Figures 2.6c and 2.6d presents the elements that make up the composition of the sample and also the spatial distribution of the elements. This as well as the EDX spectra in Figure 2.7d confirms the presence of sulphur in the CaCO_3 crystals. A bulk view of the CaCO_3 crystals presented in Figure 2.6e shows vaterite as the predominant CaCO_3 morphology. A wider view of the precipitate shows the long elongated halite structure (see Figure 2.6f).

Experiment E2

Figure 2.8 shows the SEM and EDX images of the precipitate formed from experiment E2. The SEM analyses conducted on this crystals show that the little spherical shaped crystals are vaterite and the thick mass is halite. The EDX spectra in Figure 2.8f confirms the presence of sulphur in the CaCO_3 crystals.

Experiment E5

The SEM and EDX analyses from this experiment are shown in Figure 2.9. The SEM analyses conducted on this crystals show that the rhombohedral shaped crystals are calcite and the elongated crystals is halite. It can be seen that no vaterite was detected from this experiment. It is also apparent from Figure 2.9a that the rhombohedral calcite crystals are attached to an elongated halite crystal.

2.4 Discussion

Before launching into a discussion of the results, we need to provide some details which are needed to interpret the results. The first point to be aware of is that we employed a sequential procedure during the experiments, these are: dissolution, dissociation and reaction (see Figure 2.10). To illustrate this point clearly, we will briefly consider the processes leading up to the formation of precipitate in E1 as an example. A schematic representation of the sequence of events that lead to

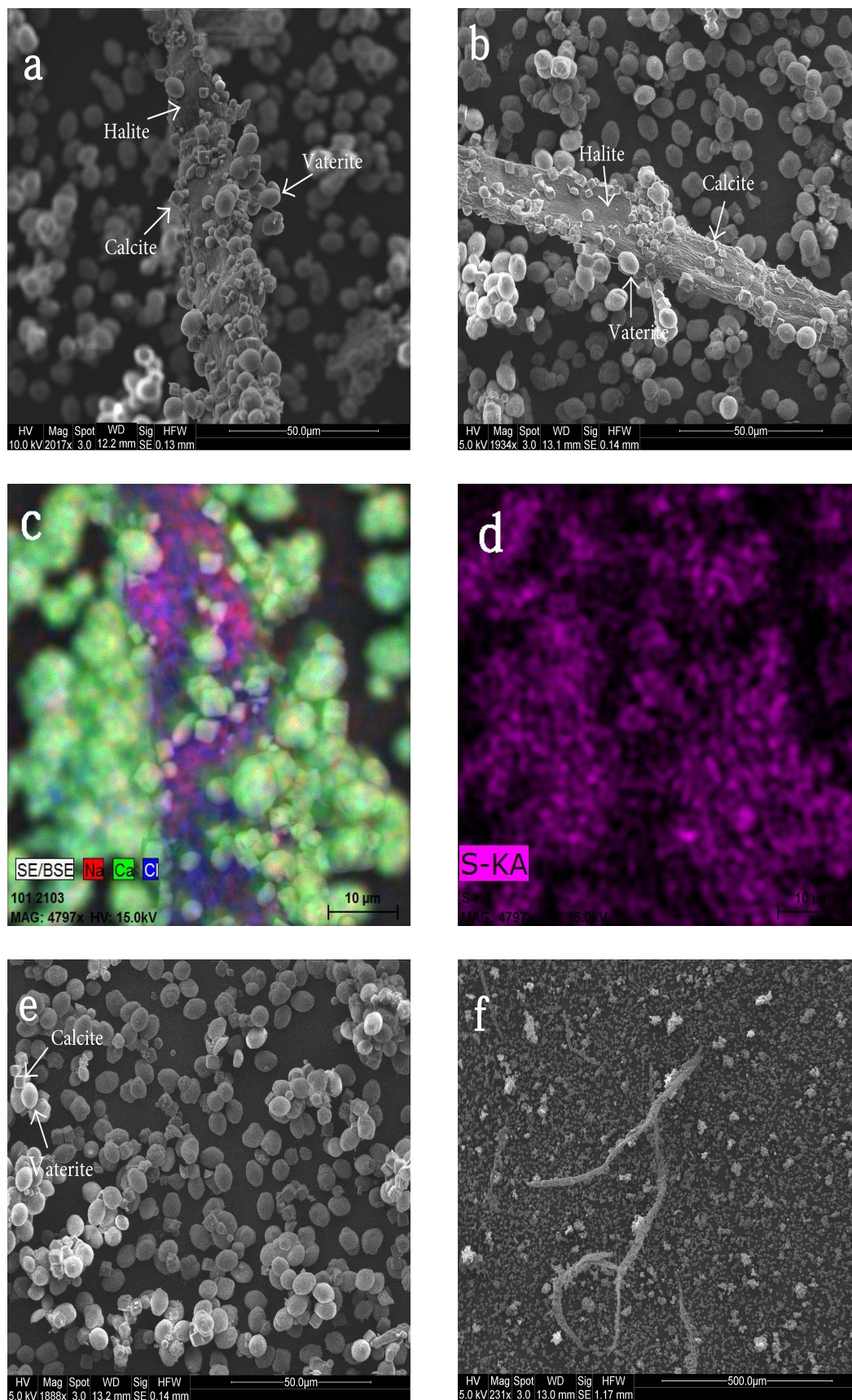
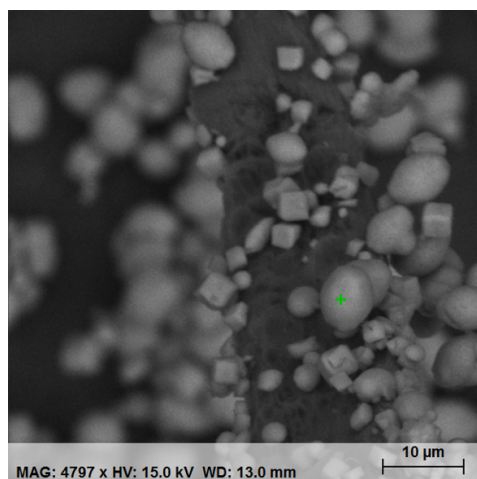
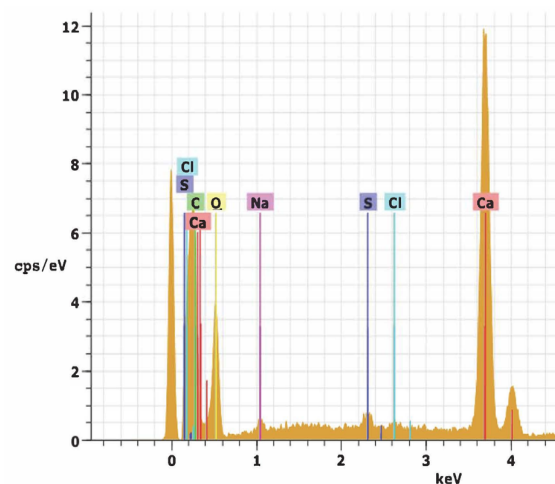


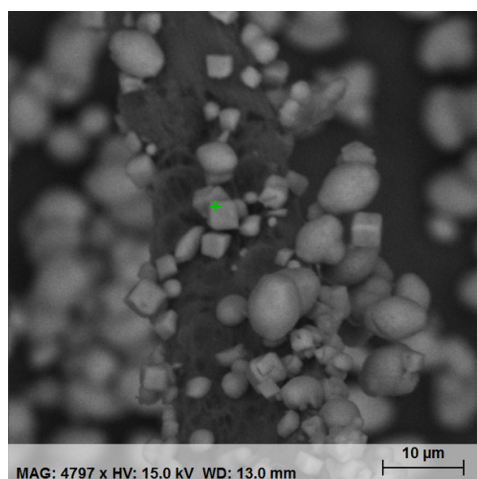
Figure 2.6: SEM and EDX images of the precipitate formed in experiment E1 containing SO_4^{2-} and HCO_3^- anions. In these images, calcite appears as a rhombohedral crystal, vaterite appears as spherical crystals and halite as an elongated crystal.



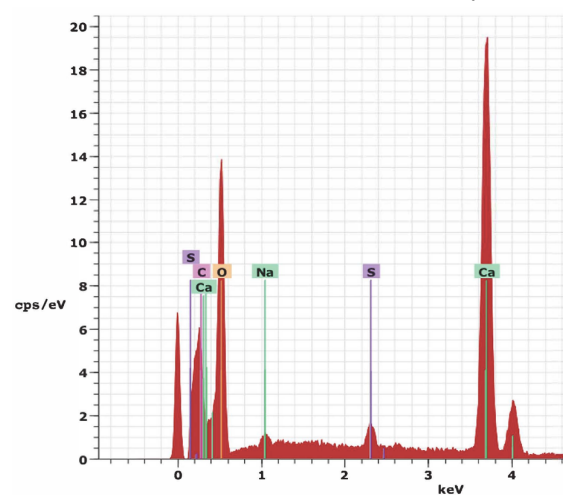
(a) SEM image pointing to the vaterite crystal.



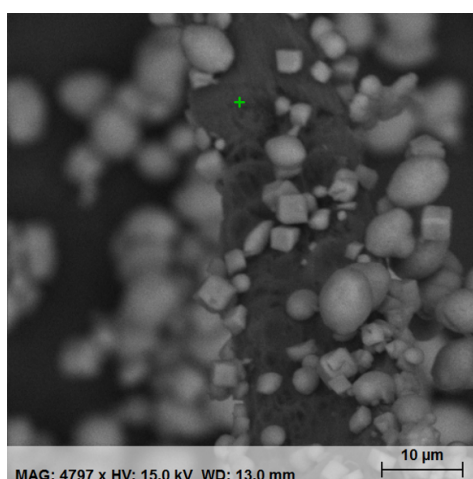
(b) EDX for vaterite shows that calcium Ca is the dominant element in the vaterite crystal.



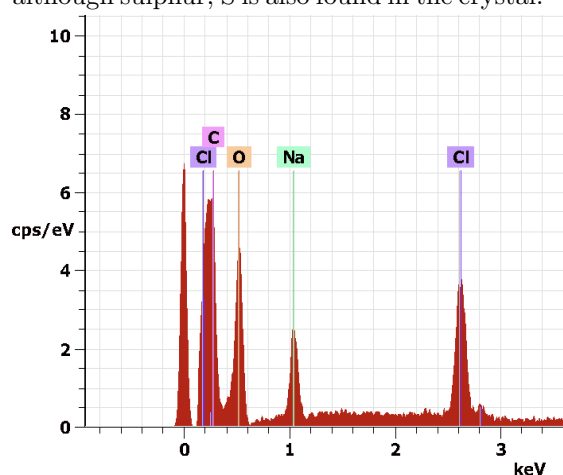
(c) SEM image pointing to the calcite crystal.



(d) EDX for calcite shows that calcium Ca is the dominant element in the calcite crystal although sulphur, S is also found in the crystal.

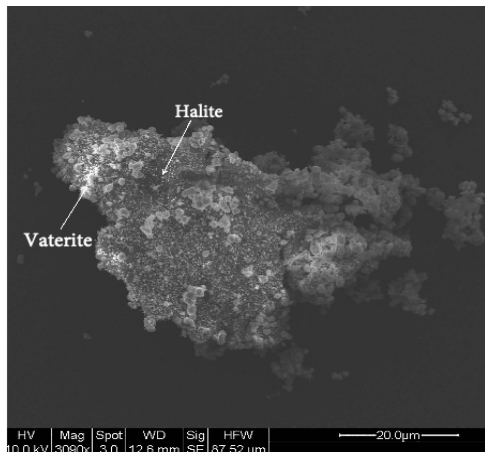


(e) SEM image pointing to the elongated halite crystal.

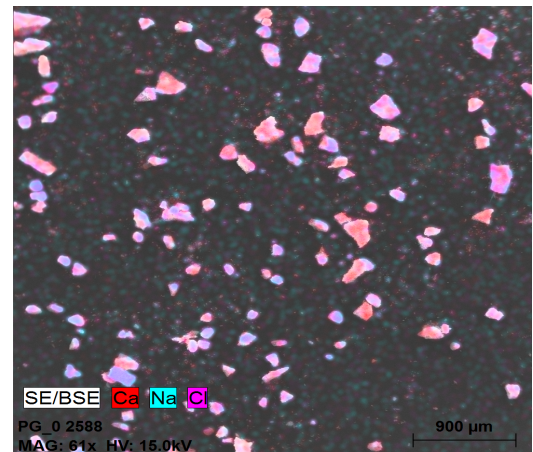


(f) EDX for halite shows that Sodium, Na and Chloride, Cl are the dominant elements in the elongated halite crystal.

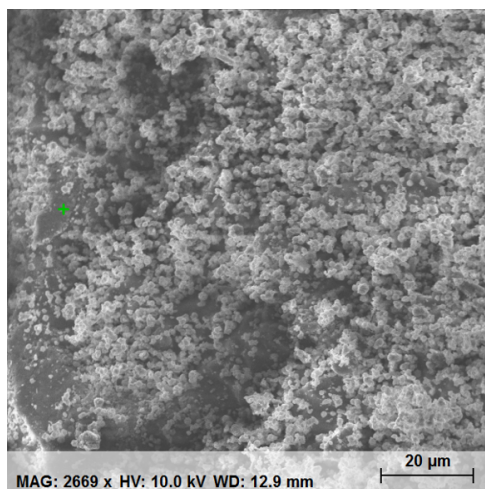
Figure 2.7: SEM and EDX images of the precipitate from E1. The green pointers in the SEM images on the left hand side points to the crystal of interest and the right images are the corresponding elemental composition in that location.



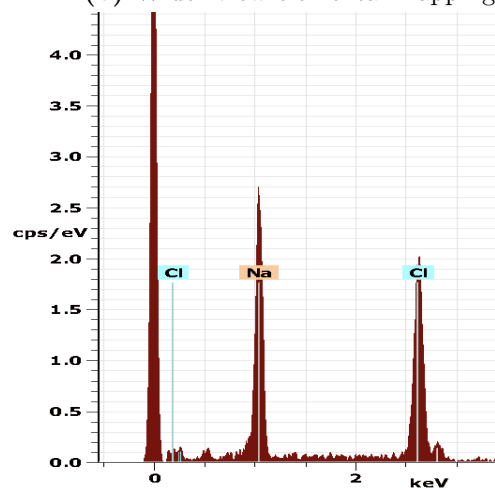
(a) SEM image of precipitate from E2



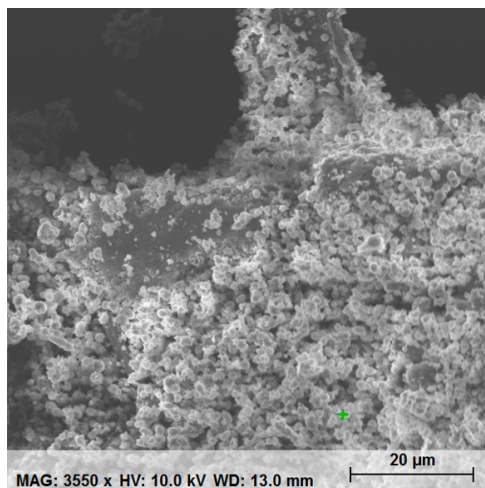
(b) Wider view elemental mapping



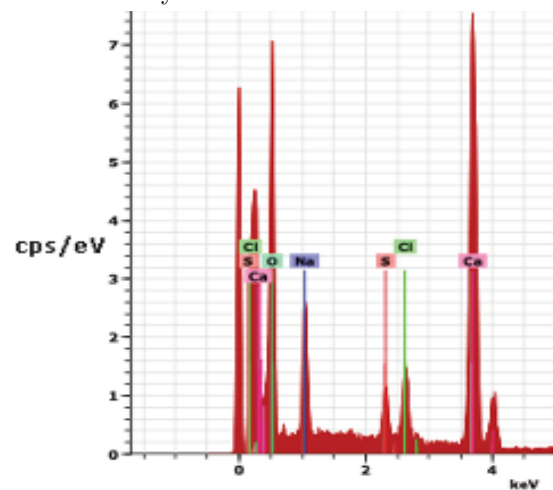
(c) SEM image pointing to the thick halite mass crystal.



(d) EDX for halite shows that Sodium, Na and Chloride, Cl are the dominant elements in the thick mass crystal.

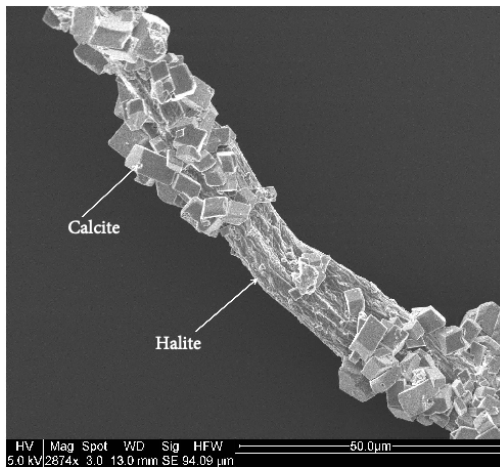


(e) SEM image pointing to the white vaterite crystal.

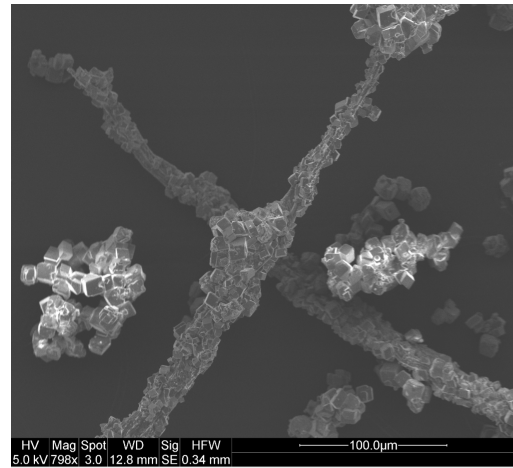


(f) EDX for vaterite shows that calcium Ca, is the dominant element in the vaterite crystal although chloride, sodium and sulphur are also found in the crystal.

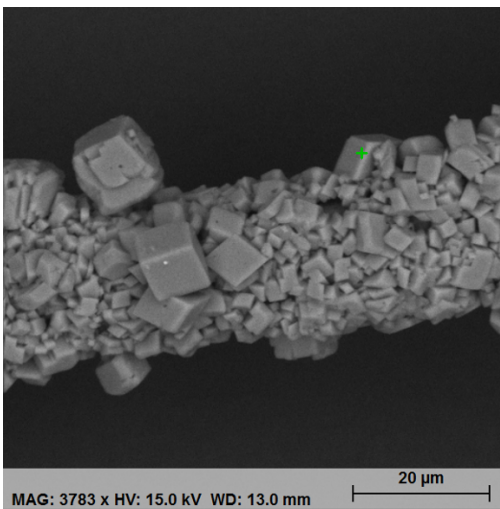
Figure 2.8: SEM and EDX images of the precipitate from E2. The green pointers in the SEM images (c & e) points to the crystal of interest and the right images (d & f) are the corresponding elemental composition in that location.



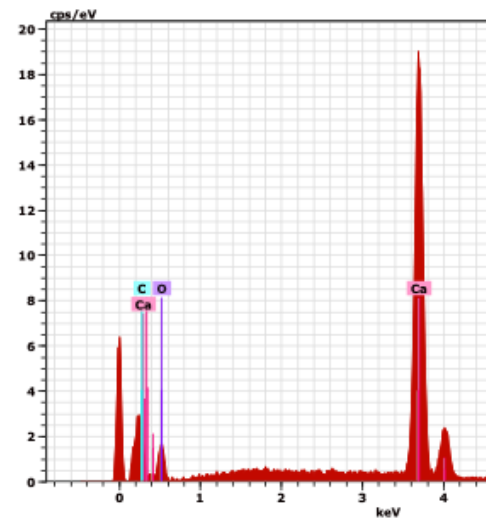
(a) SEM image of experiment from E5



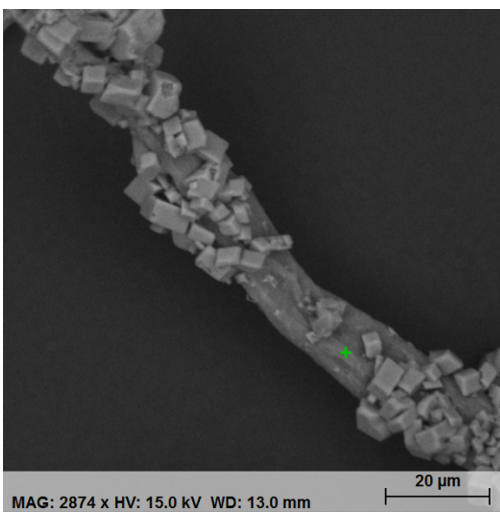
(b) A wider angle view of the crystals



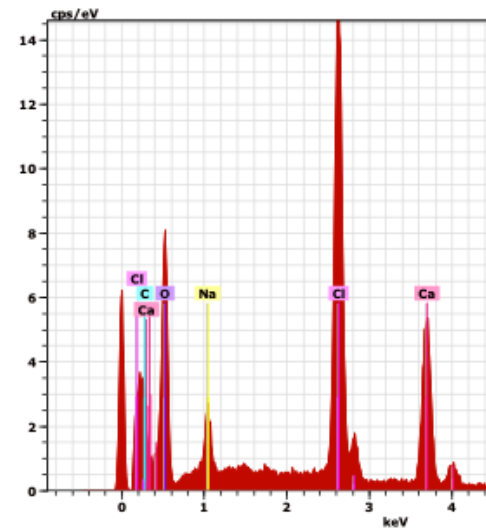
(c) SEM image pointing to the calcite crystal



(d) EDX for calcite shows that Calcium, Ca is the dominant element in the rhombohedral crystals



(e) SEM image pointing to the halite crystal



(f) EDX for halite shows that Sodium, Na, Calcium, Ca and Chloride Cl, are the dominant elements in the halite crystal

Figure 2.9: SEM and EDX images of the precipitate from E5. Calcite appears as cuboid/rhombohedral aggregates while halite appears as an elongated crystal.

precipitation in E1 are shown in Figure 2.11. The individual events are explained in more detail below.

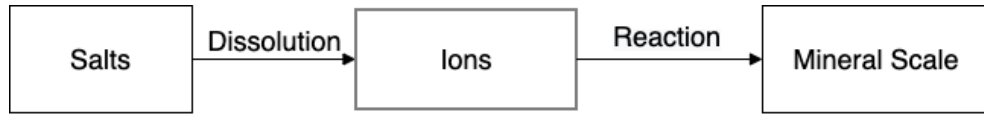


Figure 2.10: Sequential process that led to precipitation in E1, E2 and E5.

Dissolution & Dissociation

As explained in section 2.2.1, calcium chloride (CaCl_2), sodium bicarbonate (NaHCO_3), sodium sulphate (Na_2SO_4) and sodium chloride (NaCl) were separately dissolved in water to form salt solutions. Calcium chloride was used as the source of Ca^{2+} , sodium bicarbonate as the source of HCO_3^- , sodium sulphate as the source of SO_4^{2-} and sodium chloride was included to mimic the salinity levels found in natural waters. These salts are ionic compounds that are soluble in aqueous solution so they dissociated into cations and anions. For example, Na_2SO_4 dissociates into sodium cations (2Na^+) and sulphate anion SO_4^{2-} as shown in Figure 2.11.

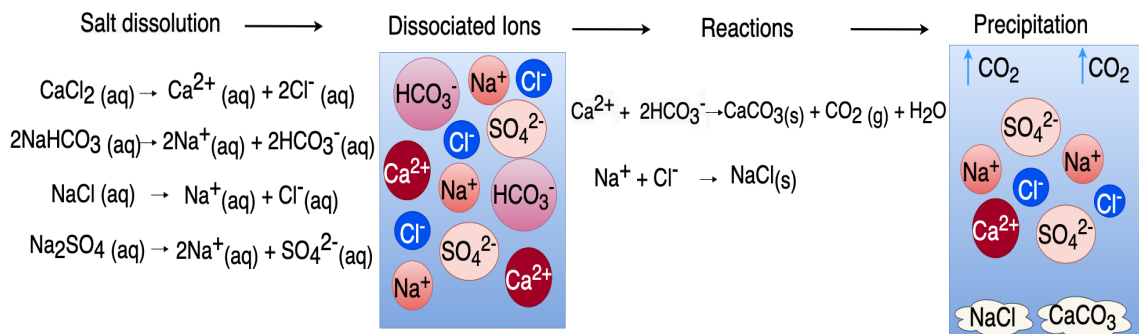


Figure 2.11: Sequential processes leading to precipitation in E1.

Reaction & Precipitation

Following dissolution and dissociation, the solutions were mixed together, beginning the nucleation process for the precipitates. As can be seen in Figure 2.11, the ions present in feed water react to form two main precipitates NaCl and CaCO_3 i.e Ca^{2+} and bicarbonate HCO_3^- react to form calcium carbonate, CaCO_3 whereas sodium Na^+ and chlorine Cl^- react to form halite NaCl . Having established the ions and reactions occurring in the system, we can now proceed to the discussion of the crystals resulting from the precipitation process in E1, E2 and E5. In the following subsections we will discuss the key results of this chapter.

2.4.1 Influence of Sulphate Anions on CaCO₃ Scale

In this study, SO₄²⁻ influences the precipitation of CaCO₃ crystals in three ways: the crystal morphology, the size and roughness of calcite formed. We offer more details on this below; we will compare the size, morphology and shape of CaCO₃ crystals formed with sulphate present (i.e. E1 & E2) and without sulphate present (i.e. E5).

Impact on morphology

As mentioned in section 2.3.1 when the reactants were mixed in E1 and E5, the formation of CaCO₃ was instantaneous, indicating supersaturation. The solubility of all CaCO₃ polymorphs was exceeded ($SI_{calcite} = 3.74$; $SI_{aragonite} = 3.60$; $SI_{vaterite} = 3.17$), hence the rapid formation of the most soluble phase vaterite is kinetically favoured [33, 81]. Generally, it is expected that as the system approaches equilibrium, the more soluble vaterite will be dissolved and the less soluble calcite will grow. However, the findings from [33] suggest that when sulphate anions are present, they incorporate into the CaCO₃ crystal structure during crystal growth, inhibiting this transformation of vaterite to calcite. Our results are in line with this as we observe calcite in the experiment without sulphate present (i.e. E5) and detect vaterite in the experiment with sulphate present (i.e. E1 & E2). In addition, Figure 2.7 shows that the vaterite and calcite from experiment E1 have sulphur incorporated in their structure. Similarly, Figure 2.8 also shows sulphur present in the precipitate recovered from E2.

It has been reported by [33] that in solutions with high SO₄²⁻:HCO₃⁻ ratio, vaterite is the major constituent phase in the precipitate. Our study does confirm the association between the SO₄²⁻:HCO₃⁻ ratio in the solution and the resulting vaterite component. We can see from Table 2.3 that in E2, where the SO₄²⁻:HCO₃⁻ is the highest, we detect only vaterite. This can also be confirmed by looking at Figure 2.8e, one would see that all the CaCO₃ crystals from E2 are vaterite. However in E1, where the SO₄²⁻:HCO₃⁻ is comparatively lower, we observe both calcite and vaterite crystals (see Figures 2.6a,b,e). It is also likely that an early precipitation of vaterite would reduce the concentration of HCO₃⁻ in the later stages of this experiment. Therefore the calcite crystals forming thereafter would be grown from a medium with a significantly higher SO₄²⁻:HCO₃⁻ ratio than the initial solution. In contrast, in E5 (the SO₄²⁻ free experiment), no vaterite was observed, only calcite was detected.

Table 2.3: $\text{SO}_4^{2-}:\text{HCO}_3^-$ of the solutions from which precipitate was recovered.

Exp	SO_4^{2-} (mg/L)	HCO_3^- (mg/L)	$\text{SO}_4^{2-}:\text{HCO}_3^-$	Polymorph
E2	5540	183	30	Vaterite
E1	5540	293	19	Vaterite + Calcite
E5	0	293	-	Calcite

Impact on calcite formed

The influence of SO_4^{2-} on the shape of CaCO_3 crystals has been noted by several authors [71, 119]. Single crystals with rhombohedral shape is seen in experiment E1 whereas rhombohedral aggregates were observed in E5. Compare, for example, the calcite crystals in Figures 2.6 a, b, e to that in Figure 2.9a. Although these are of the same resolution (i.e 50 μm), it can be seen that the calcite crystal in Figure 2.9a which was grown in the absence of dissolved sulphate is considerably larger than the crystals in Figure 2.6 a, b, e which were grown in the solution with sulphate present. The difference in crystal size could be attributed to the longer induction period for calcite in experiment E1. We believe the calcite formed in E5 is formed early on, allowing sufficient time for the growth of larger crystals whereas in the experiment with sulphate, E1, we assume calcite is formed in the later stages which implies a shorter growth period resulting in smaller crystals.

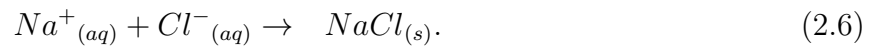
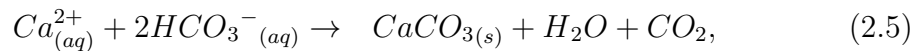
The calcite from E5 (Figures 2.9a and 2.9b) appears to be tenacious, that is the crystals are closely arranged together and several crystals seem to agglomerate to form large crystals. This is consistent with previous findings of Chong and Sheikholeslami [20]. A study by Sheikholeslami and Ong [105] showed that pure calcium carbonate are more adherent and tenacious in nature which could explain why calcite in experiment E5, are densely packed and clustered together as shown in Figure 2.9. This might suggest that pure calcite might be more difficult to remove in desalination systems due to its tenacious nature.

The calcite crystals in E5 appear to be have smooth and/or irregular surfaces. Here, we refer to smooth calcite crystals as those having a surface that is perfectly regular with no areas that rise or fall suddenly whereas the irregular calcite crystals are those with deformed surfaces as shown in Figure 2.9c. It is possible that the crystals undergo an evolution characterised by an increase in elongation (that is a higher width:length ratio). This evolution could be because

the calcite in this experiment (E5) was formed instantaneously after mixing, with many crystals precipitating at the same time and thus colliding with each other resulting in distorted edges and faces. In contrast, the calcite formed in E1 appear to have even and regular surfaces. This might be because there's less competition for space during nucleation.

2.4.2 Co-precipitation of NaCl with CaCO₃

One unanticipated finding from the study was co-precipitation of NaCl with CaCO₃ in E1, E2 and E5. Due to its solubility, halite (mineral form of NaCl) does not commonly reach supersaturation in RO membrane systems, hence it is expected that halite would remain dissolved in water [29]. The reason for the precipitation of halite in our experiments is not clear but we believe it may be related to the nucleation mechanism of the crystals. It seems possible that the crystallisation of CaCO₃ might have initiated the growth of NaCl. The co-precipitation of NaCl with CaCO₃ indicates that the following reactions must have occurred in these experiment.



Halite's shape & role

Halite crystal is commonly known to be cubic shaped so what is striking about the SEM figures presented in the preceding section is the shape of halite. In Figures 2.6, 2.7 and 2.9 halites appears as an elongated structure whereas in Figure 2.8 appears as a thick mass. It can be seen from these figures that a significant portion of the calcium carbonate crystal that precipitates sticks onto the halite structure. This might imply that halite acts as a binding agent for the CaCO₃ crystals. Only one study has mentioned the involvement of sodium chloride ions in the precipitation of CaCO₃. This study was by [57] who reported that sodium ion can be incorporated into CaCO₃ crystals but did not provide any information on the binding role of sodium chloride as seen in these figures.

Lack of previous research

No studies have been found which examines this structure of halite or explains the nucleation of calcite on halite in desalination systems. This is understandable because halite readily dissolves in water thus it's crystallisation is overlooked. There have been a few studies showing SEM morphologies of halite in soils which

confirm that elongated halite structures do exist in nature [29, 57]. These studies suggest that an elongated halite structure could be as a result of a dissolution-recrystallisation mechanism whereby halite dissolved in its own absorbed water and re-precipitated as a glassy fibrous crystal.

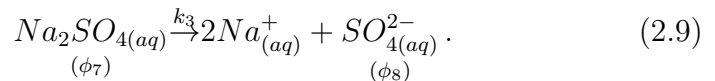
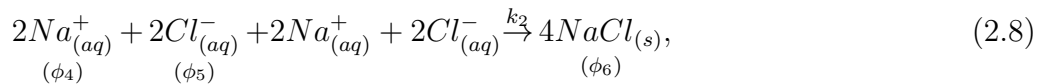
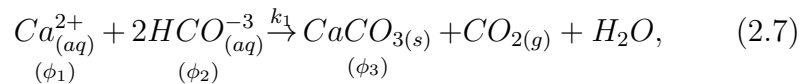
We believe the co-precipitation and unique halite crystal structures observed are as a result of the saturation levels and water chemistry used in this study. As we have emphasised earlier, past studies often fail to mimic the saturation levels and water chemistry encountered in concentrate streams of desalination systems so there is little or no published data on this kind of co-precipitation. This indicates that more experimental studies should be conducted representative of the molar ratios, chemistry and supersaturation levels found in desalination plants.

2.5 Kinetic Model

In this section, we formulate expressions to describe the behaviour of species in the co-precipitation experiment, E1. From the law of mass action, we derive a set of ordinary differential equations (ODEs) that describes the rate of change of species concentration. Here, we limit our attention to ODE formulations which will later be included in the PDEs describing solute transport in Chapter 3.

2.5.1 Reaction Network

The experimental results suggest co-precipitation of NaCl and CaCO₃ and the presence of sulphate in the CaCO₃ crystals. In light of our earlier discussions on the dissociation, dissolution and reaction procedure employed in the experiments, we propose the following mechanism to represent the precipitation observed in E1



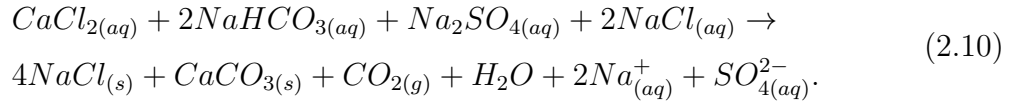
In addition to the stated reactions, we make the following assumptions about the reaction mechanisms:

1. Reaction (2.7) occurs at a faster rate and CaCO₃ is formed instantaneously.
2. Experimental observations show that the CaCO₃ crystals formed contain

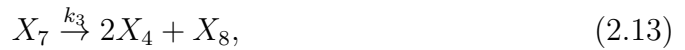
SO_4^{2-} . We believe the SO_4^{2-} present in the crystal is that from the sodium sulphate (Na_2SO_4) dissociation in reaction (2.9).

3. A glassy form of halite is formed during the experiment and this is described in (2.8).
4. The speed of the reactions will be dictated by the rate constants, k_1 , k_2 and k_3 . Therefore $k_1 > k_2$ which implies that the rate of formation of CaCO_3 is greater than the formation of halite.

Collectively, the overall reaction can be summarised by:



The quantities on the left-hand side of reactions (2.7) - (2.9) are the reactants whereas the quantities on the right-hand side are the products, k_i is the reaction rate (where $i = 1, \dots, 3$). The reactants and products are collectively referred to as the species of the reaction. Now let $X_1, X_2, X_3, X_4, X_5, X_6, X_7$ and X_8 denote the chemical species Ca^{2+} , HCO_3^- , CaCO_3 , Na^+ , Cl^- , NaCl , Na_2SO_4 and SO_4^{2-} respectively, so that equations (2.7) - (2.10) can be written as



or compactly in matrix-vector form as



where $X = [X_1, X_2, X_3, X_4, X_5, X_6, X_7, X_8]^T$ is the column vector of species, $k = [k_1, k_2, k_3]^T$ denotes the reaction rate and A and B are the stoichiometric coefficients. We exclude CO_2 and H_2O as we assume these do not impact the present developments.

It thus follows that A and B are given by

$$A = \begin{bmatrix} 1 & 2 & 0 & 0 & 0 & 0 & 0 & 0 \\ 0 & 0 & 0 & 1 & 1 & 0 & 0 & 0 \\ 0 & 0 & 0 & 0 & 0 & 0 & 1 & 0 \end{bmatrix}, \quad B = \begin{bmatrix} 0 & 0 & 1 & 0 & 0 & 0 & 0 & 0 \\ 0 & 0 & 0 & 0 & 0 & 1 & 0 & 0 \\ 0 & 0 & 0 & 2 & 0 & 0 & 0 & 1 \end{bmatrix} \quad (2.15)$$

2.5.2 Rate Equations

Although the molecular interaction is driven by the random collision of reactants, when their concentration is large enough, we can idealise the reaction as a deterministic, continuous process. A widely used principle that supports the modelling of a reaction rate under the presence of a large enough reactant concentration is the law of mass action. This states that the rate of reaction is proportional to the product of the concentrations of the reactant species.

Following the principles of mass action, the dynamic behaviour of the chemical system can be described by a set of first order differential equations with time as the independent variable [118]:

$$\begin{aligned} \frac{d\phi_1}{dt} &= f_1(\phi_1, \phi_2, \dots, \phi_n, t), \\ \frac{d\phi_2}{dt} &= f_2(\phi_1, \phi_2, \dots, \phi_n, t), \\ &\vdots \\ \frac{d\phi_n}{dt} &= f_n(\phi_1, \phi_2, \dots, \phi_n, t), \end{aligned} \quad (2.16)$$

where $\phi_i(t) \in \mathbb{R} (i = 1, \dots, n)$ denotes the volume molar concentration of chemical species X_i , at time t . Then following the law of mass action, the dynamics of the reaction network are given by the kinetic equations [18]

$$\dot{\phi}(t) = (B - A)^T K \phi^A(t), \quad \phi(0) = \phi_0, \quad t \geq 0, \quad (2.17)$$

where $K \triangleq \text{diag}(k_1, \dots, k_3)$, ϕ^A denotes matrix exponentiation operations and ϕ_0 is the initial concentration [18].

Consequently, the kinetic equations have the form

$$N = (B - A)^T = \begin{bmatrix} -1 & 0 & 0 \\ -2 & 0 & 0 \\ 1 & 0 & 0 \\ 0 & -1 & 2 \\ 0 & -1 & 0 \\ 0 & 1 & 0 \\ 0 & 0 & -1 \\ 0 & 0 & 1 \end{bmatrix}, \quad K\phi^A(t) = \begin{bmatrix} k_1\phi_1(t)\phi_2^2(t) \\ k_2\phi_4(t)\phi_5(t) \\ k_3\phi_7(t) \end{bmatrix}. \quad (2.18)$$

The system of ODEs for this mass action system is

$$\frac{d\phi_1}{dt} = -k_1\phi_1(t)\phi_2^2(t), \quad \phi_1(0) = \phi_{10}, \quad t \geq 0, \quad (2.19)$$

$$\frac{d\phi_2}{dt} = -2k_1\phi_1(t)\phi_2^2(t), \quad \phi_2(0) = \phi_{20}, \quad (2.20)$$

$$\frac{d\phi_3}{dt} = k_1\phi_1(t)\phi_2^2(t), \quad \phi_3(0) = \phi_{30}, \quad (2.21)$$

$$\frac{d\phi_4}{dt} = -k_2\phi_4(t)\phi_5(t) + 2k_3\phi_7(t), \quad \phi_4(0) = \phi_{40}, \quad (2.22)$$

$$\frac{d\phi_5}{dt} = -k_2\phi_4(t)\phi_5(t), \quad \phi_5(0) = \phi_{50}, \quad (2.23)$$

$$\frac{d\phi_6}{dt} = k_2\phi_4(t)\phi_5(t), \quad \phi_6(0) = \phi_{60}, \quad (2.24)$$

$$\frac{d\phi_7}{dt} = -k_3\phi_7(t), \quad \phi_7(0) = \phi_{70}, \quad (2.25)$$

$$\frac{d\phi_8}{dt} = k_3\phi_7(t), \quad \phi_8(0) = \phi_{80}. \quad (2.26)$$

It is clear that there are five conservation relations

$$\frac{d\phi_1}{dt} + \frac{d\phi_3}{dt} = 0 \Rightarrow \phi_1 + \phi_3 = A, \quad (2.27)$$

$$\frac{d\phi_2}{dt} + 2\frac{d\phi_3}{dt} = 0 \Rightarrow \phi_2 + 2\phi_3 = B, \quad (2.28)$$

$$\frac{d\phi_4}{dt} + \frac{d\phi_6}{dt} + 2\frac{d\phi_7}{dt} = 0 \Rightarrow \phi_4 + \phi_6 + 2\phi_7 = C, \quad (2.29)$$

$$\frac{d\phi_5}{dt} + \frac{d\phi_6}{dt} = 0 \Rightarrow \phi_5 + \phi_6 = D, \quad (2.30)$$

$$\frac{d\phi_7}{dt} + \frac{d\phi_8}{dt} = 0 \Rightarrow \phi_7 + \phi_8 = E. \quad (2.31)$$

This reduces the system of equations to

$$\frac{d\phi_3}{dt} = k_1(A - \phi_3)(B - 2\phi_3)^2, \quad (2.32)$$

$$\frac{d\phi_6}{dt} = k_2(C - 2(E - \phi_8) - \phi_6)(D - \phi_6), \quad (2.33)$$

$$\frac{d\phi_8}{dt} = k_3(E - \phi_8). \quad (2.34)$$

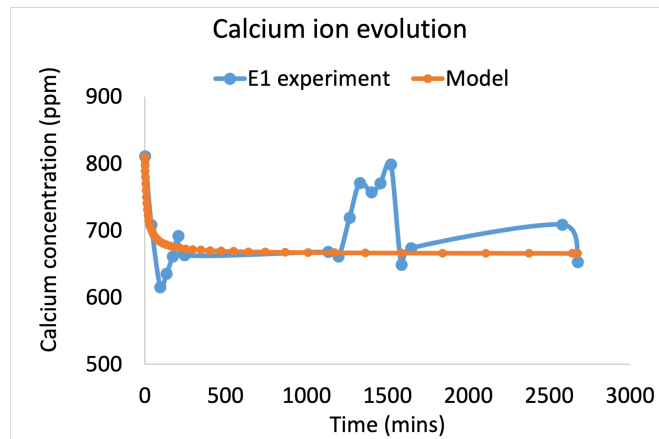
where ϕ_3 , ϕ_6 , and ϕ_8 denote the molar concentrations of CaCO_3 , NaCl and SO_4^{2-} respectively. Recall, in the reaction system (2.11) - (2.13), X_1 and X_2 react to form X_3 whereas X_4 and X_5 react to form X_6 and X_7 dissociates into X_4 and X_8 . The conservation of concentration requires that the total concentration of reactants at the initial state be equal to the total concentration of the products at the final state. Hence the reduction from 8 ODEs (2.19) - (2.26) to 3 ODEs (2.32) - (2.34) is to be expected because the reactant species (X_1 , X_2 , X_4 , X_5 and X_7) no longer exist after the precipitation reaction and the constituents of the final precipitate are X_3 , X_6 , and X_8 .

Furthermore, it can be seen from (2.32) - (2.34) that ϕ_3 and ϕ_8 completely decouple however ϕ_6 depends on ϕ_8 . This implies that ϕ_8 influences ϕ_6 but not vice versa. Physically this makes sense because in cases where the control over ϕ_6 might be desired, one would have to manipulate ϕ_7 which in turn influences ϕ_4 and ϕ_8 , demonstrating that ϕ_6 and ϕ_8 are somehow connected. However, ϕ_3 does not influence ϕ_6 or ϕ_8 because the precipitation of ϕ_3 is to some extent an independent process.

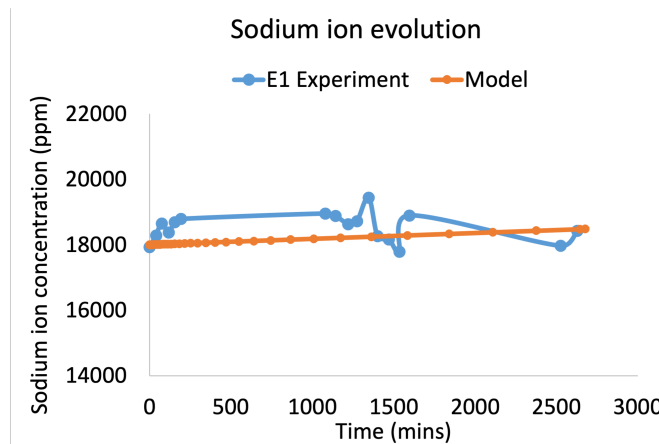
At equilibrium $\frac{d\phi_3}{dt} = 0$ and $\phi_3 = A$ or $\phi_3 = \frac{B}{2}$. The former suggests that all of species X_1 is used up and the latter suggests that all of species X_2 is consumed in the reaction. The former case is more relevant here because we can see from Table 2.1 that ϕ_1 is present in excess so ϕ_2 is the limiting reactant and would be entirely consumed. Similarly at equilibrium $\frac{d\phi_8}{dt} = 0$ and $E = \phi_8$. This implies that ϕ_8

is totally consumed as it completely dissociates into ϕ_4 and ϕ_7 . From a chemical perspective, this is reasonable because it is expected that during the dissolution of an ionic compound like Na_2SO_4 , the water molecules would break apart the ionic crystal into ions Na^+ and SO_4^{2-} . We expect the equilibration of ϕ_3 to occur at a faster rate than ϕ_8 because during the experiments, the precipitate X_3 was formed as soon as the reaction was initiated whereas the complete dissociation of ϕ_7 involved some mixing.

Now that we have the kinetic equations that we believe somewhat captures the chemical reactions occurring in experiment E1, we can proceed with fitting this model to our experimental results. In the following subsection, the simulation associated with this is presented.



(a) Fit between model and experimental results for calcium concentration in E1.



(b) Fit between model and experimental results for sodium concentration in E1.

Figure 2.12: Fit between model and experimental results for cation concentrations in E1.

2.5.3 Simulation

The kinetic model described in (2.19) - (2.26) was implemented in MATLAB using an ODE solver (ode23s). It is of interest to mention that ode23s was selected because the system of ODEs is considered to be stiff as the eigenvalues of the linearised equation are of different orders magnitudes. In Chapter 4, we present the eigenvalues in the context of the stability analysis.

The ode23s solver numerically integrates the equations with the specified initial conditions and produces a concentration plot as a function of time. Experimental rate constants were not available as previous studies has been mostly limited to qualitative or semi-quantitative investigations. Hence, rate constants were estimated by fitting the model with experimental results. Figure 2.12 shows the fitting of the model's equations to the experimental results. The values of the rate constants that match the experimental results are $k_1 = 7 \times 10^{-10} m^6 . mol^{-2} . s^{-1}$, $k_2 = 3 \times 10^{-12} m^3 . mol^{-1} . s^{-1}$, $k_3 = 3 \times 10^{-12} s^{-1}$.

The kinetic equations and rate constants estimated from the simulation will form part of the building blocks of the overall model framework. The values of the rate constant will be particularly important in Chapter 4 when we perform a stability analysis on the system.

2.6 Summary

In this chapter we have presented the main results from the experimental study. The results presented are consistent with published reports in [33, 71, 119]. The experimental results generated fresh insights into scaling mechanisms and how this can be altered by the ions present in the feed. The experiments demonstrated co-precipitation of more than one type of inorganic scale, which is consistent with what is typically observed in RO operations. We proposed that the co-precipitation in E1 occurs via the following sequence of steps:

1. Halite is initially formed but dissolves and recrystallises which results in the glassy elongated form shown in the SEM images in section 2.3.
2. The high supersaturation levels and presence of sulphate at the start promotes the formation of vaterite. Over time, a small portion of the vaterite is dissolved and converted to calcite.
3. The calcite crystals forming thereafter would be grown from a medium with a significantly higher $SO_4^{2-} : HCO_3^-$ ratio than the initial solution.

We proposed that the co-precipitation in E2 occurs via the following sequence of

steps:

1. Halite is initially formed but dissolves and recrystallises which results in the thick mass shown in the SEM images in section 2.3.
2. The presence of sulphate at the start promotes the formation of vaterite. Due to the high $\text{SO}_4^{2-}:\text{HCO}_3^-$ ratio, no calcite is formed.

We proposed that the co-precipitation in E5 occurs via the following sequence of steps:

1. Halite is initially formed but dissolves and recrystallises which results in the elongated form shown in the SEM images in section 2.3.
2. The high supersaturation levels promotes the formation of calcite instantaneously with many crystals precipitating at the same time, colliding with each other resulting in distorted edges and faces.

One of the more significant findings to emerge from this study is that at concentration levels similar to seawater levels, crystallisation of halite could occur even if it's not supersaturated. This study has found that halite could act as a binding agent for CaCO_3 crystals during crystallisation. Little is known about this and it is not clear which factors contribute to this. Infact, the present study appears to be the first study to observe an elongated or thick mass of halite during crystallisation (as opposed to the common cubic shaped crystals). This might suggest that the precipitates that actually form in desalination operations contain NaCl . Further work is needed to fully understand the reason for NaCl precipitation. In addition, it would be beneficial if this study could be repeated with more ions (e.g magnesium ion, phosphate ion, silicone ion) present to truly capture the complex process that occurs in industrial scale. In reality, it would be tedious to analyse the influence of all the ions present in the feed on the possible precipitate that could form e.g CaCO_3 , CaSO_4 . However, we believe this would provide significant insight on salt ion interactions and the end effect on desalination.

The results presented here also indicates that sulphate might reduce the tenacious nature of calcite implying that CaCO_3 crystals formed in the presence of sulphate might be easier to remove during membrane operations. It might be worthwhile to conduct experiments to test this hypothesis. In the latter part of the chapter, we formulated a kinetic model based on experimental observations. This was implemented in MATLAB, generating rate constants which will be instrumental to our model analysis in Chapter 4.

Chapter 3

Model Development

In this chapter we provide details of the macroscopic model developed, particularly in terms of the science and mathematics. We begin with a presentation of key definitions and basic ideas needed to develop, implement and analyse the model. In some cases we provide precise and detailed definitions, while in others we present only the basic concept. We follow this with a review of the literature but we make no claim as to completeness of this; the intent is merely to indicate the amount of work that has been done. We then present the model and note the couplings that exist between processes in the system. We conclude by describing the numerical procedure employed to produce solutions.

3.1 Introductory Remarks

In this section, we present a number of terms and definitions that are specifically related to reverse osmosis membrane operation. We describe the spiral wound membrane configuration and the various modes of operation in RO membrane systems. We remark that these topics impact details of the numerical analysis and are thus important for both theoretical and computational purposes. An understanding of these topics will serve as adequate preparation for the development and implementation of the model/algorithms to be introduced later.

3.1.1 Membrane Terms and Definitions

Osmotic Pressure

It is probably useful at this point to recall that in Chapter 1 we defined osmosis as the flow of fluid from a region of lower concentration to a region of higher

concentration [22]. Now we define the term “osmotic pressure” as the minimum pressure necessary to stop osmosis or the natural flow of the fluid. This osmotic pressure is a function of the individual solute concentration as we can see in equation (3.1). It is also related to the mole fraction of water; from a practical point of view this implies that as water is extracted from the feed solution during desalination (i.e the mole fraction of water reduces), the osmotic pressure increases [22].

The osmotic pressure of a fluid can be expressed as [22]

$$\pi(\phi_1, \dots, \phi_n) = RT\varphi \sum_i^n \phi_i, \quad (3.1)$$

where R is the gas constant in $J.mol^{-1}.K^{-1}$, T temperature in K , φ is the osmotic coefficient, a dimensionless quantity which characterises the deviation of a solvent from ideal behaviour and ϕ_i is the concentration of $i = 1, \dots, n$ components in mol/m^3 .

Natural waters treated by RO have substantial osmotic pressure. To put this into perspective, the osmotic pressure for tap water is around 0.4 bar [51] while that of seawater is around 25 bar. On the other hand, the osmotic pressure of brackish water is between 1-4 bar [51].

Rejection

Rejection measures the membrane’s ability to selectively transport water and reject other target components. Salt rejection is a function of feed pressure. Hence it is expected that increasing the feed pressure will increase rejection [50].

Salt rejection is defined as

$$r_i = 1 - \frac{\phi_p}{\phi_i}, \quad (3.2)$$

where r_i is the rejection which is obtained from the permeate concentration ϕ_p and feed concentration ϕ_i . The r value gives an indication of how effective the membrane is at rejecting salt ions. To put this into perspective, reverse osmosis membranes are capable of rejecting 99% of monovalent ions such as Na^+ and Cl^- [22]. A lower value would suggest that the membrane is underperforming.

Recovery

The membrane performance can also be evaluated using the recovery. The recovery can be loosely described as the ratio of the permeate flow rate to feed

flow rate. Mathematically this is written as [22]

$$r_e = \frac{Q_p}{Q_i} \quad (3.3)$$

where r_e is recovery, Q_p is the permeate flow rate and Q_i is the feed flow rate. Note Q_p can be estimated from the permeate area, A_p and permeate velocity v as follows

$$Q_p = v_p A_p. \quad (3.4)$$

Similarly, Q_i can be estimated from the inlet area, A_{in} and inlet velocity U_{in} as follows

$$Q_i = U_{in} A_{in}. \quad (3.5)$$

Therefore, the recovery can be written as

$$r_e = \frac{v A_p}{U_{in} A_{in}}. \quad (3.6)$$

The value of r_e provides insight on the quantity of clean water collected as permeate. As one might imagine, a high value of r_e is desirable as this implies that a high fraction of feed water is being recovered. However, as we have stressed previously, this comes at a cost because the osmotic pressure increases with higher recovery. This in turn reduces the permeate flux by inducing mineral scaling. Generally, the recovery achievable in RO systems is limited, ranging from 35-50% for seawater desalination and 70-85% for brackish water RO [3, 65].

Concentration Polarisation

Several lines of evidence suggest that concentration polarisation is the precursor to mineral scaling [22, 65]. There are a few ways to define concentration polarisation, and it is worthwhile to adopt various approaches to acquire a more complete understanding than can be obtained from a single viewpoint. We begin by recalling from our introductory discussions of reverse osmosis in section 1.2 that the membrane selectively rejects salts ions and generally transports only water through the membrane. This selective rejection results in a rise in ion concentration in the vicinity around the membrane surface [110]. This leads to two related consequences. First, a boundary layer (also known as polarised layer) of higher concentration is formed near the membrane (see Figure 3.1). Second, there is a concentration gradient between the membrane surface and the bulk feed which causes a diffusive back-flow to the bulk fluid [14]. These implications are of sufficient significance because the solubility limits of salt ions

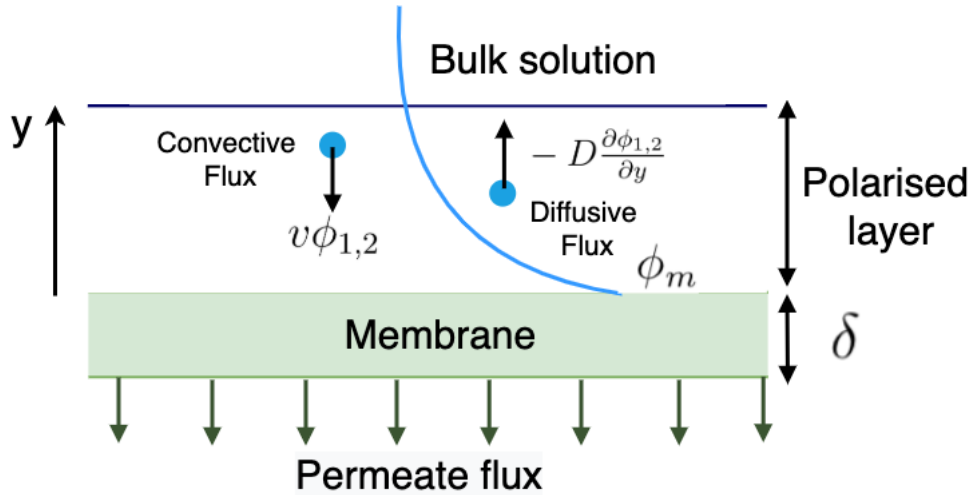


Figure 3.1: Illustration of the polarised layer occurring as a result of concentration polarisation.

are likely to be exceeded in these concentrated zones near the membrane surface, leading to salt precipitation. In fact, experimental studies have shown that CaCO_3 scaling could be exacerbated by concentration polarization [65] and primarily for that reason we include it in our model analysis.

The boundary layer film model has been used to describe the concentration polarisation phenomenon. It is assumed the convective flux of solute toward the membrane equals the sum of the diffusive back transport of solute and the permeate flux passing through the membrane [4]. The solute material balance in the polarised layer is thus given by [4]

$$\underbrace{v\phi_m}_{\text{Convective flux}} = \underbrace{-D\frac{d\phi}{dy}}_{\text{Back diffusion}} + \underbrace{v\phi_p}_{\text{Permeate flux}}, \quad (3.7)$$

where ϕ_m is the solute concentration at the membrane, ϕ_p is the permeate concentration, v is the fluid velocity and D is the solute diffusivity.

3.1.2 Membrane Mode of Operation

Reverse osmosis membranes can be operated in either dead-end mode or cross-flow mode. In the former, flow direction is normal to the membrane whereas in latter, the feed flows tangentially across the membrane surface as shown in Figure 3.2. Stirring is adopted in dead-end mode to reduce polarization effects and obtain a sufficiently high Reynolds number. In dead-end mode, flux decline is typically observed as a result of the additional resistance from accumulated salts [67]. In most applications, it is so severe that this mode of operation becomes unsuitable and cross-flow operation is adopted. The tangential flow in cross

flow mode creates a shearing effect on the surface of the membrane which helps minimise concentration polarisation [51]. Although, this mode of operation is more energy intensive and expensive, it is the mode of operation most often used for reverse osmosis operations [67].

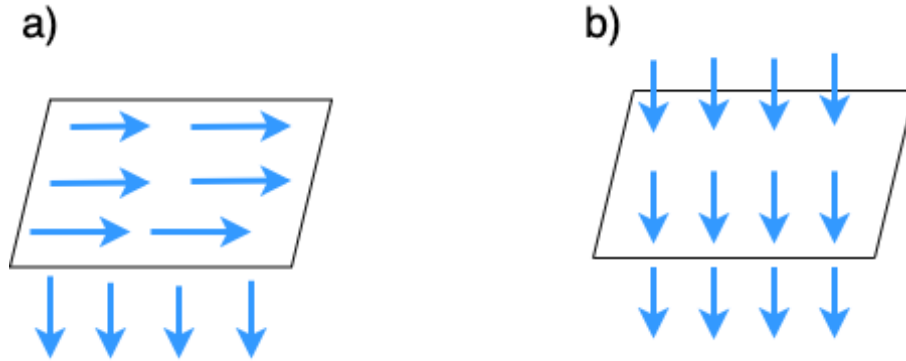


Figure 3.2: Schematic representation of (a) cross-flow mode and (b) dead-end mode.

3.1.3 Membrane Configuration

In the literature, membrane configuration is used to refer to the geometry of the membrane and its position in space in relation to the flow of the feed and of the permeate [11]. Most industrial membrane installations use modules as the basis of design or construction. Generally the membrane module consists of a feed stream (inlet), a permeate stream and a retentate stream (outlet) [22].

The main types of membrane configurations used in industrial scale are: plate-and-frame, tubular, spiral wound and hollow-fiber configurations [69]. The membrane geometry is planar in the first two and cylindrical in the last two. A desirable configuration is one that is compact, easy to clean, supports uniform velocity distribution and has a low resistance to fluid flow. Some degree of turbulence at the retentate side is also a desirable property, as it minimises scaling and promotes mass transfer [11].

In what follows we describe the flat sheet and spiral wound configuration as these are the configurations most relevant to our investigation.

Flat Sheet Membranes

In industrial applications, flat sheet membranes are seldom used on their own, due to their low packing density (i.e. the surface area to packing volume ratio) [133]. They are instead pleated into spiral wound modules. However, flat sheet membrane configuration are often favoured for laboratory scale applications on

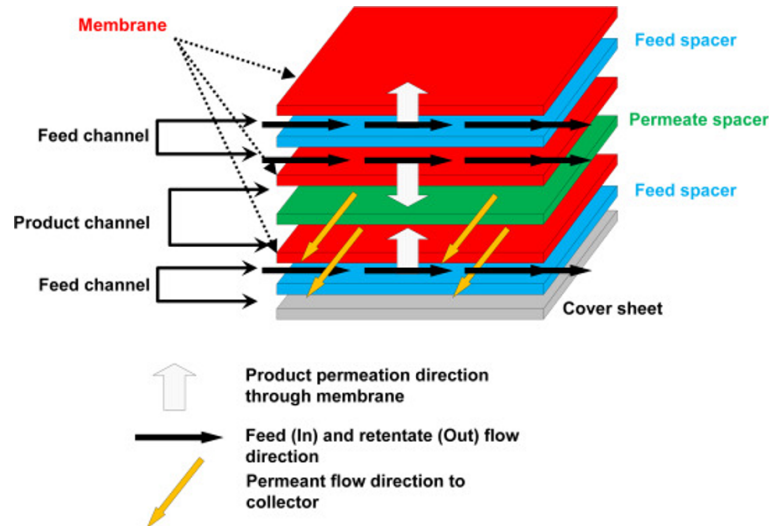


Figure 3.3: This illustration depicts an unwound configuration to demonstrate the flow direction in a spiral wound configuration [73].

the basis of their operational simplicity. Spiral wound modules on the other hand can be complicated and very difficult to simulate.

Spiral Wound Configuration

Spiral wound membranes (SWM) are used in large scale industrial applications due to their high surface area to volume ratio [11]. The module consists of several flat sheet membranes (see Figure 3.3) assembled in a spiral wound configuration. The edges of the membranes are sealed with glue to form several membrane envelopes as depicted in Figure 3.4. The open ends of the envelopes are connected to a perforated central tube which is commonly referred to as the permeate collection tube. Thus, during operation when the feed solution is exposed to the membrane surface, a portion of the water in the feed passes through the membrane surface and permeates the membrane envelope, spiraling toward the collection tube as shown in Figure 3.4 [22].

The membrane modules are typically manufactured with membrane area of 20–40 m², diameters of 10 to 40 cm and lengths of 1 m giving flowrates of up to 28 m³ per day [10, 99]. To reduce concentration polarisation in spiral-wound elements, turbulent conditions are promoted with the use of feed spacers as shown in Figure 3.4. The feed spacers provides a reduced channel for feed flow by maintaining a space between two membrane sheets in the range of 0.6 to 0.9 mm [10, 22, 73, 99, 135]. The spacers are used not only to enhance the mass transfer but to maintain the fluid velocity [124]. However, these complicates the flow pattern.

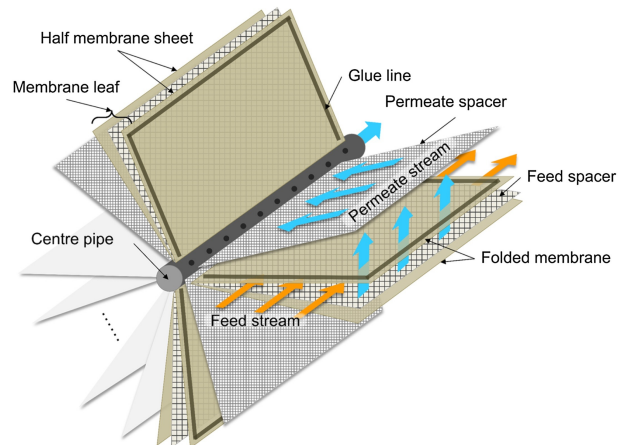


Figure 3.4: The assembly and fabrication of spiral wound membrane module [73].

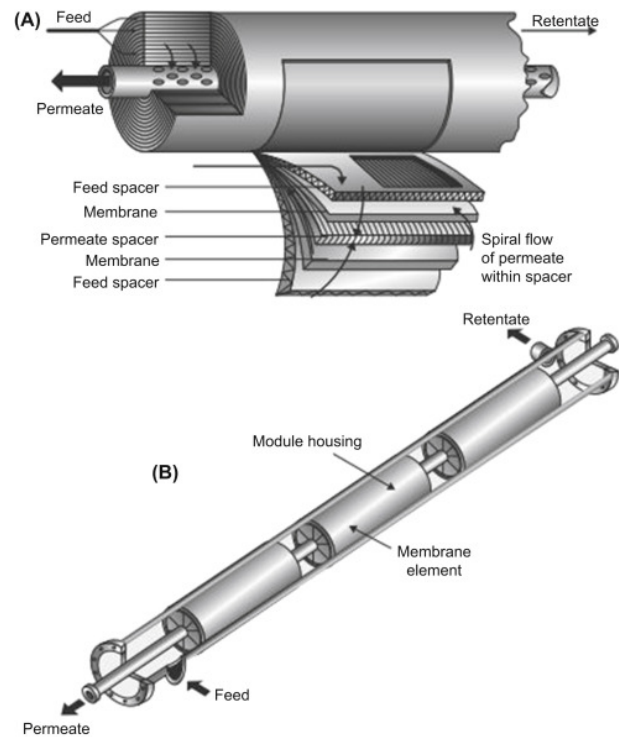


Figure 3.5: (a) Schematic illustration of the arrangement of the feed channel, spacer, membrane and permeate channel in a spiral wound membrane module (b) Typical industrial unit showing several spiral wound elements in series [124].

Recovery & Rejection in Spiral Wound Modules

The RO membrane separation process reduces the total dissolved solids concentration in feed water from 242 mg/l to less than 4 mg/l corresponding to an average salt rejection of 98% [106]. However, higher salt rejections in the range of 99.75% - 99.8% can also be achieved. To achieve a high recovery, the spiral wound installation usually consists of six to eight modules connected in series as shown in Figure 3.5b. Hence, the concentrate from the first element becomes the feed for the next element in series as depicted in Figure 3.5b. This process is repeated until the concentrate from the last RO element exits the pressure vessel [22]. Individual spiral wound membrane elements have a permeate recovery of 5 to 15 percent. Desalination operators increase feed pressures to allow sufficient permeation through the membrane and maintain the desired permeate flows. Pumps are used to achieve relatively high operating pressures, with pressures ranging between 10 - 25 bar for brackish water and 50 - 80 bar for seawater [23, 101]. Therefore, overall water conversion can reach as high as 70–85% in the case of brackish water and 35–50% in the case of seawater. It is important to note that pressure loss develops as feed water flows through the feed channels and spacers, which reduces the driving force for flow through the membrane surface. Although, the feed side head loss across a membrane element is typically less than 0.5 bar [22, 23, 99].

This concludes our review of the relevant membrane topics, terms and definitions. We once again emphasize that the main factors that limit recovery include: osmotic pressure, concentration polarisation and precipitation of mineral salts [22]. Therefore in this study, we will develop a holistic macroscopic model which integrates all the aforementioned processes and unravels the complex interactions between them. In the following section we provide an overview of the relevant models associated with these processes.

3.2 Literature Review

A number of researchers have carried out studies on various aspects of the reverse osmosis process [35, 47, 48, 50, 87, 98, 110, 113, 125, 129]. There have been many approaches for doing this; spatial scale models are often used to capture the scale dependence of the underlying processes. In contrast, time dependent models aim at optimising membrane design (steady state models [59]) or at capturing time dependent phenomena (unsteady state models) such as mineral precipitation which may deteriorate the membrane over time [58]. Such an approach allows researchers to quantify the effect of design and

operating variables on specific reverse osmosis problems and performance [22, 130]. In this section we will present some of the models that have been developed and used through the years in efforts to predict membrane performance. We will do this by means of a more or less chronological ordering to provide a sense of how the current understanding of reverse osmosis modelling has evolved.

3.2.1 Fluid Dynamics

One of the early studies on fluid flow in a membrane channel was conducted by Berman [12] in the second half of the 20th Century. Berman [12] investigated the flow field in a rectangular membrane channel with two membranes by solving the Navier-Stokes equations which is given by

Continuity equation

$$\frac{\partial \rho}{\partial t} + \frac{\partial(\rho u)}{\partial x} + \frac{\partial(\rho v)}{\partial y} = 0, \quad (3.8)$$

Momentum equation

$$\frac{\partial(\rho u)}{\partial t} + u \frac{\partial(\rho u)}{\partial x} + v \frac{\partial(\rho u)}{\partial y} = -\frac{\partial p}{\partial x} + \frac{\partial}{\partial x} \left(\mu \frac{\partial u}{\partial x} \right) + \frac{\partial}{\partial y} \left(\mu \frac{\partial u}{\partial y} \right) + S_i, \quad (3.9)$$

$$\frac{\partial(\rho v)}{\partial t} + u \frac{\partial(\rho v)}{\partial x} + v \frac{\partial(\rho v)}{\partial y} = -\frac{\partial p}{\partial y} + \frac{\partial}{\partial x} \left(\mu \frac{\partial v}{\partial x} \right) + \frac{\partial}{\partial y} \left(\mu \frac{\partial v}{\partial y} \right) + S_j. \quad (3.10)$$

where u is i component of velocity (ms^{-1}), v is j component of the velocity (ms^{-1}) and S are source terms. (3.8) is the continuity equation whereas (3.9) and (3.10) are the momentum equations, expressing the principles of conservation of mass and momentum respectively.

The exact solution of the flow equations was obtained leading to a third-order nonlinear differential equation which was solved by a perturbation method. Although, the scope of the investigation was limited to two-dimensional incompressible steady-state laminar flow $Re \approx 1$, the study made an important contribution to the field. With the assumption of constant permeation velocity along the channel, it was shown that, in a thin layer near the permeable walls, the flow field at any location in the channel can be well approximated by combination of a shear tangential flow and a constant perpendicular flow. The findings from this study provided the context for numerous works on the Navier–Stokes equations by [17, 28, 83, 103, 122, 132] and many others. Since then researchers have studied the computational fluid dynamics (CFD) of

reverse osmosis by solving Navier-Stokes equations coupled with Darcy's law. Many numerically solve the Navier-Stokes equation using the finite volume method [125] and use the Semi-Implicit Method for Pressure Linked Equations (SIMPLE) algorithm for the pressure velocity coupling [47, 82, 129]. There are a few studies that have also used the finite difference scheme to numerically solve the Navier-Stokes equation [24].

3.2.2 Membrane Transport Theory

In the 1960s much of the research was dedicated to understanding the transport in RO membranes [46, 66, 115]. It was shown by Lonsdale *et al.* [66] that the fluid flux through the membrane can be represented reasonably well by linear models such as the solution-diffusion model. However, Spiegler and Kedem [115] argued that this model which is purely diffusive is not in line with experimentally observed fluxes which consists of both a diffusive flux and a convective flux. Therefore, [115] solved the differential equation of transport within the membrane and proposed the pore-flow model which accounts for convective effects through the membrane. This model is also known as the Spiegler-Kedem model.

It is worthwhile to examine the details of each of these theories as they are important elements of our model. Therefore, below we describe and distinguish the solute-diffusion model and the pore model.

Solution-Diffusion Model

The model is based on the premise that the membrane's pores are infinitesimally small and so transport is through a dense permeable membrane layer with finite thickness. Transport of the fluid and salt is believed to take place independent of one another and the effects of fluid on the other side of membrane are neglected. It is assumed that the fluid and salt ions are transported according to the following processes: adsorption, diffusion and desorption. First, the water and solutes are absorbed (either through chemical bonding to membrane surface or dissolution within membrane) into the solid membrane material then they independently diffuse through the membrane down a concentration gradient and re-liquefy at the permeate side of the membrane [128].

The mathematical description of the solution diffusion water flux, v_s through a reverse osmosis membrane is described by

$$v_s = A(\Delta p - \Delta\pi), \quad (3.11)$$

where A is the water permeability constant in $m.s^{-1}.Pa^{-1}$, Δp is the pressure

gradient and $\Delta\pi$ is the osmotic pressure gradient. The equivalent expression for J , salt flux is

$$J = B(\phi_f - \phi_p), \quad (3.12)$$

where B is the salt permeability of the active membrane layer in m/s , ϕ_f and ϕ_p are the solute concentration at the feed interface and permeate interface respectively. (3.11) and (3.12) suggests that the water flux through a reverse osmosis membrane increases with applied pressure while the salt flux is proportional to the concentration difference across the membrane and is independent of applied pressure.

Pore model

The solution-diffusion model does not consider convective flow through the membrane. The pore flow model on the other hand assumes that RO membranes have tiny pores through which water moves. This model is based on the premise that the fluid permeates the membranes through physical pores present in the membrane. Separation is achieved through size discrimination where large molecules of salt ions are rejected by the membrane [130]. It is assumed that in cases where the dissolved solutes and water molecules are similar in size, separation is not solely physical sieving but also involves chemical effects such as electrostatic repulsion between salt ions and membrane material.

In the pore flow model, there is no concentration gradient across the membrane. The flow through the membrane is given as

$$v_p = \frac{k(p_f - p_p)}{\delta}, \quad (3.13)$$

where k is the membrane permeability, p_f is the pressure at the feed side of the membrane, p_p is the pressure at the permeate side of the membrane and δ is the membrane thickness. It should be noticed that the pore model is identical to Darcy's law.

The work of Lonsdale *et al.* [66] and Spiegler and Kedem [115] spurred considerable development in membrane transport theory in the 20th Century, and it is often claimed that they are one of the main progenitors of reverse osmosis membrane transport theory. Following their work, studies showed that the contribution of pore flow to the solvent flux is negligible however the pore flow has significant effect on the solute flux [60, 112]. The solution diffusion model is the most commonly used model for the prediction of water and salt flow through a reverse osmosis membrane. Although, there are a number of

studies which use the combination of both models to predict transport flow through reverse osmosis membranes [22, 37]. It is also worth mentioning that some studies [7, 8] have combined the solution-diffusion model with the concentration polarization model given by the film theory (described earlier when concentration polarisation was introduced in section 3.1.1) to explain solute transport through the membrane [102].

3.2.3 Design Studies

Beginning in the early 1970s numerous works [79, 80, 85, 86, 108, 114] began to appear that focused on developing analytical design equations that could be used for preliminary design studies. The benefit of this approach was that it allowed investigators to quickly obtain prediction results that might be helpful during design stage. For simple equations, an analytical solution was possible after some assumptions have been introduced [85, 108, 109]. Typical assumptions include average conditions on either side of the membrane, constant or total separation, dilute solution, negligible concentration polarization and constant mass transport coefficient.

Sirkar *et al.* [108] developed simple analytical design equations for single-solute RO with the aim of calculating channel length and average permeate concentration for spiral wound RO modules. In this work, pressure drop in feed and permeate channels were neglected and linear approximation for the concentration polarization term was assumed. Evangelista [30] and Evangelista and Jonsson [31] also developed explicit analytical equations for water flux and tested these equations for dilute solutions. All these analytical solutions mentioned above are based on assumptions of average and uniform fluid conditions in feed and permeate channels. Avlonitis *et al.* [7, 8] proposed an analytical solution for spiral wound RO modules, which is the only analytical model reported in the literature that accounts for spatial variations in pressure, velocity and concentration in both the feed and permeate channels. This analytical model assumes constant value for mass transfer coefficient along the membrane and a linear approximation for the concentration polarization term.

For more complicated equations researchers adopted an iterative approach [1]. For example, Agarwal *et al.* [1] developed design equations for power law fluids for both laminar and turbulent flow regimes. The equations were solved using fourth order Runge-Kutta method and the Newton-Raphson technique. It is however important to recognize that although this method of analysis is useful for fast estimation of preliminary results, they are however less suitable for module development and optimisation due to the many approximations and assumptions

made.

3.2.4 Geometry Studies

At the end of the 20th Century, researchers started to pay more consideration to the geometry of the membrane module. Some researchers such as Boudinar *et al.* [16] incorporated the spiral geometry of the spiral wound membrane in their simulations whilst many adopted an unwound approach whereby the membrane channel is modelled as a stack of flat sheet membranes [7, 8, 31, 102, 135]. Even in the 21st Century, with advanced computation facilities, many studies are still conducted under the assumption that the spiral membrane module can be represented as a stack of thin channels as shown in Figure 3.6b. Although there has been an increasing interest in the effects of spacer geometry on the performance of the module [63, 98]. For example, Santos *et al.* [96] investigated the effect of the geometry of the spacer structure on the fluid flow and concentration patterns. The continuity, momentum and mass transport equations with the corresponding boundary conditions were solved with the open-source CFD software package called OpenFOAM. Finite volume method was used to discretise the momentum and mass transport equations and the pressure-velocity coupling was achieved using the Pressure-Implicit with Splitting of Operators (PISO) algorithm. Researchers are also developing models which incorporate a detailed description of the geometric features of spiral wound membrane such as the number of membrane envelopes, the radius of the collection pipe, and the thickness of permeate and feed spacers [39].

3.2.5 Precipitation Studies

A number of experimental studies have shown the impact of precipitation on membrane systems [52, 105, 123]. However it was not until recently that studies began to appear that employed numerical modelling in the study of precipitation in RO membrane desalination. To the best of our knowledge, the first study to formulate a kinetic model and couple this with the concentration field was by Karabelas *et al.* [52]. Although, it is worth mentioning that this study did not consider the fluid dynamics of the system. The evolution of the salt ions concentration at the membrane surface was determined by solving the following one-dimensional transient convection-diffusion equation using finite-difference method

$$\frac{\partial \phi}{\partial t} = v \frac{\partial \phi}{\partial y} + D \frac{\partial^2 \phi}{\partial y^2}, \quad (3.14)$$

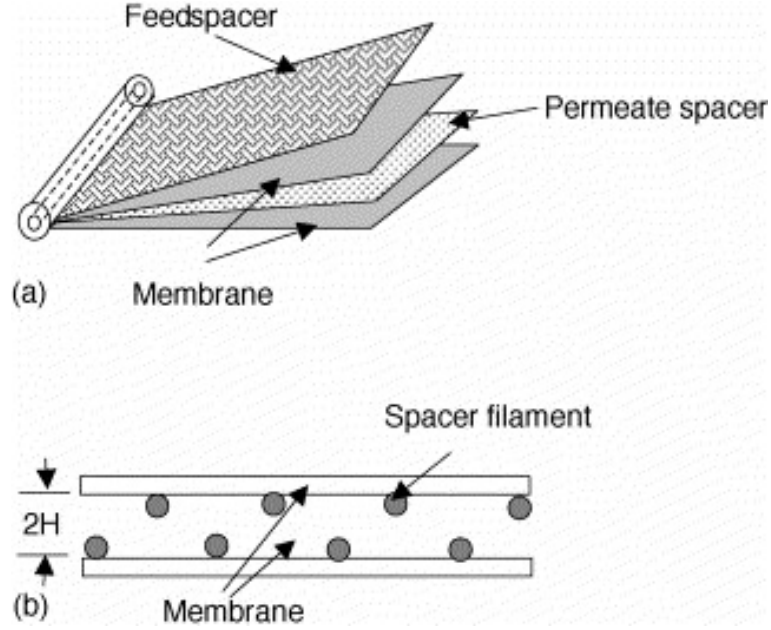


Figure 3.6: Schematic of (a) spiral wound reverse osmosis membrane module and (b) cross section of a feed channel sandwiched by two pieces of membranes.

where y is the direction normal to the membrane, ϕ is the concentration of the ionic species, v is the velocity at the membrane which is a function of time and D is the diffusion coefficient of salt ions. The initial conditions are

$$\phi(y, 0) = \phi_{in}(y) \quad \text{in } \Omega. \quad (3.15)$$

In this study, it was assumed that scaling occurs only at the membrane surface. Therefore the nucleation and growth kinetics of the salt ions which are based on the method of moments are included in the boundary condition. The nucleation step (introduced earlier in section 2.1.1) was described according to the nucleation theory and the crystal growth (also introduced earlier in section 2.1.1) was modelled using a poly-nuclear surface reaction rate expression. We will not dwell here with the derivation of this models because our main purpose in presenting this study is simply to make the reader aware that such efforts have previously been made. For the reader interested in the details associated with the derivation of the nucleation and growth kinetics, this text by [52] is recommended. The membrane boundary condition was formulated based on the assumption that the precipitation of the solid crystalline phase must be equal to consumption of solute, this results in

$$-R\phi v = D \frac{d\phi}{dy} - \frac{a}{V_m N_A} \frac{dM}{dt}, \quad (3.16)$$

where R is the rejection coefficient of the species, a is the number of moles of the ionic species, V_m is the molecule volume of the solid phase, N_A is the Avogadro number and M denotes the moments which describes the particle number and deposit mass per surface area.

Another notable work is the study by Radu *et al.* [87] who developed a two-dimensional mathematical model integrating fluid flow and solutes mass transport with a particle-based approach for crystal nucleation and growth. The geometry was representative of an unwounded membrane channel (similar to that in Figure 3.6b) consisting of two parallel flat sheet membranes (at $y = 0$ and $y = L_y$) and a feed spacer. The flow field was computed using the incompressible Navier–Stokes and the transport of salt ions was described using the following advection-diffusion-reaction equation

$$\underbrace{\frac{\partial \phi}{\partial t}}_{\text{transient term}} + \underbrace{\nabla \cdot (\mathbf{u}\phi)}_{\text{convective term}} = \underbrace{\nabla \cdot (D\nabla\phi)}_{\text{diffusion term}} + \underbrace{Q^\phi}_{\text{source term}}, \quad (3.17)$$

where Q^ϕ is a source term which represents chemical reactions of ions with other ions dissolved in the fluid. Radu *et al.* [87] held the view that the precipitate layer may be permeable to liquid flow and described this by the Brinkman equation

$$\frac{\mu}{k}\mathbf{u} + \nabla p = \frac{\mu}{\epsilon}\nabla^2\mathbf{u}, \quad (3.18)$$

where k is the permeability of the precipitate and ϵ is the local precipitate porosity. At the channel inlet ($x = 0$), a no-slip condition was prescribed as it was assumed the feed spacer is impermeable.

$$u = 0 \quad \text{on } y = 0, L_y. \quad (3.19)$$

The flow through the membranes was described using

$$v = A(\Delta p - \Delta\pi) \quad \text{on } y = 0, L_y, \quad (3.20)$$

while the solute transport through the membrane was described by the following flux condition

$$v\phi - D\frac{d\phi}{dy} = v\phi(1 - R). \quad (3.21)$$

In their model, the mineral scale is represented by a collection of discrete hard particles of crystalline matter, each characterized by a diameter, mass and position vector. The approach followed for precipitate development in this study follows the process described by Bird *et al.* [15] in that the precipitate

formation is based on two processes: nucleation and crystal growth. However, in the present case nucleation was modelled as a stochastic event which depends on the local solution supersaturation. Furthermore, the crystal growth model consists of two domains; an outer layer where the mass of each particle increases and an inner layer where the particles are immobile and do not increase in volume. We will not dwell on the details here, we refer the reader to [87] for a complete treatment.

It is also worth mentioning that Tartakovsky *et al.* [120] investigated the mixing-induced precipitation in porous medium using a combination of laboratory experiments, pore-scale simulations and continuum scale simulations. The effect of the Peclet number and the Damköhler number on mixing induced precipitation was also investigated. However, it is important to note that this study was not conducted in a desalination context.

3.2.6 Our Approach

We have now presented all the tools needed to formulate a model of our own. Similar to some of the authors above, we investigate the flow field in a rectangular membrane channel with a flat sheet membrane by numerically solving the Navier-Stokes equations presented in (3.8)-(3.10). We describe the salt transport using (3.17) and the fluid flow through the membrane using a combination of the pore flow (3.13) and solution-diffusion model (3.11) described in section 3.2.2. We integrate the precipitation kinetic model developed earlier in section 2.5 into the membrane boundary condition to describe the precipitation process that occurs at the membrane. Similar to [96], we use OpenFOAM to discretise the momentum and mass transport equations. We also further analyse experimental observations through stability analysis and use the dimensionless groups that will be identified later to evaluate the interaction between various sub-processes. We remark that to the best of our knowledge, this is the first study to propose a deterministic formulation for precipitation in a reverse osmosis membrane, conduct stability analysis on the experimental results and present dimensionless groups that capture the entire physics of the system. Below we make a few comments on our precipitation approach, this is intended to provide motivation/justification for the kinetic model formulated.

Precipitation Approach

It is apparent from our review that much of the modelling formulation describing precipitation in membrane desalination have been stochastic-inclined. Although

these models provide a useful approximation to crystal population growth they are considerably complicated and are in general more difficult to analyze compared to their deterministic counterparts. Moreover, our goal is to develop a simplified framework that synthesises the essential features of reverse osmosis desalination. This at least in part motivated the development of a deterministic formulation, simpler than its stochastic counterparts but capable of capturing the interactions observed in experiments.

3.3 Model Formulation

The mathematical model presented in this section consists of coupled equations with non-linear terms appearing in some equations, rendering the system nonlinear. We begin by illustrating some of the interactions between the processes and follow this with details of the feedback mechanisms that exist in the system. Next we present the details (i.e. geometry, spacial domain, initial and boundary data) required to construct a mathematically well-posed problem.

3.3.1 Interactions & Feedbacks

Figure 3.7 illustrates some of the interactions between individual sub-processes. It can be seen that even in the absence of scaling/precipitation, a clear coupling exists between fluid flow and solute transport. This is because the distribution of solutes influences the local permeate velocity via the osmotic pressure, which is determined from the solute concentration. The solute concentration is also dependent on the flow through advective transport.

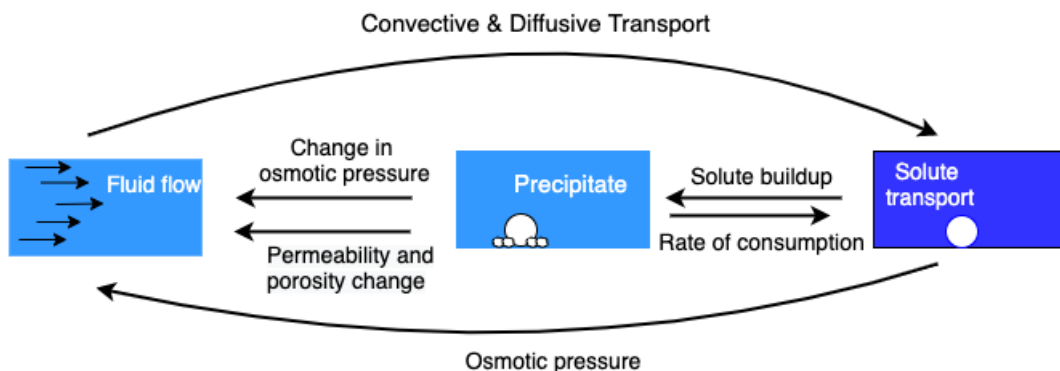


Figure 3.7: Schematic illustration of the interactions between flow, solute transport processes and scaling in RO feed channel.

At this point, one might wonder how precipitation fits into this. The answer is quite straightforward. It is easily seen from Figure 3.7 that precipitation of mineral scalants will lead to a decline in porosity which in turn will cause

changes in permeability. This affects the fluid flow which influences the solute transport and eventually precipitation again. Figure 3.8 highlights the couplings between equations and individual field variables. Represented in the figure are the equations for conservation of solute concentration (the convection–diffusion equation), conservation of momentum and mass (Navier–stokes equation, Darcy’s Law) and a variety of constitutive laws for key parameters such as the osmotic pressure, porosity and permeability. The constitutive laws are the relations between the forces imposed on the membrane and the resulting deformation at a macroscopic level. In essence, they represent the collaborative effects of the intermolecular forces when the membrane is sheared or otherwise deformed. In our case, the membrane has three constitutive laws pertaining to different deformations caused by changes in permeability k , porosity ϵ and osmotic pressure π . Considering these equations together, it becomes clear that mineral precipitation has the potential to directly affect fluid flow (via porosity and permeability) and advective solute transport. A list of some of the important feedbacks between the equations/processes shown in Figure 3.8 include:

- Coupling between the conservation of momentum and the conservation of mass typically treated by solving the two together to obtain the flow field.
- Coupling between fluid flow and solute concentrations, primarily through the advection of solutes and through modifications in the porosity and permeability as a result of mineral precipitation.

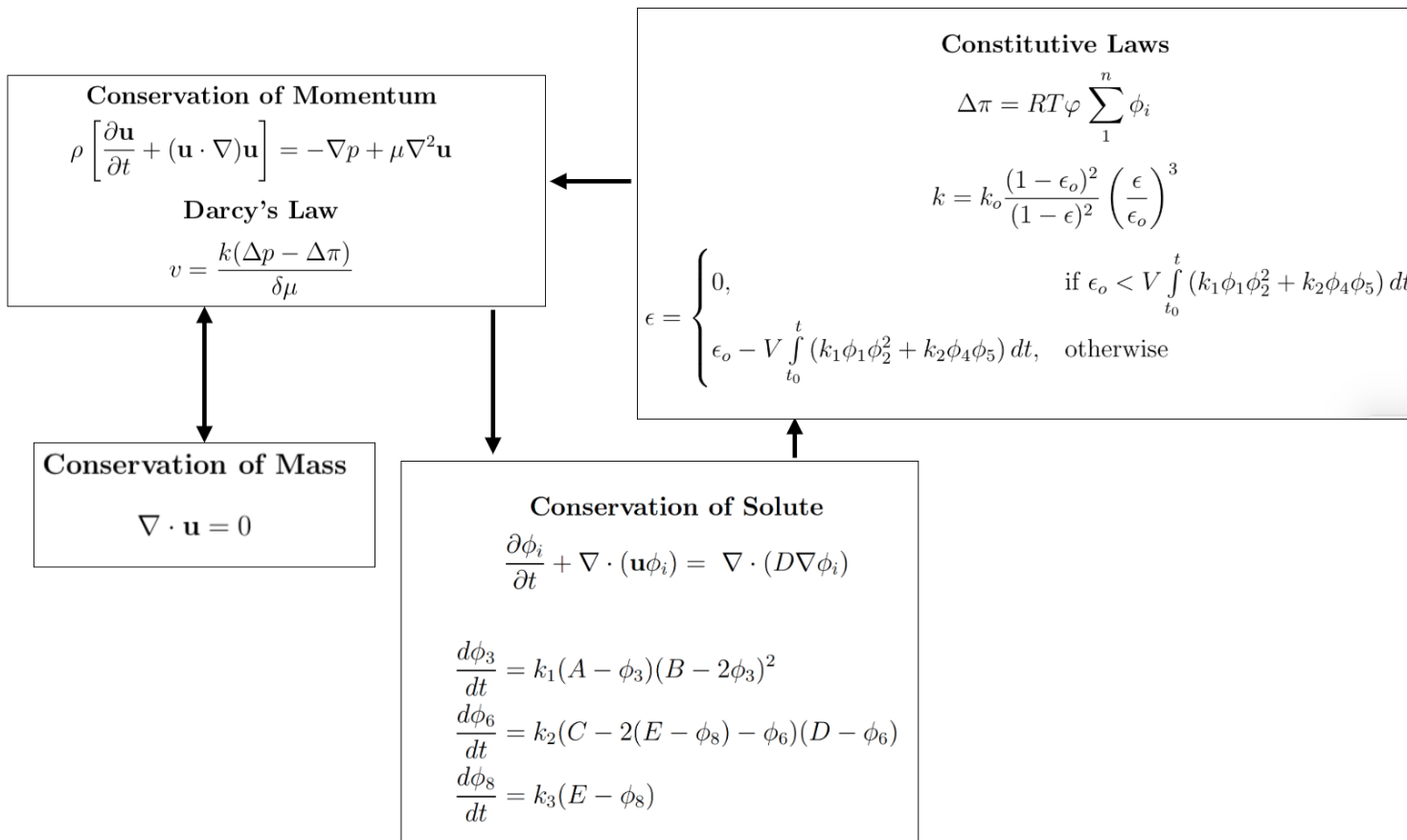


Figure 3.8: Coupling between processes can be seen in the governing equations describing the system.

3.3.2 Model Geometry

The reader will recall that earlier in section 3.1.3, we mentioned that the membrane modules are typically manufactured with lengths of 1 m and the distance between two membrane sheets in the range of 0.6 to 0.9 mm [10, 22, 73, 99, 135]. We illustrate this configuration in Figure 3.9. It can be seen that the fluid flows in the x direction between two membrane sheets and the width is large in the z direction when compared to the separation in the y direction. We have shown this configuration so the reader understands the physical geometry being considered. However, for simplicity and computational efficiency, we will consider only a small section of a larger membrane channel. This means the fluid dynamics and transport will be investigated over a smaller length scale, covering 2% of the membrane element which is equivalent to ~ 20 mm membrane length.

The geometry used in this study is similar to that shown in Figure 3.9. However, our analysis will be restricted to two-dimensional coordinates as shown in Figure 3.10. The geometry presented in Figure 3.10 is representative of a cross section of an unwound spiral configuration consisting of a flat sheet membrane. The mode of operation depicted here is a cross flow; whereby the feed flows tangentially to the membrane surface and permeate flows tangentially to the membrane surface [41].

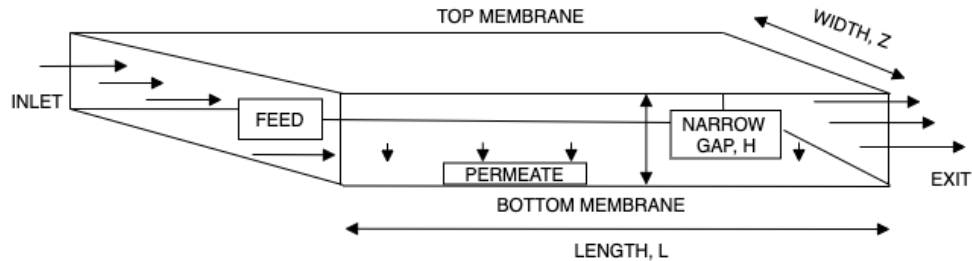


Figure 3.9: Geometry for flow through a membrane channel, three-dimensional.

It is important to point out that the membrane is a thin layer in reality. Hence from a computational point of view, it is better to consider it as an interface rather than a complete domain as we are only interested in taking into account the scaling of salt ions on the surface. We believe the membrane properties will evolve over time due to the changes in porosity and permeability so a time dependent system with finite domain is considered here.

For convenience we will assume Ω is a rectangular type domain in \mathbb{R}^2 and define the domain $\Omega \equiv (0, L) \times (0, H)$ as shown in Figure 3.10. We set $\Gamma = \partial\Omega$ to

represent the boundary of Ω which consists of different parts defined as

$$\Gamma_m = (0, L) \times \{0\}, \quad (3.22)$$

$$\Gamma_i = \{0\} \times (0, H), \quad (3.23)$$

$$\Gamma_o = \{L\} \times (0, H), \quad (3.24)$$

where Γ_m represents the membrane boundary, Γ_i is the inlet boundary and Γ_o is the outlet boundary. The rest of the domain boundary corresponds to solid boundaries, denoted by Γ_w so that $\Gamma_w = \Gamma \setminus (\Gamma_i \cup \Gamma_o \cup \Gamma_m)$.

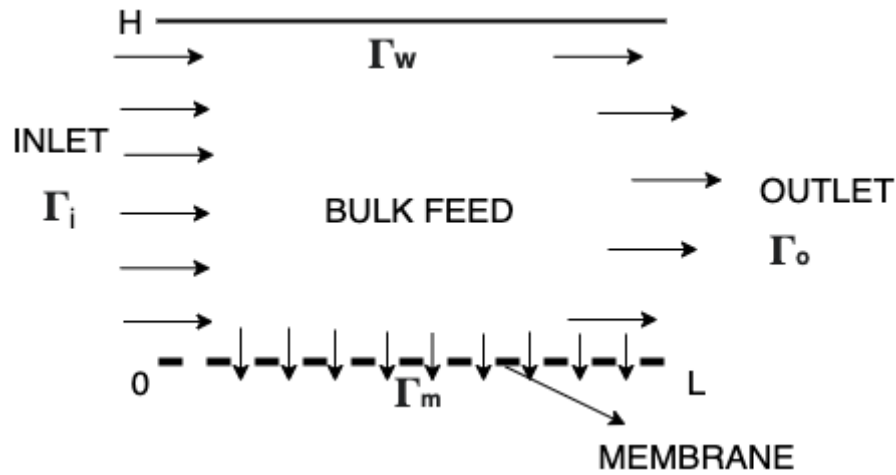


Figure 3.10: Rectangular two-dimensional domain with boundary locations.

Scale of Consideration

It is useful to mention again the spatial scale that would be considered in our investigation. We begin by noting that there are three different types of scales commonly used which are: 1) continuum models, 2) porescale models, and 3) multiple continua or hybrid models. Pore scale models include pore network and lattice Boltzmann models whereas multiple continuum models combine both pore scale and continuum scale [27, 100].

For our investigation, we adopt the continuum model because flow, transport and reaction are conventionally described by macro-scale models. In addition, the continuum approach is the most advanced in terms of its treatment of multicomponent chemical processes. Hence, we will model our processes over macro length scales.

3.3.3 Fluid Flow

The fluid flow is described by the Navier-Stokes equations of motion for an incompressible viscous fluid. We recall the vector form of the equation

$$\rho \left[\frac{\partial \mathbf{u}}{\partial t} + (\mathbf{u} \cdot \nabla) \mathbf{u} \right] = -\nabla p + \mu \nabla^2 \mathbf{u} \quad \text{in } \Omega, \quad t > 0, \quad (3.25)$$

$$\nabla \cdot \mathbf{u} = 0 \quad \text{in } \Omega, \quad t > 0, \quad (3.26)$$

where ρ is the density of the fluid, \mathbf{u} is the velocity vector which will often be written as $(u, v, w)^T$, p is the fluid pressure and μ is the dynamic viscosity. ∇ is the gradient operator, ∇^2 is the Laplacian operator and $\nabla \cdot$ is the divergence operator. The dimensional parameters of density ρ and viscosity μ are assumed to be constant. For simplicity, body-force terms are omitted because they will not influence present developments.

Initial & Boundary Conditions

It is consistent with the general principle of PDEs to solve the Navier-Stokes equation (which is an initial boundary value problem) by providing boundary conditions for pressure and velocity at the boundary of the solution domain Ω . Generally, boundary conditions may be prescribed by a variable value (this is the Dirichlet condition), gradient of the variable (Neumann condition) or a combination of the variable and its gradient (Robin condition). We assign boundary conditions at all points of the boundary of the solution domain Ω i.e Γ_i , Γ_w , Γ_m and Γ_o .

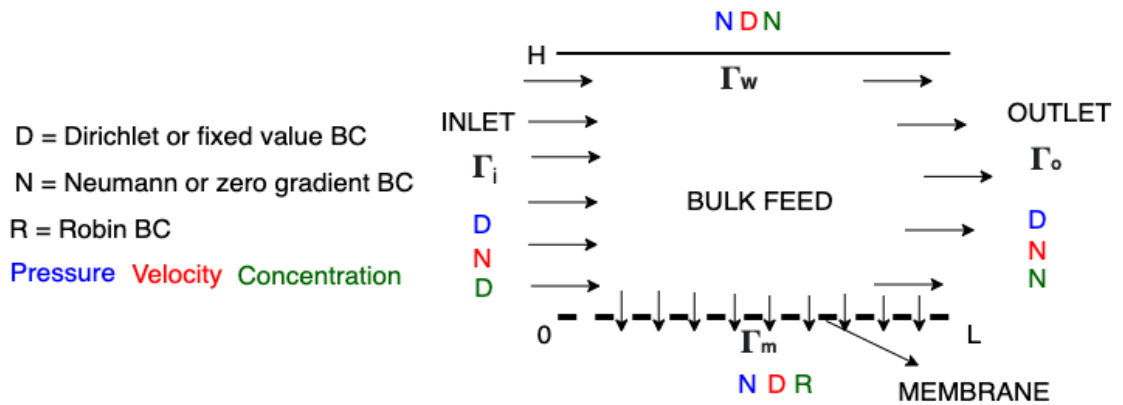


Figure 3.11: Schematic illustration of the membrane boundary conditions used in the simulation.

The initial condition is given by

$$\mathbf{u} = 0 \quad \text{in } \Omega, \quad t = 0. \quad (3.27)$$

We do not use a fully developed flow here because our goal is to capture the evolution of precipitation and polarisation and how this can alter the fluid dynamics.

At the inflow boundary Γ_i , Dirichlet condition is prescribed for pressure

$$u = 0, \quad \nabla v \cdot \mathbf{n} = 0, \quad p = P_{in} \text{ on } \Gamma_i. \quad (3.28)$$

At all solid boundaries, the velocity of the fluid must be equal to the velocity at the solid boundary so we impose the usual no-slip/no-flux boundary condition for velocity and Neumann for pressure

$$u = 0, \quad v = 0. \quad (3.29)$$

The outflow boundary conditions are given by

$$p = P_{out} \text{ on } \Gamma_o. \quad (3.30)$$

At the membrane boundary we prescribe Neumann condition for pressure whereas we adopt a combination of the solution–diffusion model and the pore model reviewed in section 3.2 to describe the velocity through the membrane. Recall the solution-diffusion model is

$$v = A(\Delta p - \Delta \pi), \quad (3.31)$$

where A is the water permeability constant, Δp is the pressure gradient and $\Delta \pi$ is the osmotic pressure gradient. The equivalent expression for the pore model is

$$u = 0, \quad v = \frac{k(p_m - p_p)}{\delta} \text{ on } \Gamma_m, \quad (3.32)$$

where k is the membrane permeability, p_m is the pressure at the feed side of the membrane, p_p is the pressure at the permeate side of the membrane and δ is the membrane thickness. A combination of the solution–diffusion model and the pore model yields a variation of Darcy's law as shown below

$$u = 0, v = \frac{k(\Delta p - \Delta \pi)}{\delta \mu} \text{ on } \Gamma_m, \quad (3.33)$$

where μ is fluid viscosity and the other parameters retain the same meaning. Equation (3.33) shows that the flux through the membrane is proportional to the difference between the applied and osmotic pressure differentials.

The applied pressure gradient Δp is expressed as the pressure gradient between

the feed side of the membrane p_m , and the permeate side of the membrane p_p as shown by

$$\Delta p = p_m - p_p, \quad (3.34)$$

where p_m is computed at the membrane boundary Γ_m .

The osmotic pressure difference is defined as follows

$$\Delta\pi = \pi - \pi_p = \pi(\phi_1, \dots, \phi_n) - \pi(\phi_{p,1}, \dots, \phi_{p,n}), \quad (3.35)$$

where π is the feed osmotic pressure which is a function of n ion concentrations on the feed side of the membrane i.e. $\phi_i (i = 1, \dots, n)$ and π_p is the permeate osmotic pressure which is a function of n ion concentrations on the permeate side of the membrane i.e. $\phi_{p,i} (i = 1, \dots, n)$.

The osmotic pressure is a colligative property. This means that it depends on the number of solute ions present in the solution i.e. $\left(\sum_{i=1}^n \phi_i\right)$. The osmotic pressure of an ‘ideal’ solution is described by van’t Hoff’s law [84]

$$\pi = \sum_{i=1}^n \phi_i RT, \quad (3.36)$$

where R is the gas constant and T is the temperature. To account for the deviation of a solution from ideal behaviour, we introduce φ the osmotic coefficient, a dimensionless quantity which characterises the solution’s deviation from ideal behaviour. Hence, the feed side osmotic pressure becomes

$$\pi(\phi_1, \dots, \phi_n) = RT\varphi \sum_{i=1}^n \phi_i, \quad (3.37)$$

which is commonly known as Pitzer’s model. Similarly, the permeate side osmotic pressure is

$$\pi_p(\phi_{p,1}, \dots, \phi_{p,n}) = RT\varphi \sum_{i=1}^n \phi_{p,i}, \quad (3.38)$$

Substituting (3.37) and (3.38) this into equation (3.35) results in

$$\Delta\pi = RT\varphi \left[\sum_{i=1}^n \phi_i - \sum_{i=1}^n \phi_{p,i} \right]. \quad (3.39)$$

We note at this point that due to the pressure-velocity coupling problem that arises when solving the incompressible Navier Stokes equations, pressure and velocity are solved iteratively and thus we specify additional boundary conditions

for the numerical simulations. In addition to the boundary conditions stated above, Neumann condition is prescribed for the velocity at the inflow Γ_i and Neumann condition for the pressure at the outflow boundary Γ_o .

The relationship between the permeate concentration and the feed concentrations is given by [87]

$$\phi_{p,i} = \phi_i(1 - r_i), \quad (3.40)$$

where r_i is the rejection coefficient for chemical species X_i . The r_i value gives an indication of how effective the membrane is at rejecting salt ions. For RO membranes, the rate of ion rejection varies for each salt. Monovalent ions such as Na^+ and Cl^- permeate better than divalent ions such as Ca^{2+} and SO_4^{2-} because the divalent ions have greater electrostatic repulsion. RO membranes are capable of rejecting up to 99 percent of monovalent ions and divalent ions typically have rejection near 100 percent [22].

The value $r_i = 1$ corresponds to the complete rejection of chemical species X_i , smaller values correspond to partial rejection and a value of zero corresponds to no rejection [87]. In our simulations, it is assumed $r_i = 1 \forall i$, that is the complete rejection of all the ions occurs at the membrane which means the ion concentration at the permeate side is 0, i.e. $\phi_{p,i} = 0$. As a result the permeate osmotic pressure, $\pi_p = 0$.

The membrane performance can be evaluated from the recovery which was described in section 3.6 as

$$r_e = \frac{vA_p}{U_{in}A_{in}}. \quad (3.41)$$

It is easily seen from Figure 3.9 that the inlet area, A_{in} is

$$A_{in} = H \times Z, \quad (3.42)$$

and the permeate area, A_p is

$$A_p = L \times Z. \quad (3.43)$$

Thus the recovery can be rewritten as

$$r_e = \frac{vL}{U_{in}H}. \quad (3.44)$$

3.3.4 Solute Transport

To simplify the mathematical analysis, the following assumptions were made:

1. The precipitation reaction is irreversible and only occurs on the membrane

surface.

2. The chosen relation for decrease of permeability and porosity in equation (3.53) captures the intuitively expected behavior during growth of crystals.
3. The transport processes are similar for all the salt ions and the diffusion coefficients are independent of concentration.
4. The salt ions have the same velocity as the fluid.
5. Complete rejection (i.e. $r = 1$) of the ions occurs at the membrane, hence no salt ion is present in the permeate.
6. The porous medium is homogeneous.

As we already mentioned above, we assume the bulk conservation equations are not influenced by scaling. Hence, no reaction occurs in the bulk liquid and the salt ions are only consumed at the membrane surface. The transport equation for each of the salt ions in the bulk liquid is then given by

$$\frac{\partial \phi_i}{\partial t} + \nabla \cdot (\mathbf{u}\phi_i) = \nabla \cdot (D\nabla\phi_i) \quad \text{in } \Omega, \quad t > 0. \quad (3.45)$$

Initial & Boundary conditions

The initial condition is

$$\phi_i = 0 \quad \text{in } \Omega, \quad t = 0. \quad (3.46)$$

There is no concentration in Ω at $t = 0$ because our goal is to capture how the system evolves overtime due to the rate of change of precipitation and modifications of the membrane porosity and permeability.

Dirichlet condition is prescribed at the inflow boundary,

$$\phi_i = \phi_{in} \quad \text{on } \Gamma_i. \quad (3.47)$$

Neumann condition at the outflow and solid boundary,

$$\nabla \cdot \phi_i = 0 \quad \text{on } \Gamma_o, \Gamma_w. \quad (3.48)$$

It is worthwhile to remark on the implication of this. It is that at the solid boundary, the concentration is conserved and there is no flow across the solid boundaries. However, at the outflow boundary ϕ_i is not conserved because the total flux is not equal to zero, it is the diffusive flux that is equal to zero. Physically, the effect of this is that the ions are transported across the outflow boundary via advection not diffusion.

Robin condition is prescribed for the membrane boundary. As we will see shortly, the Robin condition is essentially the combination of the Dirichlet and Neumann condition. We construct the Robin condition using the concept that the salt ions do not permeate through the membrane boundary (i.e. $\phi_{p,i} = 0$). Therefore, the flux of ions entering the membrane boundary, Γ_m (defined as the sum of a convective term and diffusive term) is consumed by the precipitation reaction as illustrated in Figure 3.12. As a result, two precipitates are formed ϕ_1 and ϕ_2 react to form ϕ_3 . Similarly ϕ_4 and ϕ_5 react to form ϕ_6 . Thus, a more logical selection of units at the membrane boundary is $\text{mol} \cdot \text{m}^{-2} \cdot \text{s}^{-1}$ such that the reaction rate is expressed in terms of the number of moles of ion i entering the reactive surface per unit area per second.

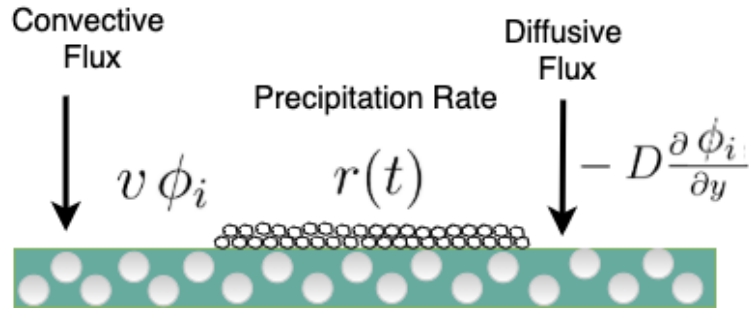


Figure 3.12: Illustration of the fluxes at the membrane.

Having established this we can now proceed with integrating the kinetic model developed in Chapter 2 with the Dirichlet and Neumann condition to give

$$\left. \begin{aligned} v\phi_1 - D\frac{\partial\phi_1}{\partial y} &= -k_1\delta\phi_1\phi_2^2 \\ v\phi_2 - D\frac{\partial\phi_2}{\partial y} &= -2k_1\delta\phi_1\phi_2^2 \\ v\phi_3 - D\frac{\partial\phi_3}{\partial y} &= k_1\delta\phi_1\phi_2^2 \\ v\phi_4 - D\frac{\partial\phi_4}{\partial y} &= -k_2\delta\phi_4\phi_5 + 2k_3\delta\phi_7 \\ v\phi_5 - D\frac{\partial\phi_5}{\partial y} &= -k_2\delta\phi_4\phi_5 \\ v\phi_6 - D\frac{\partial\phi_6}{\partial y} &= k_2\delta\phi_4\phi_5 \\ v\phi_7 - D\frac{\partial\phi_7}{\partial y} &= -k_3\delta\phi_7 \\ v\phi_8 - D\frac{\partial\phi_8}{\partial y} &= k_3\delta\phi_7 \end{aligned} \right\} \text{ on } \Gamma_m, \quad (3.49)$$

where k_i (for $i = 1, \dots, n$) is the model dependent rate constant, δ is the thickness of the membrane and $\phi_1, \phi_2, \phi_3, \phi_4, \phi_5, \phi_6, \phi_7$ and ϕ_8 denote the volume molar concentration of Ca^{2+} , HCO_3^- , CaCO_3 , Na^+ , Cl^- , NaCl , Na_2SO_4 and SO_4^{2-} respectively. Recall, we assume the salt ions have the same velocity as the fluid, hence v obtained from equation (3.33) gives us an idea of the velocity of salt ions arriving at the membrane.

Permeability and porosity model

The reaction between salt ions and subsequent precipitation of minerals often alters the membrane properties, particularly the porosity and permeability. As crystals grow, it is expected that the permeability k , in equation (3.33) and the porosity will decrease, reducing the liquid flow through the membrane [116]. To account for the modification of the porosity and permeability as a result of mineral precipitation, we employ the Kozeny–Carman model [42]. This permits us to quantify the porosity-permeability relations and estimate the resulting changes.

The Kozeny–Carman equation was originally developed to calculate the pressure difference, Δp , required for fluid flow at velocity, v , through a particle packing of the length, L

$$\frac{\Delta p}{L} = \frac{180\mu}{\Psi_s^2 D_p^2} \frac{(1 - \epsilon)^2}{\epsilon^3} v, \quad (3.50)$$

where Ψ_s is the sphericity, a dimensionless particle geometry parameter, D_p is the characteristic particle diameter in m , and ϵ is the porosity. Equation (3.50) can be reformulated using Darcy’s Law to estimate the permeability

$$k = \frac{\Psi_s^2 D_p^2}{180} \frac{\epsilon^3}{(1 - \epsilon)^2}. \quad (3.51)$$

The permeability evolution widely applied in the literature follows the form

$$\frac{k}{k_o} = \frac{f(\epsilon)}{f(\epsilon_o)}, \quad (3.52)$$

where the change in permeability is calculated by relating the current permeability, k , based on the current porosity ϵ , to the initial permeability k_o corresponding to the initial porosity ϵ_o [42].

Using the original form of the Kozeny–Carman relation presented in (3.50) and assuming negligible geometry changes ($\Psi_s, D_p \approx \text{constant}$), this becomes [42]

$$\frac{k}{k_o} = \frac{(1 - \epsilon_o)^2}{(1 - \epsilon)^2} \left(\frac{\epsilon}{\epsilon_o} \right)^3, \quad (3.53)$$

where k is the current permeability, ϵ is the current porosity, k_o is the initial permeability and ϵ_o is the initial porosity. The rate at which porosity reduction occurs is given by [43, 77]

$$\epsilon = \epsilon_o - \frac{V}{\delta} \int_{t_0}^t r(t) dt, \quad (3.54)$$

where ϵ_o denotes the initial porosity at t_0 , V is the molar volume of precipitate in m^3/mol and $r(t)$ is the rate of precipitation in $mol \cdot m^{-2} \cdot s^{-1}$. Taking into account the co-precipitation of species X_3 and X_6 as observed in our experiments, equation (3.54) becomes

$$\epsilon = \begin{cases} 0, & \text{if } \epsilon_o < V \int_{t_0}^t (k_1 \phi_1 \phi_2^2 + k_2 \phi_4 \phi_5) dt \\ \epsilon_o - V \int_{t_0}^t (k_1 \phi_1 \phi_2^2 + k_2 \phi_4 \phi_5) dt, & \text{otherwise} \end{cases} \quad (3.55)$$

where k_1 and k_2 are rate constants obtained from MATLAB simulations described in Chapter 2.

We should again observe the inter-dependencies and feedback mechanisms between fluid flow, transport and reaction. Namely, in equation (3.55) we see the precipitation reaction leads to a change in porosity which in turn affects the permeability in equation (3.53). This change in permeability impacts the flow via the fluid velocity in equation (3.33). The effects of this alters the solute concentration distribution (via equation (3.45)) which ultimately impacts the rate of precipitation again via (3.49).

3.4 Model Implementation

In this section we describe the implementation of some of the governing equations presented earlier. OpenFOAM, a open-source finite volume software (based on object-oriented C++ framework) for computational fluid dynamics was used to discretise and solve the given PDEs. OpenFOAM includes several ready solvers and utilities. These were used as a template to generate a solver specific to our model (by manipulating meshes, geometries and discretisation techniques).

3.4.1 Numerical Procedure

The first step in initiating the numerical solution was to create a discretised geometric domain and prescribe appropriate boundary conditions. The geometric domain was discretised by subdividing it into discrete non-overlapping cells that completely fill the computational domain. The next step was the discretisation of the set of PDEs using finite volume [34]. This transform these equations into a set of discrete algebraic equations. The solution of the resulting set of equations was obtained using the solver developed for this project which is discussed in more detail below. The solution was processed using an application called paraView

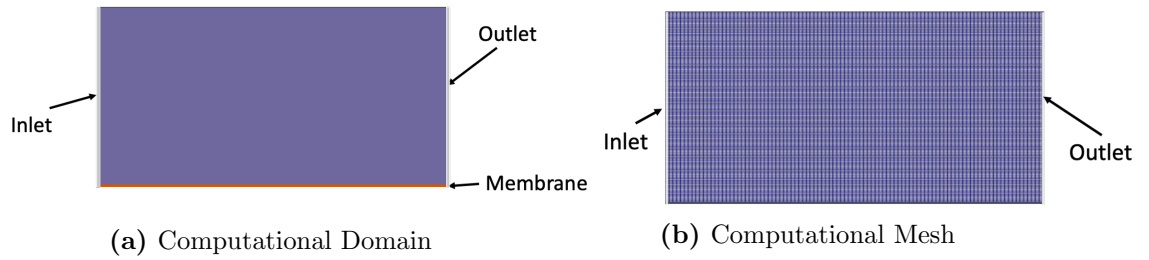


Figure 3.13: Computational domain and mesh of the main study.

[74].

Domain

The solution domain is 2 dimensional and consists of flow through a channel with inflow at the left, outflow at the right and membrane at the base. A schematic illustration of the computational domain and mesh used is shown in Figure 3.13. It should be further noted that a finer mesh resolution was used near the membrane boundary.

Solvers

It is worthwhile to first note that for an incompressible flow, the momentum equation is usually viewed as the equation that describes the velocity field while the continuity equation specifies the divergence-free condition used to set the pressure [72]. However, pressure does not appear explicitly in the continuity equation or in the momentum equation. It is the gradient of pressure that is present in the momentum equation; this has caused significant problems from a computational standpoint. Various algorithms and methods have been developed through the years in efforts to rectify and mitigate some of the difficulties arising from numerical simulations. In all of these, coupling the continuity and momentum equation is necessary so that the solution satisfies the divergence-free constraint.

The three widely-used numerical procedure for solving the Navier-Stokes equations are PISO, SIMPLE and PIMPLE algorithms. PISO is the acronym for Pressure-Implicit Split Operator, SIMPLE is the acronym for the Semi-Implicit Method for Pressure-Linked Equations algorithm and PIMPLE is the combination of the PISO and SIMPLE algorithm. These algorithms are iterative procedures for coupling the continuity and momentum equation; PISO and PIMPLE being used for transient flows and SIMPLE for steady-state flows.

In OpenFOAM, *pimpleFoam* is the transient solver for incompressible flow based on the PIMPLE algorithm and *scalarTransportFoam* is a concentration

transport solver which uses a user-specified velocity field [126]. For this study, we combined both solvers to develop two new solvers called *binaryReactionFoam* and *scalingReactionFoam*. These two solvers are both based on *pimpleFoam* and *scalarTransportFoam*; the only difference between them is that *binaryReactionFoam* is based on a binary reaction which we describe in the next chapter. *scalingReactionFoam* on the other hand is based on the reaction scheme developed in section 2.5. The reason for having two solvers will become apparent in the next chapter.

There are two main factors motivating *pimpleFoam* as the algorithm of choice for the pressure-velocity coupling. First, our goal is to capture precipitation which is a time dependent phenomena so a transient algorithm is required. Second, a better stability is obtained from PIMPLE over PISO, especially when dealing with large time steps where the maximum Courant number may consistently be above 1 [126]. It is important to also note that the two solvers developed here are capable of simulating fluid flow, solute transport and precipitation at the membrane surface.

3.5 Summary

In this chapter we have presented a number of terms, models, definitions and descriptions unique to membrane operations. We noted that some of main factors that limit recovery include: osmotic pressure, concentration polarisation and precipitation of mineral salts. We introduced the configurations used in desalination and described the flat sheet and spiral wound configuration. It was emphasised that the simulation of spiral wound membranes can be complex due to the turbulent conditions. Subsequently, we presented what is already known about the several aspects of the process. These include: fluid flow, flow through the membrane, design studies, geometry studies and precipitation studies. We examined the pore flow model which is based on porosity and the solution-diffusion model which is based on diffusion. We then noted the limitations of design studies that were carried out. Subsequently, it becomes evident that many modelling studies adopt a flat sheet approach whereby the membrane unit is modelled as an unwound element thus simplifying the complex spiral wound geometry.

We discussed the computational approaches that have been employed to describe precipitation in a reverse osmosis membrane system. It becomes clear that the few investigators who have conducted research on the subject adopted a statistical approach. For instance [15] employed the method of moments to compute the

moments of the probability density function of the particles surface concentration and [87] described the nucleation process as a stochastic event. We noted that [120] conducted experimental studies, pore-scale simulations and continuum-scale simulations on precipitation, although this was not done in a desalination context. At this point, we had all the tools needed to construct a framework capable of capturing what happens in reality. We identified the modelling approach that we will follow in this study and laid out the governing equations for the model formulated.

We emphasised the couplings between variables and processes which makes the system non-linear. In particular, the coupling between fluid flow and solute concentrations through modifications in the porosity and permeability as a result of precipitation. Understanding the significance of this will make it easier to grasp the behavior of the solutions obtained in Chapter 5. We noted that our model and analysis will be restricted to Cartesian coordinates in two-dimensional space. We have chosen this because it results in a much simpler presentation and at the same time, there are no fundamental changes needed for any of the methods treated here when upgrading to three space dimensions and/or generalized coordinates. The presented model formulation is based on a cross-flow mode of operation whereby the convective and diffusive flux transports fluid in a direction tangential to the membrane surface.

We then described the numerical implementation of the model. We noted that the continuity, momentum and mass transport equations with the corresponding boundary conditions were solved with the open-source OpenFOAM CFD software. We then stated that the software uses the finite volume method to discretise the momentum and mass transport equations. Finally, we make some remarks about the solvers developed for this project and the algorithm of choice for the pressure-velocity coupling.

Chapter 4

Mathematical Treatment

It is easily seen from the preceding chapter that there are a large number of parameters in the system, thus it can be difficult to predict how varying a single parameter will influence the solution. In this chapter we introduce an important technique, called non-dimensionalisation, that will benefit us in several ways. With non-dimensionalisation we do not need to consider parameters individually as we will be able to define parameter groupings that will influence the solutions in the same way as individual parameters. This provides us with a means of assessing the model's performance efficiently.

We begin the chapter with a brief stability analysis of the nonlinear differential equations which describes the experimental observations documented in Chapter 2. We believe a further qualitative characterisation of the systems properties by means of stability analysis will help classify the results even further, thereby providing a clearer understanding of the process itself. We then proceed with a presentation of the non-dimensionalisation technique by stating the chosen scales and corresponding dimensionless variables and groups of the governing equations.

4.1 Stationary States and Stability

In this section we will briefly consider the dynamics of the reaction system near its stationary points. We start by recalling the system of time dependent ODEs described in Chapter 2 and subsequently use conservation laws to reduce the number of equations. Following this, we linearize the system at its equilibria and identify the sign of the eigenvalues to gain a general understanding of the solutions.

4.1.1 Linear Stability Analysis

Recall the mass action system for the precipitation reaction is

$$\frac{d\phi_1}{dt} = -k_1\phi_1(t)\phi_2^2(t), \quad \phi_1(0) = \phi_{10}, \quad t \geq 0, \quad (4.1)$$

$$\frac{d\phi_2}{dt} = -2k_1\phi_1(t)\phi_2^2(t), \quad \phi_2(0) = \phi_{20}, \quad (4.2)$$

$$\frac{d\phi_3}{dt} = k_1\phi_1(t)\phi_2^2(t), \quad \phi_3(0) = \phi_{30}, \quad (4.3)$$

$$\frac{d\phi_4}{dt} = -k_2\phi_4(t)\phi_5(t) + 2k_3\phi_7(t), \quad \phi_4(0) = \phi_{40}, \quad (4.4)$$

$$\frac{d\phi_5}{dt} = -k_2\phi_4(t)\phi_5(t), \quad \phi_5(0) = \phi_{50}, \quad (4.5)$$

$$\frac{d\phi_6}{dt} = k_2\phi_4(t)\phi_5(t), \quad \phi_6(0) = \phi_{60}, \quad (4.6)$$

$$\frac{d\phi_7}{dt} = -k_3\phi_7(t), \quad \phi_7(0) = \phi_{70}, \quad (4.7)$$

$$\frac{d\phi_8}{dt} = k_3\phi_7(t), \quad \phi_8(0) = \phi_{80}, \quad (4.8)$$

where $\phi_i(t) \in \mathbb{R}$ ($i = 1, \dots, n$) denotes the volume molar concentration of chemical species X_i , at time t and ϕ_{i0} is the initial concentration at $t = 0$.

A starting point for the analysis would be to find the equilibrium points for the system described above. To this end, we note the following conservation relations in the mechanism:

$$\frac{d\phi_1}{dt} + \frac{d\phi_3}{dt} = 0 \Rightarrow \phi_1 + \phi_3 = A, \quad (4.9)$$

$$\frac{d\phi_2}{dt} + 2\frac{d\phi_3}{dt} = 0 \Rightarrow \phi_2 + 2\phi_3 = B, \quad (4.10)$$

$$\frac{d\phi_4}{dt} + \frac{d\phi_6}{dt} + 2\frac{d\phi_7}{dt} = 0 \Rightarrow \phi_4 + \phi_6 + 2\phi_7 = C, \quad (4.11)$$

$$\frac{d\phi_5}{dt} + \frac{d\phi_6}{dt} = 0 \Rightarrow \phi_5 + \phi_6 = D, \quad (4.12)$$

$$\frac{d\phi_7}{dt} + \frac{d\phi_8}{dt} = 0 \Rightarrow \phi_7 + \phi_8 = E. \quad (4.13)$$

This reduces the system of equations to:

$$\frac{d\phi_3}{dt} = k_1(A - \phi_3)(B - 2\phi_3)^2, \quad (4.14)$$

$$\frac{d\phi_6}{dt} = k_2(C - 2(E - \phi_8) - \phi_6)(D - \phi_6), \quad (4.15)$$

$$\frac{d\phi_8}{dt} = k_3(E - \phi_8). \quad (4.16)$$

Stationary points: We obtain the equilibrium point by setting all of the time

derivatives to zero. If we assume the rate constant cannot be equal to zero then (4.14) decouples; $\frac{d\phi_3}{dt} = 0$ if $A = \phi_3$ or $\phi_3 = \frac{B}{2}$. Similarly (4.15) decouples; $\frac{d\phi_6}{dt} = 0$ if $D = \phi_6$ or $C = \phi_6$ and $\frac{d\phi_8}{dt} = 0$ if $E = \phi_8$.

Hence the stationary points for the dynamics described above are:

$$P_1 = \begin{cases} \phi_1 = 0, & \phi_2 = B - 2A, & \phi_3 = A, & \phi_4 = C - D, & \phi_5 = 0, \\ \phi_6 = D, & \phi_7 = 0, & \phi_8 = E. \end{cases} \quad (4.17)$$

$$P_2 = \begin{cases} \phi_1 = A - \frac{B}{2}, & \phi_2 = 0, & \phi_3 = \frac{B}{2}, & \phi_4 = C - D, & \phi_5 = 0, \\ \phi_6 = D, & \phi_7 = 0, & \phi_8 = E. \end{cases} \quad (4.18)$$

$$P_3 = \begin{cases} \phi_1 = 0, & \phi_2 = B - 2A, & \phi_3 = A, & \phi_4 = 0, & \phi_5 = D - C, \\ \phi_6 = C, & \phi_7 = 0, & \phi_8 = E. \end{cases} \quad (4.19)$$

$$P_4 = \begin{cases} \phi_1 = A - \frac{B}{2}, & \phi_2 = 0, & \phi_3 = \frac{B}{2}, & \phi_4 = 0, & \phi_5 = D - C, \\ \phi_6 = C, & \phi_7 = 0, & \phi_8 = E. \end{cases} \quad (4.20)$$

Linearisation: We determine the nature of each of the equilibria of the system P_1, P_2, P_3 and P_4 by linearising around the respective equilibrium points. We characterize an equilibrium as stable or unstable based on the behavior of solutions. That is, if solutions near a critical point of a system stay close to the critical point as it approaches infinity, then we assume the equilibrium point is stable; however if this condition is not met then the critical point is unstable [91]

The Jacobian matrix of $J(\frac{d\phi_3}{dt}, \frac{d\phi_6}{dt}, \frac{d\phi_8}{dt})$ is given by

$$J = \begin{bmatrix} k_1^2 [(2\phi_3 - B)^2 - 4(A - \phi_3)] & 0 & 0 \\ 0 & k_2^2 [(\phi_6 - D) - (C - \phi_6 - 2(E - \phi_8))] & 2k_2^2(D - \phi_6) \\ 0 & 0 & -k_3 \end{bmatrix}$$

The Jacobian matrix at P_1 is

$$J(P_1) = \begin{bmatrix} k_1^2(2A - B)^2 & 0 & 0 \\ 0 & -k_2^2(C - D) & 0 \\ 0 & 0 & -k_3 \end{bmatrix}.$$

It is easily seen that $J(P_1)$ is a diagonal matrix and the entries on the diagonal are simply the eigenvalues of $J(P_1)$. The stability can be determined from these eigenvalues. Substituting the experimental values from Chapter 2, we have $A = 820$, $B = 293$, $C = 49390$, $D = 48962$, $E = 8195$. Also substituting the rate constants

$$k_1 = 7 \times 10^{-10} m^6 \cdot mol^{-2} \cdot s^{-1}, \quad k_2 = 3 \times 10^{-12} m^3 \cdot mol^{-1} \cdot s^{-1}, \quad k_3 = 3 \times 10^{-12} s^{-1},$$

obtained from the model fit in section 2.5.3 gives

$$J(P_1) = \begin{bmatrix} 8.89 \times 10^{-13} & 0 & 0 \\ 0 & -3.8 \times 10^{-21} & 0 \\ 0 & 0 & -3 \times 10^{-12} \end{bmatrix}.$$

Inspection of the diagonal entries shows that two of the eigenvalues have negative real parts and one of the eigenvalue has a positive real part. This equilibrium point is a saddle.

The Jacobian matrix at P_2 is

$$J(P_2) = \begin{bmatrix} -4k_1^2(A - 2\frac{B}{2})^2 & 0 & 0 \\ 0 & -k_2^2(C - D) & 0 \\ 0 & 0 & -k_3 \end{bmatrix}.$$

Substituting the experimental values and rate constants leads to

$$J(P_2) = \begin{bmatrix} -8.89 \times 10^{-13} & 0 & 0 \\ 0 & -3.8 \times 10^{-21} & 0 \\ 0 & 0 & -3 \times 10^{-12} \end{bmatrix}.$$

It is clear from the diagonal entries that all of the eigenvalues have negative real parts. This equilibrium point is a stable node.

The Jacobian matrix at P_3 is

$$J(P_3) = \begin{bmatrix} k_1^2(2A - B)^2 & 0 & 0 \\ 0 & k_2^2(C - D) & 2k_2^2(D - C) \\ 0 & 0 & -k_3 \end{bmatrix}.$$

Substituting the experimental values and rate constants gives

$$J(P_3) = \begin{bmatrix} 8.89 \times 10^{-13} & 0 & 0 \\ 0 & 3.8 \times 10^{-21} & -7.74 \times 10^{-21} \\ 0 & 0 & -3 \times 10^{-12} \end{bmatrix}.$$

Inspection of the diagonal entries shows that two of the eigenvalues have positive real parts and one of the eigenvalue has a negative real part. This equilibrium point is unstable and is a saddle.

The Jacobian matrix at P_4 is

$$J(P_4) = \begin{bmatrix} -4k_1^2(A - 2\frac{B}{2})^2 & 0 & 0 \\ 0 & k_2^2(C - D) & 2k_2^2(D - C) \\ 0 & 0 & -k_3 \end{bmatrix}.$$

Substituting the experimental values and rate constants yields

$$J(P_4) = \begin{bmatrix} -8.89 \times 10^{-13} & 0 & 0 \\ 0 & 3.8 \times 10^{-21} & -7.74 \times 10^{-21} \\ 0 & 0 & -3 \times 10^{-12} \end{bmatrix}.$$

Two of the eigenvalues have negative real parts and one of the eigenvalue has a positive real part. This equilibrium point is a saddle.

Some Conclusions

According to [117, 121], the stability of a system can change as a parameter varies. We believe the equilibrium points specified above are close to bifurcation points because $C \approx D$ so small changes in these parameters can lead to $C - D \leq 0$. As a result, the eigenvalue at the middle entry of the diagonal crosses zero and changes sign. Therefore, the stability of P_2 is altered from a stable node to a saddle whereas the stability of P_4 changes from a saddle to a stable node. P_1 and P_3 retain the same stability classification i.e. saddle.

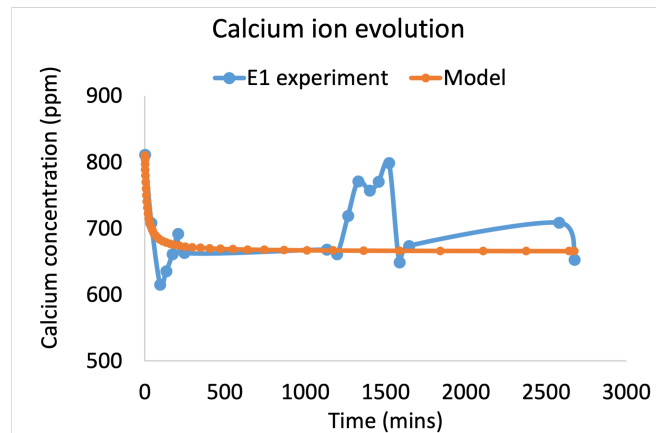


Figure 4.1: Time plots for calcium concentration (ϕ_1) in experiment E1.

This parameter sensitivity and change in stability may explain the overshoot and undershoot observed in the experiments (see Figure 4.1 for reference) to this sensitivity. It is readily seen that the system approaches equilibrium around $Ca^{2+} = \phi_1 \approx 670\text{ppm}$ which corresponds to equilibrium point P_2 and P_4 . From the analysis above, both of these points are near saddle-node bifurcation. Perhaps this might explain the variability observed during the experiments. It is possible that slight changes in experimental conditions could have altered the stability of the system from saddle to stable node (or vice-versa) giving rise to the overshoots

and undershoots observed in Figure 4.1.

4.2 Non-dimensionalisation

As we implied at the beginning of the chapter, it is useful at this point to non-dimensionalise the governing equations of the problem. The dimensionless groups (variables without units) arising from the non-dimensionalisation process allows the identification of terms and physical mechanisms which control the solution behaviour. Furthermore, the dimensionless groups consolidate the information contained in the original system, leading to a reduction in the number of parameters. As a result the governing equations are reduced to the simplest forms making quantitative analysis easier. In what follows, we lay down the procedure for the governing equations by stating the chosen scales and corresponding dimensionless variables and groups. Note that some of the technical information from previous chapters is repeated for the completeness of this section and so that the reader does not have to go back and forth between chapters to find information.

4.2.1 Fluid Flow

We begin by recalling the two-dimensional Cartesian form of the Navier-Stokes equations of motion and the boundary conditions. Then we go on to non-dimensionalise these.

$$\rho \left(\frac{\partial u}{\partial t} + u \frac{\partial u}{\partial x} + v \frac{\partial u}{\partial y} \right) = -\frac{\partial p}{\partial x} + \frac{\partial}{\partial x} \left(\mu \frac{\partial u}{\partial x} \right) + \frac{\partial}{\partial y} \left(\mu \frac{\partial u}{\partial y} \right), \quad (4.21)$$

$$\rho \left(\frac{\partial v}{\partial t} + u \frac{\partial v}{\partial x} + v \frac{\partial v}{\partial y} \right) = -\frac{\partial p}{\partial y} + \frac{\partial}{\partial x} \left(\mu \frac{\partial v}{\partial x} \right) + \frac{\partial}{\partial y} \left(\mu \frac{\partial v}{\partial y} \right). \quad (4.22)$$

The flow is incompressible, so we pose

$$\frac{\partial u}{\partial x} + \frac{\partial v}{\partial y} = 0 \quad (4.23)$$

subjected to the initial condition

$$u = v = 0 \text{ in } \Omega \text{ at } t = 0. \quad (4.24)$$

We imposed the usual no-slip/no-flux boundary on the solid-wall boundary and Dirichlet condition is prescribed for the velocity at the membrane boundary. Dirichlet condition is also prescribed for the pressure at the inflow and outflow boundary whereas a Neumann condition is imposed at the membrane boundary

and solid-wall boundary. This yields

$$\left\{ \begin{array}{l} u = v = 0 \text{ on } \Gamma_w, \\ u = 0 \text{ on } \Gamma_m, \\ v = \frac{k(\Delta p - \Delta \pi)}{\delta \mu} \text{ on } \Gamma_m, \\ p = P_{in} \text{ on } \Gamma_i, \\ p = P_{out} \text{ on } \Gamma_o, \\ \frac{\partial p}{\partial \mathbf{n}} = 0 \text{ on } \Gamma_m, \Gamma_w. \end{array} \right. \quad (4.25)$$

For the numerical simulations, pressure and velocity are solved iteratively and we specify Neumann condition for the velocity at the inflow Γ_i and outflow boundary Γ_o .

Recall from Chapter 3 that the pressure difference in (4.25) is

$$\Delta p = p - p_p, \quad (4.26)$$

and the osmotic pressure difference in (4.25) is

$$\Delta \pi = \pi = RT \varphi \sum_1^n \phi_i. \quad (4.27)$$

Fluid Flow - non-dimensionalisation

To reduce the number of parameters in the formulation, we assume dynamics occur on the length scale L in the flow direction and a smaller length scale δ_f in the membrane-normal direction. The spatial derivatives then follow the scalings

$$\partial_x \sim \frac{1}{L}, \quad \partial_y \sim \frac{1}{\delta_f}. \quad (4.28)$$

There is a *priori* reason for this choice of length scales. Namely, we assume transport in the perpendicular direction becomes significant around a length scale δ_f near the membrane. We also know the membrane channels are thin in y -direction and wide in the x -direction; the scalings have been chosen to capture

this as well. The value of δ_f can be estimated *a posteriori* from the simulations if required, however we do not compute it because it is not necessary.

It is important to note that these length scales are not comparable: $L \gg \delta_f$. We can thus introduce a small parameter $\tau \ll 1$ such that

$$\frac{\delta_f}{L} = \tau. \quad (4.29)$$

We derive the velocity scaling from the stokes equation which is given by

$$\nabla p - \mu \nabla^2 \mathbf{u} = 0. \quad (4.30)$$

The streamwise velocity scaling is thus

$$u = \frac{(P_{in} - P_{out})\delta_f^2}{\mu L} = \frac{(P_{in} - P_{out})\tau^2 L}{\mu} \approx U_{in}. \quad (4.31)$$

From (4.31) we know the order of magnitude of the streamwise velocity u however, the v -component velocity is yet to be determined. To that end, we assume that both terms in the incompressibility constraint are of the same order of magnitude. Hence

$$\frac{u}{L} \sim \frac{v}{\delta_f}, \quad (4.32)$$

which gives

$$v \sim \frac{u\delta_f}{L}, \quad (4.33)$$

$$\Rightarrow v \sim \tau u, \quad (4.34)$$

implying that the velocity normal to the membrane is smaller than the streamwise one. Let $P_{in} - P_{out} = P_c$ represent the pressure deviation in the channel, then we may non-dimensionalise (4.21) and (4.22) as follows

$$U = U_{in}\bar{u}, \quad v = \tau U_{in}\bar{u} \quad t = \frac{L}{U_{in}}\bar{t}, \quad p = P_{out} + P_c\bar{p}. \quad (4.35)$$

Note in this thesis, we denote dimensionless variables with overbar.

Using the dimensionless variables specified above, the incompressibility constraint reads

$$\frac{U_{in}}{L} \frac{\partial \bar{u}}{\partial \bar{x}} + \frac{\tau U_{in}}{\tau L} \frac{\partial \bar{v}}{\partial \bar{y}} = 0, \quad (4.36)$$

yielding

$$\frac{\partial \bar{u}}{\partial \bar{x}} + \frac{\partial \bar{v}}{\partial \bar{y}} = 0 \quad (4.37)$$

Similarly, the Navier–Stokes equation becomes

$$\rho \frac{U_{in}^2}{L} \left(\frac{\partial \bar{u}}{\partial \bar{t}} + \bar{u} \frac{\partial \bar{u}}{\partial \bar{x}} + \bar{v} \frac{\partial \bar{u}}{\partial \bar{y}} \right) = -\frac{P_c}{L} \frac{\partial \bar{p}}{\partial \bar{x}} + \mu \left(\frac{U_{in}}{L^2} \frac{\partial^2 \bar{u}}{\partial \bar{x}^2} + \frac{U_{in}}{\tau^2 L^2} \frac{\partial^2 \bar{u}}{\partial \bar{y}^2} \right) \quad (4.38)$$

$$\rho \frac{U_{in}^2}{L} \left(\tau \frac{\partial \bar{v}}{\partial \bar{t}} + \tau \bar{u} \frac{\partial \tau \bar{v}}{\partial \bar{x}} + \tau \bar{v} \frac{\partial \bar{v}}{\partial \bar{y}} \right) = -\frac{P_c}{\tau L} \frac{\partial \bar{p}}{\partial \bar{y}} + \mu \left(\frac{U_{in}}{L^2} \tau \frac{\partial^2 \bar{v}}{\partial \bar{x}^2} + \frac{U_{in}}{\tau^2 L^2} \frac{\partial^2 \tau \bar{v}}{\partial \bar{y}^2} \right) \quad (4.39)$$

We introduce the dimensionless parameters

$$Re = \frac{\rho U_{in} L}{\mu}, \quad Eu = \frac{P_c}{\rho U_{in}^2}. \quad (4.40)$$

Thus (4.38) simplifies into

$$\left(\frac{\partial \bar{u}}{\partial \bar{t}} + \bar{u} \frac{\partial \bar{u}}{\partial \bar{x}} + \bar{v} \frac{\partial \bar{u}}{\partial \bar{y}} \right) = -Eu \frac{\partial \bar{p}}{\partial \bar{x}} + \frac{1}{Re} \left(\frac{\partial^2 \bar{u}}{\partial \bar{x}^2} + \frac{1}{\tau^2} \frac{\partial^2 \bar{u}}{\partial \bar{y}^2} \right). \quad (4.41)$$

The leading order term $\frac{1}{Re\tau^2} \frac{\partial^2 \bar{u}}{\partial \bar{y}^2}$ appears to be second order, indicating that u is parabolic in y -direction, as would be expected.

Substituting the dimensionless parameters into (4.39) yields

$$\left(\frac{\partial \bar{v}}{\partial \bar{t}} + \bar{u} \frac{\partial \bar{v}}{\partial \bar{x}} + \bar{v} \frac{\partial \bar{v}}{\partial \bar{y}} \right) = -\frac{Eu}{\tau^2} \frac{\partial \bar{p}}{\partial \bar{y}} + \frac{1}{Re} \left(\frac{\partial^2 \bar{v}}{\partial \bar{x}^2} + \frac{1}{\tau^2} \frac{\partial^2 \bar{v}}{\partial \bar{y}^2} \right) \quad (4.42)$$

where $\frac{Eu}{\tau^2} \frac{\partial \bar{p}}{\partial \bar{y}}$ and $\frac{1}{Re\tau^2} \frac{\partial^2 \bar{v}}{\partial \bar{y}^2}$ are the leading order terms. This suggests that the pressure term is of the same order of magnitude as the the viscous term in the y -direction. This implies that flow in the y -direction will be significantly affected by pressure and viscous forces.

The boundary conditions become

$$\left\{ \begin{array}{l} \bar{u} = \bar{v} = 0 \quad \text{on } \Gamma_w \\ \bar{p}_{in} = 1 \quad \text{on } \Gamma_i \\ \bar{p}_{out} = 0 \quad \text{on } \Gamma_o \\ \frac{\partial \bar{p}}{\partial \mathbf{n}} = 0 \quad \text{on } \Gamma_m, \Gamma_w \end{array} \right. \quad (4.43)$$

We non-dimensionalise the v -component velocity at the membrane boundary Γ_m

as follows

$$v = \tau U_{in} \bar{v}, \quad \Delta p = P_c(\bar{p} - \bar{p}_p), \quad \Delta \pi = RT\varphi\phi_{in} \sum \bar{\phi}_i. \quad (4.44)$$

Substituting these into the velocity membrane condition in (4.25), we obtain

$$\bar{v} = \frac{k}{\mu\delta\tau U_{in}} \left[P_c(\bar{p} - \bar{p}_p) - RT\varphi\phi_{in} \sum \bar{\phi}_i \right]. \quad (4.45)$$

Substituting U_{in} from (4.31) gives

$$\bar{v} = \frac{k}{\delta} \frac{1}{\tau^3 L} \left(\frac{P_c(\bar{p} - \bar{p}_p)}{P_c} - \frac{RT\varphi\phi_{in} \sum \bar{\phi}_i}{P_c} \right). \quad (4.46)$$

Using the pressure scaling, we obtain

$$\bar{p}_p = \frac{P_p - P_{out}}{P_c} \quad (4.47)$$

Equation (4.46) becomes

$$\bar{v} = \frac{k}{\delta} \frac{1}{\tau^3 L} \left(\bar{p} - \frac{P_p - P_{out}}{P_c} - \frac{RT\varphi\phi_{in} \sum \bar{\phi}_i}{P_c} \right). \quad (4.48)$$

We introduce the dimensionless parameters

$$\beta = \frac{P_p - P_{out}}{P_c}, \quad \theta = \frac{RT\varphi\phi_{in}}{P_c}, \quad Da = \frac{k}{\delta\delta_f}. \quad (4.49)$$

Hence we have

$$\bar{v} = \left(\bar{p} - \beta - \theta \sum \bar{\phi}_i \right) Da\tau^{-2} \quad \text{on } \Gamma_m. \quad (4.50)$$

It is also essential to non-dimensionalise the membrane recovery as this will allow us evaluate the membrane performance in subsequent sections. Recall that the recovery is defined as the ratio between the total flux through the membrane and the total flux into the membrane channel

$$r_e = \frac{\int_{\Gamma_m} v dx}{\int_{\Gamma_i} u dy}. \quad (4.51)$$

We non-dimensionalise v as follows

$$v = \tau U_{in} \bar{v}, \quad u = U_{in} \bar{u}. \quad (4.52)$$

Substituting the velocity scalings and integrating yields

$$r_e = \frac{\tau \bar{v} L}{\bar{u} H} \quad (4.53)$$

Substituting \bar{v} from (4.50) yields

$$r_e = \left(\bar{p} - \beta - \theta \sum \bar{\phi}_i \right) Da \tau^{-1} \frac{L}{\bar{u} H}. \quad (4.54)$$

We introduce the dimensionless parameter

$$\vartheta_g = \frac{L}{H}. \quad (4.55)$$

Therefore (4.55) becomes

$$r_e = \left(\bar{p} - \beta - \theta \sum \bar{\phi}_i \right) Da \tau^{-1} \frac{\vartheta_g}{\bar{u}}. \quad (4.56)$$

It is readily seen from (4.56) that the recovery depends on several dimensionless groups. Namely, the dominant pressure difference in the channel (presented by β), the ratio between osmotic pressure and the channel's pressure (presented by θ), the sum of concentration at the membrane, the membrane characteristics (represented by Da), the ratio of the boundary layer thickness to the channel length (represented by τ), the channel geometry (represented by ϑ_g) and the streamwise velocity. (4.56) further confirms the complex interplay between mass transport, fluid dynamics, geometry and membrane properties. In the following chapter we will attempt to understand the relative influence of these groups.

4.2.2 Solute Transport

We begin this section by recalling the transport equation and boundary conditions. Then we subsequently non-dimensionalise these. In two spatial dimension the bulk conservation equation can be written in the following form

$$\frac{\partial \phi_i}{\partial t} + u \frac{\partial \phi_i}{\partial x} + v \frac{\partial \phi_i}{\partial y} = D \frac{\partial^2 \phi_i}{\partial x^2} + D \frac{\partial^2 \phi_i}{\partial y^2}, \quad (4.57)$$

subjected to the following boundary conditions

$$\phi_i = \phi_{in} \text{ on } \Gamma_i, \quad (4.58)$$

$$\frac{\partial \phi_i}{\partial \mathbf{n}} = 0 \text{ on } \Gamma_o, \Gamma_w, \quad (4.59)$$

$$\left. \begin{aligned} v\phi_1 - D\frac{\partial\phi_1}{\partial y} &= -k_1\delta\phi_1\phi_2^2 \\ v\phi_2 - D\frac{\partial\phi_2}{\partial y} &= -2k_1\delta\phi_1\phi_2^2 \\ v\phi_3 - D\frac{\partial\phi_3}{\partial y} &= k_1\delta\phi_1\phi_2^2 \\ v\phi_4 - D\frac{\partial\phi_4}{\partial y} &= -k_2\delta\phi_4\phi_5 + 2k_3\delta\phi_7 \\ v\phi_5 - D\frac{\partial\phi_5}{\partial y} &= -k_2\delta\phi_4\phi_5 \\ v\phi_6 - D\frac{\partial\phi_6}{\partial y} &= k_2\delta\phi_4\phi_5 \\ v\phi_7 - D\frac{\partial\phi_7}{\partial y} &= -k_3\delta\phi_7 \\ v\phi_8 - D\frac{\partial\phi_8}{\partial y} &= k_3\delta\phi_7 \end{aligned} \right\} \text{ on } \Gamma_m, \quad (4.60)$$

and initial condition

$$\phi_i = 0 \quad \text{in } \Omega \quad \text{at } t = 0. \quad (4.61)$$

Note, the rate of change of porosity of the membrane is

$$\epsilon = \epsilon_o - V \int_{t_0}^t (k_1\phi_1\phi_2^2 + k_2\phi_4\phi_5) dt. \quad (4.62)$$

Solute Transport - non-dimensionalisation

To reduce the number of parameters in the solute transport equation, we non-dimensionalise as follows

$$U = U_{in}\bar{u}, \quad v = \tau U_{in}\bar{v}, \quad \phi_i = \phi_{in}\bar{\phi}_i, \quad t = \frac{L}{U_{in}}\bar{t}, \quad \partial_x = \frac{1}{L}, \quad \partial_y = \frac{1}{\delta_f}. \quad (4.63)$$

The solute transport equation in (4.57) becomes

$$\frac{U_{in}\phi_{in}}{L} \left(\frac{\partial\bar{\phi}_i}{\partial\bar{t}} + \bar{u}\frac{\partial\bar{\phi}_i}{\partial\bar{x}} + \bar{v}\frac{\partial\bar{\phi}_i}{\partial\bar{y}} \right) = \frac{D\phi_{in}}{L^2} \left(\frac{\partial^2\bar{\phi}_i}{\partial\bar{x}^2} + \frac{1}{\tau^2} \frac{\partial^2\bar{\phi}_i}{\partial\bar{y}^2} \right) \quad (4.64)$$

We introduce the dimensionless parameter

$$Pe = \frac{LU_{in}}{D}. \quad (4.65)$$

Hence we obtain

$$\frac{\partial\bar{\phi}_i}{\partial\bar{t}} + \bar{u}\frac{\partial\bar{\phi}_i}{\partial\bar{x}} + \bar{v}\frac{\partial\bar{\phi}_i}{\partial\bar{y}} = \frac{1}{Pe} \left(\frac{\partial^2\bar{\phi}_i}{\partial\bar{x}^2} + \frac{1}{\tau^2} \frac{\partial^2\bar{\phi}_i}{\partial\bar{y}^2} \right) \quad (4.66)$$

subjected to the following boundary conditions

$$\bar{\phi}_i = 1 \text{ on } \Gamma_i, \quad (4.67)$$

$$\frac{\partial \bar{\phi}_i}{\partial \mathbf{n}} = 0 \text{ on } \Gamma_o, \Gamma_w, \quad (4.68)$$

We may non-dimensionalise the boundary condition on Γ_m as follows

$$v = \tau U_{in} \bar{v}, \quad y = \delta_f \bar{y}, \quad \phi_{1,2,4,5,7} = \phi_{in} \bar{\phi}_{1,2,4,5,7}. \quad (4.69)$$

This yields

$$\tau U_{in} \bar{v} \phi_{in} \bar{\phi}_1 - D \frac{\partial \phi_{in} \bar{\phi}_1}{\partial \delta_f \bar{y}} = -k_1 \delta \phi_{in}^3 \bar{\phi}_1 \bar{\phi}_2^2, \quad (4.70)$$

$$\tau U_{in} \bar{v} \phi_{in} \bar{\phi}_2 - D \frac{\partial \phi_{in} \bar{\phi}_2}{\partial \delta_f \bar{y}} = -2k_1 \delta \phi_{in}^3 \bar{\phi}_1 \bar{\phi}_2^2, \quad (4.71)$$

$$\tau U_{in} \bar{v} \phi_{in} \bar{\phi}_3 - D \frac{\partial \phi_{in} \bar{\phi}_3}{\partial \delta_f \bar{y}} = k_1 \delta \phi_{in}^3 \bar{\phi}_1 \bar{\phi}_2^2, \quad (4.72)$$

$$\tau U_{in} \bar{v} \phi_{in} \bar{\phi}_4 - D \frac{\partial \phi_{in} \bar{\phi}_4}{\partial \delta_f \bar{y}} = -k_2 \delta \phi_{in}^2 \bar{\phi}_4 \bar{\phi}_5 + 2k_3 \delta \phi_{in} \bar{\phi}_7, \quad (4.73)$$

$$\tau U_{in} \bar{v} \phi_{in} \bar{\phi}_5 - D \frac{\partial \phi_{in} \bar{\phi}_5}{\partial \delta_f \bar{y}} = -k_2 \delta \phi_{in}^2 \bar{\phi}_4 \bar{\phi}_5, \quad (4.74)$$

$$\tau U_{in} \bar{v} \phi_{in} \bar{\phi}_6 - D \frac{\partial \phi_{in} \bar{\phi}_6}{\partial \delta_f \bar{y}} = k_2 \delta \phi_{in}^2 \bar{\phi}_4 \bar{\phi}_5, \quad (4.75)$$

$$\tau U_{in} \bar{v} \phi_{in} \bar{\phi}_7 - D \frac{\partial \phi_{in} \bar{\phi}_7}{\partial \delta_f \bar{y}} = -k_3 \delta \phi_{in} \bar{\phi}_7, \quad (4.76)$$

$$\tau U_{in} \bar{v} \phi_{in} \bar{\phi}_8 - D \frac{\partial \phi_{in} \bar{\phi}_8}{\partial \delta_f \bar{y}} = k_3 \delta \phi_{in} \bar{\phi}_7. \quad (4.77)$$

Rearranging gives

$$\frac{\partial \bar{\phi}_1}{\partial \bar{y}} = \frac{\tau U_{in} \delta_f}{D} \bar{v} \bar{\phi}_1 + k_1 \delta \phi_{in}^2 \frac{\delta_f}{D} \bar{\phi}_1 \bar{\phi}_2^2, \quad (4.78)$$

$$\frac{\partial \bar{\phi}_2}{\partial \bar{y}} = \frac{\tau U_{in} \delta_f}{D} \bar{v} \bar{\phi}_2 + 2k_1 \delta \phi_{in}^2 \frac{\delta_f}{D} \bar{\phi}_1 \bar{\phi}_2^2, \quad (4.79)$$

$$\frac{\partial \bar{\phi}_3}{\partial \bar{y}} = \frac{\tau U_{in} \delta_f}{D} \bar{v} \bar{\phi}_3 - k_1 \delta \phi_{in}^2 \frac{\delta_f}{D} \bar{\phi}_1 \bar{\phi}_2^2, \quad (4.80)$$

$$\frac{\partial \bar{\phi}_4}{\partial \bar{y}} = \frac{\tau U_{in} \delta_f}{D} \bar{v} \bar{\phi}_4 + k_2 \delta \phi_{in} \frac{\delta_f}{D} \bar{\phi}_4 \bar{\phi}_5 - 2k_3 \delta \frac{\delta_f}{D} \bar{\phi}_7, \quad (4.81)$$

$$\frac{\partial \bar{\phi}_5}{\partial \bar{y}} = \frac{\tau U_{in} \delta_f}{D} \bar{v} \bar{\phi}_5 + k_2 \delta \phi_{in} \frac{\delta_f}{D} \bar{\phi}_4 \bar{\phi}_5. \quad (4.82)$$

$$\frac{\partial \bar{\phi}_6}{\partial \bar{y}} = \frac{\tau U_{in} \delta_f}{D} \bar{v} \bar{\phi}_6 - k_2 \delta \phi_{in} \frac{\delta_f}{D} \bar{\phi}_4 \bar{\phi}_5. \quad (4.83)$$

$$\frac{\partial \bar{\phi}_7}{\partial \bar{y}} = \frac{\tau U_{in} \delta_f}{D} \bar{v} \bar{\phi}_7 + k_3 \delta \frac{\delta_f}{D} \bar{\phi}_7 \quad (4.84)$$

$$\frac{\partial \bar{\phi}_8}{\partial \bar{y}} = \frac{\tau U_{in} \delta_f}{D} \bar{v} \bar{\phi}_8 - k_3 \delta \frac{\delta_f}{D} \bar{\phi}_7 \quad (4.85)$$

We introduce the dimensionless parameters

$$Pe_m = \frac{U_{in} \delta_f}{D}, \quad D_{AI} = \frac{k_1 \delta \phi_{in}^2 \delta_f}{D}, \quad D_{AII} = \frac{k_2 \delta \phi_{in} \delta_f}{D}, \quad D_{AIII} = \frac{k_3 \delta \delta_f}{D}. \quad (4.86)$$

Substituting the v -component velocity from (4.50) gives

$$\frac{\partial \bar{\phi}_1}{\partial \bar{y}} = \left(\bar{p} - \beta - \theta \sum \bar{\phi}_i \right) Da Pe_m \epsilon^{-1} \bar{\phi}_1 + D_{AI} (\bar{\phi}_1 \bar{\phi}_2^2), \quad (4.87)$$

$$\frac{\partial \bar{\phi}_2}{\partial \bar{y}} = \left(\bar{p} - \beta - \theta \sum \bar{\phi}_i \right) Da Pe_m \epsilon^{-1} \bar{\phi}_2 + 2D_{AI} (\bar{\phi}_1 \bar{\phi}_2^2), \quad (4.88)$$

$$\frac{\partial \bar{\phi}_3}{\partial \bar{y}} = \left(\bar{p} - \beta - \theta \sum \bar{\phi}_i \right) Da Pe_m \epsilon^{-1} \bar{\phi}_3 - D_{AI} (\bar{\phi}_1 \bar{\phi}_2^2), \quad (4.89)$$

$$\frac{\partial \bar{\phi}_4}{\partial \bar{y}} = \left(\bar{p} - \beta - \theta \sum \bar{\phi}_i \right) Da Pe_m \epsilon^{-1} \bar{\phi}_4 + D_{AII} (\bar{\phi}_4 \bar{\phi}_5) - 2D_{AIII} \bar{\phi}_7, \quad (4.90)$$

$$\frac{\partial \bar{\phi}_5}{\partial \bar{y}} = \left(\bar{p} - \beta - \theta \sum \bar{\phi}_i \right) Da Pe_m \epsilon^{-1} \bar{\phi}_5 + D_{AII} (\bar{\phi}_4 \bar{\phi}_5), \quad (4.91)$$

$$\frac{\partial \bar{\phi}_6}{\partial \bar{y}} = \left(\bar{p} - \beta - \theta \sum \bar{\phi}_i \right) Da Pe_m \epsilon^{-1} \bar{\phi}_6 - D_{AII} (\bar{\phi}_4 \bar{\phi}_5), \quad (4.92)$$

$$\frac{\partial \bar{\phi}_7}{\partial \bar{y}} = \left(\bar{p} - \beta - \theta \sum \bar{\phi}_i \right) Da Pe_m \epsilon^{-1} \bar{\phi}_7 + D_{AIII} \bar{\phi}_7, \quad (4.93)$$

$$\frac{\partial \bar{\phi}_8}{\partial \bar{y}} = \left(\bar{p} - \beta - \theta \sum \bar{\phi}_i \right) Da Pe_m \epsilon^{-1} \bar{\phi}_8 - D_{AIII} \bar{\phi}_7. \quad (4.94)$$

We should also again observe that (4.87) - (4.94) suggests that the concentration gradient at the membrane is influenced by many interacting mechanisms. Namely, the dominant pressure difference in the channel (represented by β), the ratio between osmotic pressure and the channel's pressure (represented by θ), the sum of concentration at the membrane, the membrane characteristics (represented by Da), the dominant mass transport mechanism at the membrane (represented by Pe_m), the concentration of salt ions at the membrane and the relationship between precipitation and diffusion (represented by D_A). Note when we are referring to the general group and not a subset of the group, we simply represent

it as D_A .

We may non-dimensionalise the porosity in (4.62) as follows

$$\epsilon = \epsilon_o \bar{\epsilon}, \quad \phi_i = \phi_{in} \bar{\phi}_i, \quad t = \frac{L}{U_{in}} \bar{t}, \quad (4.95)$$

we then obtain

$$\bar{\epsilon} = \bar{\epsilon}_o - \left(\frac{V k_1 \phi_{in}^3 L}{U_{in} \epsilon_o} \bar{\phi}_1 \bar{\phi}_2 + \frac{V k_2 \phi_{in}^2 L}{U_{in} \epsilon_o} \bar{\phi}_4 \bar{\phi}_5 \right) (\bar{t} - \bar{t}_o). \quad (4.96)$$

We introduce the dimensionless parameters

$$Ma_I = \frac{V k_1 \phi_{in}^3 L}{U_{in} \epsilon_o}, \quad Ma_{II} = \frac{V k_2 \phi_{in}^2 L}{U_{in} \epsilon_o}. \quad (4.97)$$

Hence we have

$$\bar{\epsilon} = \bar{\epsilon}_o - [Ma_I \bar{\phi}_1 \bar{\phi}_2 + Ma_{II} \bar{\phi}_4 \bar{\phi}_5] (\bar{t} - \bar{t}_o). \quad (4.98)$$

Again this is reasonable from a physical perspective as we would expect the membrane deterioration to be influenced by the advective timescale, the solutes concentration and rate of reaction.

4.2.3 Single-precipitation

At this point, we will consider a simplified bi-molecular reaction scheme. There are few reasons for doing this. First, this approach will help us understand the model solution without the complexity of co-precipitation. This allows us to develop a deeper understanding of the overall framework, not only the model solutions but also the limitations. At the same time, this enables us to build an intuition of when and under what circumstances the model can be used. In addition, this approach offers us the chance to compare the result obtained in a single-precipitation (with bi-molecular ionic species) to co-precipitation (with several ionic species) which again furthers our understanding.

Membrane boundary condition simplification

In an effort to understand the model solution and the role of each dimensionless parameter we will employ the following simplified binary irreversible reaction scheme



As this is a second order reaction, we can deduce from (4.87) - (4.94) that

$$\frac{\partial \bar{\phi}_a}{\partial \bar{y}} = (\bar{p} - \beta - \theta(\bar{\phi}_a + \bar{\phi}_b)) DaPe_m \epsilon^{-1} \bar{\phi}_a + D_{AII}^*(\bar{\phi}_a \bar{\phi}_b), \quad (4.100)$$

and

$$\frac{\partial \bar{\phi}_b}{\partial \bar{y}} = (\bar{p} - \beta - \theta(\bar{\phi}_a + \bar{\phi}_b)) DaPe_m \epsilon^{-1} \bar{\phi}_b + D_{AII}^*(\bar{\phi}_a \bar{\phi}_b) \quad (4.101)$$

For the numerical simulations, we go further to reduce the number of independent variables by employing the notion of mixture fractions and reaction progress variable defined by [36]. The progress variable χ and the mixture fraction ξ are defined as

$$\chi = \frac{\bar{\phi}_a + \bar{\phi}_b}{2}, \quad (4.102)$$

and

$$\xi = \frac{\bar{\phi}_a - \bar{\phi}_b}{2}. \quad (4.103)$$

χ tracks the progress of the reaction and ξ a conserved quantity. The inverse transformation is

$$\bar{\phi}_a = \chi + \xi, \quad (4.104)$$

$$\bar{\phi}_b = \chi - \xi. \quad (4.105)$$

Using the progress variables, the membrane boundary condition becomes

$$\frac{\partial \chi}{\partial \bar{y}} = (\bar{p} - \beta - 2\theta\chi) DaPe_m \epsilon^{-1} \chi - D_{AII}^*(\chi^2 - \xi^2) \text{ on } \Gamma_m, \quad (4.106)$$

where $D_{AII}^* = \frac{k_r \delta \phi_{in} \delta_f}{D}$. Then the change in porosity would be

$$\epsilon = \epsilon_o - V \int_{t_0}^t (k_r ab) dt. \quad (4.107)$$

The non-dimensionalisation procedure would be similar, so the dimensionless form of the porosity equation is

$$\bar{\epsilon} = \bar{\epsilon}_o - Ma^* [(\chi^2 - \xi^2)] (\bar{t} - \bar{t}_o), \quad (4.108)$$

where

$$Ma^* = \frac{V k_r \phi_{in}^2 L}{U_{in} \epsilon_o}. \quad (4.109)$$

We can now track the progress of the bi-molecular reaction in (4.99) using only one variable χ . In addition, we only need to consider only one Ma group instead of two and one D_A group instead of three. As our main goal in the next chapter

is to investigate the role of each dimensionless group, the overall simplicity of this membrane boundary condition is an advantage.

4.2.4 Co-precipitation

In this section, we present a simplified membrane boundary condition for the co-precipitation process. Once again we employ the notion of mixture fractions and progress variable to simplify the numerical simulation. This reduces the number of concentration variables specified in the simulation, thereby making analysis easier.

Membrane boundary condition simplification

For simplicity, we assume ϕ_7 is constant in the numerical simulations. Therefore, we define the following progress variables to track the progress of precipitation ϕ_3 and ϕ_6

$$\gamma_1 = \frac{2\bar{\phi}_1 + \bar{\phi}_2}{2}, \quad (4.110)$$

$$\gamma_2 = \frac{\bar{\phi}_4 + \bar{\phi}_5 + 2\bar{\phi}_7}{2}. \quad (4.111)$$

The mixture fractions are conserved quantities given by

$$\eta_1 = \frac{2\bar{\phi}_1 - \bar{\phi}_2}{2}, \quad (4.112)$$

$$\eta_2 = \frac{\bar{\phi}_4 - \bar{\phi}_5 + 2\bar{\phi}_7}{2}. \quad (4.113)$$

The inverse transformation is then

$$\bar{\phi}_1 = \frac{\gamma_1 + \eta_1}{2} \quad (4.114)$$

$$\bar{\phi}_2 = \gamma_1 - \eta_1, \quad (4.115)$$

$$\bar{\phi}_4 = \gamma_2 + \eta_2 - 2\bar{\phi}_7, \quad (4.116)$$

$$\bar{\phi}_5 = \gamma_2 - \eta_2. \quad (4.117)$$

It is assumed that

$$\bar{\phi}_{1,2,3,4,5,7}(\mathbf{x}) \in [0, 1] \forall \mathbf{x}. \quad (4.118)$$

Using the progress variables and mixture fractions, the membrane boundary

condition becomes

$$\frac{\partial \gamma_1}{\partial \bar{y}} = \left(\bar{p} - \beta - \theta \left(\frac{3\gamma_1 + \eta_1}{2} \right) \right) DaPe_m \epsilon^{-1} \gamma_1 + 2D_{AI} \left(\frac{\gamma_1 + \eta_1}{2} \right) (\gamma_1 - \eta_1)^2 \text{ on } \Gamma_m, \quad (4.119)$$

$$\frac{\partial \gamma_2}{\partial \bar{y}} = (\bar{p} - \beta - \theta(2\gamma_2 - \phi_7)) DaPe_m \epsilon^{-1} \gamma_2 + D_{AII}(\gamma_2 + \eta_2 - 2\phi_7)(\gamma_2 - \eta_2), \text{ on } \Gamma_m. \quad (4.120)$$

Applying this transformation procedure to the porosity equation (4.98), we have

$$\epsilon = \bar{\epsilon}_o - \left[Ma_I \left(\frac{\gamma_1 + \eta_1}{2} \right) (\gamma_1 - \eta_1)^2 + Ma_{II}(\gamma_2 + \eta_2 - 2\phi_7)(\gamma_2 - \eta_2) \right]. \quad (4.121)$$

We now have all the tools needed to assess the model solutions and influence of each dimensionless group in the overall process. This will be our main focus in the next chapter.

4.2.5 Characteristic Timescales

Before we proceed, we note the characteristic timescales associated with the system. The advective timescale, L/U_{in} describes the time taken for the fluid to be transported along the length of the channel. The diffusion timescale $\frac{HL}{D}$ is the time taken for the salts to fully diffuse across the domain. The reactive timescales are presented in Table 4.2. These are the time taken for each of the precipitation reaction to reach equilibrium. Intuitively, we expect that the advective transport will reach equilibrium before the other two timescales due to the high pressures associated with reverse osmosis operations.

We note that the solutions we present in the next chapter might not capture all of these timescales because we will be considering a wide range of dimensionless groups. It is likely that it will take a long time for the associated processes to reach equilibrium at different regimes. We have included it here simply to make the reader aware that the model formulated captures multiple timescales which often characterise membrane systems.

4.2.6 Summary of Dimensionless Equations

To reduce the number of parameters in the formulation, we defined non-dimensional variables (denoted with an overbar) and different dimensional scales (see Table 4.1). For easy reference, in this subsection, we list all the dimensionless equations and groups obtained from the non-dimensionalisation procedure.

Table 4.1: Summary of the chosen scales for the several variables.

Chosen scales
$u = U_{in}\bar{u}$
$v = \tau U_{in}\bar{v}$
$p = P_{out} + (P_{in} - P_{out})\bar{p}$
$t = \frac{L}{U_{in}}\bar{t}$
$\Delta p = P_c(\bar{p} - \bar{p}_p)$
$\Delta\pi = RT\varphi\phi_{in} \sum \bar{\phi}_i$
$\partial_x = \frac{1}{L}$
$\partial_y = \frac{1}{\delta_f}$
$\phi_i = \phi_{in}\bar{\phi}_i$
$\epsilon = \epsilon_o\bar{\epsilon}$

Fluid Transport

$$\left(\frac{\partial \bar{u}}{\partial \bar{t}} + \bar{u} \frac{\partial \bar{u}}{\partial \bar{x}} + \bar{v} \frac{\partial \bar{u}}{\partial \bar{y}} \right) = -Eu \frac{\partial \bar{p}}{\partial \bar{x}} + \frac{1}{Re} \left(\frac{\partial^2 \bar{u}}{\partial \bar{x}^2} + \frac{1}{\tau^2} \frac{\partial^2 \bar{u}}{\partial \bar{y}^2} \right) \text{ on } \Omega, \quad (4.122)$$

$$\left(\frac{\partial \bar{v}}{\partial \bar{t}} + \bar{u} \frac{\partial \bar{v}}{\partial \bar{x}} + \bar{v} \frac{\partial \bar{v}}{\partial \bar{y}} \right) = -\frac{Eu}{\tau^2} \frac{\partial \bar{p}}{\partial \bar{y}} + \frac{1}{Re} \left(\frac{\partial^2 \bar{v}}{\partial \bar{x}^2} + \frac{1}{\tau^2} \frac{\partial^2 \bar{v}}{\partial \bar{y}^2} \right) \text{ on } \Omega, \quad (4.123)$$

subjected to the following boundary conditions

$$\left\{ \begin{array}{l} \bar{u} = \bar{v} = 0 \text{ on } \Gamma_w, \\ \bar{p}_{in} = 1 \text{ on } \Gamma_i, \\ \bar{p}_{out} = 0 \text{ on } \Gamma_o, \\ \frac{\partial \bar{p}}{\partial \mathbf{n}} = 0 \text{ on } \Gamma_m, \Gamma_w. \end{array} \right. \quad (4.124)$$

Solute Transport

$$\frac{\partial \bar{\phi}_i}{\partial \bar{t}} + \bar{u} \frac{\partial \bar{\phi}_i}{\partial \bar{x}} + \bar{v} \frac{\partial \bar{\phi}_i}{\partial \bar{y}} = \frac{1}{Pe} \left(\frac{\partial^2 \bar{\phi}_i}{\partial \bar{x}^2} + \frac{1}{\tau^2} \frac{\partial^2 \bar{\phi}_i}{\partial \bar{y}^2} \right) \text{ on } \Omega, \quad (4.125)$$

subjected to the following boundary conditions

$$\bar{\phi}_i = 1 \text{ on } \Gamma_i, \quad (4.126)$$

$$\frac{\partial \bar{\phi}_i}{\partial \mathbf{n}} = 0 \text{ on } \Gamma_o, \Gamma_w, \quad (4.127)$$

$$\left. \begin{aligned} \frac{\partial \bar{\phi}_1}{\partial \bar{y}} &= (\bar{p} - \beta - \theta \sum \bar{\phi}_i) DaPe_m \epsilon^{-1} \bar{\phi}_1 + D_{AI}(\bar{\phi}_1 \bar{\phi}_2^2) \\ \frac{\partial \bar{\phi}_2}{\partial \bar{y}} &= (\bar{p} - \beta - \theta \sum \bar{\phi}_i) DaPe_m \epsilon^{-1} \bar{\phi}_2 + 2D_{AI}(\bar{\phi}_1 \bar{\phi}_2^2) \\ \frac{\partial \bar{\phi}_3}{\partial \bar{y}} &= (\bar{p} - \beta - \theta \sum \bar{\phi}_i) DaPe_m \epsilon^{-1} \bar{\phi}_3 - D_{AI}(\bar{\phi}_1 \bar{\phi}_2^2) \\ \frac{\partial \bar{\phi}_4}{\partial \bar{y}} &= (\bar{p} - \beta - \theta \sum \bar{\phi}_i) DaPe_m \epsilon^{-1} \bar{\phi}_4 + D_{AII}(\bar{\phi}_4 \bar{\phi}_5) - 2D_{AIII} \bar{\phi}_7 \\ \frac{\partial \bar{\phi}_5}{\partial \bar{y}} &= (\bar{p} - \beta - \theta \sum \bar{\phi}_i) DaPe_m \epsilon^{-1} \bar{\phi}_5 + D_{AII}(\bar{\phi}_4 \bar{\phi}_5) \\ \frac{\partial \bar{\phi}_6}{\partial \bar{y}} &= (\bar{p} - \beta - \theta \sum \bar{\phi}_i) DaPe_m \epsilon^{-1} \bar{\phi}_6 - D_{AII}(\bar{\phi}_4 \bar{\phi}_5) \\ \frac{\partial \bar{\phi}_7}{\partial \bar{y}} &= (\bar{p} - \beta - \theta \sum \bar{\phi}_i) DaPe_m \epsilon^{-1} \bar{\phi}_7 + D_{AIII} \bar{\phi}_7 \\ \frac{\partial \bar{\phi}_8}{\partial \bar{y}} &= (\bar{p} - \beta - \theta \sum \bar{\phi}_i) DaPe_m \epsilon^{-1} \bar{\phi}_8 - D_{AIII} \bar{\phi}_7 \end{aligned} \right\} \text{ on } \Gamma_m. \quad (4.128)$$

Recovery

$$r_e = \left(\bar{p} - \beta - \theta \sum \bar{\phi}_i \right) Da\tau^{-1} \frac{\vartheta_g}{\bar{u}} \quad (4.129)$$

Porosity

$$\bar{\epsilon} = \bar{\epsilon}_o - [Ma_I \bar{\phi}_1 \bar{\phi}_2 + Ma_{II} \bar{\phi}_4 \bar{\phi}_5] (\bar{t} - \bar{t}_o). \quad (4.130)$$

Table 4.2: Characteristic timescales.

Process	Characteristic time
Advection	L/U_{in}
Diffusion	HL/D
Single-precipitation	$V\phi_{in}^2 k_r$
Co-precipitation	$V\phi_{in}^2 (k_1 \phi_{in} + k_2)$

Numerical Simplifications: Boundary Conditions

Single-Precipitation

$$\left. \begin{aligned} \frac{\partial \chi}{\partial \bar{y}} &= (\bar{p} - \beta - 2\theta\chi) DaPe_m \epsilon^{-1} \chi - D_{AII}^* (\chi^2 - \xi^2) \\ \bar{\epsilon} &= \bar{\epsilon}_o - Ma^* [(\chi^2 - \xi^2)] (\bar{t} - \bar{t}_o) \end{aligned} \right\} \text{ on } \Gamma_m. \quad (4.131)$$

Co-Precipitation

$$\left. \begin{aligned} \frac{\partial \gamma_1}{\partial \bar{y}} &= (\bar{p} - \beta - \theta \left(\frac{3\gamma_1 + \eta_1}{2}\right)) DaPe_m \epsilon^{-1} \gamma_1 + 2D_{AI} \left(\frac{\gamma_1 + \eta_1}{2}\right) (\gamma_1 - \eta_1)^2 \\ \frac{\partial \gamma_2}{\partial \bar{y}} &= (\bar{p} - \beta - \theta(2\gamma_2 - \phi_7)) DaPe_m \epsilon^{-1} \gamma_2 + D_{AII} (\gamma_2 + \eta_2 - 2\phi_7) (\gamma_2 - \eta_2) \\ \epsilon &= \bar{\epsilon}_o - [Ma_I \left(\frac{\gamma_1 + \eta_1}{2}\right) (\gamma_1 - \eta_1) + Ma_{II} (\gamma_2 + \eta_2 - 2\phi_7) (\gamma_2 - \eta_2)]. \end{aligned} \right\} \text{ on } \Gamma_m. \quad (4.132)$$

4.3 Summary

In this chapter we have presented a number of special aspects of the model framework which specifically distinguishes this work from those existing in the literature. We began the chapter by analysing the stability of the system. As we hoped, the linear stability analysis provided a further qualitative characterisation of the reaction system, which in turn provided a clearer understanding of the process itself. We found that the fixed points are borderline saddle-node cases. This means altering the coefficients/parameters slightly can alter the stability of the system. We believe the overshoots and undershoots observed during the experiments could be attributed to this as slight changes in experimental conditions could have changed the stability from a stable node to a saddle (or vice-versa).

Following the linear stability analysis we non-dimensionalised the problem formulation. The formulation now contains more or less nine dimensionless groups as opposed to the twenty dimensional variables in the original system. This reduction in the number of parameters greatly simplifies the problem in two aspects. Firstly, the dimensionless groups consolidate the information contained in the twenty original parameters, making analysis easier to carry out. Secondly, this makes it possible to compare different systems even if they have different scales. For example, two incompressible flows which have the same Darcy number have very similar properties, even if the pressure scales and the velocity scales are different. The only important factor of comparison is that the dimensional group have to be the same (i.e., kept constant).

Table 4.3: Dimensionless numbers obtained from non-dimensionalisation of Navier–Stokes Equations and Solute Transport Equation.

Dimensionless Formula	Interpretation	Symbol	Dimensionless Group
$\frac{\rho U_{in} L}{\mu}$	Ratio of inertia to viscous forces	Re	Reynolds number
$\frac{P_c}{\rho U_{in}^2}$	Ratio of pressure forces to the inertial forces	Eu	Euler number
$\frac{L}{H}$	Ratio of the geometry length to the width	ϑ_g	
$\frac{P_p - P_{out}}{P_c}$	Indicates the dominant pressure deviation	β	
$\frac{RT\varphi\phi_{in}}{P_c}$	Ratio of osmotic pressure to the channel's pressure	θ	
$\frac{k}{\delta\delta_f}$	Ratio of permeability to membrane area	Da	Darcy number
$\frac{LU_{in}}{D}$	Ratio of convection to diffusion in the bulk fluid	Pe	Bulk Peclet number
$\frac{U_{in}\delta_f}{D}$	Ratio of convection to diffusion at the membrane layer	Pe_m	Membrane Peclet number
$\frac{k_1\delta\phi_{in}^2\delta_f}{D}$	Ratio of precipitation of ϕ_3 to diffusion	D_{AI}	Damköhler number
$\frac{k_2\delta\phi_{in}\delta_f}{D}$	Ratio of precipitation of ϕ_6 to diffusion	$D_{AII} \sim D_{AII}^*$	Damköhler number
$\frac{k_3\delta\delta_f}{D}$	Ratio of dissolution of ϕ_7 to diffusion	D_{AIII}	Damköhler number
$\frac{Vk_1\phi_{in}^3 L}{U_{in}\epsilon_o}$	Gives an indication of how fast precipitation of ϕ_3 occurs	Ma_I	
$\frac{Vk_2\phi_{in}^2 L}{U_{in}\epsilon_o}$	Gives an indication of how fast precipitation of ϕ_6 occurs	$Ma_{II} \sim Ma^*$	

We then stated that we would consider two different types of precipitation mechanisms in our analysis. Namely, single-precipitation resulting from bi-molecular reactants and co-precipitation (as observed in our experimental study in Chapter 2) which is the product of several ions. We noted the benefit of this approach; these are

- (i) It allows us to develop a deeper understanding of the overall framework, not only the model solutions but also the limitations.
- (ii) It offers us the chance to compare the result obtained in a single-precipitation to co-precipitation which again furthers our understanding.

We also identified the various timescales in the model which are the advective timescale, the diffusive timescale and the reactive timescales. It was noted that the solutions we present in the next chapter might not capture all of these timescales because we will be considering a wide range of dimensionless groups. We included it to show that the model formulated captures multiple timescales which characterises reverse osmosis desalination systems.

Chapter 5

Model Assessment

In preceding chapters, we presented the experimental results, model formulation and its dimensionless form. The current model framework distinguishes itself from those existing in the literature in several ways. Firstly, the model captures the complex feedback and interaction between fluid dynamics, solute transport and precipitation. It also employs a deterministic approach for the reaction kinetics which describes co-precipitation of salts as observed in reality. In addition, we are able to perform a stability analysis of the system's behaviour and nondimensionalise the governing equations.

In this chapter, we will investigate the influence of different dimensionless groups on the model solution. The goal is to (a) develop an understanding of the model solutions and limitations, (b) distinguish the role of each process and (c) evaluate the interplay between fluid flow, material transport and precipitation. To this end, we will first analyse the results obtained for the simplified bimolecular reaction scheme presented in section 4.2.3. Results from this simplification will help us develop an understanding of the model solutions. This knowledge will be useful when we subsequently analyse the more complicated co-precipitation mechanism in following sections.

Overall, this chapter serves as an assessment of the model's performance to ensure that the predictions from the model are consistent with its principles and assumptions.

5.1 Outline of Model Assessment

We begin by recalling from our introductory discussions in section 3.1.1 that the main factors that limit recovery in reverse osmosis operations include: osmotic

pressure, concentration polarisation and precipitation of mineral salts. As these are the main mechanisms/phenomena governing reverse osmosis operations, in this section (and subsequent sections) we will investigate the effects of various dimensionless groups on these mechanisms.

There are nine dimensionless groups that are of specific interest in this study. These are $Da, Re, Ma, Eu, \theta, D_A, Pe, \beta, \vartheta_g$. Note we use D_A and M_A here because we are referring to the general group. Taken collectively, these nine non-dimensional groups control the behaviour of the system. Therefore, we will analyse the different types of behaviour obtained for various ratios of the dimensionless groups. The values of specific variables will be varied to obtain a range of values. The physically relevant values presented in Tables 5.1 were used as a guide to generate the wide range of dimensionless groups shown in Table 5.2. Some of the dimensionless group range presented in Table 5.2 may not be physically relevant because our intention is to cover a broad spectrum of regimes and identify the model/code's limitations.

We obtain different dimensionless ratios by merely varying one of the parameters present in the group. The specific parameter varied for each dimensionless group is presented in Table 5.2. For instance, the Peclet number Pe is described as LU_{in}/D . Therefore doubling L has the same effect on the Pe as decreasing D by a factor of 2. Similarly, doubling the velocity (i.e. U_{in}) has the same effect on Pe as decreasing D by a factor of 2. Therefore, we do not have to vary L, D, U_{in} separately but instead only D and that changes the Peclet grouping as a whole. However, it is important to note that varying parameters in one group could also influence other dimensional groups. For instance, increasing D would not only increase Pe but also D_A . For consistency, we avoid varying more than one dimensionless groups at once. For this reason, the Euler number Eu analysis has been excluded from this thesis because varying any of the parameters in Eu affects other dimensionless group. For instance, varying P_c i.e. $P_{in} - P_{out}$, invariably alters the velocity which in turn influences other dimensionless groups such as Pe, Re and Ma . Thus, we are unable to evaluate the relative influence of varying Eu only because the the result obtained is a combined effect of varying Pe, Re, Eu and Ma .

5.2 Single-precipitation

Before presenting the results, we recall a few basic features about the model that would be important when interpreting the results. The first of these is that the qualitative results presented in this sections consists of flow through a

Table 5.1: Range of the dimensional variables from the Navier-Stokes equation and the solute transport equation.

Physical Variable	Symbol	Units	Physically Relevant Range	Source
Diffusivity	D	m^2s^{-1}	$0.92 \times 10^{-9} - 1.3 \times 10^{-9}$	[13, 38, 87]
Reaction rate	k_r	$\frac{\text{m}^3}{\text{mol}^{-1}\text{s}^{-1}}$	$0.045 - 5 \times 10^{-8}$	[75, 87]
Molar Volume	V	m^3/mol	100	[22]
Channel height	H	m	1×10^{-2}	[10, 73, 87]
Membrane permeability	k	m^2	9×10^{-19}	[87]
Permeate pressure	P_p	Pa	1×10^5	[22]
Osmotic Coefficient	φ	-	0.0217 - 0.89	[32, 94]
Viscosity	μ	Pas	9.7×10^{-4}	[45]
Fluid density	ρ	kgm^{-3}	1000	[87]
Gas constant	R_G	$\text{JK}^{-1}\text{mol}^{-1}$	8.314	[87]
Temperature	T	K	298	[87]
Membrane thickness	δ	μm	30 - 60	[137]
Porosity	ϵ_o	-	0.3 - 0.85	[2]
Channel length	L	m	1	[10, 73, 99]
Inlet Velocity	U_{in}	m/s	0.1	[22, 87]
Inlet Concentration	ϕ_{in}	mol/m^3	1	[87]
Inlet pressure	P_{in}	Pa	5.5×10^6	[22]
Outlet pressure	P_{out}	Pa	5×10^6	[22]

Table 5.2: Table showing the range of physically realistic dimensionless group values deduced from Table 5.1 and the range of dimensionless group values used in simulations

Dimensionless Group	Formula	Physically Realistic Range	Range of Dimensions Group in Simulations
Pe	$\frac{LU_{in}}{D}$	326 – 5796	7.4 - 740
D_{AII}^*	$\frac{k_3\delta\delta_f}{D}$	$1 \times 10^{-6} - 1$	$3 \times 10^{-3} - 3000$
Ma	$\frac{Vk_r\phi_{in}^2 L}{U_{in}\epsilon_o}$	$1.7 \times 10^{-8} - 1$	$7.7 \times 10^{-4} - 0.77$
ϑ_g	$\frac{L}{H}$	1000	2 - 20 ¹
Da	$\frac{k}{\delta\delta_f}$	$3 \times 10^{-14} - 1.5 \times 10^{-14}$	$6.7 \times 10^{-18} - 3 \times 10^{-14}$
$ \beta $	$\frac{P_p - P_{out}}{P_c}$	10	1.5 - 1140
θ	$\frac{RT\varphi\phi_{in}}{P_c}$	$1.1 \times 10^{-4} - 4.4 \times 10^{-3}$	$4 \times 10^{-9} - 4.3 \times 10^{-3}$
Re	$\frac{\rho U_{in} L}{\mu}$	30 – 773	$6 \times 10^{-6} - 123$

¹ For simplicity and computational efficiency, in our simulations we considered a small section of a larger membrane channel corresponding to 2% of the typical membrane length which is equivalent to ~ 20 mm. As a result, we scaled back the recovery rates as we expect a a lower recovery in a shorter membrane.

channel with inflow at the left, outflow at the right and membrane at the base. This is representative of a crossflow configuration where the feed solution flows tangentially (parallel) to the membrane. Second, the flow consists of a streamwise velocity u parallel to the membrane and a transverse velocity v normal to the membrane flow. The streamwise velocity u is several orders of magnitude larger than the permeate velocity across the membrane v as shown in (4.34).

In the following subsections we will present the results at a fixed value of t unless otherwise stated. It is important to note that these results are based on the simplified single precipitation membrane boundary condition presented in (4.106).

5.2.1 Concentration Polarisation & Osmotic Pressure

In this section we will investigate the effect of each dimensionless group on polarisation and osmotic pressure. We have grouped polarisation and osmotic pressure together in this section because we expect that an increase in

membrane concentration (which is usually attributed to polarisation) would raise the osmotic pressure of the fluid. Hence, we have juxtaposed the results to show the similarities between both of these mechanisms.

A quick inspection of the quantitative figures presented in this section show a plot of “polarisation factor” (on the y-axis) against the corresponding dimensionless group. The degree of polarisation factor is obtained by solving the solute material balance in the polarised layer which is given by

$$v\phi_m = r(t)dt + D\frac{d\phi}{dy}, \quad (5.1)$$

where ϕ_m is the solute concentration at the membrane and $r(t)$ is the precipitation reaction at the membrane.

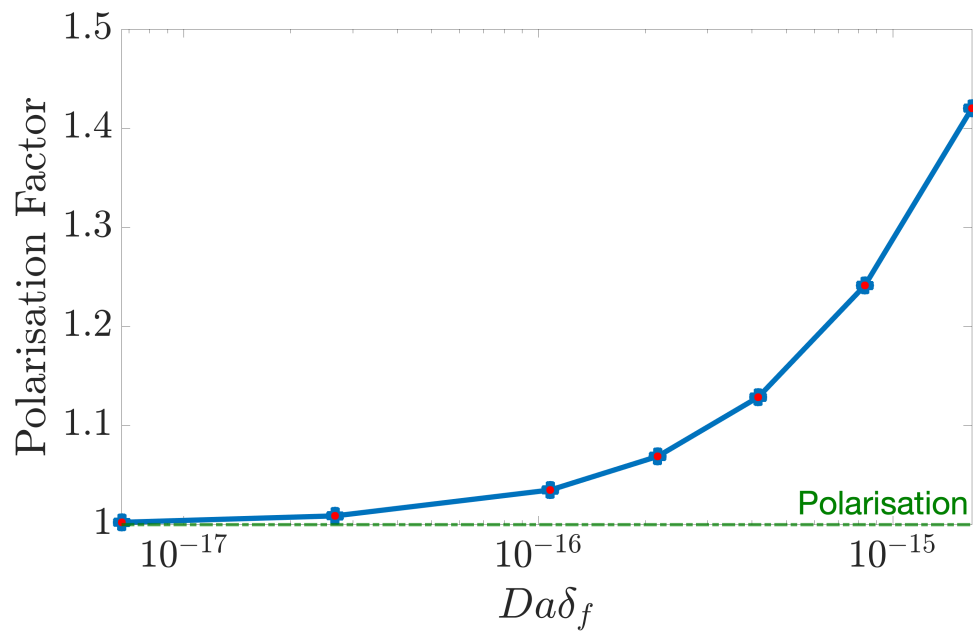
The polarisation factor represents the severity of polarisation, that is, how much higher the solute membrane concentration is in comparison to the bulk concentration. Therefore a value < 1 implies that the membrane concentration is lower than the bulk concentration. A value of 1 is an indication of uniform concentration, that is, the membrane concentration is equivalent to the bulk concentration. As one might expect, a value > 1 means that the membrane concentration is higher than the bulk concentration, which is concentration polarisation [110].

For later purposes it is useful to provide an indication of what we should expect regarding the nature of the results. In the present context, we believe four properties/phenomena will be responsible for the growth and extent of the membrane polarised layer introduced in section 3.1.1. These are: precipitation/reaction, advection, diffusion and the membrane characteristics. Indeed as we will see shortly the dimensionless groups that contribute most to polarisation are the ones that are related to the four properties just mentioned.

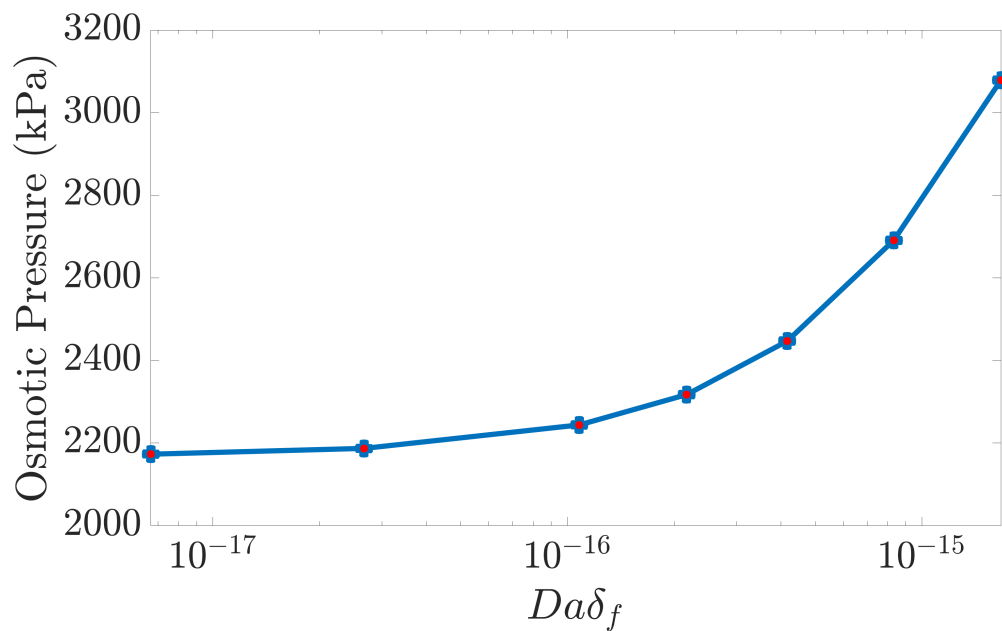
Impact of Da on polarisation & Osmotic Pressure

The Darcy number Da , is a measure of how much fluid flows through the membrane. It is directly proportional to the membrane permeability so that a high permeability would result in high velocity flow through the membrane whereas a low permeability inhibits flow through the membrane.

Figure 5.1a displays the variation of the Darcy number Da and the effect on concentration polarisation. It is clear from Figure 5.1a that Da has a noticeable effect on concentration polarisation. It should further be observed that the magnitude of polarisation tends to increase with increasing Da . Figure 5.1b on



(a) Graph of concentration polarisation (as a ratio of membrane concentration to inlet concentration) against the dimensionless group $Da\delta_f$, which shows how polarisation depends on Darcy's number.



(b) Graph of osmotic pressure against the dimensionless group $Da\delta_f$, which shows how the osmotic pressure depends on Darcy's number.

Figure 5.1: Effect of $Da\delta_f$ on (a) polarisation and (b) osmotic pressure.

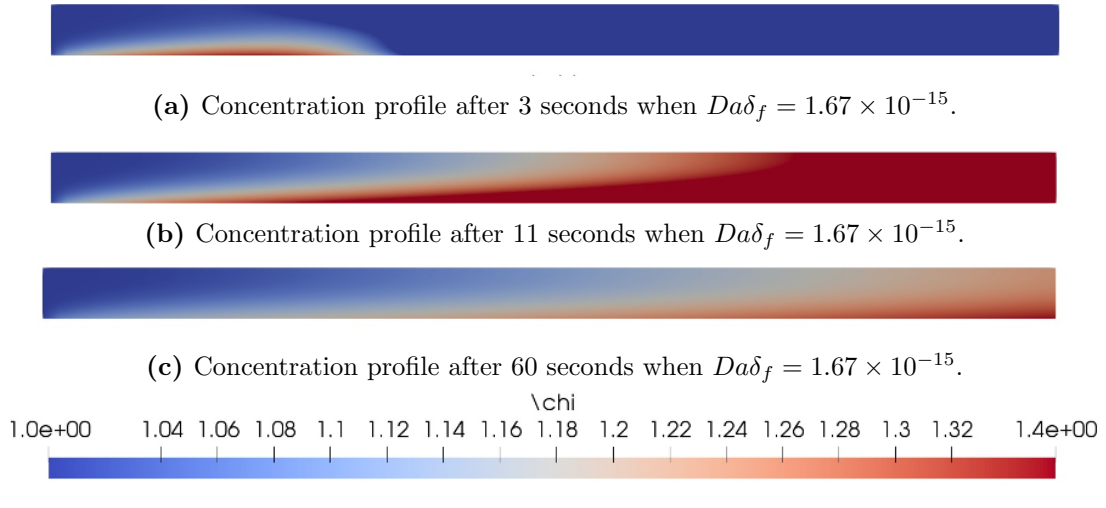


Figure 5.2: Concentration profile observed at different times when $Da\delta_f = 1.67 \times 10^{-15}$.

the other hand illustrates the effect of Da on osmotic pressure. The increasing trend observed in this figure is similar to that in Figure 5.1a.

It is of interest at this point to understand why Da influences polarisation. First, it might be worthwhile to take a look at the evolution of the concentration profile in Figure 5.2. The first thing to notice regarding this result is that the solute progress variable (χ) is transported downstream (to the right) by a combination of advection and diffusion. The red color indicates a high concentration of solute, whereas the blue color indicates the initial value of the solute progress variable. We can also see that after some time the concentration in the channel becomes more uniform as depicted in Figure 5.2c. This solute spatial distribution observed is a consequence of diffusion as this phenomena acts to distribute solutes uniformly.

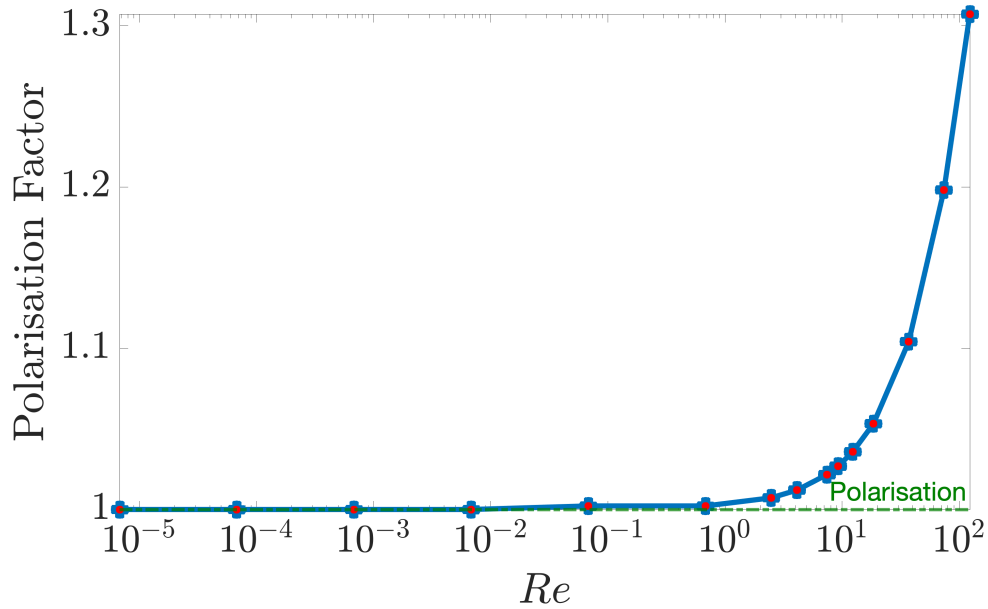
Having established this, we can now proceed to understand the reason for the trend observed in Figure 5.1. It is clear that a higher Da is associated with a high permeability system. One of the implications of this is that the magnitude of the permeate velocity v (i.e normal component of the velocity) increases with increasing Da . Therefore more fluid is able to pass through the membrane. This increase in permeate velocity causes more solute to be transported to the membrane surface. However, due to the no-flux solute condition and 100% salt rejection condition at the membrane (specified when the model was developed in Chapter 3) all the solutes arriving at the membrane surface are rejected leading to a higher concentration of solutes near the membrane which gives rise to polarisation. The consequence of this is readily seen in Figures 5.1b and 5.2c. Namely, the rise in osmotic pressure and thick polarised layer near the

membrane surface.

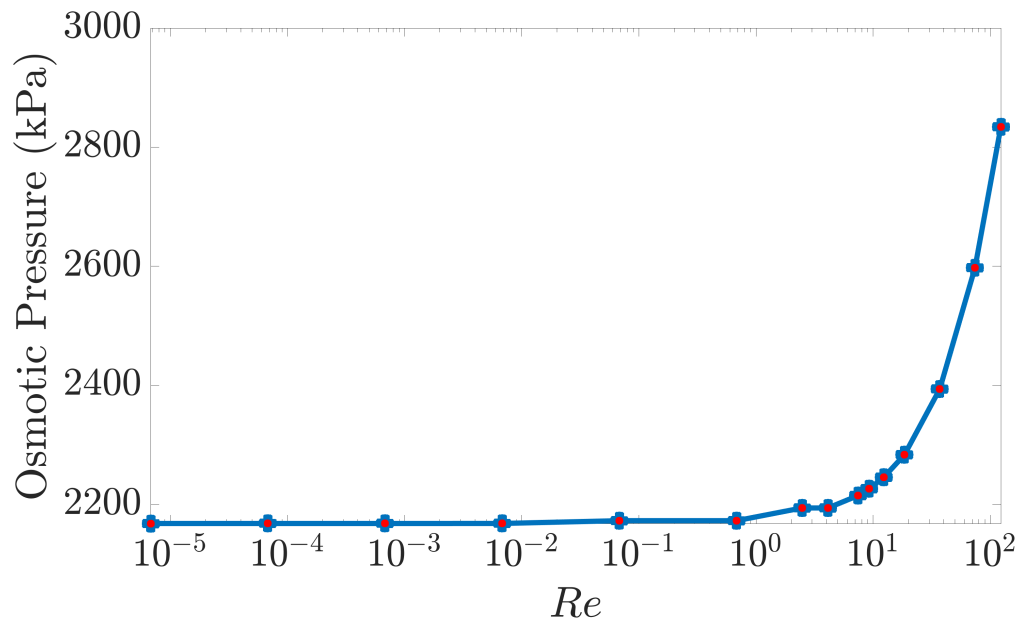
The result in Figure 5.2c is consistent with the existing literature on concentration polarisation which have demonstrated that polarisation is most severe closer to the outlet of a membrane channel. This is because the streamwise velocity u creates a shearing effect which “washes” away the accumulated solutes around the inlet, causing a lower buildup of solute concentration near the channel entrance. In addition, the results in Figures 5.1a seem to support arguments from previous studies [28] that mineral scaling might be exacerbated at higher water fluxes due to the polarised layer. This suggests that highly permeable membranes might make it possible to use a smaller membrane area (as a high recovery is anticipated) reducing capital cost but this increases polarisation.

Impact of Re on concentration polarisation

The Reynolds number Re is the ratio of the inertia forces to viscous forces. It gives an indication of which of the two mechanisms dominates. In low velocity flow, advective mass transport plays a minor role and diffusion is the dominant mechanism. However in relatively high velocity flows, advective transport plays a significant role. Figure 5.3 depicts the variation of Re and the corresponding effect on concentration polarisation and osmotic pressure. It is apparent from the figure, that for creeping flow, that is at very low Reynolds number ($Re \ll 1$), Re has a minimal effect on polarisation and osmotic pressure. For instance, we can see from Figure 5.3a that in this regime, increasing Re by 5 orders of magnitude has little or no effect on polarisation. However as the flow approaches the laminar regime we start to see a noticeable effect on polarisation. It is easily seen from Figure 5.3a that in this regime, increasing Re by 2 orders of magnitude increases polarisation and osmotic pressure by a factor of ~ 1.3 . A possible explanation for this is related to the permeate velocity v . Recall v is several orders of magnitude smaller than the streamwise velocity u . From our simulations, we know that v is relatively low (range $\sim 10^{-19}$ m/s) over the creeping flow regime shown in Figure 5.3a therefore in essentially all these cases the flow towards the membrane surface is small. By contrast, the value of v over the laminar flow regime is substantially higher (range $\sim 10^{-12}$ m/s) which in turn increases the quantity of solute transported to membrane. However, due to the 100% rejection specified at the membrane, all the solutes arriving at the membrane are rejected and only water is transported through the membrane. As a result, the concentration at the membrane increases which explains the rise in polarisation and osmotic pressure observed in Figure 5.3 as Re increases.



(a) Graph of concentration polarisation (as a ratio of membrane concentration to inlet concentration) against the dimensionless group Re , which shows how polarisation depends on Reynold's number.



(b) Graph of osmotic pressure against the dimensionless group Re , which shows how the osmotic pressure depends on Reynold's number.

Figure 5.3: Effect of Re on (a) polarisation and (b) osmotic pressure.

Impact of Ma^* on polarisation & osmotic pressure

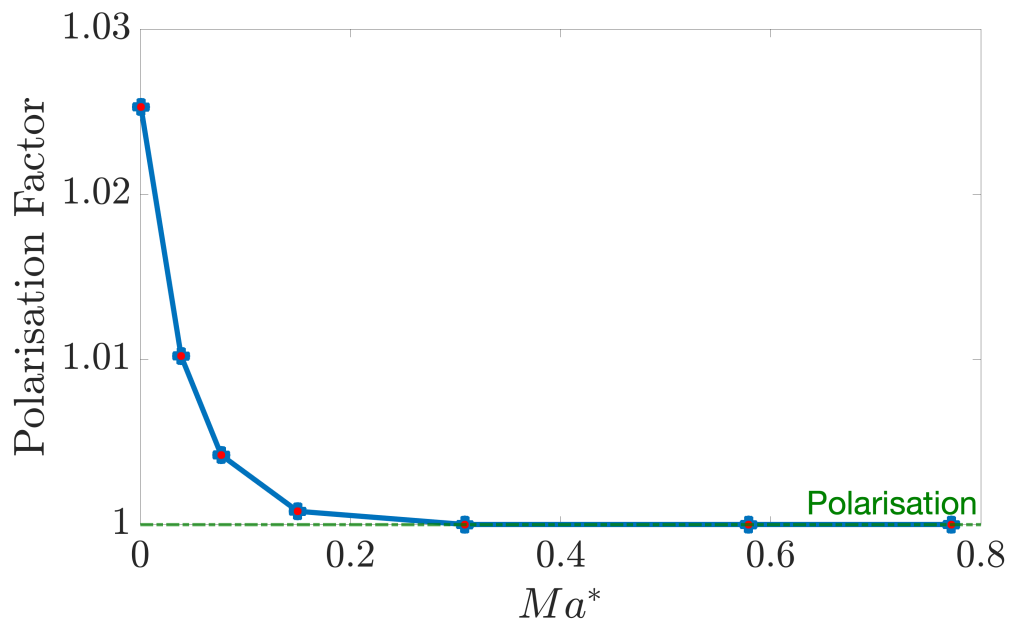
Ma^* gives an indication of how quickly precipitation occurs and its severity. It is directly proportional to the precipitation reaction, reaction rate and solute concentration. Therefore we expect that a fast reaction or high concentration would have a significant effect on Ma^* . Figure 5.4 shows the variation of Ma^* and the corresponding effect on polarisation and osmotic pressure. It can be seen that polarisation reduces with increasing Ma^* . This is expected because a higher Ma^* translates to a fast reaction at the membrane. Therefore, more solutes are consumed in the precipitation process which in turn reduces polarisation and osmotic pressure as depicted in Figure 5.4.

Furthermore, it can also be observed from Figure ??b that the average concentration in the channel is ≤ 1 (with 1 being the inlet concentration). We assume this is generally the case as Ma^* increases. This suggests that increasing Ma^* acts to maintain the inlet concentration as the bulk concentration.

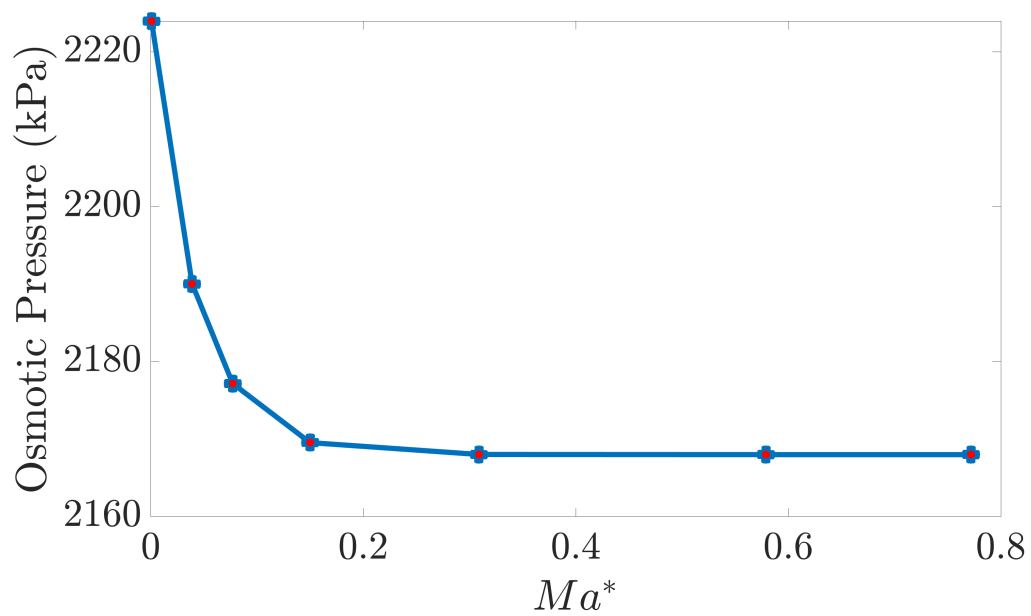
Impact of θ on polarisation & osmotic pressure

θ measures the relation between osmotic pressure and the channel's pressure. The osmotic pressure is closely related to polarisation so we also expect θ to have an effect on the process. Indeed, we see from Figure 5.5b that osmotic pressure increases with θ . This is to be expected as θ is directly proportional to osmotic pressure as shown in (4.49).

Figure 5.5a reveals that although polarisation reduces with increasing θ , there are certain values of θ that do not impact polarisation. It appears that θ begins to have an effect on polarisation as the value approaches 1 which is when the osmotic pressure is equivalent to the channel's pressure. This result may be explained by the fact that osmotic pressure is closely related to the transverse velocity described in (4.25). It is clear from this equation that a lower osmotic pressure increases the magnitude of the transverse velocity and as we already pointed out earlier, in higher velocity flows, the flow and solute transport towards the membrane surface is increased giving rise to polarisation. In contrast, a higher osmotic pressure reduces the magnitude of the transverse velocity which in turn results in a lower quantity of solute at the membrane. These results seem to suggest that polarisation occurs when the channel's pressure is significantly higher than the osmotic pressure.

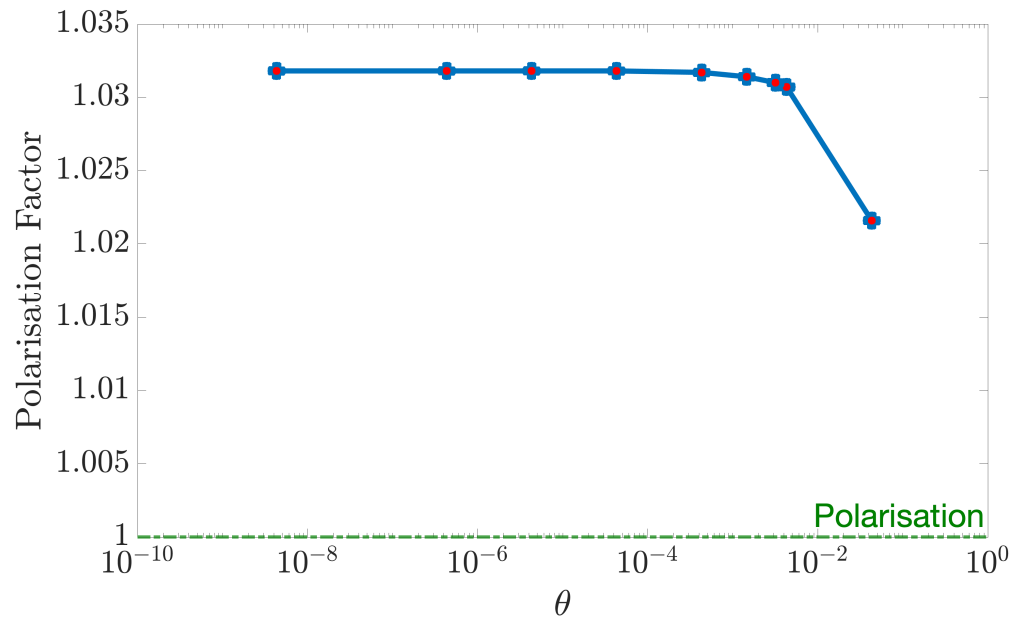


(a) Graph of concentration polarisation (as a ratio of membrane concentration to inlet concentration) against the dimensionless group Ma^* , which shows how polarisation depends on the severity of polarisation.

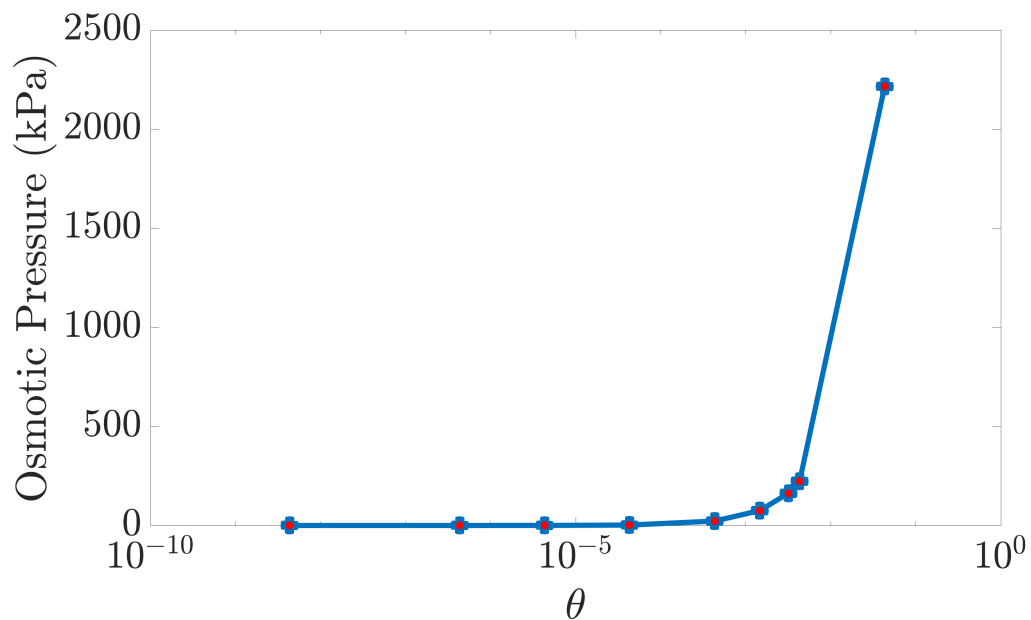


(b) Graph of osmotic pressure against the dimensionless group Ma^* , which shows how the osmotic pressure depends on the severity of polarisation.

Figure 5.4: Effect of Ma^* on (a) polarisation and (b) osmotic pressure.



(a) Graph of concentration polarisation (as a ratio of membrane concentration to inlet concentration) against the dimensionless group θ , which shows how polarisation depends on the ratio between osmotic pressure and the channel's pressure.



(b) Graph of osmotic pressure against the dimensionless group θ , which shows how the osmotic pressure depends on the ratio between osmotic pressure and the channel's pressure.

Figure 5.5: The effect of θ on (a) polarisation and (b) osmotic pressure.

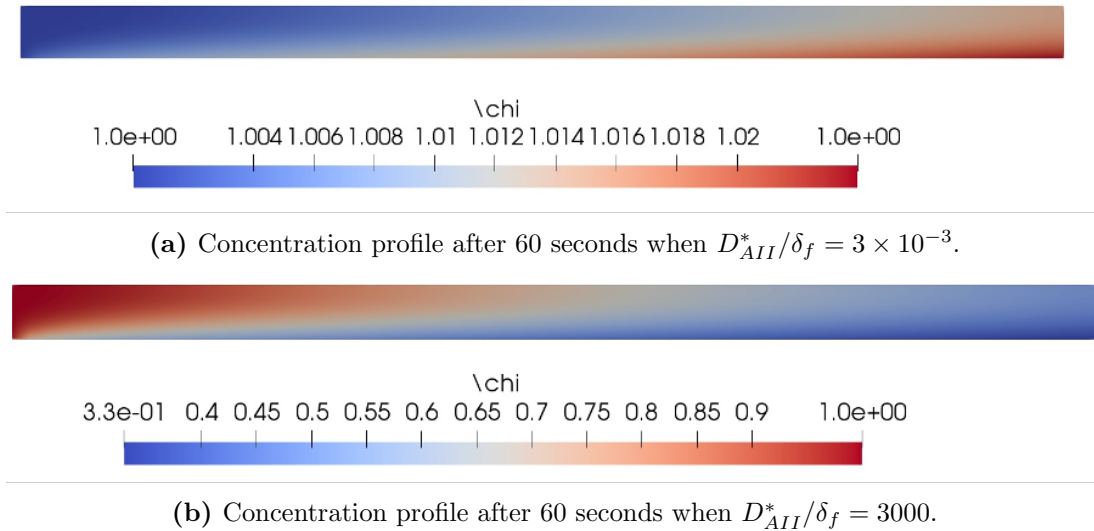
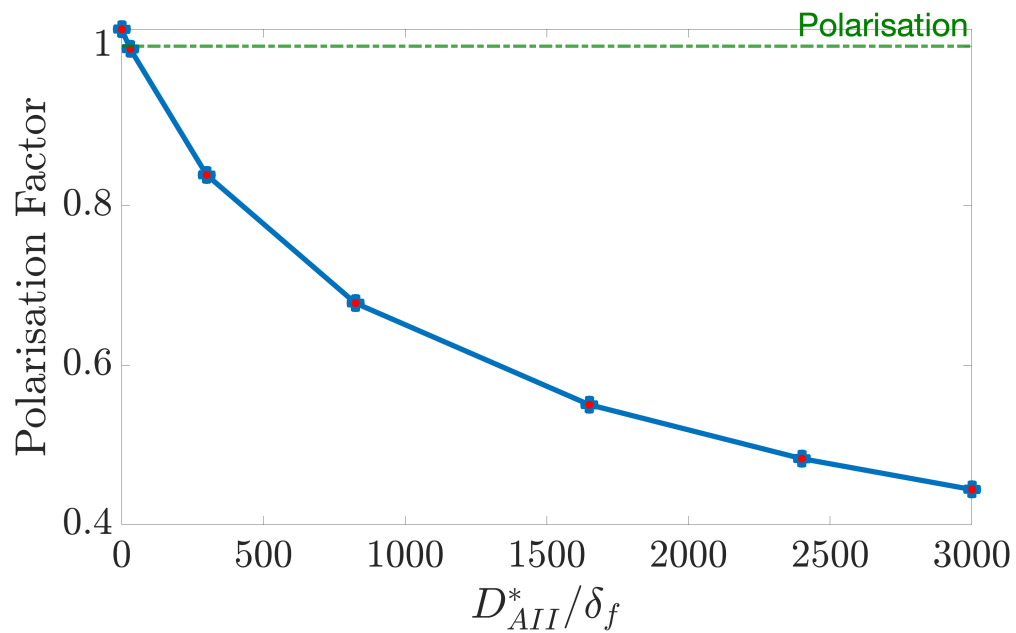


Figure 5.6: Concentration profile observed at 60 seconds for different values of D_{AII}^* .

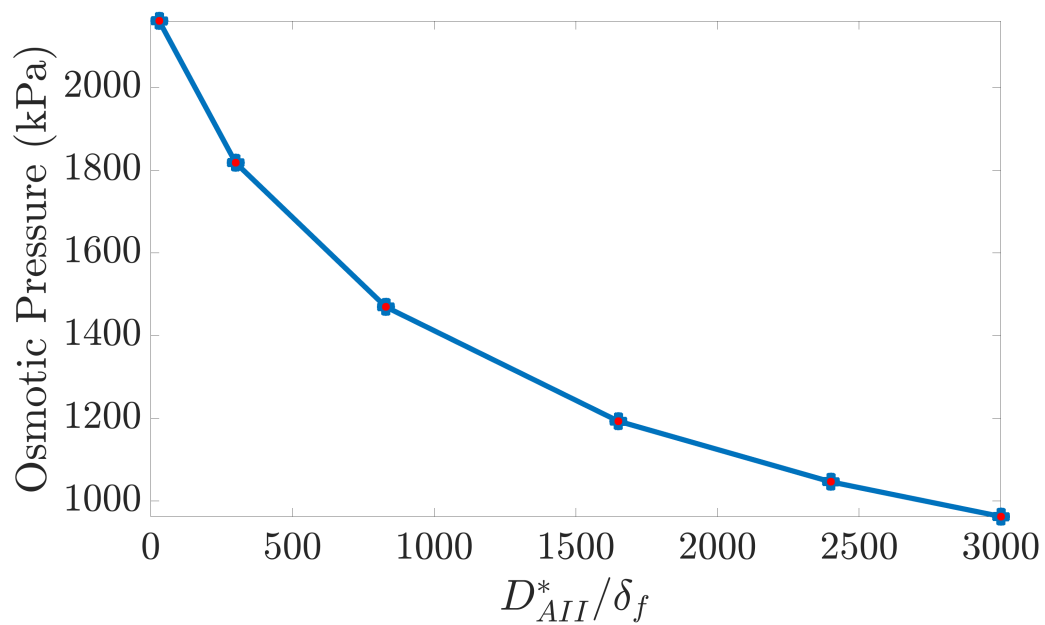
Impact of D_{AII}^* on concentration polarisation

D_{AII}^* provides an indication of which mass transport between precipitation and diffusion dominates. We can see from Figure 5.6 that D_{AII}^* dictates the concentration distribution at the membrane boundary layer. In addition, it is easily seen from Figure 5.7 that polarisation and osmotic pressure reduces with increasing D_{AII}^* .

We can associate an increasing D_{AII}^* to a faster reaction system however some care must be exercised in using such interpretations too literally. This is because one might initially think that the declining trend in Figures 5.7a and 5.7b is due to faster reaction at the membrane which reduces the membrane concentration. This is in fact not the case. Recall D_{AII}^* is the ratio between precipitation and diffusion so an increasing D_{AII}^* can also be attributed to decreasing diffusion. It is useful for our purposes here to consider the transport process as a two stage process: first diffusion of ions with a rate D occurs until the ions arrive at the membrane surface. This is followed by the precipitation reaction via rate constant k_r which forms mineral salts (scalants). For $D_{AII}^* \gg 1$, the rate of stage 1 (diffusion) limits the overall reaction as a result the quantity of solute transported to the membrane is low. The uneven concentration distribution and low membrane concentration in Figure 5.6b illustrates this. Figure 5.6a on the other hand shows the concentration profile of a much smaller D_{AII}^* ($D_{AII}^* \ll 1$) which represents a reaction-limited case. In this case, there is a large amount of diffusion towards the membrane and the concentration distribution is spread out quickly. However the overall process is inhibited by stage 2 (reaction) because the reaction is much slower. Consequently, we observe a build up of solutes at



(a) Graph of concentration polarisation (as a ratio of membrane concentration to inlet concentration) against the dimensionless group D_{AII}^*/δ_f , which shows how polarisation depends on Damköhler's number.



(b) Graph of osmotic pressure against the dimensionless group D_{AII}^*/δ_f , which shows how osmotic pressure depends on Damköhler's number.

Figure 5.7: The effect of D_{AII}^*/δ_f on (a) polarisation and (b) osmotic pressure.

the membrane (and polarisation) due to a slower reaction.

Impact of Pe on concentration polarisation

The Peclet number, Pe can be interpreted as the Reynolds number counterpart for mass transport - it is the ratio of the advective transport rate of the solute to its diffusive transport rate. We can see from Figure 5.8a that polarisation increases with increasing Pe . A similar trend can also be observed in Figure 5.8b for osmotic pressure. This is expected because Pe is proportional to the flow velocity, therefore as Pe increases the transport of solute towards the membrane increases which in turn increases polarisation and osmotic pressure.

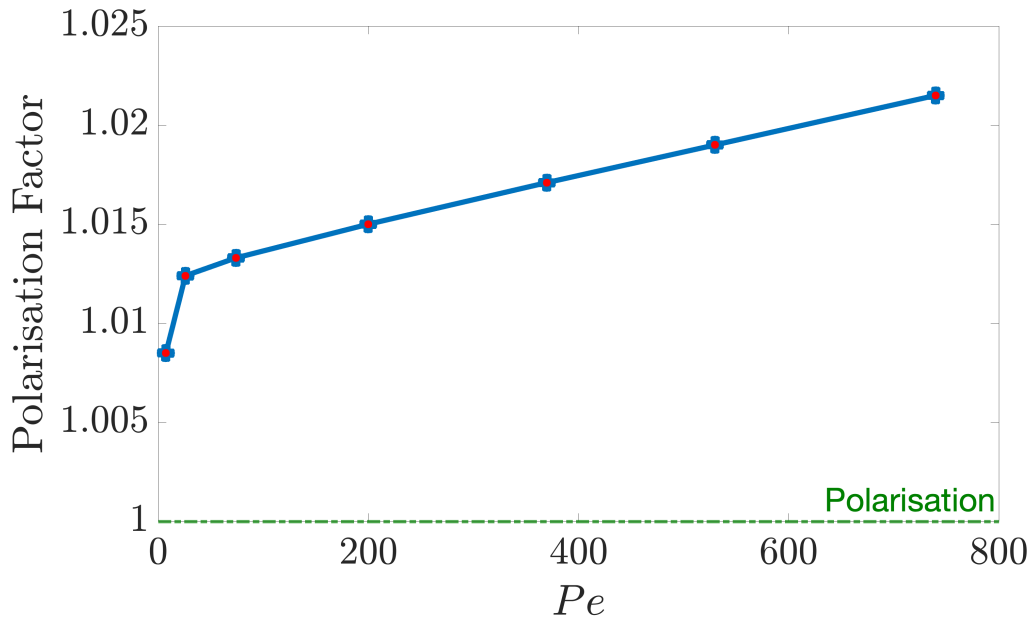
Impact of β on concentration polarisation

The quantity β provides an indication of which pressure gradient is dominant - it is the ratio between $P_p - P_{out}$ and $P_{in} - P_{out}$. To put this into perspective, a $|\beta|$ value of 1 implies that the pressure gradient across the feed channel (i.e. $P_{in} - P_{out}$) is identical to the pressure gradient between the feed channel and permeate channel (i.e. $P_p - P_{out}$). It is important to note that β is a negative value but we presented the results in terms of $|\beta|$ for convenience.

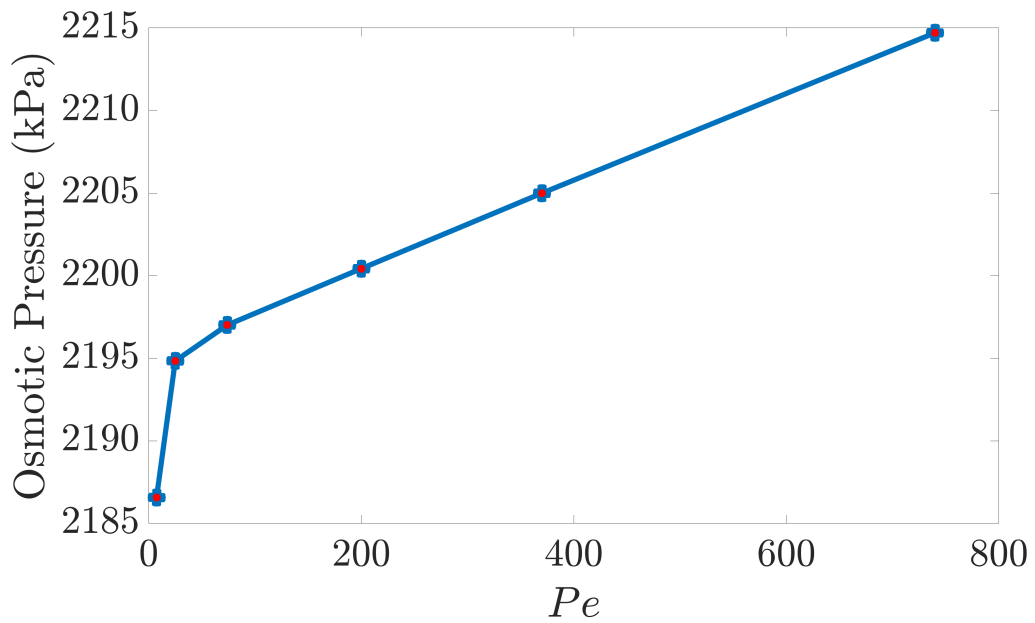
There are two remarks that should be made at this point. First, it seems reasonable to assume that there may be a competition between the pressure gradient across the feed channel (i.e. $P_{in} - P_{out}$) which pushes flow forward towards the outlet and the pressure gradient which drives flow in the perpendicular direction towards the membrane. Second we expect that $|\beta|$ would provide an indication of what to expect regarding the flow distribution.

Figure 5.9 indicates that polarisation and osmotic pressure increases with increasing $|\beta|$. Physically, a low β ($\beta \sim 1$) could be associated with a system with a pressurised permeate channel. We know that the driving force for fluid flow is the pressure difference, and the greater the pressure gradient, the greater the driving force. In this case the driving force for flow towards the membrane is low as $P_p - P_{out} \sim P_c$ hence the portion of the fluid that would have flowed perpendicularly towards the membrane is instead diverted towards the outlet thereby reducing polarisation. Physically the possible implication of this is that pressurised permeate channel may reduce polarisation but this could in turn increase operating cost and energy requirements of desalination systems.

As one might imagine $|\beta| > 1$ means that the pressure gradient between the feed channel and permeate channel is greater than the pressure gradient across the feed channel. In this case the permeate pressure plays a more significant

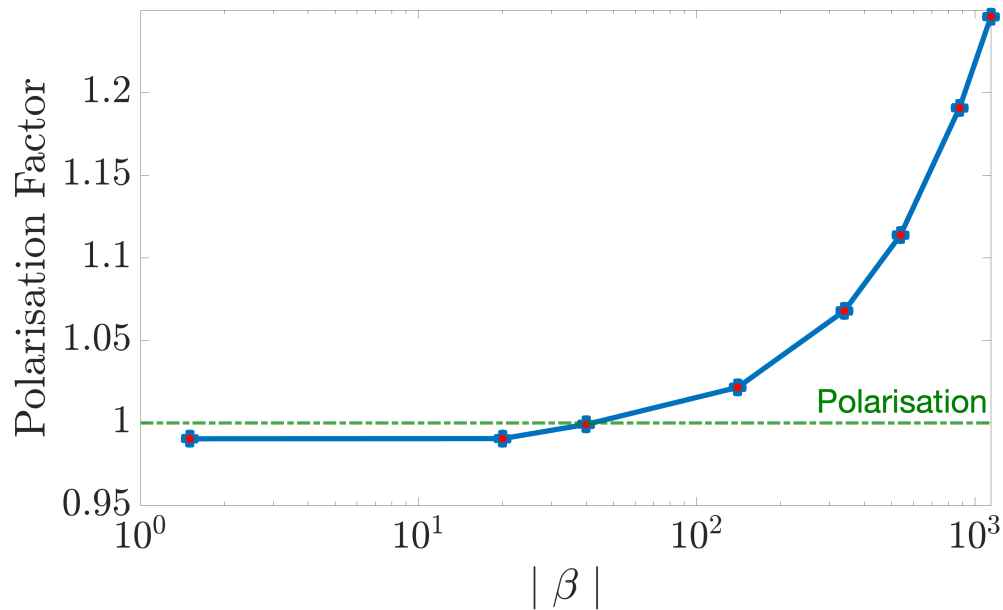


(a) Graph of concentration polarisation (as a ratio of membrane concentration to inlet concentration) against the dimensionless group Pe , which shows how polarisation depends on Peclet's number.

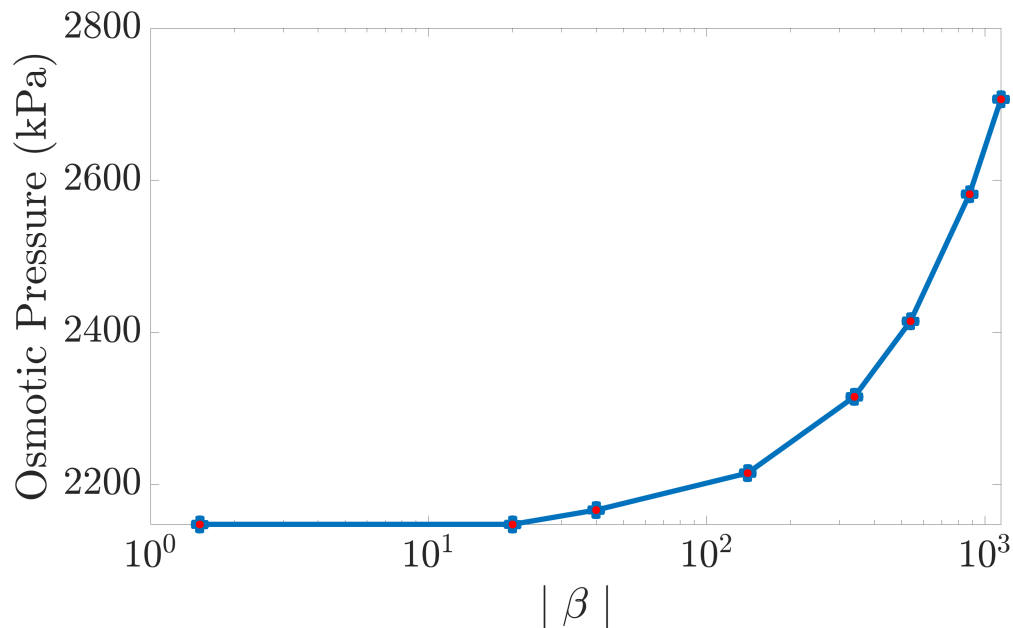


(b) Graph of osmotic pressure against the dimensionless group Pe , which shows how osmotic pressure depends on Peclet's number.

Figure 5.8: The effect of Pe on (a) polarisation and (b) osmotic pressure.



(a) Graph of concentration polarisation (as a ratio of membrane concentration to inlet concentration) against the dimensionless group $|\beta|$, which shows how polarisation depends on the ratio between the pressure gradient across the feed channel (i.e. $P_{in} - P_{out}$) and the pressure gradient between the feed channel and permeate channel (i.e. $P_p - P_{out}$).



(b) Graph of osmotic pressure (as a ratio of membrane concentration to inlet concentration) against the dimensionless group $|\beta|$, which shows how osmotic pressure depends on the ratio between the pressure gradient across the feed channel (i.e. $P_{in} - P_{out}$) and the pressure gradient between the feed channel and permeate channel (i.e. $P_p - P_{out}$).

Figure 5.9: The effect of β on (a) polarisation and (b) osmotic pressure.

role as the permeate pressure is around atmospheric pressure. Due to this lower pressure, it is plausible to expect more of the fluid to be diverted towards the membrane. The implications of this is that the magnitude of the permeate velocity increases therefore more fluid and solute is transported to the membrane increasing polarisation and osmotic pressure as seen in Figures 5.9a and 5.9b. It is worth noting that we believe extremely high $|\beta|$ is physically unrealistic due to the velocity field produced and low pressure requirements.

It appears our initial hypothesis was plausible. Indeed $|\beta|$ does provide an indication of what to expect regarding the flow distribution. We have seen that a lower $|\beta|$ (i.e., $|\beta| \sim 1$) inhibits polarisation because most of the flow is directed to the outlet. By contrast, increasing beta ($|\beta| > 1$) causes more of the fluid and solute to be transported to the membrane thereby increasing polarisation.

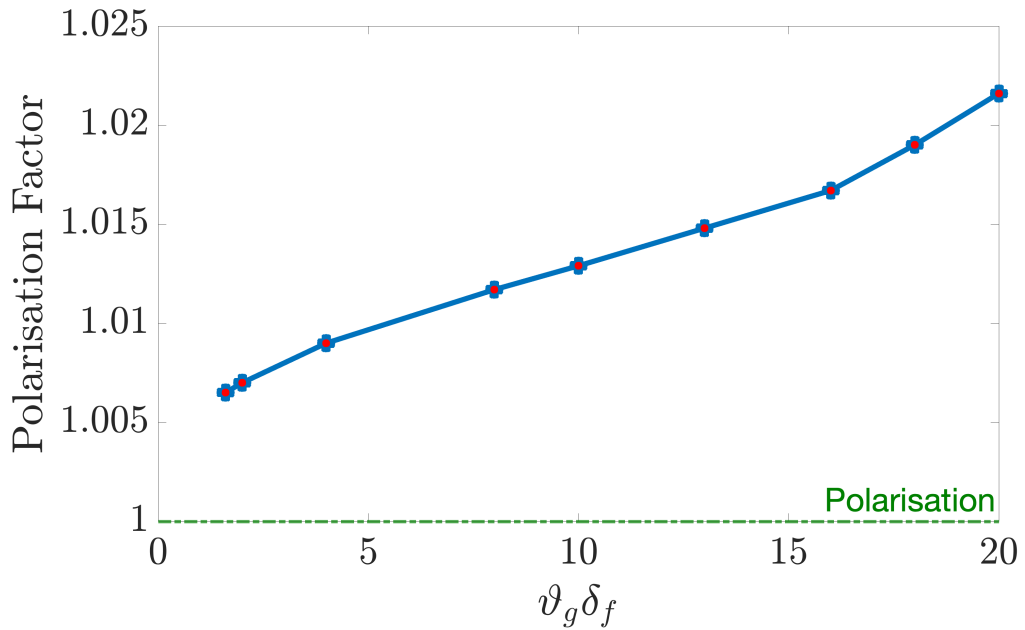
Impact of ϑ_g on concentration polarisation

The quantity ϑ_g is related to the geometry of the system; it is the ratio between the channel length and channel width. Figure 5.10 displays the variation of ϑ_g and the effect on polarisation and osmotic pressure. It is worth noting that the value of ϑ_g in the analysis was limited to cases where the length of the channel is significantly larger than the width (i.e $L \gg H$) because this is the case in reality. We can see that polarisation and osmotic pressure increases with increasing ϑ_g . This is expected as high ϑ_g can be associated with either a longer channel or a narrower channel. It is easily deduced that as the channel width reduces, the flow velocity increases which in turn increases polarisation because the amount of solute transported to the membrane increases.

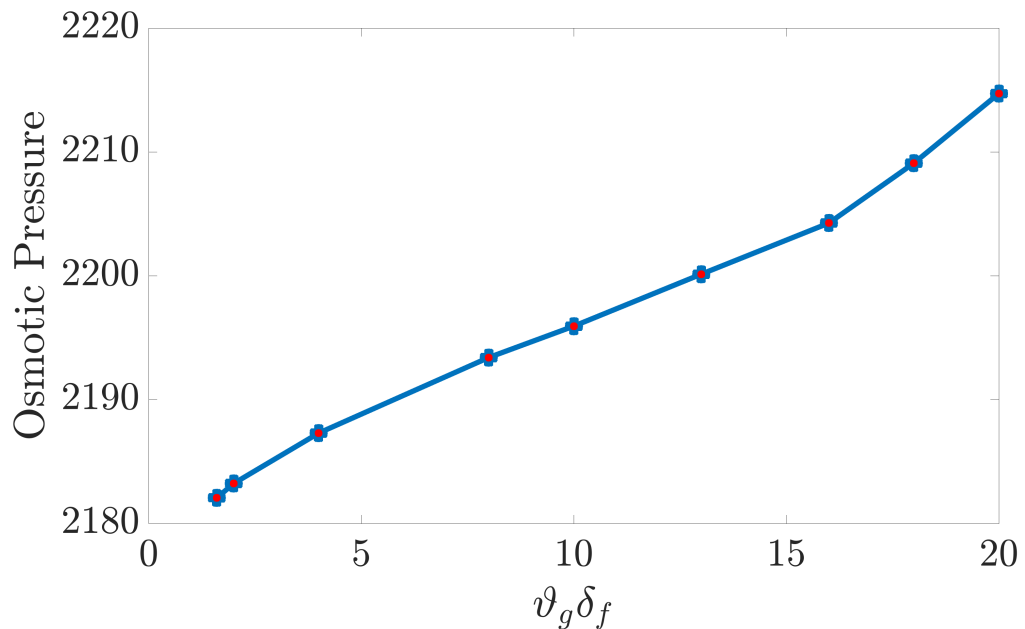
5.2.2 Recovery

One of the main objectives of desalination systems is to optimize and increase the overall feed water recovery. The overall recovery usually obtained in a spiral wound seawater desalination process is between 35 - 50 %. Although, the individual spiral wound membrane elements have a recovery of 5 - 15 %.

It is useful at this point to provide an indication of what we should expect regarding the nature of the results. We have seen in the previous section that the magnitude of the permeate velocity v determines the severity of polarisation. From a physical perspective, it seems plausible to also expect v to be one of the main factors affecting the recovery as a higher v means more fluid is being transported to the membrane. From a mathematical perspective,



(a) Graph of concentration polarisation (as a ratio of membrane concentration to inlet concentration) against the dimensionless group $\vartheta_g \delta_f$, which shows how polarisation depends on the ratio between the channel's length and channel's width.



(b) Graph of osmotic pressure against the dimensionless group $\vartheta_g \delta_f$, which shows how osmotic pressure depends on the ratio between the channel's length and channel's width.

Figure 5.10: The effect of $\vartheta_g \delta_f$ on (a) polarisation and (b) osmotic pressure.

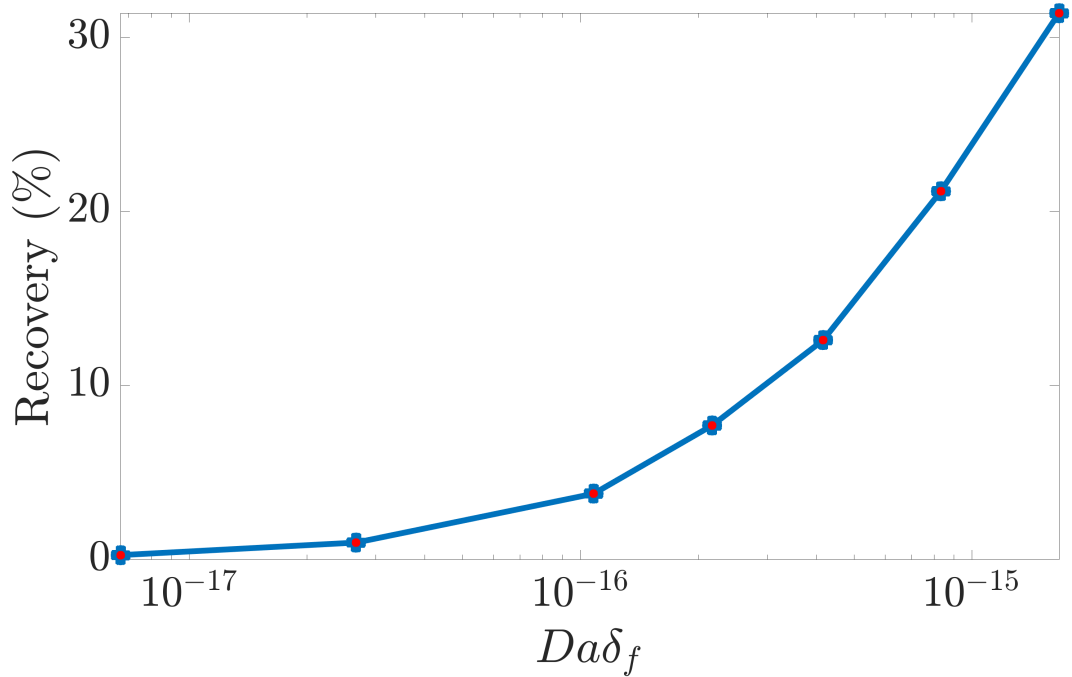


Figure 5.11: Graph of recovery as a percentage against the dimensionless group $Da\delta_f$, which shows how the recovery depends on Darcy's number.

equation (4.51) confirms this hypothesis as we can see that the recovery is proportional to the permeate velocity. In addition, (4.56) also indicates that 4 dimensionless groups ($\beta, \theta, Da, \vartheta_g$) directly influence recovery.

It should be noted that in the preceding subsection we established the basic concept needed to understanding all the model solutions. Hence we would be providing a less rigorous discuss hereon as it saves us from repeating the same information over several sections. With this in mind, we will now present the recovery results obtained for the given values in Table 5.1.

Impact of Da on recovery

Figure 5.11 depicts the variation of Da and the corresponding effect on recovery. We can see that the recovery increases with increasing Da . This is as we expected as a higher Da is associated with a high permeability system. The implies that the magnitude of the permeate velocity v (i.e normal component of the velocity) increases therefore more fluid is able to pass through the membrane. This in turn increases the fraction of the feed water that is recovered.

Impact of Re on recovery

Figure 5.12 displays the relationship between Re and recovery. It is apparent from this figure that at very low Reynolds number ($Re \ll 1$), Re has a minimal effect

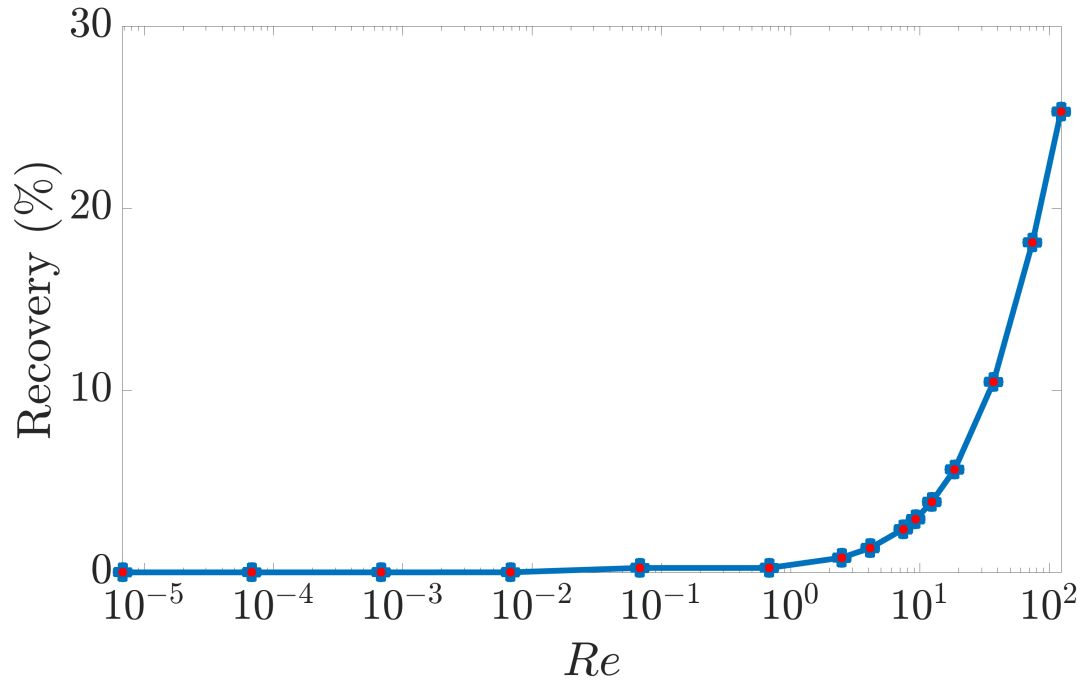


Figure 5.12: Graph of recovery as a percentage against the dimensionless group Re , which shows how the recovery depends on Reynold's number.

on recovery. However as the flow approaches the laminar regime ($Re \gg 1$) we start to see a significant effect on recovery. This is because the magnitude of the permeate velocity increases with increasing Re . As a result, the quantity of fluid transported towards the membrane increases which in turn increases recovery as seen in Figure 5.12.

Impact of Ma^* on recovery

Figure 5.13 shows the variation of Ma^* and the corresponding effect on recovery. It is clear that recovery reduces with increasing Ma^* . Recall Ma^* gives an indication of how quickly precipitation occurs and its severity. Therefore, an increase in Ma^* implies that precipitation is occurring at a fast rate. This leads to two related consequences. First, the porosity of the membrane decreases as the solutes are consumed by the reaction resulting in a decrease in membrane permeability. This reduction in permeability induces a flow resistance at the membrane surface so the membrane retains most of the fluid on the feed side, reducing the fraction of water recovery as seen in Figure 5.13.

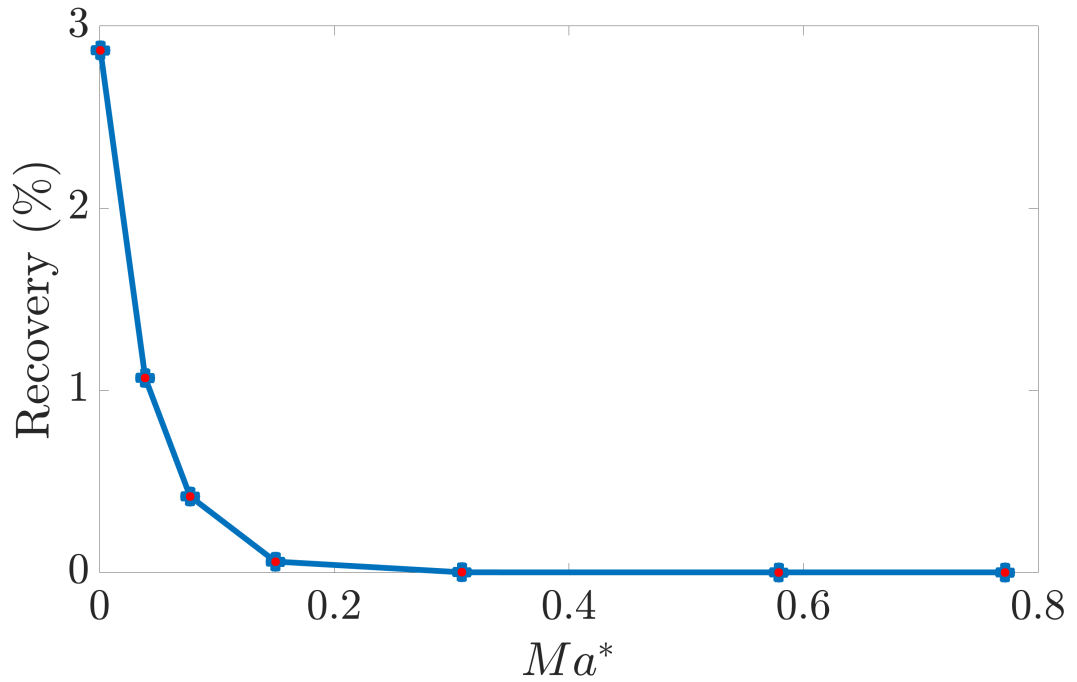


Figure 5.13: Graph of recovery as a percentage against the dimensionless group Ma^* , which shows how the recovery depends on how quickly precipitation occurs.

Impact of θ on recovery

Recall θ measures the relation between the osmotic pressure and the channel's pressure. Values greater than one means that osmotic pressure is greater than the channel's pressure. Reverse osmosis desalination is based on the premise of applying a pressure greater than the osmotic pressure. Therefore θ values greater than 1 are undesirable as flow would then move in the opposite direction, that is flow would naturally move away from the membrane towards the concentrated fluid. Consequently, the results presented in Figure 5.14 are for θ values lower than 1.

We first observe that θ has a little effect of recovery. We can see from Figure 5.14 that increasing θ by 6 orders of magnitude reduces the recovery by only a factor of ~ 1.03 . Although its effect on recovery is minimal, it is still useful to understand why θ generally results in a decrease in recovery. We believe the decreasing trend observed in Figure 5.14 could be attributed to the decline in the magnitude of the transverse velocity which is likely due to the increase in osmotic pressure. We already know from preceding sections that a lower transverse velocity reduces the quantity of fluid transported towards membrane which in turn reduces recovery.

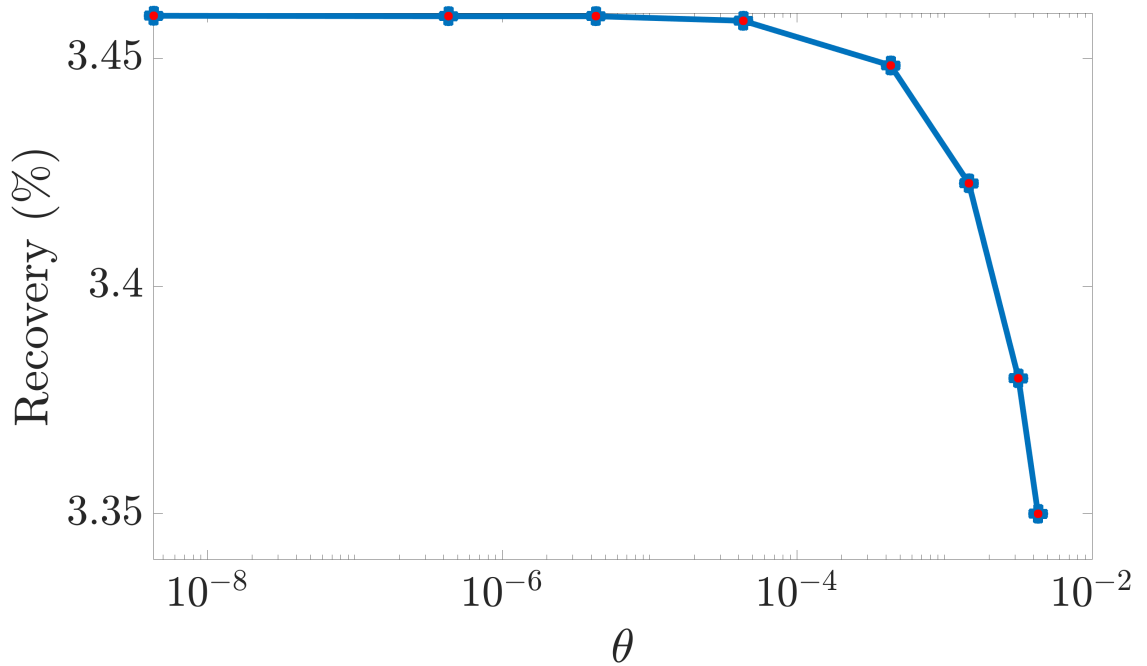


Figure 5.14: Graph of recovery as a percentage against the dimensionless group θ , which shows how the recovery depends on the relation between the osmotic pressure and the channel's pressure.

Impact of D_{AII}^* on recovery

Figure 5.15 reveals that recovery increases with increasing D_{AII}^* . We remind the reader that $D_{AII}^* \gg 1$ is attributed to a diffusion-limited system. In this case, the fluid is transported at streamwise velocity v however due to the low diffusion, the solute transport is much slower. One might question why we then see an increase in recovery. The answer is straightforward; recall recovery is a fluid dynamic property so increasing D_{AII}^* reduces the membrane concentration (and in turn polarisation and scaling) but the flux of water is unaffected.

Impact of Pe on recovery

Recall the Peclet number, Pe is a measure of the relative importance of solute advection versus diffusion, where a large number indicates an advectively dominated distribution, and a small number indicates a diffusive flow. Figure 5.16 shows the variation of Pe and the corresponding effect on recovery. It is clear that Pe has a minimal effect on recovery. This is probably due to the range considered in Figure 5.16. We expect that for substantially high velocity flows, that is $Pe > 5000$, there would be a significant increase in fluid transport towards the membrane which will in turn increase recovery (and potentially polarisation).

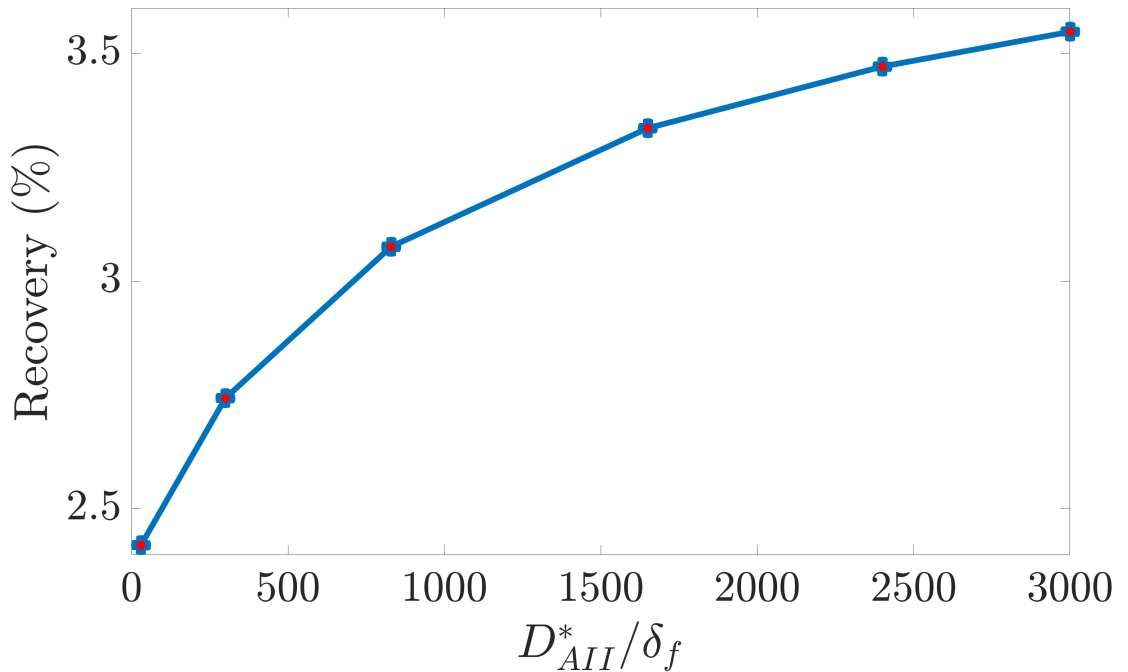


Figure 5.15: Graph of recovery as a percentage against the dimensionless group D_{AII}^*/δ_f , which shows how the recovery depends on Damköhler number.

It is of interest at this point to note that under high Peclet conditions the code breaks down due to the extremely high flow velocities which translate to turbulent flow. The model is only suitable for Darcy flow in a laminar regime.

Impact of β on recovery

We remind the reader again that β is the ratio between $P_p - P_{out}$ and P_c (recall $P_c = P_{in} - P_{out}$). Figure 5.17 indicates that recovery increases with increasing β . We already know from the previous section that low β translates to a system with a pressurised permeate channel. We expect a lower recovery in this case because the driving force for flow towards the membrane is lower. This might explain the initial decline seen in Figure 5.17. As β increases, the permeate pressure plays a more significant role because it is substantially lower thereby increasing the pressure gradient which drives flow in the perpendicular direction towards the membrane. This in turn increases the flux towards the membrane. However we again stress that extremely high β is physically unrealistic due to the low pressure requirements.

Impact of ϑ_g on recovery

ϑ_g compares the length of the channel to the width. Figure 5.18 shows the variation of ϑ_g and the corresponding effect on recovery. It is clear that recovery

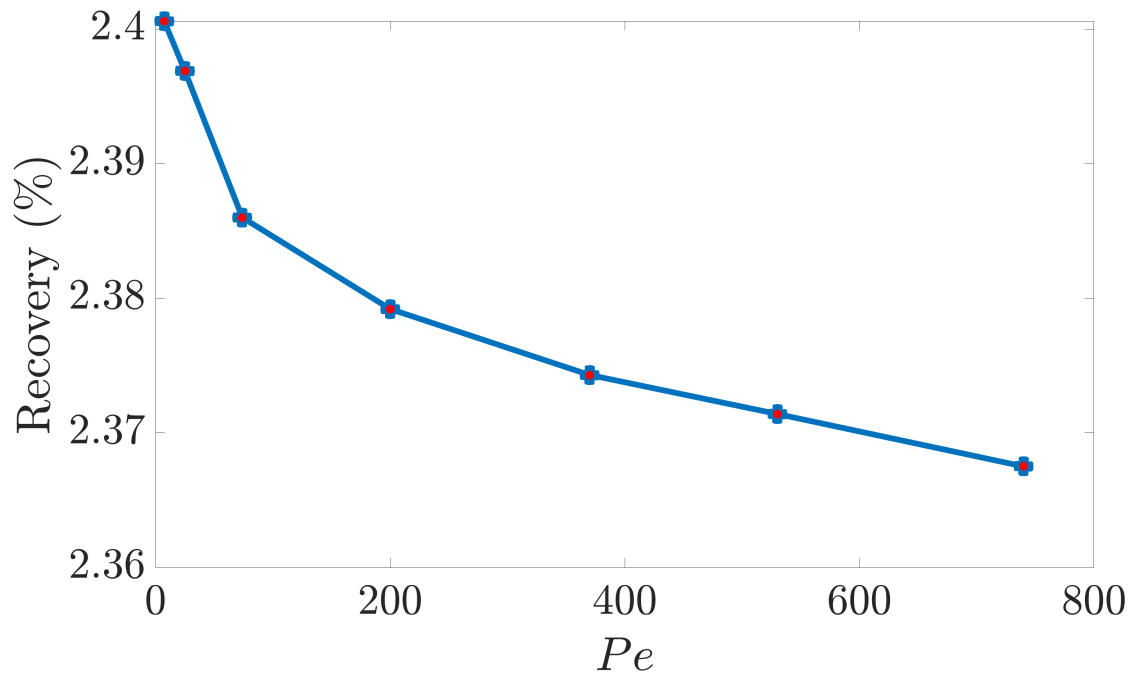


Figure 5.16: Graph of recovery as a percentage against the dimensionless group Pe , which shows how the recovery depends on Peclet number.

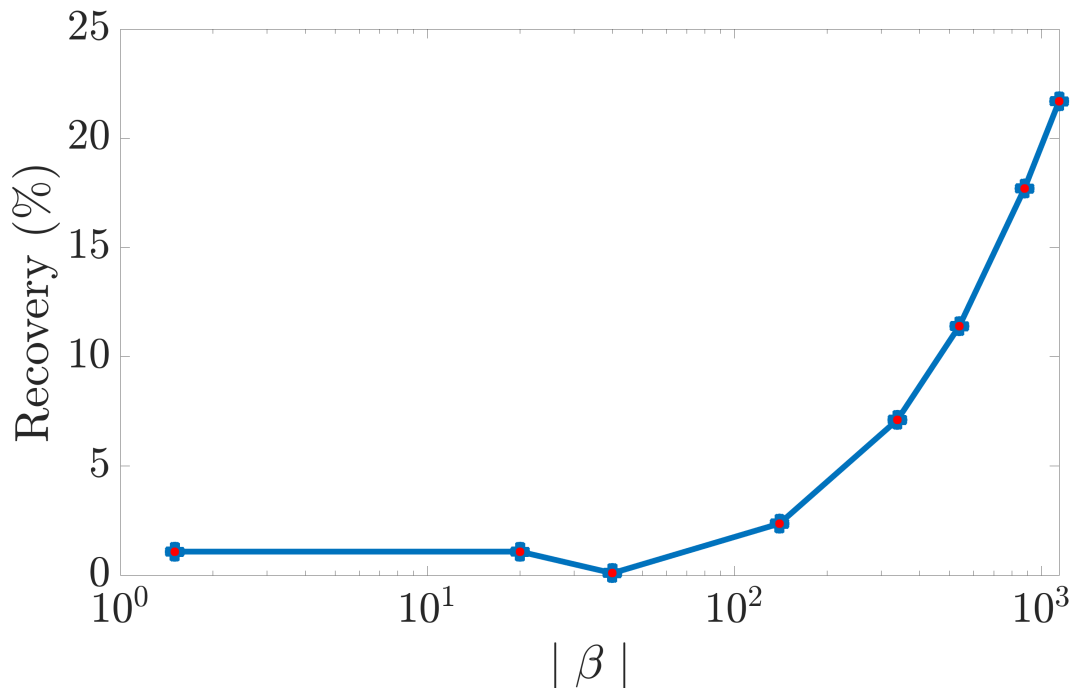


Figure 5.17: Graph of recovery as a percentage against the dimensionless group $|\beta|$, which shows how recovery depends on the ratio between the pressure gradient across the feed channel (i.e. $P_{in} - P_{out}$) and the pressure gradient between the feed channel and permeate channel (i.e. $P_p - P_{out}$).

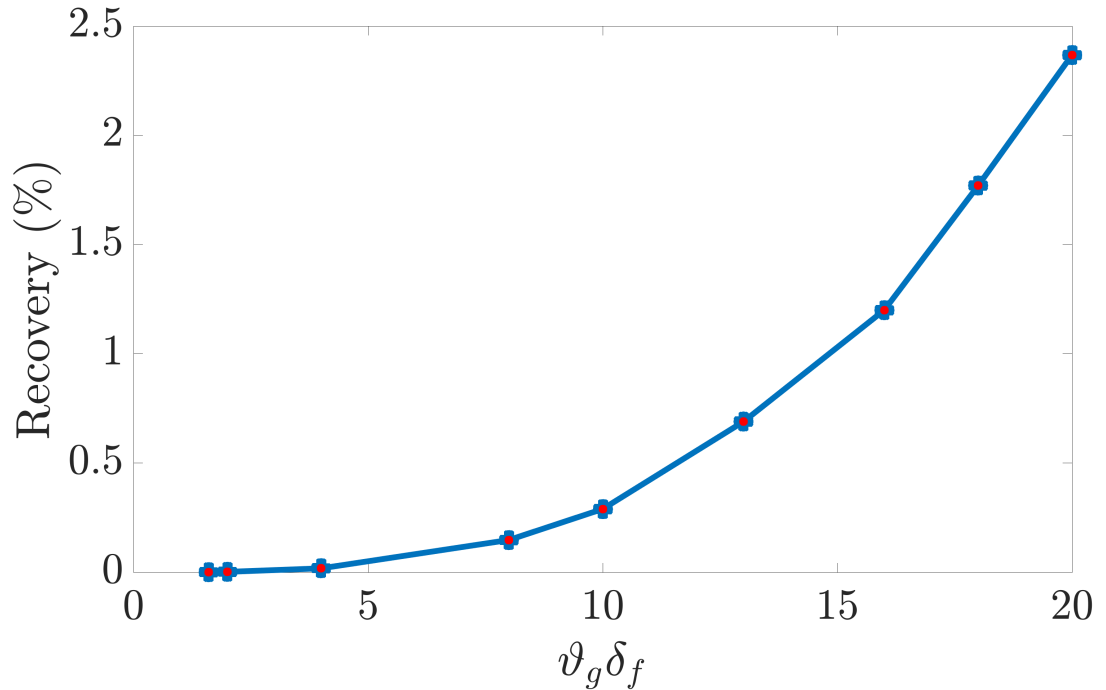


Figure 5.18: Graph of recovery as a percentage against the dimensionless group $\vartheta_g \delta_f$, which shows how the recovery depends on the ratio between the channel's length and width.

increases with increasing ϑ_g . This is expected because we know from equation (4.56) that ϑ_g is directly proportional to the recovery. Even from a physical perspective, this seems reasonable and we would explain why. Increasing ϑ_g can be associated with either an increase in the channel length or a decrease in the channel width. It is easier for our purposes here to consider the former because intuitively one can understand that increasing the membrane length increases the area available for flow which in turn leads to a higher recovery.

5.2.3 Porosity

Recall part of the objective of this investigation was to conduct qualitative and quantitative analysis on sub-processes such as fluid dynamics, mass transport and scaling which impact the fraction of clean water that can be recovered. In preceding sections we have seen the quantities and dimensionless groups that contribute most to recovery and polarisation. Here, we investigate the effects of various dimensionless groups on the porosity. This is because the porosity is the variable that gives us an indication of the extent of scaling/precipitation. We expect that the mineral salts produced from the precipitation reaction will change the void space (and pores) available on the membrane.

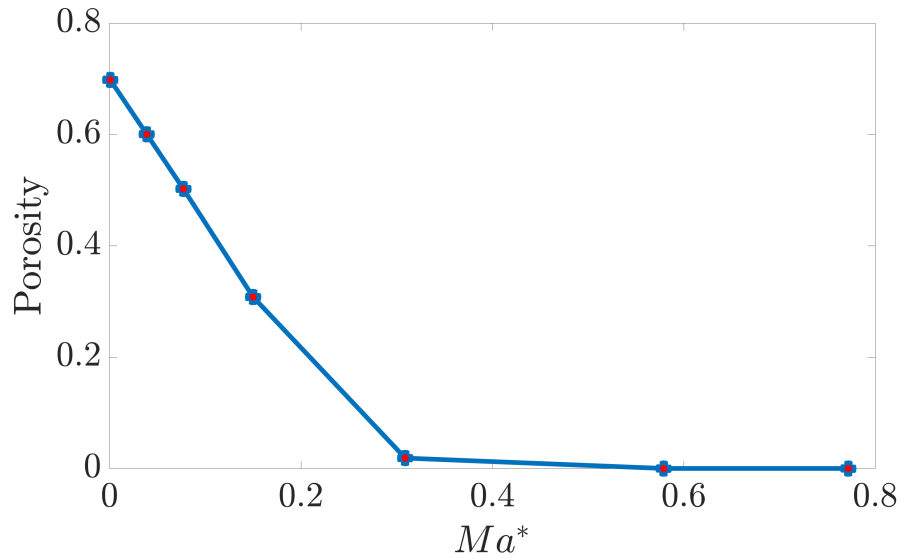


Figure 5.19: Graph of porosity (as a pore fraction of the membrane) against the dimensionless group Ma^* , which shows how the porosity depends on the severity of precipitation.

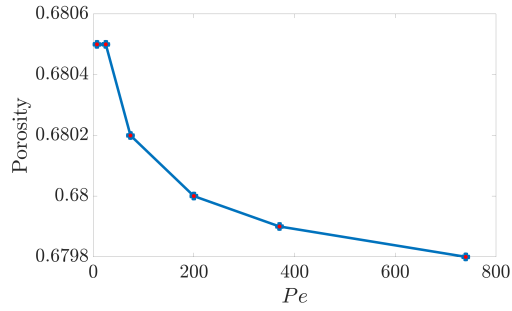
Dimensionless groups with significant effect on porosity

During the analysis of the result, it became clear that Ma^* is the only dimensionless group that has a significant effect on porosity and scaling as seen in Figure 5.19. This is understandable because Ma^* directly controls the porosity change which measures the degree of scaling.

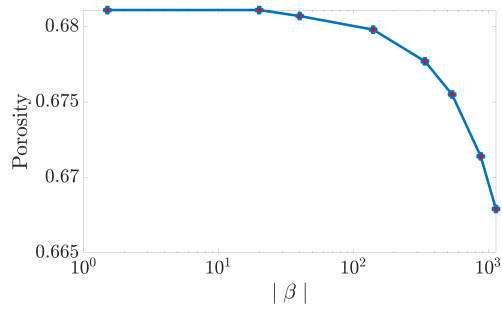
The other dimensionless groups however have little or no effect on porosity and as such we will only consider them briefly. We have included them here simply for the sake of completeness. For simplicity, we have grouped the results on the basis of the trend they have in common. For instance, Figure 5.20 presents the set of dimensionless groups that lead to a minimal decrease in porosity whereas Figure 5.21 displays the dimensionless groups which lead to a minimal increase in porosity.

Dimensionless groups that minimally reduce porosity

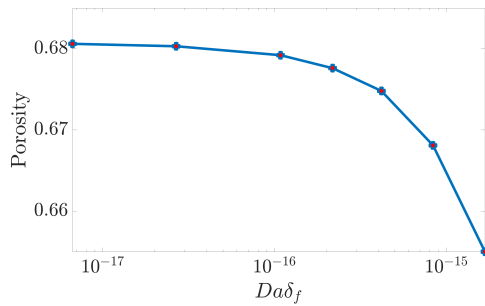
Figures 5.20a, 5.20b, 5.20c and 5.20d shows that porosity slightly decreases as the value of the corresponding dimensionless groups increases. This decrease can be explained by the fact that Pe, Da, Re & β are proportional to the flow velocity, therefore as the value of these dimensionless groups increases the transport of solute towards the membrane increases which in turn increases the concentration available for precipitation. This also increases the precipitation rate which results in the decrease in porosity observed in Figures 5.20a, 5.20b, 5.20c, and 5.20d.



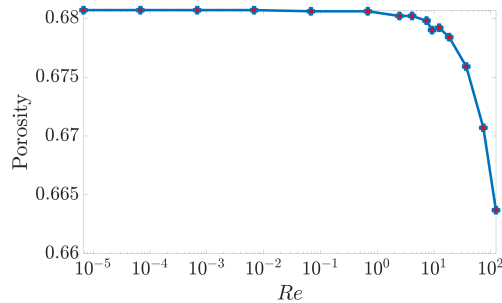
(a) Graph of porosity (as a pore fraction of the membrane) against the dimensionless group Pe , which shows how the porosity depends on Peclet number.



(b) Graph of porosity (as a pore fraction of the membrane) against the dimensionless group $|\beta|$, which shows how the porosity depends on the pressure gradient across the feed channel and the pressure gradient between the feed channel and permeate channel.



(c) Graph of porosity (as a pore fraction of the membrane) against the dimensionless group $Da\delta_f$, which shows how the porosity depends on Darcy number.



(d) Graph of porosity (as a pore fraction of the membrane) against the dimensionless group Re , which shows how the porosity depends on Reynolds number.

Figure 5.20: Increasing these dimensionless groups ($Pe, |\beta|, Da, Re$) results in a minimal decrease in porosity.

Dimensionless groups that minimally increase porosity

Figures 5.21a and 5.21b, reveals that porosity mildly increases with increasing D_{AII}^* . This is most likely because the membrane concentrations reduces with increasing D_{AII}^* as shown in Figure 5.7. This in turn limits the solutes available for the precipitation reaction which reduces the precipitation rate. A possible explanation for the relationship between ϑ_g and porosity may associated with the time it takes for mineral scalants to fill a longer membrane (which is associated with increasing ϑ_g). However, with a shorter membrane it takes a shorter time for scales to completely cover the membrane surface as such the global porosity decreases faster.

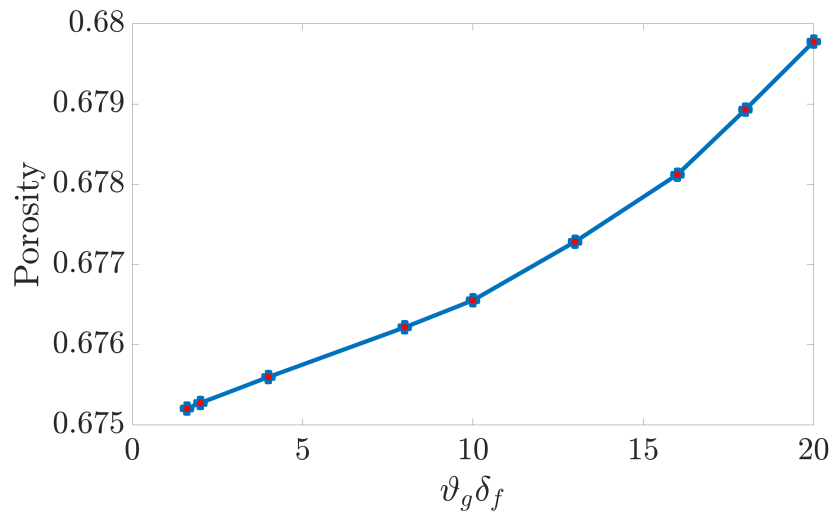
Dimensionless groups that do not impact porosity.

We already know from preceding sections that increasing θ reduces the magnitude of the transverse velocity which in turn results in a lower quantity of solute at the membrane. Hence we would expect the porosity to reduce with increasing θ but instead it appears that θ has no effect on porosity as shown in Figure 5.22. This might probably be because of the value range considered however as we have mentioned previously θ values greater than 1 are unrealistic as flow would then move in the opposite direction, away from the membrane which is against the premise of reverse osmosis.

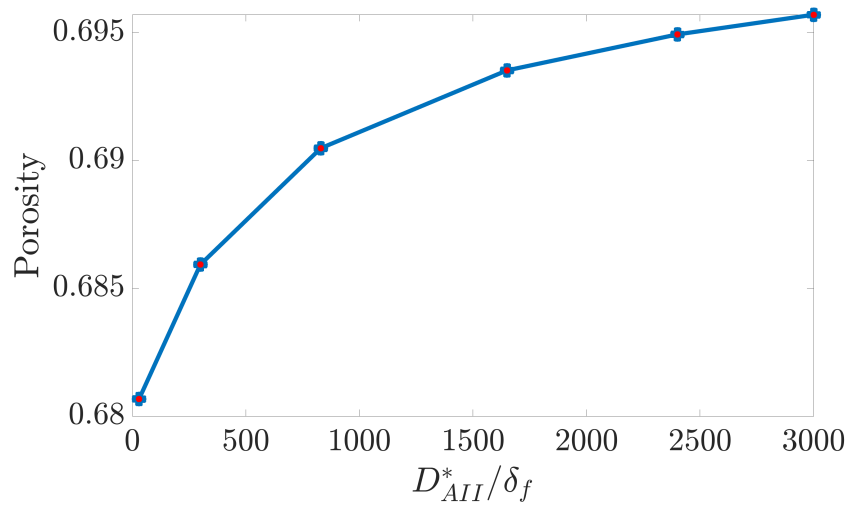
In this section we have seen how the different dimensionless group impacts fluid dynamics (recovery, flux), mass transport processes and the state of the membrane. At this point, the question that arises is “what happens in the presence of more salt ions i.e. co-precipitation”. This will be our task in the next section.

5.3 Co-precipitation

In an effort to understand the relative influence of each of the dimensionless groups we considered a simplified bimolecular reaction scheme and analysed the results. This simplification provided significant insights on the model solution. Now that we have accumulated sufficient information/understanding we will return to our initial reaction scheme with several ions and co-precipitation. We again remind the reader that the results presented here are based on the simplified co-precipitation membrane boundary condition presented in (4.119) and (4.120). These boundary conditions were constructed using the concept that the flux of chemical species entering the membrane boundary, Γ_m (defined



(a) Graph of porosity (as a pore fraction of the membrane) against the dimensionless group $\vartheta_g \delta_f$, which shows how the porosity depends on the ratio of the channel's length to the channel's width



(b) Graph of porosity (as a pore fraction of the membrane) against the dimensionless group D_{AII}^* / δ_f which shows how the porosity depends on Damköhler number.

Figure 5.21: Increasing these dimensionless groups ($\vartheta_g \delta_f, D_{AII}^* / \delta_f$) results in a minimal increase in porosity

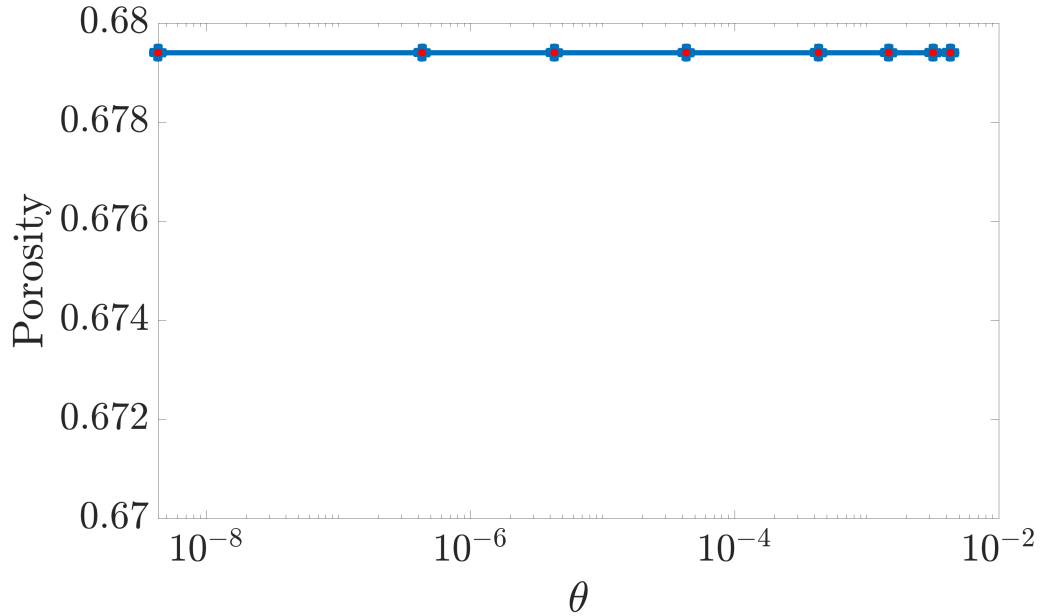
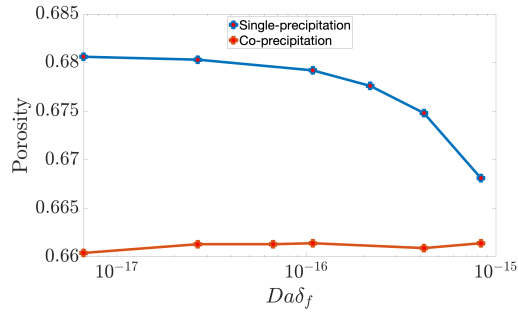


Figure 5.22: Graph of porosity (as a pore fraction of the membrane) against the dimensionless group θ , which shows that the ratio between the osmotic pressure and the channel's pressure has no effect on porosity

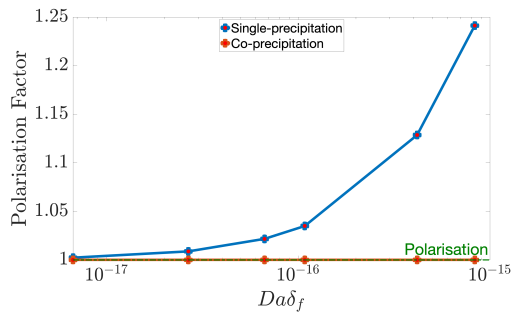
as the sum of a convective flux and diffusive flux) is consumed by the precipitation reaction.

The main purpose of this section is to examine and compare the changing nature of solutions when we move from a single-solute systems to a multi-component system (i.e co-precipitation). At the same time, it is hoped that this would enhance our understanding of the complex precipitation mechanisms that occur in desalination plants as these usually contains several interacting salt ions.

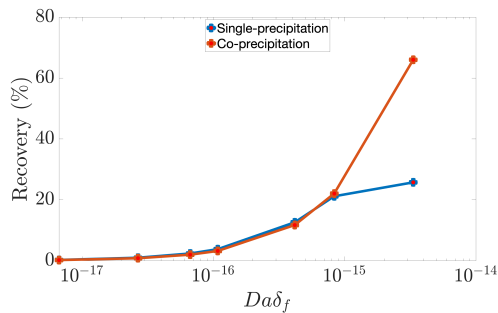
It is of interest at this point to provide an indication of what we should expect regarding the nature of the co-precipitation results. Based on our understanding of the dimensionless groups, we expect the presence of more salt ions to have a direct effect on Ma , D_A and θ as these groups are dependent on salt concentration. This can be confirmed by quickly inspecting Table 4.3 in Chapter 4. However we emphasize that co-precipitation is effected by combinations of salt ions. As a consequence, it would influence parameters where concentration arithmetic is required; that is, sum of concentrations. Hence we expect co-precipitation to have the greatest effect on recovery and porosity as these are dependent on the sum of salt concentration as shown in (4.129) and (4.130). With these basic ideas in mind, we will now present the co-precipitation below.



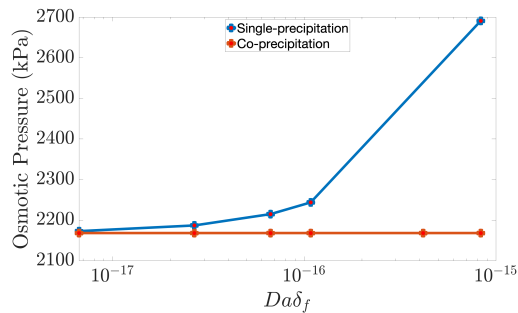
(a) Graph of porosity (as a pore fraction of the membrane) against the dimensionless group $Da\delta_f$, which shows the effect of co-precipitation on porosity when varying Darcy's number.



(b) Graph of concentration polarisation (as a ratio of membrane concentration to inlet concentration) against the dimensionless group $Da\delta_f$, which shows the effect of co-precipitation on polarisation when varying Darcy's number.



(c) Graph of recovery as a percentage against the dimensionless group $Da\delta_f$, which shows the effect of co-precipitation on recovery when varying Darcy's number.



(d) Graph of osmotic pressure against the dimensionless group $Da\delta_f$, which shows the effect of co-precipitation on osmotic pressure when varying Darcy's number.

Figure 5.23: Comparison between single-precipitation and co-precipitation at different values of $Da\delta_f$.

5.3.1 Effect of Co-precipitation on Da & Re

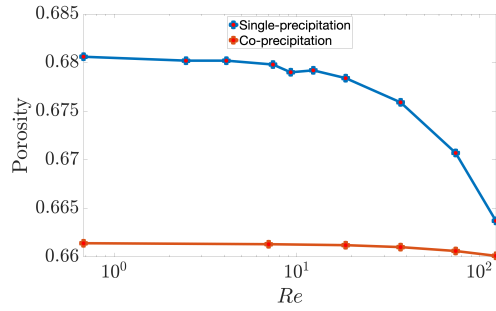
We will see as we proceed that the computed results for Da and Re are in many respects quite similar. Therefore, we would discuss the results obtained for both groups in this subsection to avoid repeating the same information later on. Figure 5.23 displays the variation of Da and the effect on porosity, polarisation, recovery and osmotic pressure. Figure 5.24 shows the corresponding figures for Re . It appears that a higher recovery is achieved with co-precipitation. This is counter-intuitive as one would expect that the presence of more salt ions will lead to clogging of the membrane which would in turn impact recovery. However, once we consider this result in the context of the other processes at work, particularly osmotic pressure and polarisation the reason for this trend becomes apparent.

It is easily seen from Figures 5.23d and 5.24d that for co-precipitation there is no change in osmotic pressure. This implies that the membrane concentration is uniform with the bulk concentration; Figures 5.23b and 5.24b also confirms this. This may explain why we see an increase in recovery for co-precipitation in Figures 5.23c and 5.24c. Recall that in subsection 5.2.1 we established that a lower osmotic pressure increases the magnitude of the transverse velocity giving rise to a high permeate velocity which in turn increases recovery.

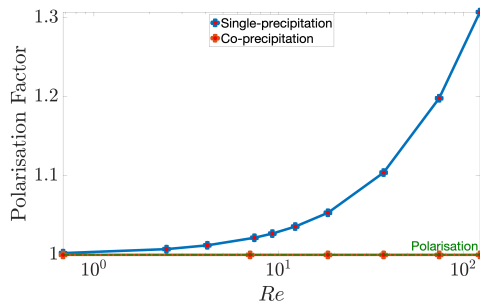
It should be observed from Figures 5.23a and 5.24a that co-precipitation reduces the porosity further than single-precipitation. However it is important to also recognise that varying Da and Re by 2 orders of magnitude appears to have a minimal effect on porosity. We observe a more prominent decline in porosity, in the case of single-precipitation, albeit small. We believe this is again related to the polarisation and osmotic pressure. For single-precipitation, we see that there is an increase in membrane concentration. This in turn increases the concentration available for precipitation, thereby reducing porosity. However for co-precipitation, the solutes concentration is uniform. This reduces the reaction rate which is why we see a nearly steady porosity in Figure 5.23a and 5.24a.

5.3.2 Effect of Co-precipitation on Ma

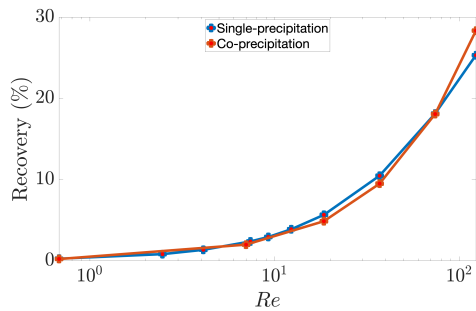
Figure 5.25 shows the variation of Ma and the corresponding effect on porosity, polarisation, recovery and osmotic pressure. Again we can see here that co-precipitation acts to maintain a uniform concentration (inferred from Figures 5.25d and 5.25b). As expected, co-precipitation has a noticeable effect on both porosity and recovery. We observe steeper decline in Figures 5.25a and 5.25c in comparison with single precipitation. The trends observed are consistent with what we expect from the dimensionless relations presented in (4.129) and (4.130).



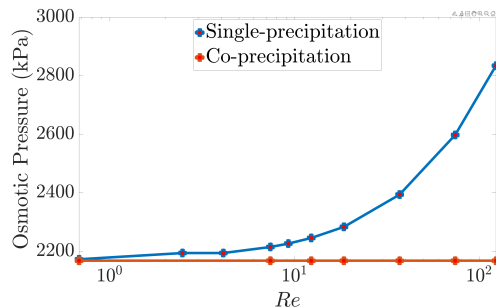
(a) Graph of porosity (as a pore fraction of the membrane) against the dimensionless group Re , which shows the effect of co-precipitation on porosity when varying Reynold's number.



(b) Graph of concentration polarisation (as a ratio of membrane concentration to inlet concentration) against the dimensionless group Re , which shows the effect of co-precipitation on polarisation when varying Reynold's number.



(c) Graph of recovery as a percentage against the dimensionless group Re , which shows the effect of co-precipitation on recovery when varying Reynold's number.



(d) Graph of osmotic pressure against the dimensionless group Re , which shows the effect of co-precipitation on osmotic pressure when varying Reynold's number.

Figure 5.24: Comparison between single-precipitation and co-precipitation at different values of Re .

As we pointed out earlier, the porosity and recovery are proportional to the sum of salt concentrations. That is, increasing the number of salt components present in the system will result in a decrease in porosity and recovery.

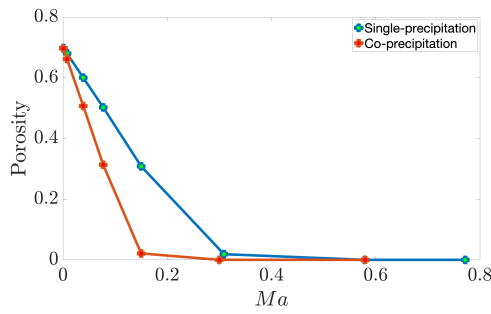
5.3.3 Effect of Co-precipitation on θ

We note that for θ , the trends for single precipitation and co-precipitation are generally the same except in the case of polarisation (see Figure 5.26). Hence, we would not offer explanations for the trends here as we have already discussed it in section 5.2. Instead we will focus on why porosity and recovery is lower for co-precipitation. The observed difference in porosity and recovery in Figures 5.26a and 5.26c could be attributed to the presence of more ions. This increases the reaction rate which reduces porosity and in turn the membrane permeability. Consequently, the magnitude of the permeate velocity reduces giving rise to a lower recovery.

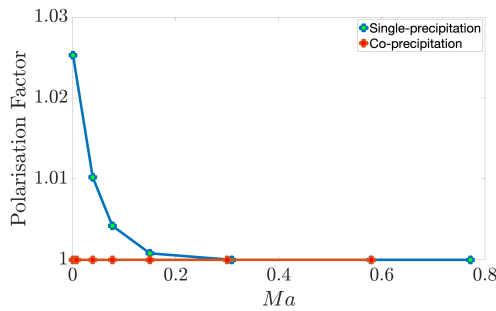
We do not observe any polarisation because the solutes that would have otherwise accumulated at the membrane surface have been consumed by the precipitation reaction (inferred from the porosity). We again note that the results obtained for osmotic pressure matches that for single precipitation which have already been discussed in section 5.2.1. Hence, we refer the reader to section 5.2.1 for an explanation for the trend observed in Figure 5.26d.

5.3.4 Effect of Co-precipitation on D_A

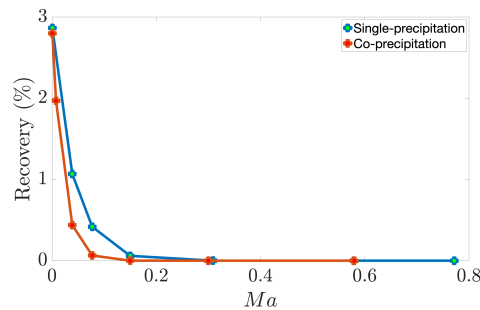
What is striking about the figures in Figure 5.27 is that we observe complete opposite trends in each case. However a common feature all of these figures share is that when $D_A \ll 1$ no change occurs. Therefore we can restrict our attention to $D_A \gg 1$. Recall that in subsection 5.2.1 we noted that $D_A \gg 1$ represents a diffusion-limited case where the reaction is fast but diffusion limits the overall reaction. We have also already established that with co-precipitation, the reaction rate is greater due to the presence of more salt ions. Therefore it is not surprising that increasing D_A increases the reaction rate even further which increases precipitation.



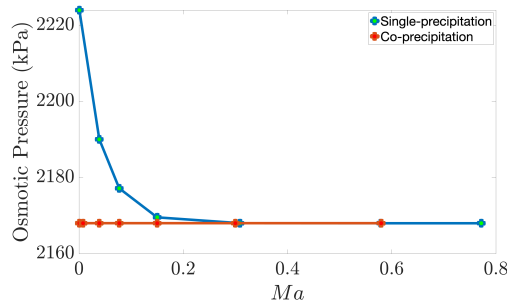
(a) Graph of porosity (as a pore fraction of the membrane) against the dimensionless group Ma , which shows the effect of co-precipitation on porosity.



(b) Graph of concentration polarisation (as a ratio of membrane concentration to inlet concentration) against the dimensionless group Ma , which shows the effect of co-precipitation on polarisation.

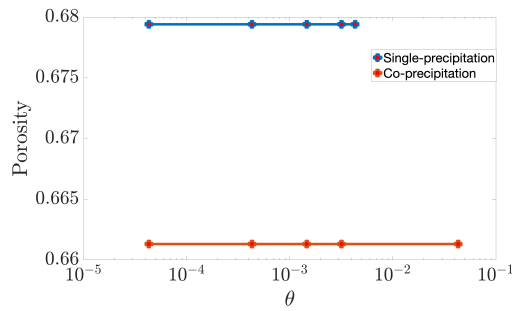


(c) Graph of recovery as a percentage against the dimensionless group Ma , which shows the effect of co-precipitation on recovery.

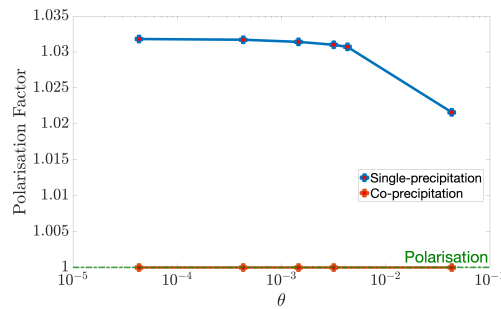


(d) Graph of osmotic pressure against the dimensionless group Ma , which shows the effect of co-precipitation on osmotic pressure.

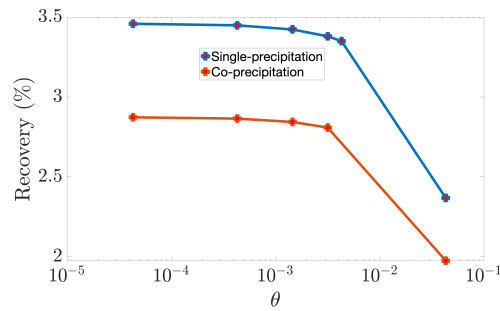
Figure 5.25: Comparison between single-precipitation and co-precipitation at different values of Ma .



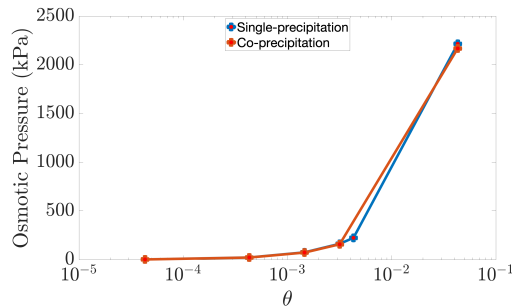
(a) Graph of porosity (as a pore fraction of the membrane) against the dimensionless group θ , which shows the effect of co-precipitation on porosity.



(b) Graph of concentration polarisation (as a ratio of membrane concentration to inlet concentration) against the dimensionless group θ , which shows the effect of co-precipitation on polarisation.



(c) Graph of recovery as a percentage against the dimensionless group θ , which shows the effect of co-precipitation on recovery.



(d) Graph of osmotic pressure against the dimensionless group θ , which shows the effect of co-precipitation on osmotic pressure.

Figure 5.26: Comparison between single-precipitation and co-precipitation at different values of θ .

Considering the following sequence might help us understand the results better

Increasing $D_A \Rightarrow$ increases precipitation \Rightarrow decreases porosity,
 \Rightarrow decreases permeability \Rightarrow decreases permeate velocity,
 \Rightarrow decreases recovery \Rightarrow increases polarisation,
 \Rightarrow increases osmotic pressure \Rightarrow decreases permeate velocity.

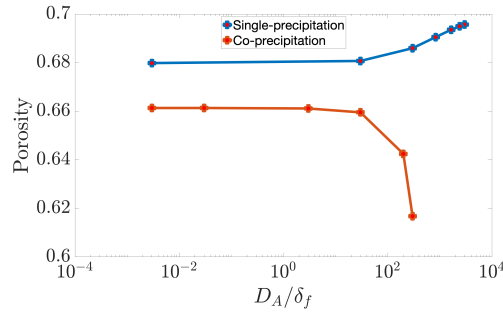
What we are basically trying to demonstrate with this is that increasing D_A increases precipitation which leads to a decline in porosity and permeability. This then reduces recovery because the magnitude of the permeate velocity reduces. As recovery reduces, polarisation is induced due to higher concentration near the membrane. This then raises the osmotic pressure which again influences permeate velocity via (3.33). Therefore, the opposing trends observed in Figure 5.27 could be attributed to the non-linearity between the various sub-processes.

5.3.5 Effect of Co-precipitation on Pe

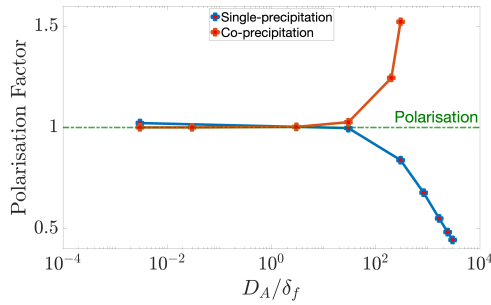
The co-precipitation results obtained for Pe are somewhat similar to those of Re and Da . This seems reasonable as Pe is often interpreted as the Reynolds number counterpart for mass transport [68]. We make this remark because we believe the explanations given for those cases are applicable here. Therefore we wouldn't dwell much on it here but instead briefly highlight the following. We do not observe any polarisation because the solutes that would have otherwise accumulated at the membrane surface have been consumed by the precipitation reaction. This is inferred from the porosity difference in Figure 5.28a. As there is no polarisation, the osmotic pressure remains constant as seen in Figure 5.28d.

5.3.6 Effect of Co-precipitation on β

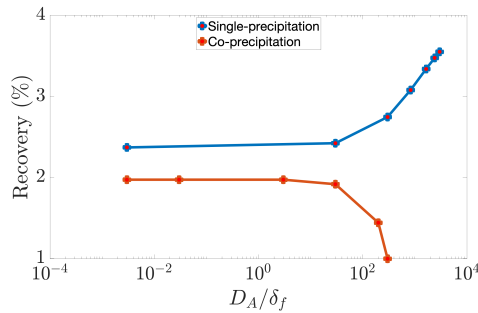
We again highlight here that the co-precipitation results obtained for porosity, polarisation and osmotic pressures are somewhat similar to those of Re , Da and Pe . That is, the polarisation, porosity and osmotic pressure follow a constant trend. We have explained a few times why this is the case so we would not repeat it here. We only note that co-precipitation appears to have the same influence on recovery as single precipitation. This is reasonable because β is a pressure related dimensionless groups (which directly influences recovery via (4.56)) that has no correlation with concentration. Hence increasing the number of salt ions present should not affect recovery via β .



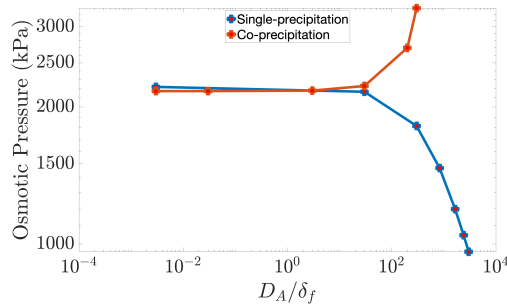
(a) Graph of porosity (as a pore fraction of the membrane) against the dimensionless group D_A/δ_f , which shows the effect of co-precipitation on porosity.



(b) Graph of concentration polarisation (as a ratio of membrane concentration to inlet concentration) against the dimensionless group D_A/δ_f , which shows the effect of co-precipitation on polarisation.

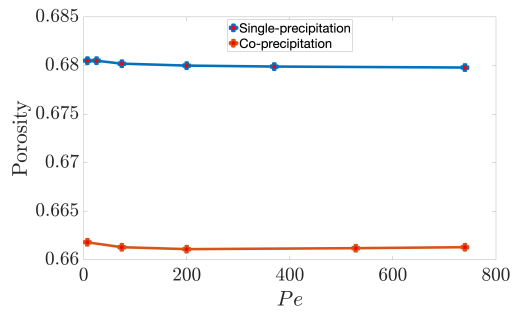


(c) Graph of recovery as a percentage against the dimensionless group D_A/δ_f , which shows the effect of co-precipitation on recovery.

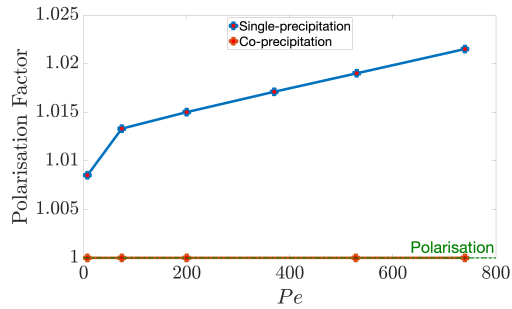


(d) Graph of osmotic pressure against the dimensionless group D_A/δ_f , which shows the effect of co-precipitation on osmotic pressure.

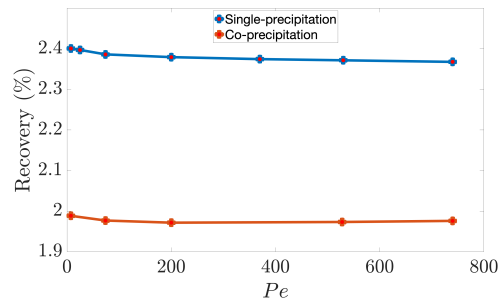
Figure 5.27: Comparison between single-precipitation and co-precipitation at different values of D_A .



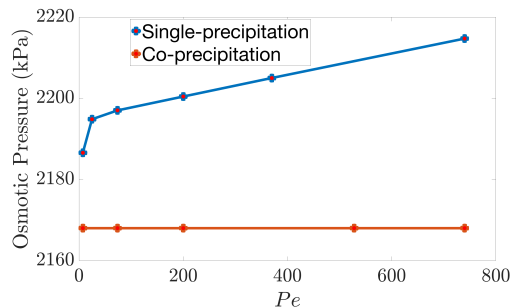
(a) Graph of porosity (as a pore fraction of the membrane) against the dimensionless group Pe , which shows the effect of co-precipitation on porosity.



(b) Graph of concentration polarisation (as a ratio of membrane concentration to inlet concentration) against the dimensionless group Pe , which shows the effect of co-precipitation on polarisation.

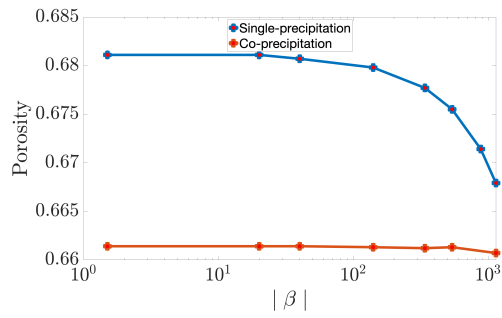


(c) Graph of recovery as a percentage against the dimensionless group Pe , which shows the effect of co-precipitation on recovery.

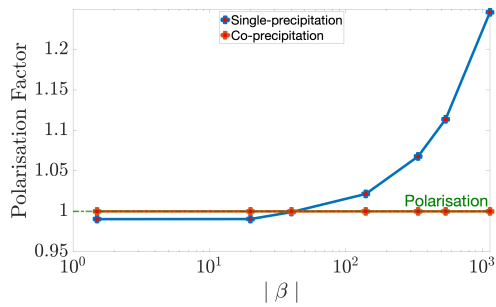


(d) Graph of osmotic pressure against the dimensionless group Pe , which shows the effect of co-precipitation on osmotic pressure.

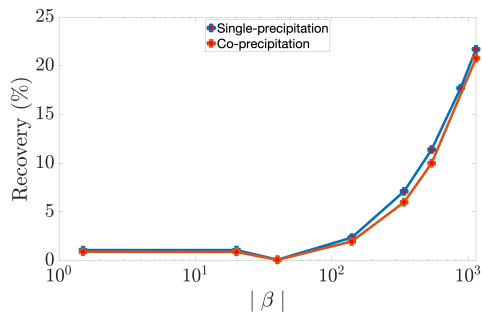
Figure 5.28: Comparison between single-precipitation and co-precipitation at different values of Pe .



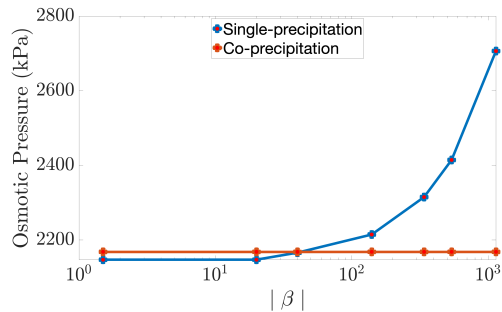
(a) Graph of porosity (as a pore fraction of the membrane) against the dimensionless group β , which shows the effect of co-precipitation on porosity.



(b) Graph of concentration polarisation (as a ratio of membrane concentration to inlet concentration) against the dimensionless group β , which shows the effect of co-precipitation on polarisation.



(c) Graph of recovery as a percentage against the dimensionless group β , which shows the effect of co-precipitation on recovery.



(d) Graph of osmotic pressure against the dimensionless group β , which shows the effect of co-precipitation on osmotic pressure.

Figure 5.29: Comparison between single-precipitation and co-precipitation at different values of β .

5.3.7 Effect of Co-precipitation on ϑ_g

Results from the single precipitation section, section 5.2 allows us to already understand the trends observed in Figures 5.30a and 5.30c. Hence we will not offer explanations for the trends here, we only remark that the difference between the single precipitation line and co-precipitation line in Figure 5.30a is related to the amount of solute that has been consumed in the precipitation reactions. Similarly, the difference between the single precipitation line and co-precipitation line seen in Figures 5.30d and 5.30b informs us that the membrane concentration is reduced by the precipitation reactions.

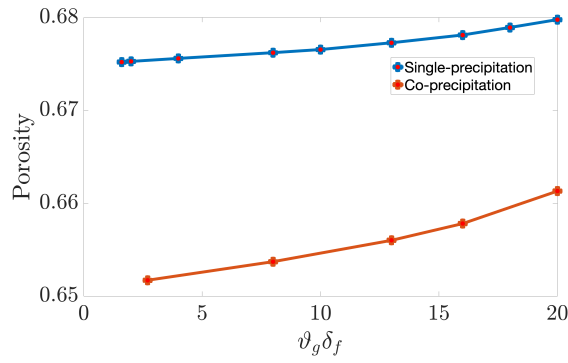
5.4 Comparison with Literature

We attempted to compare the results obtained from the preceding sections with a few cases in the literature. However, it was difficult to establish a basis of comparison because our model approach and framework is considerably different from those encountered in the literature. For instance, no other study has considered the influence of varying dimensionless groups on polarisation, osmotic pressure, recovery or precipitation. We have also not come across any mathematical study that accounts for co-precipitation using deterministic reaction kinetics. Taken together, these are the core features of our study. This therefore makes comparisons with results somewhat invalid. In addition, the outputs from their model differs from ours. For instance, Radu *et al.* [87] and Zhou *et al.* [135] investigated the impact of feed spacers on scaling and/or polarisation. Spacers significantly change the fluid dynamics of the process which would in turn impact their results. However, for the sake of completeness, we will attempt to draw general comparisons below.

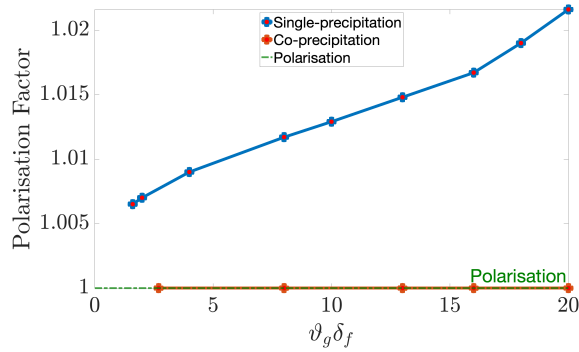
Our qualitative observation of polarisation is consistent with those of Radu *et al.* [87] which indicate that close to the channel inlet there is little precipitation, while towards the outlet a significant amount of polarisation is observed. Although, we are unable to see where the precipitate forms in our model, we can clearly see in Figure 5.2c that polarisation is more severe towards the membrane. Therefore, precipitation will be greatest at this location if the rate is large enough.

Furthermore, Radu *et al.* [87] observed that the permeate flux is severely reduced where the precipitate is formed on the membrane. Our results are in agreement with this as we also observed decline in recovery when porosity reduces.

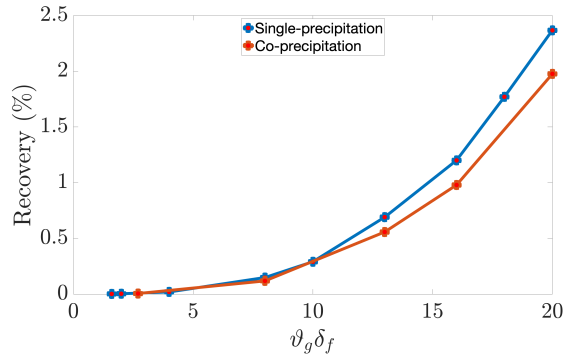
Our findings are also consistent with Zhou *et al.* [135] who suggested that for shorter membrane channels recovery increases with driving pressure. Our



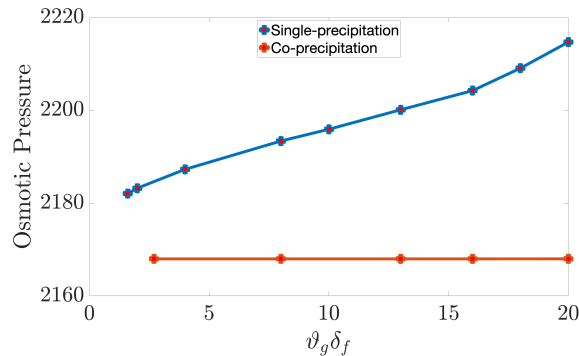
(a) Graph of porosity (as a pore fraction of the membrane) against the dimensionless group $\vartheta_g \delta_f$, which shows the effect of co-precipitation on porosity.



(b) Graph of concentration polarisation (as a ratio of membrane concentration to inlet concentration) against the dimensionless group $\vartheta_g \delta_f$, which shows the effect of co-precipitation on polarisation.



(c) Graph of recovery as a percentage against the dimensionless group $\vartheta_g \delta_f$, which shows the effect of co-precipitation on recovery.



(d) Graph of osmotic pressure against the dimensionless group $\vartheta_g \delta_f$, which shows the effect of co-precipitation on osmotic pressure.

Figure 5.30: Comparison between single-precipitation and co-precipitation at different values of $\vartheta_g \delta_f$.

simulations considered a small section of a larger membrane channel so it falls under the shorter membrane category. Indeed we observed an increase in recovery as β increases (β the dimensionless group that consolidates the pressure driving forces).

5.5 Summary

In this chapter, we made some physical interpretations of the dimensionless numbers and investigated the effects of these dimensionless groups on four quantities: namely, concentration polarisation, osmotic pressure, recovery and porosity. The intent was to assess the model's performance and ensure that its predictions are consistent with its principles and assumptions. Some of the significant findings to emerge from the investigation are summarised in Figure 5.31. More elaborate remarks on these findings are given below.

1. It became apparent that velocity, pressure diffusion and precipitation are the major parameters/quantities that determine the concentration distribution near the membrane. We observed that:
 - Increasing $Da, Re, Pe, \vartheta_g, \beta$ increased the magnitude of the permeate velocity. This caused more fluid and solutes to be transported to the membrane, increasing recovery. This increased the polarisation observed in the case of single-precipitation. However, there was no polarisation observed for co-precipitation because the reaction rate is greater so the solute that would have otherwise accumulated at the membrane surface have been consumed by the precipitation reaction.
 - Increasing Eu and θ decreased the magnitude of the permeate velocity. As a result, less fluid and solutes were transported to the membrane, decreasing recovery and polarisation. We observed this trend for both single precipitation and co-precipitation.
 - Increasing D_A decreased the diffusion of solutes. Consequently, it took a longer time for solutes to arrive at the membrane. This increased recovery and decreased polarisation for single precipitation. However for co-precipitation, we observed the opposite trend, that is a decline in recovery and increase in polarisation. This is likely because increasing D_A increases the precipitation rate which leads to a decline in recovery (via porosity and permeability). This in turn induces polarisation, raising the osmotic pressure. We stated that the opposing trends observed could be attributed to the non-linearity

between the processes.

- Increasing Ma^* increases the precipitation rate. Therefore the solutes arriving at the membrane are consumed quickly. This reduces recovery (due to a decline in porosity) and polarisation.
2. Osmotic pressure and concentration polarisation generally follow the same trend except in the case of θ where polarisation reduced with θ but osmotic pressure increased θ .
 3. Ma appears to have the most effect on porosity.
 4. In the case of single-precipitation, creeping flows have little or no effect on polarisation or recovery. However as the flow approaches the laminar regime we start to see a significant effect on recovery, osmotic pressure and polarisation.
 5. For co-precipitation we observe a constant trend for polarisation and osmotic pressure. The difference between the single precipitation and co-precipitation is related to the additional amount of solute that has been consumed.
 6. The relationship between the pressure gradient across the feed channel (which drives flow forward towards the outlet) and the pressure gradient across the membrane (which drives flow in the perpendicular direction towards the membrane) controls the flow distribution.
 7. The geometry of the channel (i.e channel width and channel height) has an effect on recovery.
 8. The channel's pressure needs to be significantly higher than the osmotic pressure. This is because reverse osmosis is based on this concept.

A few remarks are in order regarding the implications of some of these results on desalination operations.

- Results from varying Da suggests that highly permeable membranes might make it possible to use a smaller membrane area as a high recovery is likely, reducing capital cost but this increases polarisation.
- Results from varying β indicates that pressurised permeate channel may reduce polarisation but this could in turn increase operating cost and energy requirements of desalination systems.
- Results from varying θ indicate that polarisation would not occur if the channel's pressure is significantly lower than the osmotic pressure.

- The co-precipitation results suggest that the intensity of the mass transport at the membrane (particularly diffusion and reaction) could produce completely different behaviours when more salt ions are present.

A word on the limits our model; the code is only suitable for darcy flows and breaks down at high Pe, Re and θ . We end this summary by noting that the results from the numerical simulations have provided significant insight on the relative influence of fluid dynamics and solute transport on precipitation and recovery. The results obtained from the simulation were consistent with the dimensionless relations produced from the nondimensionalisation procedure in Chapter 4. In addition, we now have an idea of the limitations of the model/code.

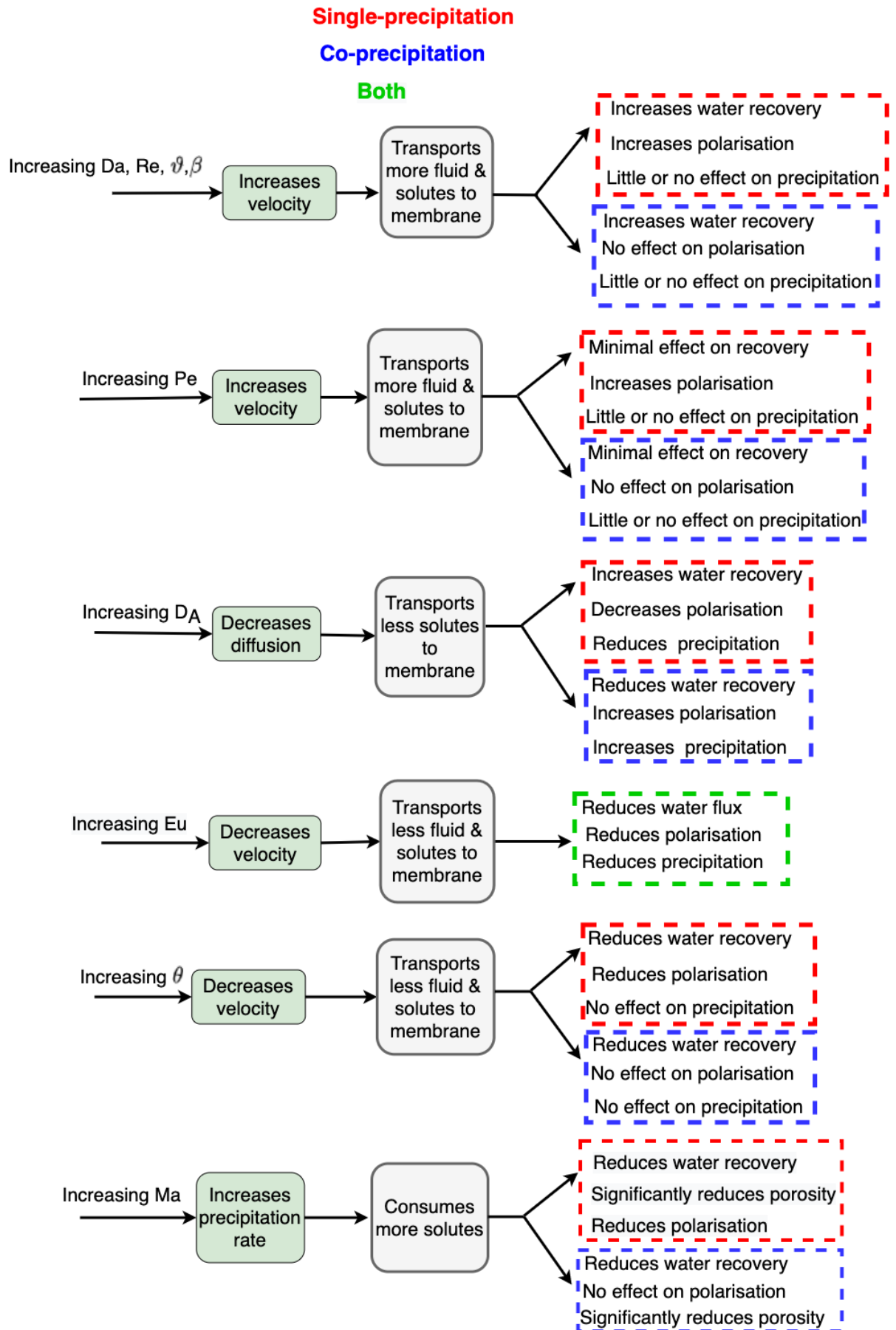


Figure 5.31: Summary of results obtained from varying the dimensionless groups.

Chapter 6

Summary and Conclusions

The aims of this project was to:

1. Unravel some of the mysteries surrounding precipitation in reverse osmosis membrane operations.
2. Synthesise models describing individual feature in reverse osmosis and integrate this with a kinetic model for precipitation.
3. Identify the dimensionless groups that control the physics of the system.
4. Investigate the relative influence of each sub-process.

In Chapter 2 - 5 we presented a number of original results in relation to the aims described above. Below, we summarise the main research findings.

The results presented in Chapter 2 demonstrated that the presence of several ions leads to co-precipitation. The experiments also confirmed that co-existing ions complicates the precipitation process that occurs in desalination operations. One of the more significant findings to emerge from this chapter is that at concentration levels similar to seawater levels, crystallisation of halite could occur even if it is not supersaturated. This project is the first comprehensive investigation on the influence of SO_4^{2-} on CaCO_3 precipitation in desalination systems. Therefore, this experimental study lays the groundwork for future research into the control of CaCO_3 precipitation in reverse osmosis operations.

In Chapter 3 we formulated a model framework which amalgamated the individual models describing fundamental processes in reverse osmosis desalination. The kinetic equation formulated in Chapter 2 was also integrated into the framework. It was shown that the coupling between sub-processes introduces non-linearity and inter-dependencies between the equations for

conservation of solute concentration, conservation of momentum/mass and the constitutive laws for key parameters.

In Chapter 4, the concept of stability analysis and non-dimensionalisation was introduced. The linear stability analysis provided a further qualitative characterisation of the precipitation reaction system, which in turn provided a clearer understanding of the process itself. One of the equilibrium point was a stable node and the rest were saddles. For the former, if there is a change, the system will adjust itself properly to return to steady state. For the latter, if there is a change in the process, arising from the process itself or from an external disturbance, the system itself will not go back to steady state. It became evident that the fixed points are near saddle-node bifurcation points, indicating that slight changes in experimental conditions could have changed the stability from a stable node to a saddle (or vice-versa).

From the non-dimensionalisation procedure, we identified nine dimensionless groups and three timescales, namely the advective timescale, the diffusive timescale and the reactive timescales. We noted that advective transport is the fastest and will reach equilibrium before the other two timescales due to the high pressures associated with reverse osmosis operations. Diffusion occurs much faster than reaction and will thus reach equilibrium before the reaction does. To the best of our knowledge, this is the first study to propose a deterministic formulation for precipitation in a reverse osmosis membrane, conduct stability analysis on the experimental results and present dimensionless groups that capture the entire physics of the system.

In Chapter 5, we investigated the influence of different dimensionless groups on the model solution. It was shown that the influence of each dimensionless group changes when we move from a single-solute systems to a multi-component system. The results presented in this chapter showed that the model's performance is consistent with its principles and assumptions. We also identified the model/code limitations; the code breaks down at high velocity regimes as it was constructed for mainly laminar flows.

In conclusion, the aims and objectives of this study was achieved. This thesis presents a model framework which captures the complex interplay between sub-processes such as precipitation, fluid flow and mass transport which together influence recovery and in turn process sustainability. Further research on the subject might highlight how this translates to the quantity of brine discharged from desalination plant as this is another factor that influences the sustainability of desalination [127]. To this end, we will make the code publicly accessible,

so interested researchers can easily build upon this research. They will have the freedom to examine the code, learn from it, adapt it and more importantly introduce concepts/features which the research community could benefit from.

In the next section we highlight some possible areas of future work.

6.1 Future Work

There are a number of areas within the scope of this research that would be ideal grounds for future work.

- Experimental Work

- The experimental scope of this study was limited in terms of the number of ions present. It would be beneficial if this study could be repeated with more ions (e.g magnesium ion, phosphate ion, silicon ion) present to truly capture the complex process that occurs in industrial scale.
- A further study with a focus on the flow (mimicking those in desalination operations) will be useful for understanding the influence of flow on co-precipitation.
- It will also be worthwhile to investigate the precipitation of CaCO_3 in the absence of sodium chloride to further understand the role it plays during crystallisation.

- Mathematical Work

- We have restricted our analysis to Cartesian coordinates in two-dimensional space. A natural progression of this work would be to extend the model to three-dimensional space and/or polar coordinates. This system will allow analytical treatment of other geometries and will be a more applicable representation of industrial scale operations.
- It is well known that spacer geometry influences the fluid dynamics in reverse osmosis operations. Including this feature into the model could produce interesting findings that further improves our understanding of the mechanisms that characterise reverse osmosis operations.
- To develop a full picture of the membrane element, further research should consider modelling the fluid dynamics and mass transport at the permeate side of the membrane.

- The current model has been designed to reject all the solutes transported to the membrane. However, we know this is not the case in reality; membranes are not 100% efficient. A further study could assess the impact of incomplete rejection on fluid dynamics, permeate quality and recovery.

Bibliography

- [1] Satish Agarwal, Ankush Aggarwal, Sunando Dasgupta, and Sirshendu De. “Performance prediction of membrane modules incorporating the effects of suction in the mass transfer coefficient under laminar and turbulent flow conditions for non-newtonian fluids”. In: *Journal of Food Process Engineering* 32.5 (2009), pp. 752–774 (cit. on p. 55).
- [2] Abdullah Alkudhiri, Naif Darwish, and Nidal Hilal. “Membrane distillation: A comprehensive review”. In: *Desalination* 287 (2012), pp. 2–18 (cit. on p. 102).
- [3] Asam Almulla, Mohamed Eid, Pierre Côté, and John Coburn. “Developments in high recovery brackish water desalination plants as part of the solution to water quantity problems”. In: *Desalination* 153.1-3 (2003), pp. 237–243 (cit. on pp. 5, 46).
- [4] Wei Lun Ang and Abdul Mohammad. “Mathematical modeling of membrane operations for water treatment”. In: *Advances in Membrane Technologies for Water Treatment* (2015), pp. 379–407 (cit. on p. 47).
- [5] Alice Antony, Jor How Low, Stephen Gray, Amy Childress, Pierre Le-Clech, and Greg Leslie. “Scale formation and control in high pressure membrane water treatment systems: A review”. In: *Journal of Membrane Science* 383.1-2 (2011), pp. 1–16 (cit. on p. 14).
- [6] Hassan Arafat. *Desalination Sustainability: A Technical, Socioeconomic, and Environmental Approach*. Elsevier, 2017. ISBN: 0128098961 (cit. on pp. 2–4, 8, 9, 16).
- [7] Savlon Avlonitis, William Hanbury, and Ben Boudinar. “Spiral wound modules performance an analytical solution: Part II”. In: *Desalination* 89.3 (1993), pp. 227–246 (cit. on pp. 55, 56).
- [8] Savlon Avlonitis, William Hanbury, and Ben Boudinar. “Spiral wound modules performance. An analytical solution, part I.” In: *Desalination* 81.1-3 (1991), pp. 191–208 (cit. on pp. 55, 56).

- [9] Yong Bai and Qiang Bai. “Subsea Corrosion and Scale”. In: *Subsea Engineering Handbook, 2nd ed.*; Gulf Professional Publishing: Oxford, UK (2019), pp. 455–487 (cit. on pp. 7, 13).
- [10] Angelo Basile, Fausto Gallucci, and Pietropaolo Morrone. “Advanced carbon dioxide (CO₂) gas separation membrane development for power plants”. In: *Advanced Power Plant Materials, Design and Technology* (2010), pp. 143–186 (cit. on pp. 49, 63, 102).
- [11] Zeki Berk. *Food process engineering and technology*. Academic press, 2018 (cit. on pp. 48, 49).
- [12] Abraham Berman. “Laminar flow in channels with porous walls”. In: *Journal of Applied physics* 24.9 (1953), pp. 1232–1235 (cit. on p. 52).
- [13] Celso Aparecido Bertran and Yongqi Wang. “Numerical Simulations for Homogenous Nucleation of Calcium Carbonate in Concentrated Electrolyte Solutions”. In: *Multiphase Flow: Theory and Applications* (2018), p. 35 (cit. on p. 102).
- [14] Subir Bhattacharjee. *Concentration Polarisation: Early Theories*. <http://www.waterplanet.com>. Date accessed: 12.08.2018. 2017 (cit. on pp. 5, 46).
- [15] Byron Bird, Warren Stewart, Edwin Lightfoot, and Klingenberg Daniel. *Introductory transport phenomena*. Wiley Global Education, 2015 (cit. on pp. 58, 74).
- [16] Ben Boudinar, William Hanbury, and Savlon Avlonitis. “Numerical simulation and optimisation of spiral-wound modules”. In: *Desalination* 86.3 (1992), pp. 273–290 (cit. on p. 56).
- [17] John Brady. “Flow development in a porous channel and tube”. In: *The Physics of fluids* 27.5 (1984), pp. 1061–1067 (cit. on p. 52).
- [18] Vijaysekhar Chellaboina, Sanjay Bhat, Wassim Haddad, and Dennis Bernstein. “Modeling and analysis of mass-action kinetics”. In: *IEEE Control Systems Magazine* 29.4 (2009), pp. 60–78 (cit. on p. 38).
- [19] Tao Chen, Anne Neville, and Mingdong Yuan. “Assessing the effect of Mg²⁺ on CaCO₃ scale formation bulk precipitation and surface deposition”. In: *Journal of Crystal Growth* 275.1-2 (2005), e1341–e1347 (cit. on p. 15).
- [20] Tzyy Haur Chong and Roya Sheikholeslami. “Thermodynamics and kinetics for mixed calcium carbonate and calcium sulfate precipitation”. In: *Chemical Engineering Science* 56.18 (2001), pp. 5391–5400 (cit. on pp. 16, 34).
- [21] Hermann Credner. *Ueber gewisse Ursachen der Krystallverschiedenheiten des kohlensauren Kalkes*. 1870 (cit. on p. 15).

- [22] John Crittenden, Rhodes Trussell, and David Hand. *MWH's Water Treatment: Principles and Design*. International series of monographs on physics. Wiley, 2014, pp. 1335–1410. ISBN: 9781118103753 (cit. on pp. 2, 3, 5, 6, 45, 46, 48, 49, 51, 52, 55, 63, 68, 102).
- [23] Efrem Curcio, Gianluca Di Profio, Enrica Fontananova, and Enrico Drioli. “Membrane technologies for seawater desalination and brackish water treatment”. In: *Advances in Membrane Technologies for Water Treatment* (2015), pp. 411–441 (cit. on p. 51).
- [24] Kamel Damak, Abdelmoneim Ayadi, Belkacem Zeghmami, and Philippe Schmitz. “A new Navier-Stokes and Darcy’s law combined model for fluid flow in crossflow filtration tubular membranes”. In: *Desalination* 161.1 (2004), pp. 67–77 (cit. on p. 53).
- [25] Walter De Keyser and Louis Degueudre. “Contribution à l’étude de la formation de la calcite, aragonite et vaterite”. In: *Bulletin des Sociétés chimiques belges* 59.1-2 (1950), pp. 40–71 (cit. on p. 15).
- [26] Yang Ding, Yunyi Liu, Yangyang Ren, Hongxu Yan, Ming Wang, Dan Wang, Xiao-Ying Lu, Bin Wang, Tianbo Fan, and Hongfan Guo. “Controllable synthesis of all the anhydrous CaCO_3 polymorphs with various morphologies in $\text{CaCl}_2\text{-NH}_3\text{-CO}_2$ aqueous system”. In: *Powder Technology* 333 (2018), pp. 410–420 (cit. on p. 14).
- [27] Enrico Drioli and Lidiotta Giorno. *Comprehensive membrane science and engineering*. Vol. 1. Newnes, 2010 (cit. on p. 64).
- [28] Menachem Elimelech and William Phillip. “The future of seawater desalination: energy, technology, and the environment”. In: *Science* 333.6043 (2011), pp. 712–717 (cit. on pp. 1–4, 52, 107).
- [29] Hariharan Eswaran, George Stoops, and Ali Abtahi. “SEM morphologies of halite (NaCl) in soils”. In: *Journal of Microscopy* 120.3 (1980), pp. 343–352 (cit. on pp. 35, 36).
- [30] Frano Evangelista. “A graphical method for the design of an electro dialysis stack”. In: *Desalination* 64 (1987), pp. 353–365 (cit. on p. 55).
- [31] Frano Evangelista and Gunnar Jonsson. “Optimal design and performance of spiral wound modules I: Numerical method”. In: *Chemical Engineering Communications* 72.1 (1988), pp. 69–81 (cit. on pp. 55, 56).
- [32] J Feher. “Osmosis and osmotic pressure”. In: *Quantitative Human Physiology* 10 (2012), pp. 141–152 (cit. on p. 102).
- [33] Lurdes Fernández-Díaz, Ángeles Fernández-González, and Manuel Prieto. “The role of sulfate groups in controlling CaCO_3 polymorphism”. In: *Geochimica et Cosmochimica Acta* 74.21 (2010), pp. 6064–6076 (cit. on pp. 7, 8, 12, 14–17, 33, 42).

- [34] Joel Ferziger and Milovan Peric. *Computational method for fluid dynamics*. Vol. 3. Springer-Verlag Berlin Heidelberg, 2002 (cit. on p. 72).
- [35] Gustavo Fimbres-Weihs and Dianne Wiley. “Review of 3D CFD modeling of flow and mass transfer in narrow spacer-filled channels in membrane modules”. In: *Chemical Engineering and Processing: Process Intensification* 49.7 (2010), pp. 759–781 (cit. on pp. 6, 51).
- [36] Rodney Fox. *Computational models for turbulent reacting flows*. Cambridge university press, 2003 (cit. on p. 92).
- [37] Clemens Fritzmann, Jonas Löwenberg, Thomas Wintgens, and Thomas Melin. “State-of-the-art of reverse osmosis desalination”. In: *Desalination* 216.1-3 (2007), pp. 1–76 (cit. on p. 55).
- [38] AAS Gallab, MEA Ali, HA Shawky, and MSA Abdel-Mottaleb. “Effect of different salts on mass transfer coefficient and inorganic fouling of TFC membranes”. In: *J Membr Sci Technol* 7.175 (2017), p. 2 (cit. on p. 102).
- [39] Boram Gu, Xiao Yun Xu, and Claire Adjiman. “A predictive model for spiral wound reverse osmosis membrane modules: The effect of winding geometry and accurate geometric details”. In: *Computers & Chemical Engineering* 96 (2017), pp. 248–265 (cit. on p. 56).
- [40] Fravel Junior Harold and Lindsey Karen. *Understanding salt solubility reaps benefits in RO system performance*. <https://www.ama.org/understanding-salt-solubility-reaps-benefits-in-ro-system-performance>. Date accessed: 27.09.2020. 2014 (cit. on pp. 5, 13).
- [41] James Herterich, Qian Xu, Robert Field, Dominic Vella, and Ian Griffiths. “Optimizing the operation of a direct-flow filtration device”. In: *Journal of Engineering Mathematics* 104.1 (2017), pp. 195–211 (cit. on p. 63).
- [42] Johannes Hommel, Edward Coltman, and Holger Class. “Porosity–permeability relations for evolving pore space: a review with a focus on (bio-) geochemically altered porous media”. In: *Transport in Porous Media* 124.2 (2018), pp. 589–629 (cit. on p. 71).
- [43] Ji-xiang Huo, Fu-heng Ma, and Xiao-lei Ji. “Porosity and permeability variations of a dam curtain during dissolution”. In: *Water Science and Engineering* 12.2 (2019), pp. 155–161 (cit. on p. 71).
- [44] William Inskeep and Paul Bloom. “An evaluation of rate equations for calcite precipitation kinetics at pCO₂ less than 0.01 atm and pH greater than 8”. In: *Geochimica et Cosmochimica Acta* 49.10 (1985), pp. 2165–2180 (cit. on p. 7).
- [45] International-Towing-Tank-Conference. “ITTC Recommended Procedures–Fresh Water and Seawater Properties”. In: (2011) (cit. on p. 102).

- [46] Fauzi Ismail, Kailash Chandra Khulbe, and Takeshi Matsuura. *Reverse Osmosis*. Elsevier, 2018 (cit. on p. 53).
- [47] Zohreh Jalilvand, Farzin Zokae Ashtiani, Amir Fouladitajar, and Hamid Rezaei. “Computational fluid dynamics modeling and experimental study of continuous and pulsatile flow in flat sheet microfiltration membranes”. In: *Journal of Membrane Science* 450 (2014), pp. 207–214 (cit. on pp. 51, 53).
- [48] Khan Jamal, Mohammad Ali Khan, and Mohammad Kamil. “Mathematical modeling of reverse osmosis systems”. In: *Desalination* 160.1 (2004), pp. 29–42 (cit. on pp. 5, 51).
- [49] John Johnson, Herbert Merwin, and Erskine Williamson. “The several forms of calcium carbonate”. In: *American Journal of Science* 41 (1916), pp. 473–512 (cit. on p. 15).
- [50] Tahereh Kaghazchi, Mahdieh Mehri, Maryam Takht Ravanchi, and Ali Kargari. “A mathematical modeling of two industrial seawater desalination plants in the Persian Gulf region”. In: *Desalination* 252.1-3 (2010), pp. 135–142 (cit. on pp. 45, 51).
- [51] Sunil Kar. “Mathematical modeling of reverse osmosis for ultrapure water production”. PhD thesis. Oklahoma State University, 1994 (cit. on pp. 3, 45, 48).
- [52] Anastasios Karabelas, Margaritis Kostoglou, and Sultana Mitrouli. “Incipient crystallization of sparingly soluble salts on membrane surfaces: The case of dead-end filtration with no agitation”. In: *Desalination* 273.1 (2011), pp. 105–117 (cit. on pp. 56, 57).
- [53] Peter Karpinski and Jongshinn Wey. “Precipitation processes”. In: *Handbook of Industrial Crystallization*. Elsevier, 2002, pp. 141–160 (cit. on pp. 7, 13).
- [54] Akili Khawaji, Ibrahim Kutubkhanah, and JongMihn Wie. “Advances in seawater desalination technologies”. In: *Desalination* 221.1-3 (2008), pp. 47–69 (cit. on p. 1).
- [55] Fredrik Kiil. “Mechanism of osmosis”. In: *Kidney International* 21.2 (1982), pp. 303–308 (cit. on p. 2).
- [56] Mitsutaka Kitamura. “Crystallization and transformation mechanism of calcium carbonate polymorphs and the effect of magnesium ion”. In: *Journal of Colloid and Interface Science* 236.2 (2001), pp. 318–327 (cit. on pp. 15, 16).
- [57] Yasushi Kitano, Minoru Okumura, and Masatoshi Idogaki. “Incorporation of sodium, chloride and sulfate with calcium carbonate”. In: *Geochemical Journal* 9.2 (1975), pp. 75–84 (cit. on pp. 16, 35, 36).

- [58] Margaritis Kostoglou and Anastasios Karabelas. “A mathematical study of the evolution of fouling and operating parameters throughout membrane sheets comprising spiral wound modules”. In: *Chemical engineering journal* 187 (2012), pp. 222–231 (cit. on pp. 6, 51).
- [59] Margaritis Kostoglou and Anastasios Karabelas. “Comprehensive simulation of flat-sheet membrane element performance in steady state desalination”. In: *Desalination* 316 (2013), pp. 91–102 (cit. on pp. 6, 51).
- [60] Krešimir Košutić, Davor Dolar, and Branko Kunst. “On experimental parameters characterizing the reverse osmosis and nanofiltration membranes’ active layer”. In: *Journal of Membrane Science* 282.1-2 (2006), pp. 109–114 (cit. on p. 54).
- [61] Imma Lebron and Donald Suarez. “Calcite nucleation and precipitation kinetics as affected by dissolved organic matter at 25 C and pH_i 7.5”. In: *Geochimica et Cosmochimica Acta* 60.15 (1996), pp. 2765–2776 (cit. on p. 15).
- [62] Kah Peng Lee, Tom Arnot, and Davide Mattia. “A review of reverse osmosis membrane materials for desalination—development to date and future potential”. In: *Journal of Membrane Science* 370.1-2 (2011), pp. 1–22 (cit. on p. 1).
- [63] Fang Li, Wytze Meindersma, Andre De Haan, and Tom Reith. “Optimization of commercial net spacers in spiral wound membrane modules”. In: *Journal of Membrane Science* 208.1-2 (2002), pp. 289–302 (cit. on p. 56).
- [64] John Lindon, George Tranter, and David Koppenaar. *Encyclopedia of spectroscopy and spectrometry*. Academic Press, 2016 (cit. on p. 14).
- [65] Qian Liu, Guo-Rong Xu, and Rasel Das. “Inorganic scaling in reverse osmosis (RO) desalination: Mechanisms, monitoring, and inhibition strategies”. In: *Desalination* 468 (2019), p. 114065 (cit. on pp. 4, 5, 9, 13, 16, 46, 47).
- [66] Henry Lonsdale, Ulrich Merten, and Robert Riley. “Transport Properties of Cellulose Acetate Osmotic Membranes”. In: *Journal of applied polymer science* 9 (1965), pp. 1341–1362 (cit. on pp. 53, 54).
- [67] Patricia Luis. *Fundamental Modeling of Membrane Systems: Membrane and Process Performance*. Elsevier, 2018 (cit. on pp. 47, 48).
- [68] Clovis Maliska. “On the Physical Significance of Some Dimensionless Numbers Used in Heat Transfer and Fluid Flow”. In: *Federal University of Santa Catarina, Florianópolis, SC* (1990) (cit. on p. 137).
- [69] Mariano Martín. *Industrial chemical process analysis and design*. Elsevier, 2016 (cit. on p. 48).

- [70] Asif Matin, Faizur Rahman, Hafiz Zahid Shafi, and Syed Zubair. “Scaling of reverse osmosis membranes used in water desalination: Phenomena, impact, and control; future directions”. In: *Desalination* 455 (2019), pp. 135–157 (cit. on pp. 13, 14).
- [71] Iris Cuesta Mayorga, José Manuel Astilleros, and Lurdes Fernández-Díaz. “Precipitation of CaCO_3 Polymorphs from Aqueous Solutions: The Role of pH and Sulfphate Groups”. In: *Minerals* 9.178 (2019), pp. 1–16 (cit. on pp. 8, 34, 42).
- [72] James McDonough. “Lectures in computational fluid dynamics of incompressible flow: Mathematics, algorithms and implementations”. In: (2007) (cit. on p. 73).
- [73] Laurence McKeen. *Permeability properties of plastics and elastomers*. William Andrew, 2016 (cit. on pp. 49, 50, 63, 102).
- [74] Fadl Moukalled, Luca Mangani, and Marwan Darwish. *The finite volume method in computational fluid dynamics*. Vol. 113. Springer International Publishing, 2016 (cit. on p. 73).
- [75] George Nancollas and Michael Reddy. “The crystallization of calcium carbonate. II. Calcite growth mechanism”. In: *Journal of Colloid and Interface Science* 37.4 (1971), pp. 824–830 (cit. on pp. 15, 102).
- [76] Mia Rohde Nielsen, Karina Sand, Juan Diego Rodriguez-Blanco, Nicolas Bovet, Johanna Generosi, Kim Nicole Dalby, and Susan Louise Svane Stipp. “Inhibition of calcite growth: combined effects of Mg^{2+} and SO_4^{2-} ”. In: *Crystal Growth & Design* 16.11 (2016), pp. 6199–6207 (cit. on p. 16).
- [77] Catherine Noiriél, Philippe Gouze, and Dominique Bernard. “Investigation of porosity and permeability effects from microstructure changes during limestone dissolution”. In: *Geophysical Research Letters* 31.24 (2004) (cit. on p. 71).
- [78] Takeshi Ogino, Toshio Suzuki, and Kiyoshi Sawada. “The formation and transformation mechanism of calcium carbonate in water”. In: *Geochimica et Cosmochimica Acta* 51.10 (1987), pp. 2757–2767 (cit. on p. 14).
- [79] Haruhiko Ohya and Srinavasa Sourirajan. *Reverse osmosis system specification and performance data for water treatment applications*. Thayer School of Engineering, Dartmouth College, 1971 (cit. on p. 55).
- [80] Haruhiko Ohya and Yoshio Taniguchi. “An analysis of reverse osmotic characteristics of ROGA-4000 spiral-wound module”. In: *Desalination* 16.3 (1975), pp. 359–373 (cit. on p. 55).
- [81] Terje Østvold and Preben Randhol. “Kinetics of CaCO_3 scale formation. The influence of temperature, supersaturation and ionic composition”.

- In: *International Symposium on Oilfield Scale*. Society of Petroleum Engineers. 2001 (cit. on pp. 8, 33).
- [82] Afshin Pak, Toraj Mohammadi, Seyed Mostafa Hosseinalipour, and Vida Allahdini. “CFD modeling of porous membranes”. In: *Desalination* 222.1-3 (2008), pp. 482–488 (cit. on p. 53).
- [83] Junhyung Park and Kwang Soon Lee. “A two-dimensional model for the spiral wound reverse osmosis membrane module”. In: *Desalination* 416 (2017), pp. 157–165 (cit. on p. 52).
- [84] David Paterson. “Circulation of fluid between plasma, interstitium and lymph”. In: *Levick’s Introduction to Cardiovascular Physiology*. CRC Press, 2018, pp. 142–150 (cit. on p. 67).
- [85] Ravi Prasad and Kamalesh Sirkar. “Analytical design equations for multicomponent reverse osmosis processes by spiral-wound modules”. In: *Industrial & Engineering Chemistry Process Design and Development* 24.2 (1985), pp. 350–358 (cit. on p. 55).
- [86] Ravi Prasad and Kamalesh Sirkar. “Analytical design equations for multisolute reverse osmosis processes by tubular modules”. In: *Industrial & Engineering Chemistry Process Design and Development* 23.2 (1984), pp. 320–329 (cit. on p. 55).
- [87] Andrea Radu, Luke Bergwerff, Loosdrecht Van, and Cristian Picioreanu. “A two-dimensional mechanistic model for scaling in spiral wound membrane systems”. In: *Chemical Engineering Journal* 241 (2014), pp. 77–91 (cit. on pp. 51, 58, 59, 68, 75, 102, 141).
- [88] Robert Raucher, Janet Clements, Pei Xu, Jeff Oxenford, John Ruetten, Zororai Choto, and Robert Reiss. “Guidelines for implementing seawater and brackish water desalination facilities”. In: *Water Research Foundation and Arsenic Water Technology Partnership* (2010) (cit. on pp. 1–3).
- [89] Michael Reddy and George Nancollas. “The crystallization of calcium carbonate: IV. The effect of magnesium, strontium and sulfate ions”. In: *Journal of Crystal Growth* 35.1 (1976), pp. 33–38 (cit. on pp. 15, 16).
- [90] Michael Reddy and Karin Wang. “Crystallization of calcium carbonate in the presence of metal ions: I. Inhibition by magnesium ion at pH 8.8 and 25°C”. In: *Journal of Crystal Growth* 50.2 (1980), pp. 470–480 (cit. on p. 15).
- [91] Marc Roussel. “Stability analysis for ODEs”. In: *Nonlinear Dynamics, lecture notes, University Hall, Canada* (2005) (cit. on p. 78).
- [92] Alan Rudie and Peter Hart. “Mineral scale management. Part II, Fundamental chemistry”. In: *Tappi Journal* 5.7 (2006), pp. 17–23 (cit. on p. 7).

- [93] Alejandro Ruiz-García, Noemi Melián-Martel, and Ignacio Nuez. “Short review on predicting fouling in RO desalination”. In: *Membranes* 7.4 (2017), p. 62 (cit. on p. 5).
- [94] Roma Rush and James Johnson. “Osmotic Coefficients of Synthetic Sea-Water Solutions at 25° C.” In: *Journal of Chemical and Engineering Data* 11.4 (1966), pp. 590–592 (cit. on p. 102).
- [95] Kyle Steven Rybacki. “Calcium carbonate precipitation mechanisms and geochemical analysis of particulate material found within the waters of Maramec Spring, St. James, Missouri”. In: (2010) (cit. on p. 14).
- [96] José Luís Santos, Vitor Geraldes, Svetlozar Velizarov, and Joao Goulao Crespo. “Investigation of flow patterns and mass transfer in membrane module channels filled with flow-aligned spacers using computational fluid dynamics (CFD)”. In: *Journal of Membrane Science* 305.1-2 (2007), pp. 103–117 (cit. on pp. 56, 59).
- [97] Kiyoshi Sawada. “The mechanisms of crystallization and transformation of calcium carbonates”. In: *Pure and Applied Chemistry* 69.5 (1997), pp. 921–928 (cit. on p. 14).
- [98] Joern Schwinge, Dianne Wiley, and David Fletcher. “Simulation of unsteady flow and vortex shedding for narrow spacer-filled channels”. In: *Industrial & Engineering Chemistry Research* 42.20 (2003), pp. 4962–4977 (cit. on pp. 51, 56).
- [99] Keith Scott. “Introduction to membrane separations”. In: *Handbook of Industrial Membranes: Introduction to Membrane Separation. 2nd ed. Elsevier Advanced Technology* (1995), pp. 3–185 (cit. on pp. 49, 51, 63, 102).
- [100] Nicolas Seigneur, Ulrich Mayer, and Carl Steefel. “Reactive transport in evolving porous media”. In: *Reviews in Mineralogy and Geochemistry* 85.1 (2019), pp. 197–238 (cit. on p. 64).
- [101] Raphael Semiat. “Water Purification: Materials and Technologies”. In: (2010) (cit. on p. 51).
- [102] Subbiah Senthilmurugan, Aruj Ahluwalia, and Sharad Gupta. “Modeling of a spiral-wound module and estimation of model parameters using numerical techniques”. In: *Desalination* 173.3 (2005), pp. 269–286 (cit. on pp. 55, 56).
- [103] Raymond Shaw and William Gill. “Reverse osmosis: increased productivity by reduction of concentration polarization in laminar flow reverse osmosis using intermediate non-rejecting membrane sections”. In: *Desalination* 11.2 (1972), pp. 189–205 (cit. on p. 52).

- [104] Roya Sheikholeslami and John Bright. “Silica and metals removal by pretreatment to prevent fouling of reverse osmosis membranes”. In: *Desalination* 143.3 (2002), pp. 255–267 (cit. on p. 16).
- [105] Roya Sheikholeslami and Henry Ong. “Kinetics and thermodynamics of calcium carbonate and calcium sulfate at salinities up to 1.5 M”. In: *Desalination* 157.1-3 (2003), pp. 217–234 (cit. on pp. 12, 16, 34, 56).
- [106] Rajindar Singh. “Hybrid membrane systems—applications and case studies”. In: *Hybrid Membrane Systems for Water Purification, Elsevier Science, Amsterdam* (2005), p. 131 (cit. on p. 51).
- [107] Rajindar Singh. *Membrane technology and engineering for water purification: application, systems design and operation*. Butterworth-Heinemann, 2014 (cit. on p. 5).
- [108] Kamalesh Sirkar, Phuong Dang, and Goruganthu Rao. “Approximate design equations for reverse osmosis desalination by spiral-wound modules”. In: *Industrial & Engineering Chemistry Process Design and Development* 21.3 (1982), pp. 517–527 (cit. on p. 55).
- [109] Kamalesh Sirkar and Goruganthu Rao. “Short cut design methods for reverse osmosis separation with tubular modules”. In: *Desalination* 48.1 (1983), pp. 25–42 (cit. on p. 55).
- [110] Stewart Slater, Jakub Zielinski, Rainer Wendel, and Christopher Uchrin. “Modeling of small scale reverse osmosis systems”. In: *Desalination* 52.3 (1985), pp. 267–284 (cit. on pp. 46, 51, 104).
- [111] Otakar Söhnel and John Garside. *Precipitation: basic principles and industrial applications*. Butterworth-Heinemann, 1992 (cit. on p. 13).
- [112] Mohammad Soltanieh and William Gill’. “Review of reverse osmosis membranes and transport models”. In: *Chemical Engineering Communications* 12.4-6 (1981), pp. 279–363 (cit. on p. 54).
- [113] Lianfa Song and Sanchuan Yu. “Concentration polarization in cross-flow reverse osmosis”. In: *AIChE journal* 45.5 (1999), pp. 921–928 (cit. on p. 51).
- [114] Srinavasa Sourirajan, Takeshi Matsuura, Fu-Hung Hsieh, and Gary Gildert. “Production, Specification, and Some Transport Characteristics of Cellulose Acetate Ultrafiltration Membranes for Aqueous Feed Solutions”. In: *Ultrafiltration Membranes and Applications*. Springer, 1980, pp. 21–43 (cit. on p. 55).
- [115] Kurt Spiegler and Ora Kedem. “Thermodynamics of hyperfiltration (reverse osmosis): criteria for efficient membranes”. In: *Desalination* 1.4 (1966), pp. 311–326 (cit. on pp. 53, 54).

- [116] Carl Steefel, Donald DePaolo, and Peter Lichtner. “Reactive transport modeling: An essential tool and a new research approach for the Earth sciences”. In: *Earth and Planetary Science Letters* 240.3-4 (2005), pp. 539–558 (cit. on p. 71).
- [117] Steven Strogatz. *Nonlinear dynamics and chaos with student solutions manual: With applications to physics, biology, chemistry, and engineering*. CRC press, 2018 (cit. on p. 81).
- [118] Jörg Stucki. “Stability analysis of biochemical systems—a practical guide”. In: *Progress in Biophysics and Molecular Biology* 33 (1979), pp. 99–187 (cit. on p. 38).
- [119] Yongming Tang, Fan Zhang, Ziyi Cao, Wenheng Jing, and Yizhozhong Chen. “Crystallization of CaCO_3 in the presence of sulfate and additives: Experimental and molecular dynamics simulation studies”. In: *Journal of colloid and interface science* 377.1 (2012), pp. 430–437 (cit. on pp. 8, 16, 34, 42).
- [120] Alexandre Tartakovsky, George Redden, Peter Lichtner, Timothy Scheibe, and Paul Meakin. “Mixing-induced precipitation: Experimental study and multiscale numerical analysis”. In: *Water Resources Research* 44.6 (2008) (cit. on pp. 59, 75).
- [121] Colorado State University. *Phase Plane Portraits: Classification of 2d Systems*.
https://www.math.colostate.edu/~gerhard/M345/CHP/ch9_3-4.pdf.
Date accessed: 14.09.2021. 2020 (cit. on p. 81).
- [122] Thein Wah. “Laminar flow in a uniformly porous channel”. In: *The Aeronautical Quarterly* 15.3 (1964), pp. 299–310 (cit. on p. 52).
- [123] Tarek Waly, Maria Kennedy, Geert-Jan Witkamp, Gary Amy, and Jan Schippers. “The role of inorganic ions in the calcium carbonate scaling of seawater reverse osmosis systems”. In: *Desalination* 284 (2012), pp. 279–287 (cit. on pp. 7, 8, 12, 15, 16, 19, 56).
- [124] Zhi Wang, Songlin Dong, Nan Li, Xiaochang Cao, Menglong Sheng, Rui Xu, Bo Wang, Hongyu Wu, Cuihua Ma, Ye Yuan, Haoqing Xu, Feng Chen, and Song Zhao. “ CO_2 Selective Membranes: How Easy Is Their Moving From Laboratory to Industrial Scale?” In: *Current Trends and Future Developments on (bio-) membranes*. Elsevier, 2018, pp. 75–102 (cit. on pp. 49, 50).
- [125] Sawsan Wardeh and Herve Morvan. “CFD simulations of flow and concentration polarization in spacer-filled channels for application to water desalination”. In: *Chemical Engineering Research and Design* 86.10 (2008), pp. 1107–1116 (cit. on pp. 51, 53).

- [126] Henry Weller. “OpenFOAM The Open Source CFD Toolbox: Programmers guide”. In: *The OpenFOAM Foundation Ltd.: London, UK* (2015) (cit. on p. 74).
- [127] Gede Wenten, Danu Ariono, Mubiar Purwasasmita, and Khoirudin. “Integrated processes for desalination and salt production: A mini-review”. In: *AIP Conference Proceedings*. Vol. 1818. 1. AIP Publishing. 2017, p. 020065 (cit. on pp. 4, 148).
- [128] Johannes Wijmans and Richard Baker. “The solution-diffusion model: a review”. In: *Journal of Membrane Science* 107.1-2 (1995), pp. 1–21 (cit. on p. 53).
- [129] Dianne Wiley and David Fletcher. “Computational fluid dynamics modelling of flow and permeation for pressure-driven membrane processes”. In: *Desalination* 145.1-3 (2002), pp. 183–186 (cit. on pp. 51, 53).
- [130] Mark Wilf, Leon Awerbuch, Craig Bartels, Mike Mickley, Graeme Pearce, and Nikolay Voutchkov. *The guidebook to membrane desalination technology*. International series of monographs on physics. Balaban Desalination Publications, 2007. ISBN: 0866890653 (cit. on pp. 52, 54).
- [131] John Wray and Farrington Daniels. “Precipitation of calcite and aragonite”. In: *Journal of the American Chemical Society* 79.9 (1957), pp. 2031–2034 (cit. on p. 15).
- [132] Samuel Yuan. “Further investigation of laminar flow in channels with porous walls”. In: *Journal of Applied physics* 27.3 (1956), pp. 267–269 (cit. on p. 52).
- [133] Sahar Zare and Ali Kargari. “Membrane properties in membrane distillation”. In: *Emerging Technologies for Sustainable Desalination Handbook* (2018), pp. 107–156 (cit. on p. 48).
- [134] Edward Zeller and John Wray. “Factors influencing precipitation of calcium carbonate”. In: *AAPG Bulletin* 40.1 (1956), pp. 140–152 (cit. on p. 15).
- [135] Wenwen Zhou, Lianfa Song, and Tay Kwee Guan. “A numerical study on concentration polarization and system performance of spiral wound RO membrane modules”. In: *Journal of Membrane Science* 271.1-2 (2006), pp. 38–46 (cit. on pp. 49, 56, 63, 141).
- [136] Pierpaolo Zuddas, Katavut Pachana, and Damien Faivre. “The influence of dissolved humic acids on the kinetics of calcite precipitation from seawater solutions”. In: *Chemical Geology* 201.1-2 (2003), pp. 91–101 (cit. on p. 15).
- [137] Abdul Karim Zulhairun, Mohd Sohaimi Abdullah, Ahmad Fauzi Ismail, and Pei Sean Goh. “Graphene and CNT technology”. In: *Current Trends*

and Future Developments on (Bio-) Membranes. Elsevier, 2019, pp. 3–26 (cit. on p. 102).